Conjugate Natural Convection Heat Transfer In Vertical Concentric Annuli

by

Aboubakr Ahmed Ali Negm

A Thesis Presented to the

FACULTY OF THE COLLEGE OF GRADUATE STUDIES

KING FAHD UNIVERSITY OF PETROLEUM & MINERALS

DHAHRAN, SAUDI ARABIA

In Partial Fulfillment of the
Requirements for the Degree of

MASTER OF SCIENCE

In

MECHANICAL ENGINEERING

May, 1998

INFORMATION TO USERS

This manuscript has been reproduced from the microfilm master. UMI films the text directly from the original or copy submitted. Thus, some thesis and dissertation copies are in typewriter face, while others may be from any type of computer printer.

The quality of this reproduction is dependent upon the quality of the copy submitted. Broken or indistinct print, colored or poor quality illustrations and photographs, print bleedthrough, substandard margins, and improper alignment can adversely affect reproduction.

In the unlikely event that the author did not send UMI a complete manuscript and there are missing pages, these will be noted. Also, if unauthorized copyright material had to be removed, a note will indicate the deletion.

Oversize materials (e.g., maps, drawings, charts) are reproduced by sectioning the original, beginning at the upper left-hand corner and continuing from left to right in equal sections with small overlaps. Each original is also photographed in one exposure and is included in reduced form at the back of the book.

Photographs included in the original manuscript have been reproduced xerographically in this copy. Higher quality 6" x 9" black and white photographic prints are available for any photographs or illustrations appearing in this copy for an additional charge. Contact UMI directly to order.

UMI

A Bell & Howell Information Company
300 North Zeeb Road, Ann Arbor MI 48106-1346 USA
313/761-4700 800/521-0600

Conjugate Natural Convection Heat Transfer in Vertical Cconcentric Annuli

BY

Aboubakr Ahmed Ali Negm

A Thesis Presented to the

FACULTY OF THE COLLEGE OF GRADUATE STUDIES

KING FAHD UNIVERSITY OF PETROLEUM & MINERALS

DHAHRAN, SAUDI ARABIA

In Partial Fulfillment of the
Requirements for the Degree of

MASTER OF SCIENCE

In

MECHANICAL ENGINEERING

May 1998

Conjugate Natural Convection Heat Transfer in Vertical Concentric Annuli

by

AbouBakr Ahmed Ali Negm

A Thesis Presented to the
FACULTY OF COLLEGE OF GRADUATE STUDIES

In Partial Fulfillment of the Requirements
for the degree

MASTER OF SCIENCE

IN

Mechanical Engineering

KING FAHD UNIVERSITY OF PETROLEUM AND MINERALS

Dhahran, Saudi Arabia

May 17, 1998

KING FAHD UNIVERSITY OF PETROLEUM AND MINERALS
DHAHRAN, SAUDI ARABIA

This thesis, written by

Aboubakr Ahmed Ali Negm

under the direction of his Thesis Advisor, and approved by his Thesis committee, has been presented to and accepted by the Dean, College of Graduate Studies, in partial fulfillment of the requirements for the degree of

MASTER OF SCIENCE IN MECHANICAL ENGINEERING

Thesis Committee:

Maged El-Sharaawi Aug 23, 1998

Dr. Maged El-Sharaawi (Chairman)

Dr. Mohammed Budair (member)

Saad Ahmed

Dr. Saad Ahmed (member)

Dr. Mohammad O. Budair
Department Chairman

Dean, College of Graduate Studies

كلية الدراسات العليا
COLLEGE OF GRADUATE STUDIES

Date: 25/5/98

THESIS ABSTRACT

NAME OF STUDENT :ABOUBAKR AHMED ALI NEGM

TITLE OF STUDY : **Conjugate Natural Convection Heat Transfer in Vertical Concentric Annuli**

MAJOR FIELD : **Mechanical Engineering**

DATE OF DEFENCE : **May 17, 1998**

The problem of combined conduction with natural convection heat transfer in vertical concentric annuli has been investigated numerically using an implicit finite-difference scheme. Both the transient and steady-state heat transfer have been considered in this investigation. The effects of the three main controlling parameters, namely. modified Grashof Number (Gr^*), thermal conductivity ratio (K_R) and thermal diffusivity ratio (α_R) have been presented over wide ranges of these parameters. The study showed that K_R and α_R have prominent effects on the flow characteristics as well as on the heat transfer. Moreover, at the values of K_R =100 and α_R =1000 the conduction effect on the heat transfer becomes negligible and for such values the results of the conventional case can be used with an acceptable accuracy.

MASTER OF SCIENCE

KING FAHD UNIVERSITY OF PETROLEUM AND MINERALS

Dhahran, Saudi Arabia

May 17, 1998

ملخص الرسالة

اسم الطالب : أبوبكر أحمد على نجم

عنوان الرسالة : تأثير التوصيل الحرارى فى جدار اسطوانتين مركزيتين على الحمل الحرارى المتولد بينهما

التخصص : الهندسة الميكانيكية

تاريخ الشهادة : ١٧ مايو ١٩٩٨

لقد تمت دراسة تأثير التوصيل الحرارى فى جدار اسطوانتين مركزيتين على الحمل الحرارى الحر المستقر والغير مستقر المتولد بينهما باستخدام طريقة الفروق العددية المحدودة. فى هذا البحث تم دراسة تأثير الخواص الحرارية لجدار الأسطوانة على سريان المائع وعلى انتقال الحرارة، وتعتمد الدراسة على قوانين حفظ المادة و الطاقة بعد تبسيطها باستخدام نظرية الطبقة المتاخمة وافتراض ثبات جميع خصائص المائع الفيزيائية وعدم اعتمادها على درجة الحرارة ما عدا الكثافة.

ولقد تم دراسة تأثير كل من رقم جراشوف والنسبة بين معامل التوصيل الحرارى لجدار الأسطوانة الى معامل التوصيل الحرارى للمائع وايضا النسبة بين معامل الأنتشارية الحرارية لجدار الأسطوانة الى معامل الأنتشارية الحرارية للمائع على نطاق واسع. وقد أظهرت الدراسة أن الخواص الحرارية لجدار الأسطوانة لها تأثير ملحوظ على سريان المائع وعلى انتقال الحرارة.

درجة الماجستير فى العلوم

جامعة الملك فهد للبترول والمعادن

الظهران، المملكة العربية السعودية

١٧ مايو ١٩٩٨ م

TO MY PARENTS

ACKNOWLEDGMENTS

First and foremost, all praise to Almighty God who gave me the courage and patience to carry out this work. I am happy to have had a chance to glorify his name in the sincerest way through this small accomplishment and ask Him to accept my efforts. May He guide us and the whole humanity to the right path(Aameen).

Acknowledgment is due to King Fahd University of Petroleum and Minerals for the support provided to carry out this research.

My deep appreciation goes to my major thesis advisor Dr. Maged El-Sharaawi for his constant help, guidance and the countless hours of attention he devoted throughout the course of this work. His priceless suggestions made this work interesting and learning for me. He was always kind, understanding and sympathetic to me. Working with him was indeed a wonderful and learning experience which I thoroughly enjoyed. Thanks are also due to my thesis committee members Dr. Mohamed Budair and Dr. Saad Ahmed for their interest, cooperation, advice and constructive criticism.

Lastly, but not the least, thanks are due to my family members especially my parents for their continuous encouragment and support.

TABLE OF CONTENTS

LIST OF FIGURES

LIST OF TABLES

NOMENCLATURE

a local heat transfer coefficient $\left(\frac{q}{T_w - T_o}\right)$

$\overline{a}$ average heat transfer coefficient over the annulus height $\left(\frac{\overline{h}}{\pi D_w l (T_w - T_o)}\right)$

b annular gap width$(r_3 - r_2)$

c_f specifice heat of the fluid at constant pressure

c_s specifice heat of the solid

D hydraulic diamater of the annulus$(2b)$

f volumetric flow rate $\left(\int_{r2}^{r3} 2\pi r u dr = \pi (r_3^2 - r_2^2) u_o\right)$

f_{ss} steady-state value of f

F dimensionless volumetric flow rate $\left(\frac{f}{\pi l \nu Gr^*}\right)$

F_{ss} steady-state value of F, $(1 - N_2^2) U_{oss}$

F_{fd} fully developed value of F

g gravitational accelaration

Gr Grashof number $\left(\frac{g\beta (T_w - T_o) D^3}{\nu^2}\right)$

Gr^* modified Grashof number $\left(\frac{GrD}{l}\right)$

h heat absorbed by the fluid from the entrance up to a particular elevation$(\rho_o f C_p (T_m - T_o))$

h_t heat absorbed by the fluid from the entrance up to the annulus exit$(\rho_o f C_p (T_{m,e} - T_o))$

H dimensionless heat absorbed from the entrance up to a particaular elevation

H_t dimensionless heat absorbed by the fluid from the entrance up to the annulus exit

$$\frac{h_t}{\pi \rho_o C_p l \nu Gr^* (T_w - T_o)} = F\theta_{m,e} = \int_{N_2}^{1} UR\theta_{m,e} dR$$

k number of time steps needed to reach steady-state conditions

k_f thermal conductivity of the fluid

k_s thermal conductivity of the solid

K_R thermal conductivity ratio $\left(\frac{k_s}{k_f}\right)$

l annulus height

L dimensionless annulus height $(\frac{1}{Gr^*})$

n number of radial increments in the fluid

$ns1$ number of radial increments in the inner wall

$ns2$ number of radial increments in the outer wall

N_1 $\left(\frac{r_1}{r_3}\right)$

N_2 $\left(\frac{r_2}{r_3}\right)$

N_4 $\left(\frac{r_4}{r_3}\right)$

p pressure of the fluid inside the annulus at any cross section

$\acute{p}$ pressure defect at any point$(p - p_s)$

p_o pressure of fluid at the annulus entrance$\left(-\frac{1}{2}\rho_o u_o^2\right)$

p_s hydrostatic pressure$(-\rho_o g z)$

P dimensionless pressure at any point$\left(\frac{\acute{p} r_3^4}{\rho_o l^2 \nu^2 Gr^{*2}}\right)$

P_o dimensionless pressure at the annulus entrance point$\left(\frac{\acute{p}_o r_3^4}{\rho_o l^2 \nu^2 Gr^{*2}}\right)$

Pr Prandtl number

r radial coordinate

r_1 inner radius of the inner tube

r_2 outer radius of the inner tube

r_3 inner radius of the outer tube

r_4 outer radius of the outer tube

R dimensionless radial coordinate$\left(\frac{r}{r_3}\right)$

t dimensionless time$\left(\frac{\tau \nu}{r_3^2}\right)$

t_{ss} dimensionless steady-state time$\left(\frac{\tau_{ss} \nu}{r_3^2}\right)$

T temperature

T_{ad} adiabatic surface temperature(inner surface of the inner tube)

T_f fluid temperature at any point inside the annulus

T_m mixing-cup temperature over any cross-section $\left[\frac{\int_{r_2}^{r_3} rutdr}{\int_{r_2}^{r_3} rudr}\right]$

$T_{m,e}$ mixing-cup temperature at the annulus exit

T_o fluid temperature at the annulus entrance

T_s solid walls temperature at any point

T_w temperature of the outer surface of the outer tube wall
u axial velocity component at any point
u_o axial velocity at the annulus entrance
U dimensionless axial velocity component at any point
U_o dimensionless axial velocity at the annulus entrance
v radial velocity component at any point
V dimensionless radial velocity at any point $\left(\frac{vr_3}{\nu}\right)$
z axial coordinate
Z dimensionless axial coordinate $\left(\frac{z}{lGr^*}\right)$

Greek symbols

α_f thermal diffusivity of the fluid
α_s thermal diffusivity of the solid
α_R thermal diffusivity ratio, $\frac{\alpha_s}{\alpha_f}$
ΔR_f radial increment in the fluid region
ΔR_s radial increment in the solid media
θ dimensionless temperature $\left(\frac{T-T_o}{T_w-T_o}\right)$
θ_{ad} dimensionless temperature of the adiabatic surface $\left(\frac{T_{ad}-T_o}{T_w-T_o}\right)$
θ_f fluid temperature
θ_s solid media temperature
θ_m dimensionless mixing-cup temperature at any cross-section $\left(\frac{T_m-T_o}{T_w-T_o}\right)$
$\theta_{m,e}$ dimensionless mixing-cup temperature at exit cross-section $\left(\frac{T_{m,e}-T_o}{T_w-T_o}\right)$
μ dynamic fluid viscosity
ν kinematic viscosity
ρ density
ρ_o fluid density at the inlet fluid temperature T_o
τ time
τ_{ss} steady-state time

CHAPTER 1

INTRODUCTION

The study of both transient and steady induced flow in concentric annuli with conjugate heat transfer is of great importance because of its many engineering applications. Design calculations and performance parameters of heat exchangers are usually based on the steady-state heat transfer values. However, processes which require the evaluation of the performance of thermal equipment in the transient free convection regime include start-up, shut down, pump failure, etc.

Considerable interest has been shown recently in the problem of natural convection heat transfer to fluids in heated, vertical, open-ended concentric annuli. Such systems are of practical importance in the field of double pipe heat exchangers. A typical application is that of gas cooled nuclear reactor, in which cylinderical fissionable fuel elements are placed axially in vertical coolant channels within the graphite moderator; the cooling gas is flowing along the channel parallel to the fuel element. In such a system, laminar free convection may provide the sole means of the necessary cooling during the shut down or accident periods.

Most of the work which handeled the problem of natural laminar convection (transient and steady) in open-ended vertical concentric annuli did not consider the effect of the wall thickness and the finite thermal conductiviy of the wall. Instead, most of the researchers used to solve the problem of natural laminar flow in open-ended ducts (like annuli) assuming high thermal conductivity and/or very small wall thickness. Thus, depending on these assumptions, they were able to neglect the effect of the thermal resistance of the wall. But in practical industrial applications, the situation is usually different as the wall thermal conductivity is usually finite and the wall may be thick. Accordingly, the neglect of the wall thermal resistance effect would lead difinitely to wrong results.

The present work is concerned with the study of combined conduction and natural laminar convection in open ended vertical concentric annuli. An implicite finite-difference scheme has been developed to study the conjugate effect on transient and steady natural convection in concentric annuli whose outer surface of the outer tube is subjected to a step-temperature change while the inner surface of the inner tube is kept adiabatic.

The literature review is presented in chapter two while the problem formulation and the initial and the boundary conditions are presented in chapter three. In chapter four, the numerical methodology of the solution is given in detail. The results of the transient case are presented and discussed in chapter five while the results for the steady case are presented and discussed in chapter six. Finally conclusions are reported in chapter seven.

CHAPTER 2

LITERATURE REVIEW

Steady natural convection heat transfer is of great importance in the design of modern free convection heat exchange devices. However, processes which require the evaluation of the performance of thermal equipment in the transient free convection regime include start-up, shut-down, pump failure, etc. Despite of many investigations available in the literature concerning steady and transient forced, natural and mixed-convection flows in vertical concentric annuli, no investigations seem to be available for steady or transient natural flow with conjugate heat transfer for this particular geometry.

Therefore, this survey will consider the research which handled natural flow with conjugate heat transfer in other relevant geometries.

2.1 Natural Convection Besides Flat Plate

Due to its simplicity, the laminar free convection of a Newtonian fluid heated by a vertical conducting flat plate of finite thickness has received much attention[1-8]. Zinnes [1] investigated, using finite-difference techniques, the steady, constant-property, two-dimensional,

laminar natural convection from a vertical flat plate with arbitrary surface heating. The obtained results indicated that the degree of coupling between conduction in the plate and natural convection in the fluid is greatly influenced by the plate-fluid conductivity ratio. Miyamoto et al. [2] investigated experimentally and analytically, using the method of local similarity solution of free convection boundary layer, the steady two dimensional conjugate heat-transfer problem of free convection from a vertical flat plate. They provided both experimental results and an approximate solution valid for a boundary-layer regime. Pozzi and Lupo [3] investigated analytically the coupling of conduction with laminar natural convection along a flat plate. They studied the two cases of isothermal and constant heat flux walls using the method of two expansions. The first one, describing the field in the lower part of the plate, was a regular series. The second expansion, an asymptotic one, required a different analysis because of the presence of eigensolutions, after that the two solutions were coupled.

Lee and Yovanovich [4] studied the problem of conjugate heat transfer from a vertical plate with discrete heat sources under natural convection. The plate was located in an extensive, quiescent fluid which is maintained at uniform temperature. Their model consisted of an approximate analytical boundary-layer solution and a one dimensional numerical conduction analysis in which an allowance is made to account for radiation heat transfer. The fluid and solid solutions were coupled through an iterative procedure, and the conjugate problem is solved when a converged temperature distribution is obtained at the plate-fluid interface, concurrently satisfying the thermal fields on both sides of the interface. Chen and

Lee [5] used a simple computational method for conjugate conduction-natural convection along a vertical plate fin. They casted the governing boundary-layer equations with their corresponding boundary conditions as well as the one-dimensional heat conduction equation in the fin with its negligible tip leakage into dimensionless forms by a non-similarity transformation. They solved the resulting system of equations numerically by using the central finite-difference approximation and the local non-similarity method. Yu and Lin [6] investigated numerically the conjugate problems of conduction and free convection on vertical and horizontal flat plates. They provided correlation equations for the local Nusselt number, from which, the local interface temperature and heat transfer rate can be estimated. Vynnycky and Kimura [7] investigated numerically and analytically the problem of conjugate free convection due to a heated vertical plate. They studied the effect of many parameters like Rayleigh and Prandtl numbers and the effect of the leading edge. They obtained results for a wide range of the non-dimensional parameters that are present in the problem, namely, the Rayleigh number, the Prandtl number, the thermal conductivity ratio between the plate and the fluid medium and the plate aspect ratio. Merkin and Pop [8] investigated numerically the problem of conjugate free convection on a vertical surface for three values of Prandtl number, namely, 0.7, 0.72 and 0.733.

2.2 Two Natural Convection Systems Separated by a Thick Wall

For two natural-convection systems separated by a vertical flat plate of finite thickness, Kelleher and Yang [9] studied analytically the problem of conduction in a heat-generating

slab combined with free convection from both sides. Lock and Ko [10] studied numerically the problem of coupling through a wall between free convection systems. More detailed discussions on the same problem were reported by Anderson and Bejan [11].

Viskanta and Lankford [12] investigated the same problem analytically and verified their results experimentally using air at atmospheric pressure as the test fluid. Sakakibara et al. [13] studied the conjugate heat transfer between two natural convection systems separated by a vertical plate. They obtained the temperature distribution in the fluid flow numerically and in the plate analytically. They combined the two solutions to satisfy the continuity of the temperature and the heat flux at both sides of the conducting wall. To verify their results, they conducted experiments for air-air systems with the conducting wall made of aluminum or glass. They found that the theoretical predictions describe well the experimental temperature distributions.

2.3 Confined Natural Convection Flows

Using the finite-difference technique, Burch et al. [14] investigated the laminar natural convection between finitely conducting vertical plates for three values of Grashof number (10, 10^3 and 10^6), two wall-to-fluid conductivity ratios(1 and 10), three channel height-to-width ratios(0.5, 1 and 5) and two wall thickness-to-width ratios(0.1 and 0.5). Their results showed that conduction has a significant effect on the natural convection heat transfer, particularly at high Grashof number, low solid-to-fluid conductivity ratios and high wall thickness-to-channel width ratios. Yeh et al. [15] solved numerically the conjugate laminar

natural convection between finitely top heating vertical channel flow. They studied the effects of Grashof number, fluid-to-wall conductivity ratio, and the channel height-to-width ratios on heat transfer phenomena between the plates. They found that conduction has a significant influence on the total heat transfer rate, particularly at high Grashof numbers and high fluid-to-wall conductivity ratios.

Lacroix and Joyeux [16] investigated numerically the natural convection heat transfer for air from two vertically separated horizontal heated cylinders confined to a rectangular enclosure having vertical walls of finite conductance and horizontal walls at the heat sink temperature. They obtained results for a wide range of Rayleigh number, different values of wall-fluid thermal conductivity ratio and different values of wall thickness. Molki and Faghri [17] used a finite-difference method based on the control volume approach to investigate the natural convection heat transfer in a vertical annular enclosure with circumferential fins mounted on the inner cylinder. Heat was generated within the inner solid cylinder, while the top, the bottom and the outer walls were exposed to convection. Their results showed that the presence of the fins reduced the mean temperature of the inner cylinder by maximum of 9.6% at low Raleigh numbers.

For transient conduction-convection heat transfer, Huang and Aggarwal [18] investigated numerically, using the finite-volume method, the effect of wall conduction on transient natural convection in an enclosure with a centered heat source. They studied the effect of the wall thickness, the Rayleigh number, the wall thermal conductivity ratio, the diffusivity ratio and the varying outside wall thermal boundary conditions. Their results indi-

cated that the qualitative features of natural convection heat transfer in the laminar range are not significantly altered by the inclusion of wall conduction. On the other hand, the quantitative results may be significantly modified by the wall conductance. Moreover, the wall conduction reduces the rate of heat dissipation from the enclosure and the average Nusselt number decreases as the wall thickness ratio is increased and/or the wall thermal conductivity ratio is reduced. Kimura et al. [19] investigated numerically the effects of the ratio of thermal conductivity of an inner body to that of the confined working fluid on the natural convection heat transfer in an inclined rectangular enclosure having two adiabatic walls and two isothermal walls at two different temperatures. They presented results for a fluid of Pr = 10, Rayleigh number in the range $5 \times 10^4 \sim 5 \times 10^6$ and different angles of inclination. They verified their results by conducting experiments using water as the working medium and bakelite or brass plate for the inner body. Sun and Emery [20] investigated numerically, using the finite-volume method, the effect of the wall thermal conductivity and internal heat sources on the natural convection in a rectangular enclosure. In this study they clarified that the average Nusselt number increases with the increase in the wall thermal conductivity. Moreover, the existence of conducting baffle reduces the overall heat transfer. However, when the baffle is adiabatic or when the convection dominates the flow due to a high level of internal heating, heat is transferred by convection no matter what is the value of the baffle conductivity.

To the best of the writer knowledge, the conjugate natural convection heat transfer (transient and steady-state) in open-ended vertical concentric annuli has not been investigated yet.

CHAPTER 3

PROBLEM FORMULATION

In this chapter, the governing equations which describe the case under consideration are given and the boundary conditions are stated. Since the governing equations are elliptic, nonlinear and strongly coupled partial differential equations, the following assumptions are imposed to facilitate the solution of the problem under consideration. Firstly, some assumptions related to the fluid and the flow are imposed on the momentum and the energy equations. Secondly, the boundary-layer approximations will be used to neglect the second derivative of the axial velocity component in the streamwise direction, the streamwise diffusion of heat, and the entire momentum equation in the transverse direction. This is done using the order of magnitude analysis. Finally, the boundary-layer equations are casted in dimensionless form to have the least possible number of computer runs and the most general numerical results.

3.1 GOVERNING EQUATIONS

Figure 3.1 depicts the geometry and coordinate system. The geometry considered in this study is a vertical annulus of finite length, open at both ends with considerable inner and outer tube thickness. The annulus is immersed in a fluid of infinite extent maintained at a constant temperature T_o. After a step rise in the temperature of the outer surface of the outer tube, the fluid rises in the annular gab between the cylindrical walls by natural convection and continue moving upward until it reaches the annulus exit. It is assumed that the time dependent entrance velocity has a uniform profile. The problem is solved for both transient and steady situations. The following assumptions related to the geometry, physical properties of the fluid and flow conditions are imposed.

1. The fluid is Newtonian.
2. The flow is axisymmetric ($\frac{\partial}{\partial\theta} = 0$).
3. The tangential (θ direction) velocity component is zero everywhere.
4. There are no internal heat generation in both the fluid and solid media.
5. Viscous dissipation and radial and tangential body forces are neglected.
6. The fluid physical properties (C_p, ρ, μ and k) are constants but Boussinesq approximation is valid according to which the density varies in only the buoyancy term in the momentum equation.

Applying the above assumptions give the following governing equations.

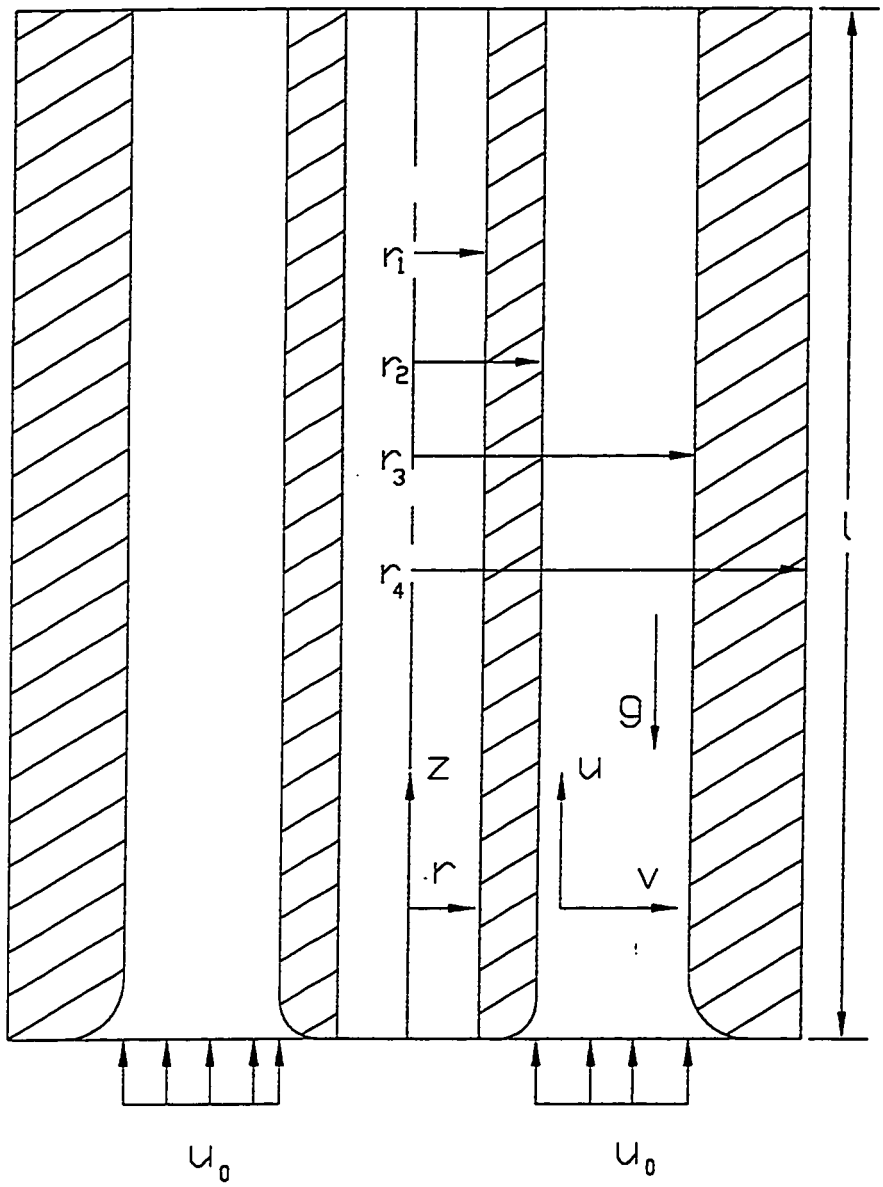

Figure 3.1: Schematic diagram of the annulus

3.1.1 For The Transient Case

- **Continuity**

$$\frac{1}{r}\frac{\partial}{\partial r}(rv) + \frac{\partial u}{\partial z} = 0 \tag{3.1a}$$

- **Radial Momentum**

$$\rho_o\left[\frac{\partial v}{\partial \tau} + v\frac{\partial v}{\partial r} + u\frac{\partial v}{\partial z}\right] = -\frac{\partial p}{\partial r} + \mu\left[\frac{\partial}{\partial r}\left(\frac{1}{r}\frac{\partial}{\partial r}(rv)\right) + \frac{\partial^2 v}{\partial z^2}\right] \tag{3.2a}$$

- **Axial Momentum**

$$\rho_o\left[\frac{\partial u}{\partial \tau} + v\frac{\partial u}{\partial r} + u\frac{\partial u}{\partial z}\right] = F_z - \frac{\partial p}{\partial z} + \mu\left[\frac{1}{r}\frac{\partial}{\partial r}\left(r\frac{\partial u}{\partial r}\right) + \frac{\partial^2 u}{\partial z^2}\right] \tag{3.3a}$$

- **Energy**

$$\frac{\partial T}{\partial \tau} + v\frac{\partial T}{\partial r} + u\frac{\partial T}{\partial z} = \alpha\left[\frac{1}{r}\frac{\partial}{\partial r}\left(r\frac{\partial T}{\partial r}\right) + \frac{\partial^2 T}{\partial z^2}\right] \tag{3.4a}$$

- **Conduction**

$$\frac{1}{r}\frac{\partial}{\partial r}\left(r\frac{\partial T}{\partial r}\right)+\frac{\partial^2 T}{\partial z^2}=\frac{1}{\alpha}\left[\frac{\partial T}{\partial \tau}\right] \tag{3.5a}$$

3.1.2 For The Steady-State Case

The equations representing the steady-state case can be obtained by putting $\frac{\partial}{\partial t}=0$ in the above equations. Thus, one obtains the following:

- **Continuity**

$$\frac{1}{r}\frac{\partial}{\partial r}(rv)+\frac{\partial u}{\partial z}=0 \tag{3.1b}$$

- **Radial Momentum**

$$\rho_o\left[v\frac{\partial v}{\partial r}+u\frac{\partial v}{\partial z}\right]=-\frac{\partial p}{\partial r}+\mu\left[\frac{\partial}{\partial r}\left(\frac{1}{r}\frac{\partial}{\partial r}(rv)\right)+\frac{\partial^2 v}{\partial z^2}\right] \tag{3.2b}$$

- **Axial Momentum**

$$\rho_o\left[v\frac{\partial u}{\partial r}+u\frac{\partial u}{\partial z}\right]=F_z-\frac{\partial p}{\partial z}+\mu\left[\frac{1}{r}\frac{\partial}{\partial r}\left(r\frac{\partial u}{\partial r}\right)+\frac{\partial^2 u}{\partial z^2}\right] \tag{3.3b}$$

- **Energy**

$$v\frac{\partial T}{\partial r}+u\frac{\partial T}{\partial z}=\alpha\left[\frac{1}{r}\frac{\partial}{\partial r}\left(r\frac{\partial T}{\partial r}\right)+\frac{\partial^2 T}{\partial z^2}\right] \tag{3.4b}$$

- **Conduction**

$$\frac{1}{r}\frac{\partial}{\partial r}\left(r\frac{\partial T}{\partial r}\right)+\frac{\partial^2 T}{\partial z^2}=0 \tag{3.5b}$$

As the flow is natural and confined, the pressure p, within the annulus, will be less than the hydrostatic ambient pressure, at the same elevation. The difference between the two pressures is known as the pressure defect (ṕ). Noting that $F_z=-\rho g$, $\rho=\rho_o\left[1-\beta(T-T_o)\right]$, and $p=\acute{p}+\rho_o g z$, the axial momentum can be rewritten in terms of the coefficient of thermal expansion $(\beta)$and the pressure defect $(\acute{p})$ as follows.

$$\frac{\partial u}{\partial \tau}+v\frac{\partial u}{\partial r}+u\frac{\partial u}{\partial z}=-\frac{1}{\rho_o}\frac{\partial \acute{p}}{\partial z}+g\beta(T-T_o)+\nu\left[\frac{1}{r}\frac{\partial}{\partial r}\left(r\frac{\partial u}{\partial r}\right)+\frac{\partial^2 u}{\partial z^2}\right] \tag{3.6a}$$

$$v\frac{\partial u}{\partial r}+u\frac{\partial u}{\partial z}=-\frac{1}{\rho_o}\frac{\partial \acute{p}}{\partial z}+g\beta(T-T_o)+\nu\left[\frac{1}{r}\frac{\partial}{\partial r}\left(r\frac{\partial u}{\partial r}\right)+\frac{\partial^2 u}{\partial z^2}\right] \tag{3.6b}$$

3.1.3 Boundary Conditions

The problem in hand is solved under the following conditions.

3.1.3.1 For The Transient Case

For $\tau \leq 0$

$u = 0, \quad v = 0, \quad \text{and} \quad T = T_o \quad$ everywhere

For $\tau > 0$

At $z = 0$ and $r_2 < r < r_3$

$u = u_o(\tau), \quad v = 0, \quad and \quad T = T_o$

At $z = 0$ and $r_1 \leq r \leq r_2$ and $r_3 \leq r \leq r_4$

$T = T_o$

At $z > 0$ and $r = r_2$ and $r = r_3$

$u = 0$ and $v = 0$ (no slip condition)

At $z > 0$ and $r = r_1$

$\frac{\partial T_s}{\partial r} = 0$ (adiabatic inner surface of the inner tube)

At $z > 0$ and $r = r_4$

$T_s = T_w$ (isothermal outer surface of the outer tube)

At $z > 0$ and $r = r_2$ and $r = r_3$

$k_s \frac{\partial T_s}{\partial r} = k_f \frac{\partial T_f}{\partial r}, \quad T_f = T_s$

At $z = l \quad p = 0$

3.1.3.2 For The Steady-State Case

At $z = 0$ and $r_2 < r < r_3$

$u = u_o, \quad v = 0, \quad and \quad T = T_o$

At $z = 0$ and $r_1 \leq r \leq r_2$ and $r_3 \leq r \leq r_4$

$T = T_o$

At $z > 0$ and $r = r_2$ and $r = r_3$

$u = 0$ and $v = 0$ (no slip condition)

At $z > 0$ and $r = r_1$

$\frac{\partial T_s}{\partial r} = 0$ (adiabatic inner surface of the inner tube)

At $z > 0$ and $r = r_4$

$T_s = T_w$ (isothermal outer surface of the outer tube)

At $z > 0$ and $r = r_2$ and $r = r_3$

$k_s \frac{\partial T}{\partial r} = k_f \frac{\partial T}{\partial r}, \quad T_f = T_s$

At $z = l$ $\quad p = 0$

3.2 BOUNDARY-LAYER EQUATIONS

It is well known that, the Navier-Stockes equations are in general elliptic, non-linear and strongly coupled. They are, therefore, extremely difficult to solve. Also, the presence of the conduction effect increases the degree of difficulty as we need to solve the fluid and wall governing equations simultaneously. Therefore, several simplifications, based on physical grounds, are made to reduce the effort of obtaining solutions. The most important simplification, from engineering point of view, was first accomplished by Prandtl (a prominent German scientist) in 1904. He introduced the concept of boundary-layer which permits the reduction of the governing equations to simpler forms(parabolic type equa-

tions) known as the boundary-layer equations. Reference may be made to Schlichting [21] for details of the boundary-layer theory and its assumptions. To obtain the boundary-layer equations from the original equations, the latter are made dimensionless by referring all the variables present in the governing equations to certain characteristic reference variables. Then the order of magnitude of each term can be checked and terms of lower order of magnitude can be dropped resulting in the so-called boundary-layer equations. Applying this procedure to the governing equations and neglecting the axial diffusion of the heat compared with the radial diffusion, the resulting governing equations, representing the case under consideration, as derived in appendix (A), are:

3.2.1 For The Transient Case

- **Continuity**

$$\frac{1}{r}\frac{\partial}{\partial r}(rv) + \frac{\partial u}{\partial z} = 0 \tag{3.7a}$$

- **Momentum**

$$\frac{\partial u}{\partial \tau} + v\frac{\partial u}{\partial r} + u\frac{\partial u}{\partial z} = -\frac{1}{\rho_o}\frac{dp}{dz} + g\beta(T - T_o) + \nu\left[\frac{1}{r}\frac{\partial}{\partial r}\left(r\frac{\partial u}{\partial r}\right)\right] \tag{3.8a}$$

- **Energy**

$$\frac{\partial T}{\partial \tau} + v\frac{\partial T}{\partial r} + u\frac{\partial T}{\partial z} = \alpha\left[\frac{1}{r}\frac{\partial}{\partial r}\left(r\frac{\partial T}{\partial r}\right)\right] \tag{3.9a}$$

- **Conduction**

$$\frac{1}{r}\frac{\partial}{\partial r}\left(r\frac{\partial T}{\partial r}\right) = \frac{1}{\alpha}\left[\frac{\partial T}{\partial \tau}\right] \tag{3.10a}$$

3.2.2 For The Steady-State Case

- **Continuity**

$$\frac{1}{r}\frac{\partial}{\partial r}(rv) + \frac{\partial u}{\partial z} = 0 \tag{3.7b}$$

- **Momentum**

$$v\frac{\partial u}{\partial r} + u\frac{\partial u}{\partial z} = -\frac{1}{\rho_o}\frac{\partial p}{\partial z} + \nu\left[\frac{1}{r}\frac{\partial}{\partial r}\left(r\frac{\partial u}{\partial r}\right)\right] \tag{3.8b}$$

- **Energy**

$$v\frac{\partial T}{\partial r} + u\frac{\partial T}{\partial z} = \alpha\left[\frac{1}{r}\frac{\partial}{\partial r}\left(r\frac{\partial T}{\partial r}\right)\right] \tag{3.9b}$$

- **Conduction**

$$\frac{1}{r}\frac{\partial}{\partial r}\left(r\frac{\partial T}{\partial r}\right) = 0 \tag{3.10b}$$

3.3 DIMENSIONLESS GOVERNING EQUATIONS

To reduce the computational effort and the time required for the numerical solution of the obtained governing equations, these equations (with their boundary conditions) should be put in dimensionless forms in a way that the least number of dimensionless numbers appear in the final forms. This makes the solution more general as possible and prevents the need for large number of computer runs. The dimensionless forms of equations (7-10) which are presented in appendix (A) are not good enough because they contain the Reynolds, Grashof and Prandtl numbers; this will make a restriction on the solution (from each computer run) to be for only one value of each of these numbers. Therefore, the following dimensionless parameters are used.

$$R = \frac{r}{r_3}, \qquad Z = \frac{z}{lGr^*}$$

$$V = \frac{vr_3}{\nu}, \qquad U = \frac{ur_3^2}{l\nu Gr^*}$$

$$P = \frac{\acute{p}r_3^4}{\rho_o l^2 \nu^2 (Gr^*)^2}, \qquad F = \frac{f}{\pi l Gr^* \nu}$$

$$\theta = \frac{T - T_o}{T_w - T_o} \qquad t = \frac{\tau \nu}{r_3^2}$$

Inserting these parameters in equations (7-10) and rearranging the terms, the following dimensionless forms of the governing equations can be obtained.

3.3.1 For The Transient Case

- **Continuity**

$$\frac{V}{R}+\frac{\partial V}{\partial R}+\frac{\partial U}{\partial Z}=0 \qquad (3.11a)$$

- **Momentum**

$$\frac{\partial U}{\partial t}+V\frac{\partial U}{\partial R}+U\frac{\partial U}{\partial Z}=-\frac{dP}{dZ}+\frac{\theta_f}{16(1-N_2)^4}+\frac{1}{R}\frac{\partial}{\partial R}\left(R\frac{\partial U}{\partial R}\right) \qquad (3.12a)$$

- **Energy**

$$\frac{\partial \theta_f}{\partial t}+V\frac{\partial \theta_f}{\partial R}+U\frac{\partial \theta_f}{\partial Z}=\frac{1}{\mathrm{Pr}}\left[\frac{1}{R}\frac{\partial}{\partial R}\left(R\frac{\partial \theta_f}{\partial R}\right)\right] \qquad (3.13a)$$

- **Conduction**

$$\frac{1}{R}\frac{\partial}{\partial R}\left(R\frac{\partial \theta_s}{\partial R}\right)=\frac{\mathrm{Pr}}{\alpha_R}\frac{\partial \theta_s}{\partial t} \qquad (3.14a)$$

3.3.2 For The Steady-State Case

- **Continuity**

$$\frac{V}{R}+\frac{\partial V}{\partial R}+\frac{\partial U}{\partial Z}=0 \qquad (3.11b)$$

- **Momentum**

$$V\frac{\partial U}{\partial Z}+U\frac{\partial U}{\partial Z}=-\frac{dP}{dZ}+\frac{\theta_f}{16(1-N_2)^4}+\frac{1}{R}\frac{\partial}{\partial R}\left(R\frac{\partial U}{\partial R}\right) \qquad (3.12b)$$

- **Energy**

$$V\frac{\partial \theta_f}{\partial R}+U\frac{\partial \theta_f}{\partial Z}=\frac{1}{\mathrm{Pr}}\left[\frac{1}{R}\frac{\partial}{\partial R}\left(R\frac{\partial \theta_f}{\partial R}\right)\right] \qquad (3.13b)$$

- **Conduction**

$$\frac{1}{R}\frac{\partial}{\partial R}\left(R\frac{\partial \theta_s}{\partial R}\right)=0 \qquad (3.14b)$$

Since the momentum equation in the r-direction has been eliminated due to the boundary-layer simplifications, another equation is needed to obtain the four unknowns V, U, P and θ. The volumetric flow rate can be written in terms of u_o as:

$$f=\int_{r_2}^{r_3}2\pi r.u.dr=\pi(r_3^2-r_2^2)u_o$$

When the dimensionless variables are substituted into this equation, the dimensionless volumetric flow rate becomes:

$$F=\frac{f}{\pi lGr^*\nu}=2\int_{N_2}^{1}R.U.dR=(1-N_2^2)U_o \qquad (3.15)$$

This equation together with equations (11-14) will be used to obtain numerical solutions for the combined conduction-natural convection heat transfer in a vertical concentric annulus.

3.3.3 Nondimensional Initial and Boundary Conditions

The initial and boundary conditions given in section 3.1 are rewritten hereunder in dimensionless forms.

3.3.3.1 For The Transient Case

For $t \leq 0$

$U = 0, \quad V = 0, \quad$ and $\quad \theta = 0 \quad$ everywhere

For $t > 0$

At $Z = 0$ and $R_2 < R < 1$

$U = U_o(t), \quad V = 0, \quad$ *and* $\quad \theta = 0$

At $Z = 0$ and $N_1 \leq R \leq N_2$ and $1 \leq R \leq N_4$

$\theta = 0$

At $Z > 0$ and $R = N_2$ and $R = 1$

$U = 0$ and $V = 0$ (no slip condition)

At $Z > 0$ and $R = N_1$

$$\frac{\partial \theta}{\partial R} = 0 \tag{3.16}$$

At $Z > 0$ and $R = N_2$ and $R = 1$

$$K_R \frac{\partial \theta_s}{\partial R} = \frac{\partial \theta_f}{\partial R}, \text{ and } \quad \theta_f = \theta_s \quad \text{(adiabatic inner surface of the inner tube)} \tag{3.17}$$

At $Z > 0$ and $R = N_4$

$\theta_s = 1$ (isothermal outer surface of the outer tube)

At $Z = L$ $P = 0$

3.3.3.2 For The Steady-State Case

At $Z = 0$ and $N_2 < R < 1$

$U = U_o$, $V = 0$, *and* $\theta = 0$

At $Z = 0$ and $N_1 \leq R \leq N_2$ and $1 \leq R \leq N_4$

$\theta = 0$

At $Z > 0$ and $R = N_2$ and $R = N_3$

$U = 0$ and $V = 0$ (no slip condition)

At $Z > 0$ and $R = N_1$

$\frac{\partial \theta_s}{\partial R} = 0$ (adiabatic inner surface of the inner tube)

At $Z > 0$ and $R = N_4$

$\theta_s = 1$ (isothermal outer surface of the outer tube)

At $Z > 0$ and $R = N_2$ and $R = N_3$

$K_R \frac{\partial \theta_s}{\partial R} = \frac{\partial \theta_f}{\partial R}$, and $\theta_s = \theta_f$

At $Z = L$ $P = 0$

CHAPTER 4

NUMERICAL APPROACH AND SOLUTION

Recent advances in computer technology made it possible to numerically solve the conservation equations describing flow and heat transfer for many problems of engineering interest. Several numerical methods such as finite element and finite-differences are used to solve the conservation equations. The finite-difference method is the most used numerical technique in handling the heat and fluid flow problems while the former is commonly used for stress analysis.

To solve the problem under consideration by a finite-difference technique, the governing partial differential equations are converted into their corresponding finite-difference equations, which form a set of algebraic equations applied to the nodes of the grid. The grid size affects the accuracy of the numerical solution. However, there is a practical limitation on the grid size, since the computational time and hence the cost required to obtain a numerical solution, is directly proportional to the number of grid points.

The present numerical technique may be considered as an indirect extension of the original work of Bodoia and Osterele [22] and that of El-Shaarawi and Sarhan [23] to in-

clude the unsteady terms and the conduction equation. In this research, an implicit method is used to convert the differential equations into finite difference equations. Thus, the unknown values at a grid point are not only a function of previous values, but also a function of unknown values at the same step. This requires solution of a set of simultaneous algebraic equations that result when the difference equations are written for all interior grid points. In most cases, implicit finite-difference techniques tend to be numerically stable. For this reason, it was decided to use an implicit method in this investigation.

4.1 The Finite-Difference Domain

In the present work, there are 3 independent variables for the transient case, namely, R, Z, and t and two independent variables for the steady case; they are R and Z. A three dimensional parallelepiped grid in R, Z and t is imposed on half of the annulus; only half of the channel is needed due to the symmetry about the Z-axis. Thus, a rectangular grid as shown in Fig. 4.1 is superimposed on half of the annulus in the R-Z plane; this grid represents the solution domain for the steady-state case and the solution for the transient case at a given t. For other values of t (for the transient case), there are other identical parallel plane-grid, i.e. the non-dimensional time is simulated as a third coordinate normal to the R-Z plane. Mesh points are numbered consecutively from the arbitrary origin (on the inner surface of the core tube at entrance) with i progressing in the radial direction, with i =1 at the inner surface of the core tube, $i = ns1+1$ at the inner cylinder solid-fluid interface, $i = ns1 + n + 1$ at the outer cylinder fluid-solid interface, and $i = ns1 + n + ns2 + 1$ at

the outer surface of the outer tube. The j progresses in the axial direction, with $j = 1$ at the inlet cross section and $j = m + 1$ at the final cross section. For the transient case, k progresses in the fictitious time direction, with $k = 1$ at the initial state and $k = nk + 1$ at the final state. The value of nk is chosen such that steady-state conditions are achieved.

4.2 Finite-Difference Formulation of the Continuity Equation

Considering the mesh network shown in Fig. 4.2, the continuity equation can be written in the following finite-difference form.

4.2.1 For The Transient and Steady-State Cases

$$\frac{V_{i+1,j+1,k+1} - V_{i,j+1,k+1}}{\Delta R_f} + \frac{V_{i+1,j+1,k+1} + V_{i,j+1,k+1}}{2\left[N_2 + (i - \frac{1}{2})\Delta R_f\right]} + \frac{U_{i+1,j+1,k+1} + U_{i,j+1,k+1} - U_{i+1,j,k+1} - U_{i,j,k+1}}{2\Delta Z} =$$

Rearranging the terms, the equation will take the following form:

$$V_{i+1,j+1,k+1} = \hat{A}_i V_{i,j+1,k+1} - \hat{B}_i \left[U_{i+1,j+1,k+1} + U_{i,j+1,k+1} - U_{i+1,j,k+1} - U_{i,j,k+1}\right] \tag{4.1}$$

where

$$\hat{A}_i = \left[\frac{N_2 + (i-1)\Delta R_f}{N_2 + i\Delta R_f}\right]$$

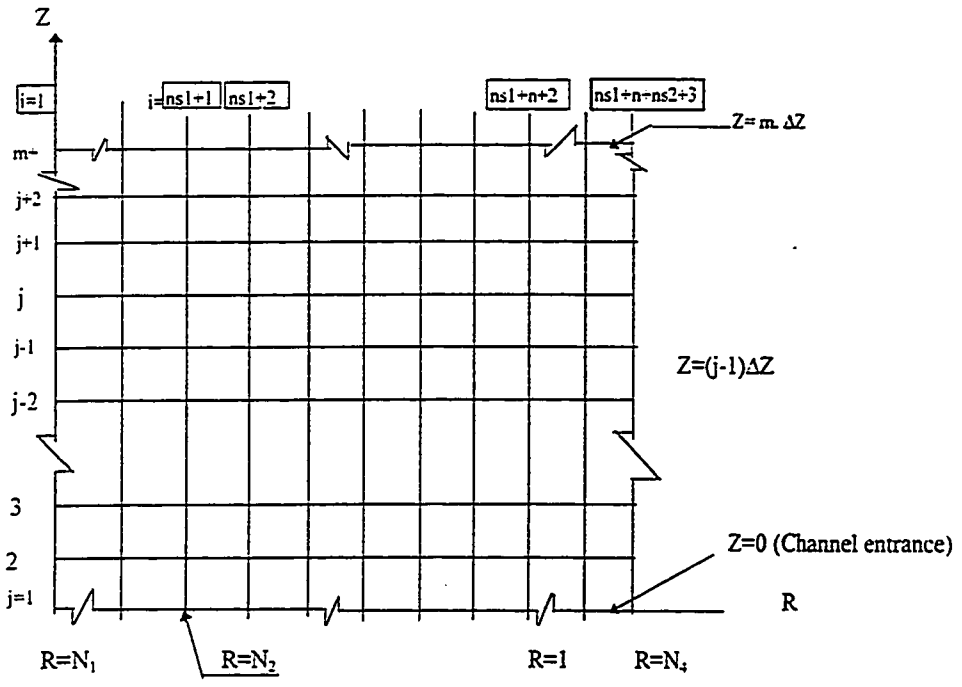

Figure 4.1: Mesh network for finite difference representation at a given time

$$\hat{B}_i = \left[\frac{2N_2 + (2i-1)\Delta R_f}{N_2 + i\Delta R_f}\right]\left[\frac{\Delta R_f}{4\Delta Z}\right]$$

4.3 Finite-Difference Formulation of the Axial Momentum Equation

Considering the mesh network shown in Fig. 4.3, the axial momentum equation can be written in the following finite difference form.

4.3.1 For The Transient Case

$$\frac{U_{i,j+1,k+1} - U_{i,j+1,k}}{\Delta t} + V_{i,j,k}\frac{U_{i+1,j+1,k+1} - U_{i-1,j+1,k+1}}{2\Delta R_f} + U_{i,j,k}\frac{U_{i,j+1,k+1} - U_{i,j,k+1}}{\Delta Z}$$
$$= \frac{P_{j,} - P_{j+1}}{\Delta Z} + \frac{\theta_{i,j+1,k+1}}{16(1-N_2)^4} + \frac{U_{i+1,j+1,k+1} - U_{i-1,j+1,k+1}}{2\left[N_2 + (i-1)\Delta R_f\right]\Delta R_f} +$$
$$\frac{U_{i+1,j+1,k+1} - 2U_{i,j+1,k+1} + U_{i-1,j+1,k+1}}{(\Delta R_f)^2}$$

rearranging the equation we get

$$\tilde{A}_i U_{i-1,j+1,k+1} + \tilde{B}_i U_{i,j+1,k+1} + \tilde{C}_i U_{i+1,j+1,k+1} + P_{j+1,k+1} = \tilde{D}_i \qquad (4.2a)$$

where;

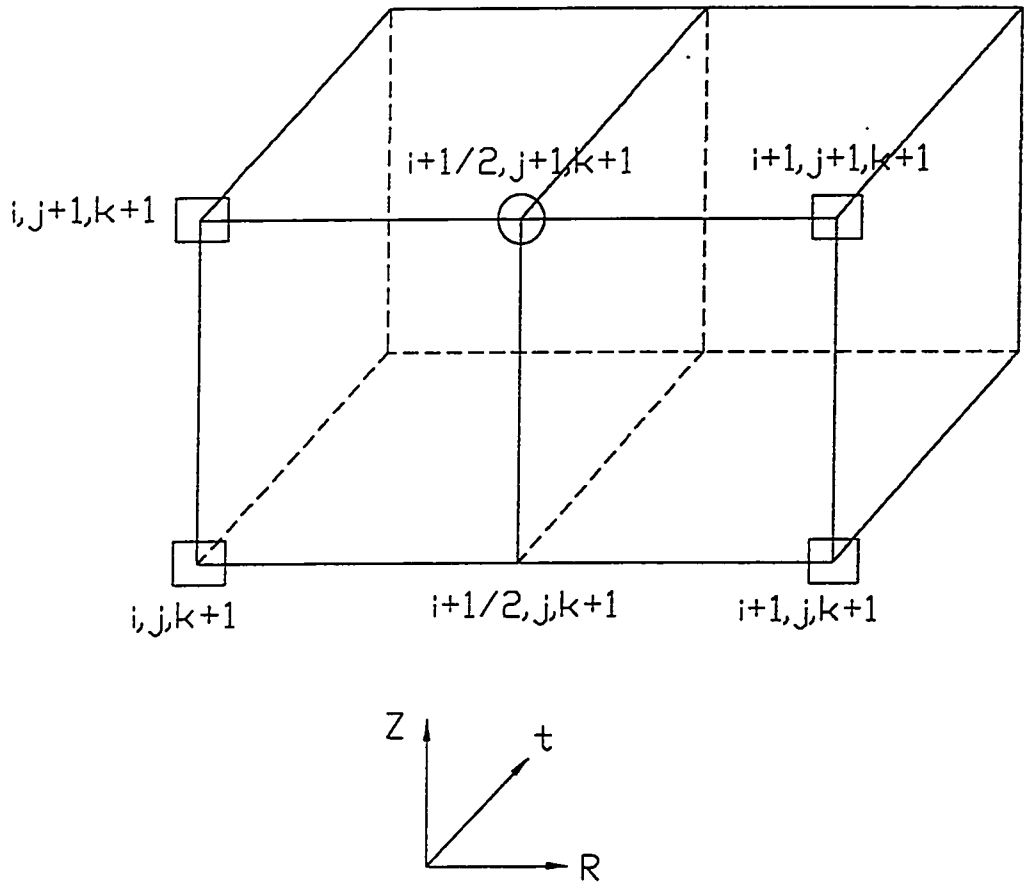

Figure 4.2: Three dimensional mesh network showing points involved in the finite-difference representation of the continuity equation and the steady-state conduction equation

$$\tilde{A}_i = \frac{\Delta Z}{2\Delta R_f\left[N_2 + (i-1)\Delta R_f\right]} - \frac{\Delta Z}{2\Delta R_f} V_{i,j,k} - \frac{\Delta Z}{(\Delta R_f)^2}$$

$$\tilde{B}_i = \frac{\Delta Z}{\Delta t} + U_{i,j,k} + \frac{2\Delta Z}{(\Delta R_f)^2}$$

$$\tilde{C}_i = \frac{-\Delta Z}{2\Delta R_f\left[N_2 + (i-1)\Delta R_f\right]} + \frac{\Delta Z}{2\Delta R_f} V_{i,j,k} - \frac{\Delta Z}{(\Delta R_f)^2}$$

$$\tilde{D}_i = \Delta Z \frac{\theta_{i,j+1,k+1}}{16(1-N_2)^4} + U_{i,j,k} * U_{i,j,k+1} + \frac{\Delta Z}{\Delta t} U_{i,j+1,k} + P_{j,k+1}$$

4.3.2 For The Steady-State Case

$$V_{i,j}\frac{U_{i+1,j+1} - U_{i-1,j+1}}{2\Delta R_f} + U_{i,j}\frac{U_{i,j+1} - U_{i,j}}{\Delta Z}$$
$$= \frac{P_j - P_{j+1}}{\Delta Z} + \frac{\theta_{i,j+1}}{16(1-N_2)^4} + \frac{U_{i+1,j+1} - U_{i-1,j+1}}{2\left[N_2 + (i-1)\Delta R_f\right]\Delta R_f} + \frac{U_{i+1,j+1} - 2U_{i,j+1} + U_{i-1,j+1}}{(\Delta R_f)^2}$$

rearranging the equation we get

$$\tilde{A}_i U_{i-1,j+1} + \tilde{B}_i U_{i,j+1} + \tilde{C}_i U_{i+1,j+1} + P_{j+1} = \tilde{D}_i \qquad (4.2b)$$

where:

$$\tilde{A}_i = \frac{\Delta Z}{2\Delta R_f \left[N_2 + (i-1)\Delta R_f\right]} - \frac{\Delta Z}{2\Delta R_f} V_{i,j} - \frac{\Delta Z}{(\Delta R_f)^2}$$

$$\tilde{B}_i = U_{i,j} + \frac{2\Delta Z}{(\Delta R_f)^2}$$

$$\tilde{C}_i = \frac{-\Delta Z}{2\Delta R_f \left[N_2 + (i-1)\Delta R_f\right]} + \frac{\Delta Z}{2\Delta R_f} V_{i,j} - \frac{\Delta Z}{(\Delta R_f)^2}$$

$$\tilde{D}_i = \Delta Z \frac{\theta_{i,j+1}}{16(1-N_2)^4} + (U_{i,j})^2 + P_j$$

It should be noted that the finite-difference equations are linearized, i.e., if two unknowns are multiplied by each other, one of them is replaced by its value at the previous time or axial step. Also, it is observed that some of the finite-difference approximations are made in central difference forms and others in backward difference forms. This is done to ensure numerical stability of the numerical solution.

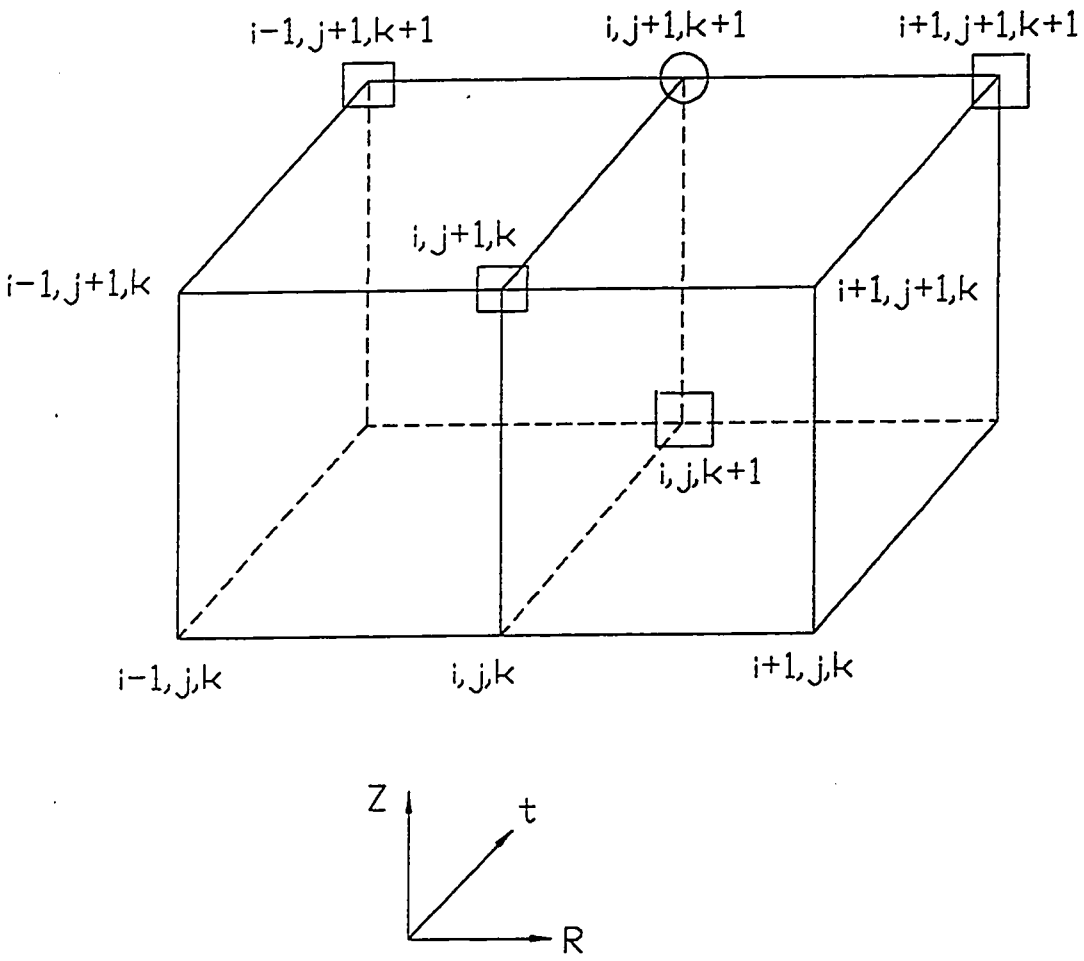

Figure 4.3: Mesh network showing points involved in the finite-difference representation of the axial momentum and energy equations for the transient case

4.4 Finite-Difference Formulation of Energy Equation

Considering the mesh networks shown in Figs. 4.3, the energy equation can be written in the following finite-difference form;

4.4.1 For The Transient Case

$$\frac{\theta_{i,j+1,k+1}-\theta_{i,j+1,k}}{\Delta t}+V_{i,j,k}\frac{\theta_{i+1,j+1,k+1}-\theta_{i-1,j+1,k+1}}{2\Delta R_f}+U_{i,j,k}\frac{\theta_{i,j+1,k+1}-\theta_{i,j,k+1}}{\Delta Z}$$

$$=\frac{1}{\mathrm{Pr}}\left[\frac{1}{N_{2+}(i-1)\Delta R_f}\frac{\theta_{i+1,j+1,k+1}-\theta_{i-1,j+1,k+1}}{2\Delta R_f}+\frac{\theta_{i+1,j+1,k+1}-2\theta_{i,j+1,k+1}+\theta_{i-1,j+1,k+1}}{(\Delta R_f)^2}\right]$$

rearranging the equation we get:

$$\bar{A}_i\theta_{i-1,j+1,k+1}+\bar{B}_i\theta_{i,j+1,k+1}+\bar{C}_i\theta_{i+1,j+1,k+1}=\bar{D}_i \qquad (4.3a)$$

where

$$\bar{A}_i=\frac{1}{2\,\mathrm{Pr}\,\Delta R_f\,[N_2+(i-1)\Delta R_f]}-\frac{1}{\mathrm{Pr}\,(\Delta R_f)^2}-\frac{V_{i,j,k}}{2\Delta R_f}$$

$$\bar{B}_i=\frac{1}{\Delta t}+\frac{U_{i,j,k}}{\Delta Z}+\frac{2}{\mathrm{Pr}(\Delta R_f)^2}$$

$$\bar{C}_i = \frac{V_{i,j,k}}{2\Delta R_f} - \frac{1}{2\,\mathrm{Pr}\,\Delta R_f\,[N_2 + (i-1)\Delta R_f]} - \frac{1}{\mathrm{Pr}(\Delta R_f)^2}$$

$$\bar{D}_i = \frac{\theta_{i,j+1,k}}{\Delta t} + U_{i,j,k}\frac{\theta_{i,j,k+1}}{\Delta Z}$$

4.4.2 For The Steady-State Case

$$V_{i,j}\frac{\theta_{i+1,j+1} - \theta_{i-1,j+1}}{2\Delta R_f} + U_{i,j}\frac{\theta_{i,j+1} - \theta_{i,j}}{2\Delta R_f}$$
$$= \frac{1}{\mathrm{Pr}}\left[\frac{1}{N_{2+}(i-1)\Delta R_f}\frac{\theta_{i+1,j+1} - \theta_{i-1,j+1}}{2\Delta R_f} + \frac{\theta_{i+1,j+1} - 2\theta_{i,j+1} + \theta_{i-1,j+1}}{(\Delta R_f)^2}\right]$$

rearranging the equation we get:

$$\bar{A}_i\theta_{i-1,j+1} + \bar{B}_i\theta_{i,j+1} + \bar{C}_i\theta_{i+1,j+1} = \bar{D}_i \qquad (4.3b)$$

where

$$\bar{A}_i = \frac{1}{2\,\mathrm{Pr}\,\Delta R_f\,[N_2 + (i-1)\Delta R_f]} - \frac{1}{\mathrm{Pr}(\Delta R_f)^2} - \frac{V_{i,j}}{2\Delta R_f}$$

$$\bar{B}_i = \frac{U_{i,j}}{\Delta Z} + \frac{2}{\mathrm{Pr}(\Delta R_f)^2}$$

$$\bar{C}_i = \frac{V_{i,j}}{2\Delta R_f} - \frac{1}{2\,\mathrm{Pr}\,\Delta R\,[N_2 + (i-1)\Delta R_f]} - \frac{1}{\mathrm{Pr}(\Delta R_f)^2}$$

$$\bar{D}_i = U_{i,j}\frac{\theta_{i,j}}{\Delta Z}$$

4.5 Finite-Difference Formulation of Conduction Equation

Considering the mesh networks shown in Figs. 4.2 and 4.3, the conduction equation can be written in the following finite difference form;

4.5.1 For The Transient Case

$$\frac{\theta_{i,j+1,k+1} - \theta_{i,j+1,k}}{\Delta t} = \frac{\alpha_R}{\mathrm{Pr}}\frac{1}{N^* + (i-1)\Delta R_s}\frac{\theta_{i+1,j+1,k+1} - \theta_{i-1,j+1,k+1}}{2\Delta R_s} + \frac{\alpha_R}{\mathrm{Pr}}\frac{\theta_{i+1,j+1,k+1} - 2\theta_{i,j+1,k+1} + \theta_{i-1,j+1,k+1}}{(\Delta R_s)^2}$$

rearranging the equation we get:

$$\acute{A}_i\theta_{i-1,j+1,k+1} + \acute{B}_i\theta_{i,j+1,k+1} + \acute{C}_i\theta_{i+1,j+1,k+1} = \acute{D}_i \qquad (4.4a)$$

where

$$\acute{A}_i = \frac{\alpha_R}{\mathrm{Pr}\,\Delta R_s\,[N^* + (i-1)\Delta R_s]} - \frac{\alpha_R}{\mathrm{Pr}(\Delta R_s)^2}$$

$$\acute{B}_i = \frac{1}{\Delta t} + \frac{2\alpha_R}{\mathrm{Pr}(\Delta R_s)^2}$$

$$\acute{C}_i = -\frac{\alpha_R}{\mathrm{Pr}\,\Delta R_s\,[N^* + (i-1)\Delta R_s]} - \frac{\alpha_R}{\mathrm{Pr}(\Delta R_s)^2}$$

$$\acute{D}_i = \frac{\theta_{i,j+1,k}}{\Delta t}$$

4.5.2 For The Steady-State Case

$$\frac{1}{N^* + (i-1)\Delta R_s}\frac{\theta_{i+1,j+1} - \theta_{i-1,j+1}}{2\Delta R_s} + \frac{\theta_{i+1,j+1} - 2\theta_{i,j+1} + \theta_{i-1,j+1}}{(\Delta R_s)^2} = 0$$

rearranging the equation leads to:

$$\acute{A}_i\theta_{i-1,j+1} + \acute{B}_i\theta_{i,j+1} + \acute{C}_i\theta_{i+,j+1} = \acute{D}_i \qquad (4.4b)$$

where

$$\acute{A}_i = -\frac{1}{2\Delta R_s\,[N^* + (i-1)\Delta R_s]} + \frac{1}{(\Delta R_s)^2}$$

$$\acute{B}_i = -\frac{2}{(\Delta R_s)^2}$$

$$\acute{C}_i = \frac{1}{2\Delta R_s\,[N^* + (i-1)\Delta R_s]} + \frac{1}{(\Delta R_s)^2}$$

where for both the transient and the steady cases:

$N^* = N_1$ for the inner tube

$N^* = N_3$ for the outer tube

4.6 Numerical Representation of the Integral Form of the Continuity Equation

For the steady-state or for the transient case, at a given instant of time, the integral form of the continuity equation can be written as

$$2\int_{N_2}^{1} URdR = (1 - N_2)U_o$$

Using the trapezoidal rule for numerical integration, the above equation can be reduced to the following form:

$$\frac{\Delta R}{2}(U_{1,j+1,k+1} + U_{n+1,j+1,k+1}) + \Delta R\sum_{i=2}^{n} U_{i,j+1,k+1}\,[N_2 + (i-1)\Delta R] = \frac{(1 - N_2^2)U_o}{2}$$

however the no slip boundary conditions are

$$U_{1,j+1,k+1} = U_{n+1,j+1,k+1} = 0$$

Substituting these conditions in the above equation leads to:

$$\Delta R\sum_{i=2}^{n} U_{i,j+1,k+1}\,[N_2 + (i-1)\Delta R] = \frac{(1 - N_2^2)U_o}{2} \qquad (4.5)$$

- **Initial and boundary conditions for the transient case**

Initially, i.e., at $t \leq 0$

$$U_{i,j,1} = V_{i,j,1} = \theta_{i,j,1} = 0 \qquad \text{everywhere}$$

For $t > 0$

$At\ R = N_2 \qquad \text{and} \qquad R = 1$

$$U_{1,j,k} = V_{1,j,k} = U_{n+1,j,k} = V_{n+1,j,k} = 0$$

$At\ R = N_4$

$$\theta_{ns1+n+ns2+1,j,k=1}$$

$At\ R = N_1$

$$\theta_{1,j,k} = \theta_{2,j,k}$$

$At\ R = N_2$

$$\theta_{ns1+1,j,k}\,|_s = \theta_{ns1+1,j,k}\,|_f \qquad \text{and } K_R \frac{\theta_{ns1+1,j,k} - \theta_{ns1,j,k}}{\Delta R_s} = \frac{\theta_{ns1+2,j,k} - \theta_{ns1+1,j,k}}{\Delta R_f}$$

$At\ R = 1$

$$\theta_{ns1+n+1,j,k}\,|_s = \theta_{ns1+n+1,j,k}\,|_f \qquad \text{and} \qquad \frac{\theta_{ns1+n+1,j,k} - \theta_{ns1+n,j,k}}{\Delta R_f} = K_R \frac{\theta_{ns1+n+2,j,k} - \theta_{ns1+n+1,j,k}}{\Delta R_s}$$

- **Boundary conditions for the steady-state case**

$At\ R = N_2 \qquad \text{and} \qquad R = 1$

$$U_{1,j} = V_{1,j} = U_{n+1,j} = V_{n+1,j} = 0$$

$At\ R = N_4$

$$\theta_{ns1+n+ns2+1,j}=1$$

$At\ R = N_1$

$$\theta_{1,j} = \theta_{2,j}$$

$At\ R = N_2$

$$\theta_{ns1+1,j}\ |_s = \theta_{ns1+1,j}\ |_f \qquad \text{and } K_R\frac{\theta_{ns1+1}-\theta_{ns1}}{\Delta R_s} = \frac{\theta_{ns1+2}-\theta_{ns1+1}}{\Delta R_f}$$

$At\ R = 1$

$$\theta_{ns1+n+1,j}\ |_s = \theta_{ns1+n+1,j}\ |_f \qquad \text{and} \qquad \frac{\theta_{ns1+n+1}-\theta_{ns1+n}}{\Delta R_f} = K_R\frac{\theta_{ns1+n+2}-\theta_{ns1+n+1}}{\Delta R_s}$$

4.7 Method of Solution

The numerical solution is obtained by first selecting values of the controlling parameters. The present conjugate heat transfer problem is dependent on six dimensionless parameters, namely, Pr, α_R, K_R, N_1, N_2, and N_4. The first and fifth of these parameters (Pr) and (N_2) are common between the present case and the conventional problem(in references [23] and [24]) while the other four parameters are the results of the wall thickness effect.

For the steady-state case and at a given time for the transient case, the solution starts by solving simultaneously the conduction and energy equations to get the temperature distribution across the annulus at the second axial position. After that, the axial momentum

equation is solved simultaneously with the integral form of the continuity equation to get the axial velocity distribution and the pressure at the same axial step for the steady-state case and at the same axial and time steps for the transient case. Obtaining the axial velocity, U, the radial velocity, V is then estimated using the continuity equation. The solution then proceeds in the axial direction until it reaches the exit of the annuli at which the pressure P is zero and the algorithm is then repeated for each time step(for the transient case).

It is worth mentioning that in practice, for confined free convection flows, such as the problem under consideration, the channel height l is usually known (i.e. L is given) while the volumetric flow rate q (hence Q) is unknown. However, the present model and method of solution for the the steady-case are handling the problem in a reversed manner, i.e., obtaining an unknown channel height for a given volumetric flow rate. Therefore, the condition $P = 0$ at $Z = L$ is not explicitly imposed on the solution, but continually checked for satisfaction. However, taking into consideration that its satisfaction establishes the unknown channel height, this condition could be regarded as being implicitly imposed. For the transient case the method of solution is different as we need an iteration process to satisfy the above criterion, i.e., $P = 0$ at $Z = L$.

4.7.1 Iteration Process

To obtain a numerical solution for the governing equations for the transient case, values of N_1, N_2, N_4, Pr, K_R, α_R, ΔZ, Δt and Gr^*, which are constant for each computer run, have to be selected. The axial and time steps are chosen in the following ranges.

$$2x10^{-7} \leq \Delta Z \leq 2x10^{-5}$$

$$10^{-3} \leq \Delta t \leq 0.005$$

For example, the values of $\Delta Z = 2x10^{-7}$ and $\Delta t = 10^{-3}$ were used for $Gr^* = 10^5$ while for $Gr^* = 500$, the values of $\Delta Z = 2x10^{-5}$ and $\Delta t = 5x10^{-3}$ were used. The number of radial increments in the inner tube wall ($ns1$), the fluid annular gap (n) and the outer tube wall ($ns2$) were chosen to be the same in all computer runs. After intensive tests to ensure grid indepenedency, the following values for the radial increments in different regions of computations were found to be good enough to produce accurate results with reasonable running time

$$ns1 = 8, n = 40 \; and \; ns2 = 16$$

This means that the radial increments in the fluid and solid media are

$$\Delta R_f = \frac{1 - N_2}{n}, \; \Delta R_s = \frac{N_2 - N_1}{ns1} = \frac{N_4 - 1}{ns2}$$

Thus the values of ΔR_f and ΔR_s for the present annulus were 0.0125.

In the present work, the numerical solutions (for the transient case) are found for pre-chosen values of Gr^*, i.e. specific values of the dimensionless annulus height, L. The value of the dimensionless pressure defect at the exit section should be zero or practically satisfies the following arbitrarily chosen criteria.

$$-10^{-15} \leq P_{m+1,k} \leq 10^{-15} \tag{4.6}$$

for $Gr^* = 10^5$ and

$$-10^{-9} \leq P_{m+1,k} \leq 10^{-9}$$

for $Gr^* = 500$

To satisfy this condition, an iteration process is used as follows. First, the inlet axial velocity, U_o, is assumed and computations continue, for the first time step, till the exit-cross section dimensionless pressure $P_{m+1,k}$ is obtained. If it does not satisfy the above criterion, another value of the inlet axial velocity has to be assumed, for the same time step, and its corresponding exit dimensionless pressure has to be computed. Then, a linear interpolation or extrapolation is done between these two assumed values of U_o to get the next trial value of the inlet axial velocity U_o. Such process continues, for the same time step, till the dimensionless exit pressure defect satisfy the criterion(4.6). The same process can then be repeated for each next time step till steady-state conditions are reached. The values of the flow rates obtained for the steady-state case are used to check the steady-state

conditions for the transient cases. If the absolute relative difference between them is less than 0.1% the steady-state conditions are considered achieved .

4.7.2 Solution of The Temperature Field

The numerical solution of the temperature field is obtained by starting with $K = 1$ (i.e., $t = \Delta t$). At $j = 1$ (entrance cross section), conduction equation (4.4) is applied with $i = 2, 3, ...ns1$ (in the inner solid wall) giving $(ns1 - 1)$ linear algebraic equations in $ns1$ unknown values of θ. The application of a finite-difference representation of condition (3.16) , mentioned in the previous chapter, at $i = ns1+1$ (i.e., at $R = N_2$) with a backward difference in the solid and a forward difference in the fluid gives an equation linking values of θ at $i = ns1$, $ns1 + 1$, $ns1 + 2$. Thus, the number of equations has increased by one but the number of unknowns has also increased by one. Now, energy equations (4.3) are applied with values of i from $ns1 + 2$ until $ns1 + n$(i.e., in the fluid region) to obtain n additional linear equations. Then, the application of the finite-difference representation of condition (3.16) at $i = ns1 + n + 1$ (i.e., at the fluid-solid interface of the outer tube) gives an equation in values of θ at $i = ns1+n$, $ns1+n+1$ and $ns1+n+2$. Conduction equation (4.4) is applied at this stage with values of i from $ns1 + n + 2$ until $ns1 + n + ns2$ to give $ns2 - 1$ additional equations. Finally, a backward difference representation of condition (3.17) is applied at $i = ns1 + n + ns2+1$ to obtain one more equation. These equations are written in a matrix form as follows:

$$\begin{bmatrix} \acute{B}_2 & \acute{C}_2 & 0 & 0 & 0 & 0 \\ \acute{A}_3 & \acute{B}_3 & \acute{C}_3 & 0 & 0 & 0 \\ - & - & - & - & 0 & 0 \\ 0 & 0 & - & - & - & 0 \\ 0 & 0 & 0 & \acute{A}_{nts-1} & \acute{B}_{nts-1} & \acute{C}_{nts-1} \\ 0 & 0 & 0 & 0 & \acute{A}_{nts} & \acute{B}_{nts} \end{bmatrix} X \begin{bmatrix} \theta_{2,j+1,k+1} \\ \theta_{3,j+1,k+1} \\ - \\ - \\ - \\ \theta_{nts,j+1,k+1} \end{bmatrix} = \begin{bmatrix} \acute{D}_2 \\ \acute{D}_3 \\ - \\ - \\ - \\ \acute{D}_{nts} \end{bmatrix}$$

where the matrix coefficients $\acute{A}$, $\acute{B}$, $\acute{C}$ and $\acute{D}$ are defined in section 4.5.1 for the transient case and in section 4.5.2 for the steady-state case. Since the matrix is tri-diagonal, it can be solved using the well known Thomas algorithm, which has the benefit of low required storage.

4.7.3 Solution of the Velocity Field

Equations (4.1), (4.2) and (4.5) govern the velocity field. It should be mentioned that for the transient case, the terms with the subscripts j or k are known while those with simultaneous subscripts $j+1$ and $k+1$ are unknown.

Starting with $j = 1$ (annulus entrance cross-section) and at the first time step (k = 1), applying equation (4.5) and equation (4.2) with $i = 2, 3, ...n$, we get n simultaneous linear algebraic equations in n unknowns $U_{2,2,2}$, $U_{3,2,2}$, $U_{4,2,2}$....., $U_{n,2,2}$, $P_{2,2}$. In a matrix form these equation can be represented as:

$$\begin{bmatrix} E_1 & E_2 & E_3 & E_4 & - & - & E_n & 0 \\ B_2 & C_2 & 0 & 0 & 0 & 0 & 0 & 1 \\ A_3 & B_3 & C_3 & 0 & 0 & 0 & 0 & 1 \\ 0 & & & & 0 & 0 & 0 & 1 \\ 0 & 0 & & & & 0 & 0 & 1 \\ 0 & 0 & 0 & & & & 0 & 1 \\ 0 & 0 & 0 & 0 & A_{n-1} & B_{n-1} & C_{n-1} & 1 \\ 0 & 0 & 0 & 0 & 0 & A_n & B_n & 1 \end{bmatrix} X \begin{bmatrix} U_{2,j+1,k+1} \\ U_{3,j+1,k+1} \\ - \\ - \\ - \\ U_{n-1,j+1,k+1} \\ U_{n,j+1,k+1} \\ P_{j+1,k+1} \end{bmatrix} = \begin{bmatrix} E \\ D_2 \\ D_3 \\ - \\ - \\ - \\ D_{n-1} \\ D_n \end{bmatrix}$$

These equations are solved by means of a special form of the Guass Jordan elimination scheme. Now the radial velocity at the grid points of the second cross section can be obtained by applying equation (4.4) in a step wise manner. This process will be repeated for each next j (cross section) after getting its temperatures (as explained in the previous section). Thus the dimensionless axial velocity, dimensionless pressure defect and the radial velocity are obtained all over the domain of solution at a given time.

CHAPTER 5

TRANSIENT CASE RESULTS

5.1 INTRODUCTION

In this chapter, the transient characteristics of the induced flow and the important pertinent engineering parameters are presented. The numerical solutions were carried out after selecting values for the controlling parameters Pr, N_1, N_2, N_3, N_4, K_R and α_R. The computations were carried out for only one value of Prandtl number, namely, Pr = 0.7, in a fluid annulus of radius ratio $N_2 = 0.5$, having solid boundaries of $N_1 = 0.4$ and $N_4 = 1.2$ for four selected values of the modified Grashof number, namely, $Gr^* = 500, 10^3, 10^4$ *and* 10^5. The fluid annulus radius ratio $N_2 = 0.5$ was chosen as it represents a typical annular geometry with its value of 0.5 far enough from unity ($N_2 = 1$) which represents the case of parallel plate channels. Moreover, the value of $N_2 = 0.5$ is common between the present computations and those for the conventional problem which has been solved by Al-Attas [24]. Consequently, comparisons between the two cases can be made. Also, the values of the boundary radius ratios (N_1 and N_4) were chosen to give wall thickness suf-

ficient enough to clarify the conjugate heat transfer phenomenon. Thus, the results to be presented in this chapter focus on the effects of Gr^* and both K_R and α_R on the transient flow characteristics and its engineering parameters.

5.2 DEFINITIONS

The parameters computed in this work are defined hereunder;

- **Mixing-cup temperature** (θ_m) :

At a given instant, the mixing-cup temperature at any cross-section is defined as follows:

$$T_m = \frac{2\pi\rho_o C_p \int_{r_2}^{r_3} ruTdr}{2\pi\rho_o C_p \int_{r_2}^{r_3} rudr}$$

and in dimensionless form

$$\theta_m = \frac{\int_{N_2}^{1} RU\theta dR}{\int_{N_2}^{1} RUdR}$$

Using the trapezoidal rule to evaluate the integrals, the numerical representation for θ_m is:

$$\theta_m = \frac{\sum_{i=2}^{n} [N_2 + (i-1)\Delta R_f] U_{i,j,k}\theta_{i,j,k}}{\sum_{i=2}^{n} [N_2 + (i-1)\Delta R_f] U_{i,j,k}}$$

– **Total heat absorbed** (H_t) :

At a given instant, the total amount of heat absorbed by the fluid as it passes through the annulus, from the entrance up to exit, is given by

$$h_t = 2\pi\rho_o C_p \int_{r_2}^{r_3} ru(T_e - T_o)dr$$

Using the dimensionless parameters given in the nomenclature, the total heat absorbed can be written as

$$H_t = 2\int_{N_2}^{1} RU\theta_e dR = 2\theta_{m,e}\int_{N_2}^{1} URdR = (1 - N_2^2)U_o\theta_{m,e} = F\theta_{m,e}$$

Evaluating the integral using the trapezoidal rule, the above expression turns to be

$$H_t = 2\Delta R_f \sum_{i=2}^{n} [N_2 + (i-1)\Delta R_f]\, U_{i,j,k}\theta_{i,m+1,k}$$

5.3 RESULTS

5.3.1 Axial Velocity

Figures 5.1 through 5.40 constitute four groups presenting the effects of K_R and α_R on the axial velocity for the four selected values of Gr^*, namely, $500, 10^3, 10^4$ *and*

10^5. Each group consists of ten figures. The first four figures in each group present, for given values of α_R, the effect of K_R on the development with time of the axial velocity at the mid-height and exit cross-sections of the annulus. The following four figures in the group present the effect of α_R on the axial velocity for given values of K_R at the aforesaid two axial cross-sections. The ninth figure in each group shows the effect of K_R on the developing axial velocity at a given value of time, i.e., it shows how this parameter affects the axial velocity as the induced fluid moves upward through the annulus if there were a time freeze. The last figure in each group shows the effect of α_R on the development with axial distance of the axial velocity profile for a given value of time.

Figure 5.1 shows how K_R affects the development with time of the mid-height axial velocity for an annulus of $Gr^* = 500$ and $\alpha_R = 1$. At early time, the axial velocity profile has small values with a peak near the heated wall, as the induced fluid has just started to feel the heat transferred from the heated wall. As time elapses, more heat is conducted to the core region of the fluid annulus increasing the buoyancy force and the induced flow rate. This induced fluid absorbs more heat of that conducted through the solid wall while the rest of the heat is convected and diffused radially towards the cold fluid near the adiabatic wall(by radial convection due to the radial velocity component and by molecular diffusion). Consequently, the values of the axial velocity profile across the fluid-annular gap increase and its peak moves gradually towards the core region of the annulus. It can be seen from Fig. 5.1 that increasing K_R increases the magnitudes of the mid-height axial velocity at a given value of time. This is attributed to the increase in the rate of heat transfer from

the heated solid wall to the fluid as K_R increases. This increase in the rate of heat transfer causes an increase in the induced flow rate(i.e., an increase in the magnitudes of the axial velocity profile).

As the fluid moves further upwards, it absorbs more heat(at the same given value of time) and hence its axial velocity increases. Hence, the maximum values for the axial velocity profile which can be achieved are at the exit cross-section. Figure 5.2 shows, for the same annulus under consideration, the effect of K_R on the axial velocity profiles at the exit cross-section. A careful comparison between the values of the axial velocity component at the mid-height and the exit cross-sections(Figs. 5.1 and 5.2), for a given value of time, reveals that the increase in the magnitudes of the axial velocity profile is unnoticeable. This can be explained as follows. An annulus of $Gr^* = 500$ (i.e. $L = 0.002$) represents a long annulus with a small hydraulic diameter. Hence, the induced fluid moves a large axial distance through which it absorbs heat. Consequently, the induced fluid may become thermally saturated, i.e., it can not absorb more heat after an axial position which means that the flow approached the fully developed state. Hence, it continues moving upward through the annulus with almost the same axial velocity profile that has been achieved at the axial position where it became thermally saturated until it reaches the exit of the annulus. It is seen in Figs. 5.1 and 5.2 that the axial velocity profile corresponding to $K_R = 1$ at time $t = 0.25$ overshoots that at $t = 0.5$. This phenomenon is a direct result of the temperature overshoot phenomenon which will be discussed in detail during the discussion of the temperature results.

Figures 5.3 and 5.4 present the effect of K_R on the variation with time of the axial velocity profiles at the mid-height and exit cross-sections of the same annulus under consideration(i.e., $Gr^* = 500$) but with walls of a larger heat capacity(i.e. smaller value of α_R; $\alpha_R = 0.1$). Comparing Figs. 5.1 and 5.2 with Figs. 5.3 and 5.4, it can be seen that, for given values of K_R and time, the value of the axial velocity component at a given cross-section increases with α_R. The reason for this behavior is explained in detail in the following paragraph.

For $K_R = 100$, respectively, Figs. 5.5 and 5.6 present the effect of α_R on the development with time of the axial velocity profile at the mid-height and exit cross-sections while such effect is shown in Figs. 5.7 and 5.8 for $K_R = 1$. It is seen from Figs. 5.5 and 5.6 that the axial velocity component increases, for given axial location, K_R and time with α_R. In fact, increasing the value of α_R means an increase in the thermal diffusivity of the solid wall material. Since $\alpha_R = K_R \frac{\rho_f C_f}{\rho_s C_s}$, hence for a given K_R, the increase in the value of α_R implies a decrease in the value of the specific heat of the solid wall material. Consequently, for a given time, increasing the value of α_R increases the amount of heat conducted through the heated wall to the fluid as compared with that absorbed by the wall material; this results in an increase in the buoyancy force. A careful comparison between Figs. 5.5 and 5.7 and between Figs. 5.6 and 5.8 reveals that, for given values of α_R, time and axial position, the magnitude of the axial velocity increases with the increase in K_R. As mentioned before, this is attributed to the increase in the rate of heat transfer through the heated solid wall to the fluid-annular gap as K_R increases.

Figure 5.9 presents, at given values of α_R and time, the effect of K_R on the axial velocity profile as the induced fluid moves upwards through the annulus while, for given values of K_R and time, Fig. 5.10 presents such effect for α_R. It is seen in these two figures that , at a given time, the velocity profiles at axial positions far from the entrance have almost the same magnitude(for given values of K_R and α_R). This means that the flow has almost reached the fully developed state.

Similar to the above group of figures, Figs. 5.11 through 5.20, Figs. 5.21 through 5.30 and Figs. 5.31 through 5.40 present other three groups for $Gr^* = 10^3, 10^4 \; and \; 10^5$, respectively. Each of these groups has the same general qualitative characteristics of the first group(Figs. 5.1 through 5.10) except that the velocity profiles have a peak distinctively shifted towards the heated wall, even at large values of time. This peak becomes easily pronounced as Gr^* increases, as can be clearly seen from the figures of the last group(Figs. 5.31 through 5.40). This behavior of the axial velocity can be explained as follows. Large values of Gr^* represent short annuli with large hydraulic diameters and large temperature differences. Consequently, as can be seen from Figs. 5.39 and 5.40 (which are for $Gr^* = 10^5$), for a given time, the uniform inlet axial velocity profile is changing as the flow moves upward into a profile indicating remarkably high velocities near the heated wall. This type of velocity distribution is akin to that about a single vertical flat plate or cylinder in free convection. On the other hand, Figs. 5.9 and 5.10 represent the developing axial velocity profiles in long annuli of small hydraulic diameters with small temperature differences.

Therefore, the axial velocity profile, in this case, has sufficient height to approach the fully developed shape as the flow approaches the annulus exit.

It is seen in Figs. 5.35 through 5.40, which are for short annuli ($Gr^* = 10^5$), that the axial velocity profiles have negative magnitudes near the adiabatic wall. This is due to the presence of back(reversed) flow. The flow reversal (which may grow up and leads to a separation) in buoyancy induced flows usually occurs when the wall heating is sufficiently intense (large values of Gr^*) and asymmetric (Cheng et al. [25]). The asymmetric heating increases the possibility of occurrence of flow reversal near the wall which has lower temperature or heat flux (the adiabatic wall in the present case). The occurrence of the back flow is attributed to the continuity principle as follows. For a given time, since the same amount of fluid is flowing across each section, the need for more fluid to flow near the heated wall is compensated by withdrawing it from regions close to the adiabatic wall. In Fig. 5.37, it is shown that there is a growth and decay of the back flow with time. This might be attributed to the following. Heat transfers radially towards the cold fluid near the adiabatic wall. Hence, the cold fluid in this area warms up and acquires positive axial velocity. However, it is worth mentioning that if this reversed flow occurs(i.e., large negative axial velocity), the boundary-layer model would be unsuitable in this case and also numerical instability might occur(e.g. such instability occurs with $Gr^* = 10^5$, when $K_R \geq 10$ and $\alpha_R \geq 1$).

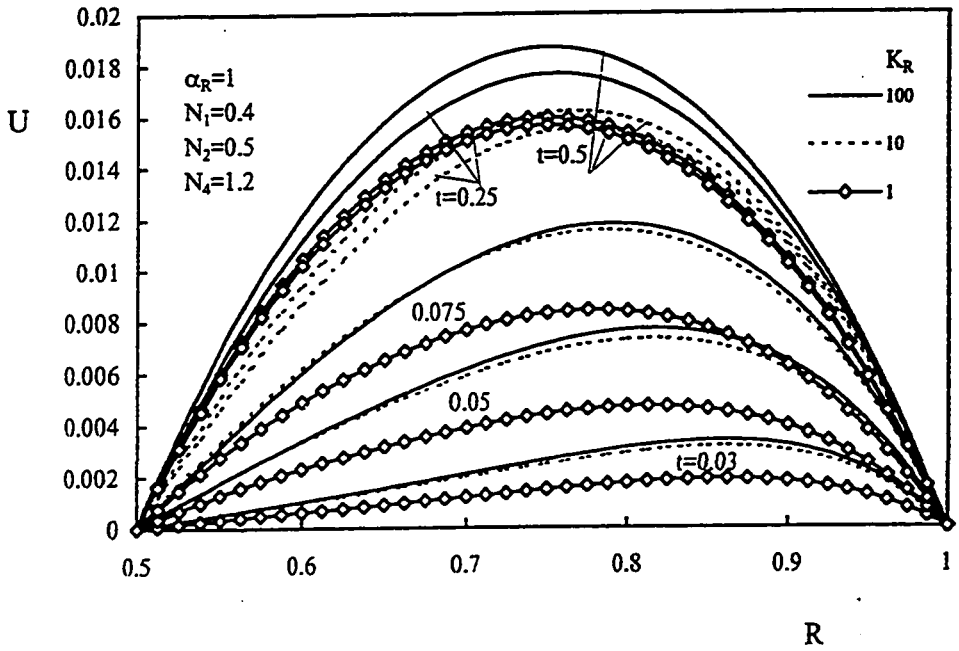

Figure 5.1: Effect of K_R on the variation of the mid-height axial velocity with time, $Gr^* = 500, \alpha_R = 1$

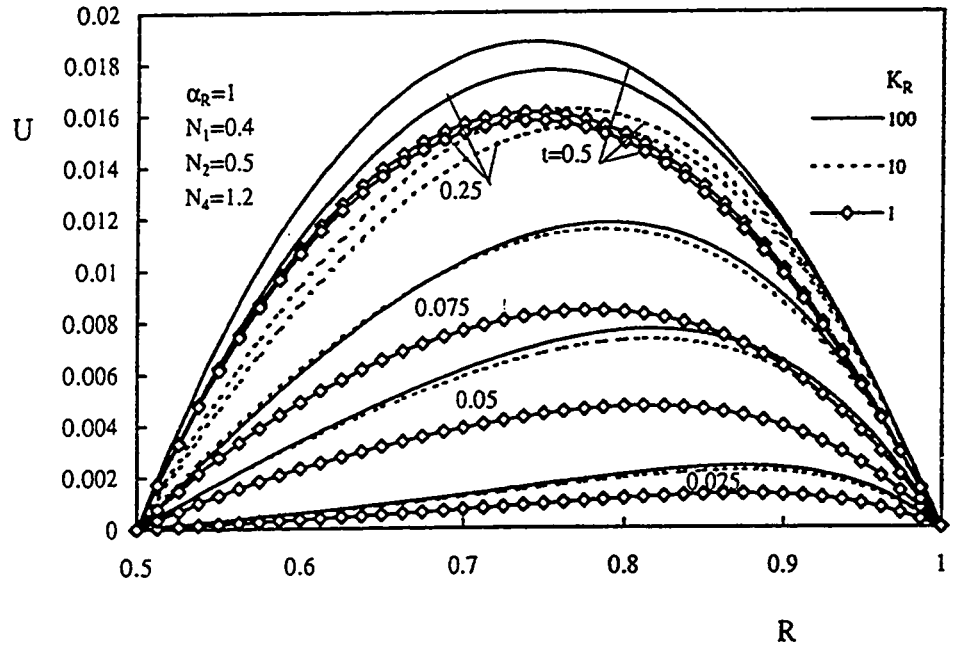

Figure 5.2: Effect of K_R on the variation of the exit axial velocity with time, $Gr^* = 500, \alpha_R = 1$

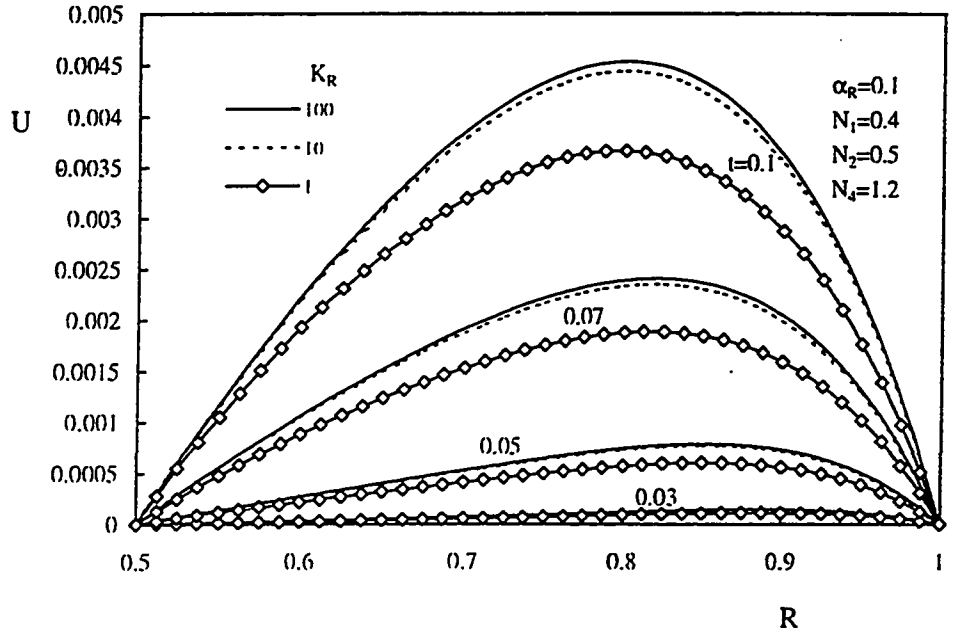

Figure 5.3: Effect of K_R on the variation of the mid-height axial velocity with time, $Gr^* = 500, \alpha_R = 0.1$

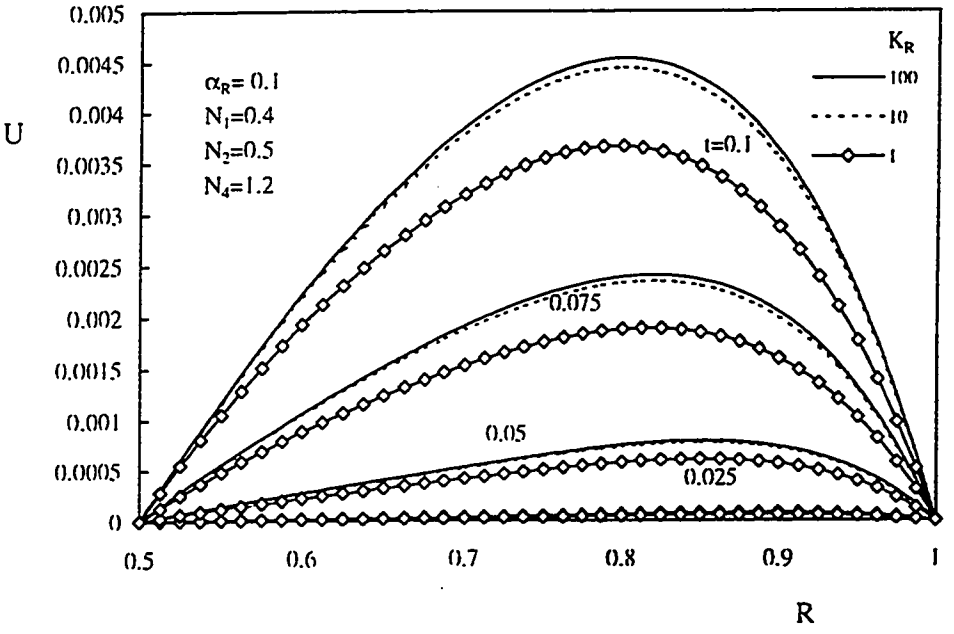

Figure 5.4: Effect of K_R on the variation of the exit axial velocity with time, $Gr^* = 500, \alpha_R = 0.1$

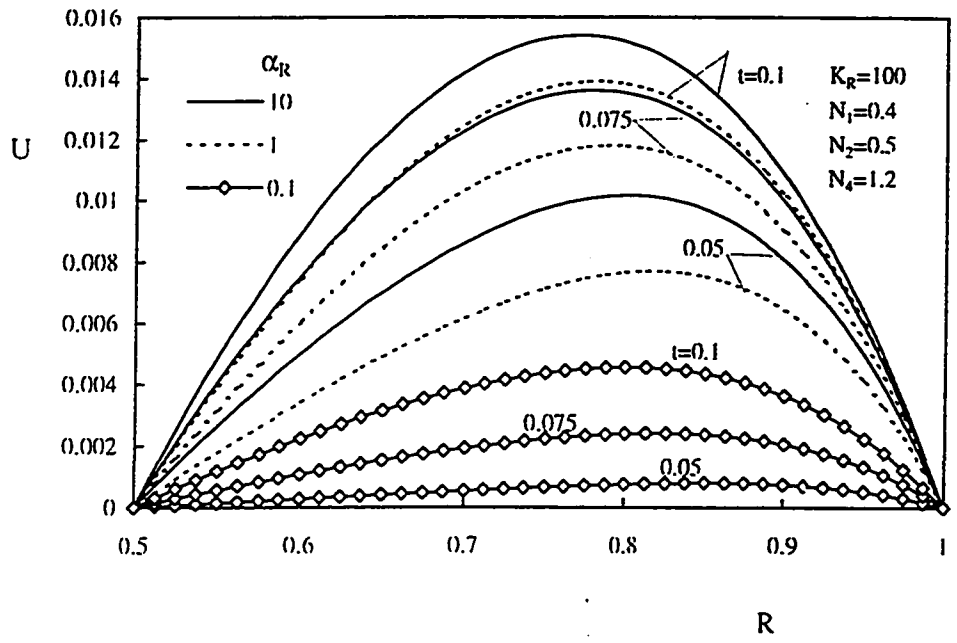

Figure 5.5: Effect of α_R on the variation of the mid-height axial velocity with time, $Gr^* = 500, K_R = 100$

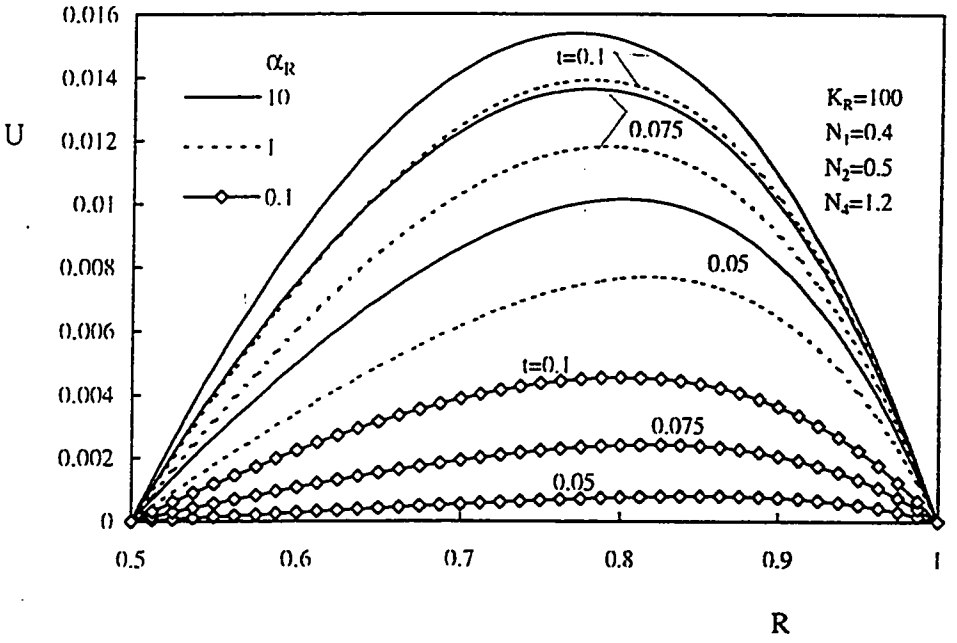

Figure 5.6: Effect of α_R on the variation of the exit axial velocity with time, $Gr^* = 500, K_R = 100$

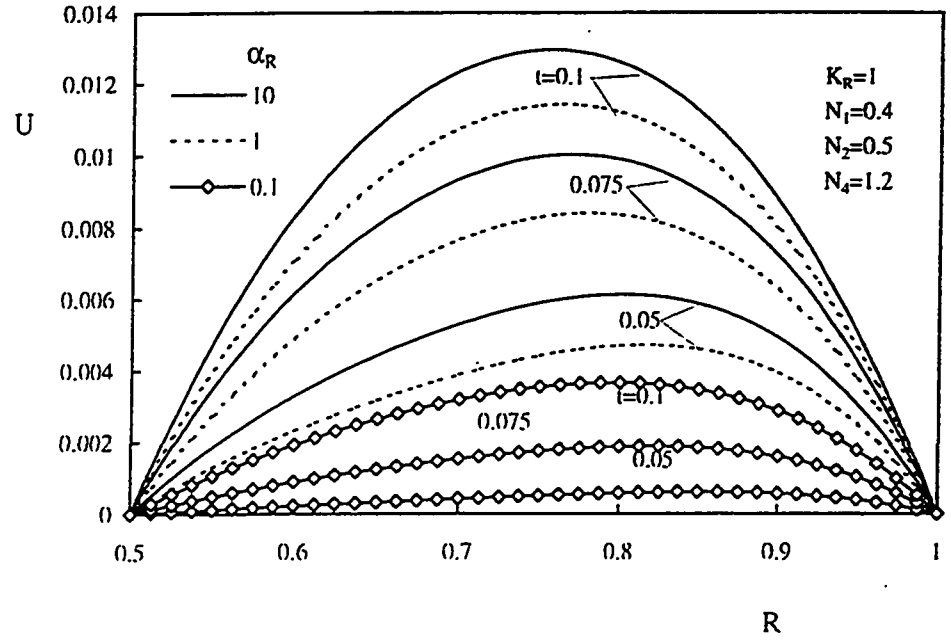

Figure 5.7: Effect of α_R on the variation of the mid-height axial velocity with time, $Gr^* = 500, K_R = 1$

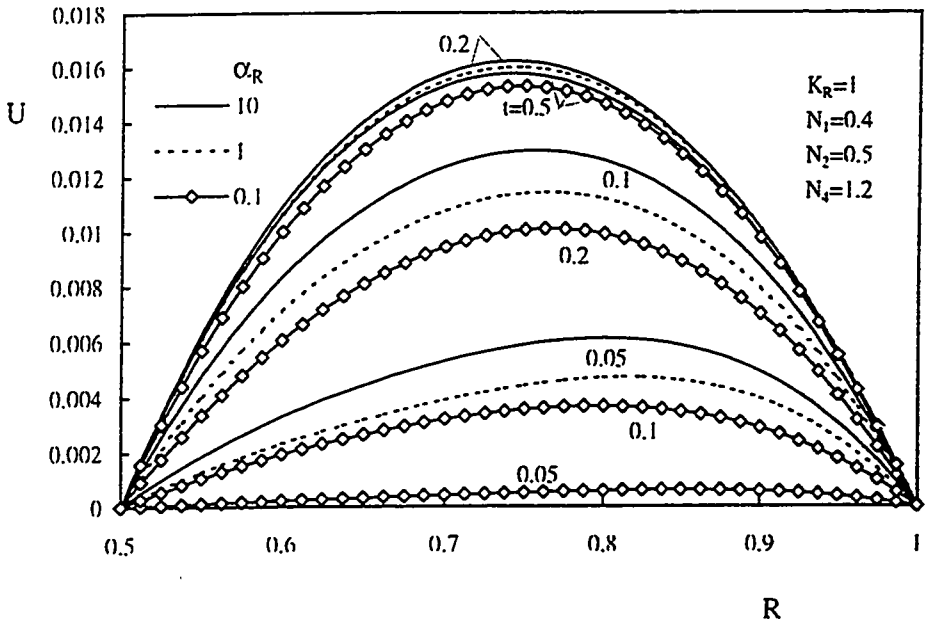

Figure 5.8: Effect of α_R on the variation of the exit axial velocity with time, $Gr^* = 500, K_R = 1$

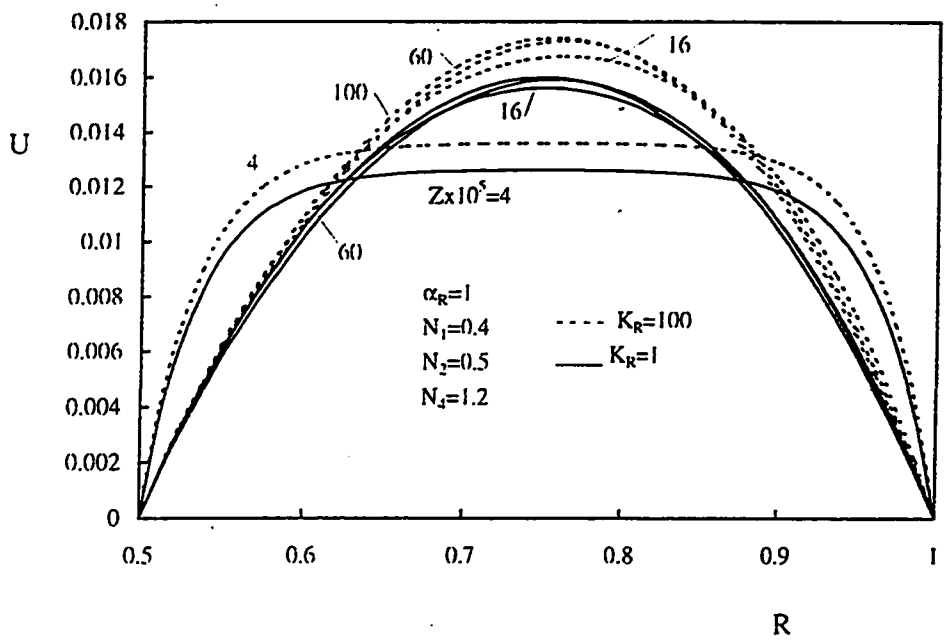

Figure 5.9: Effect of K_R on the developing axial velocity, $t = 0.225, Gr^* = 500$

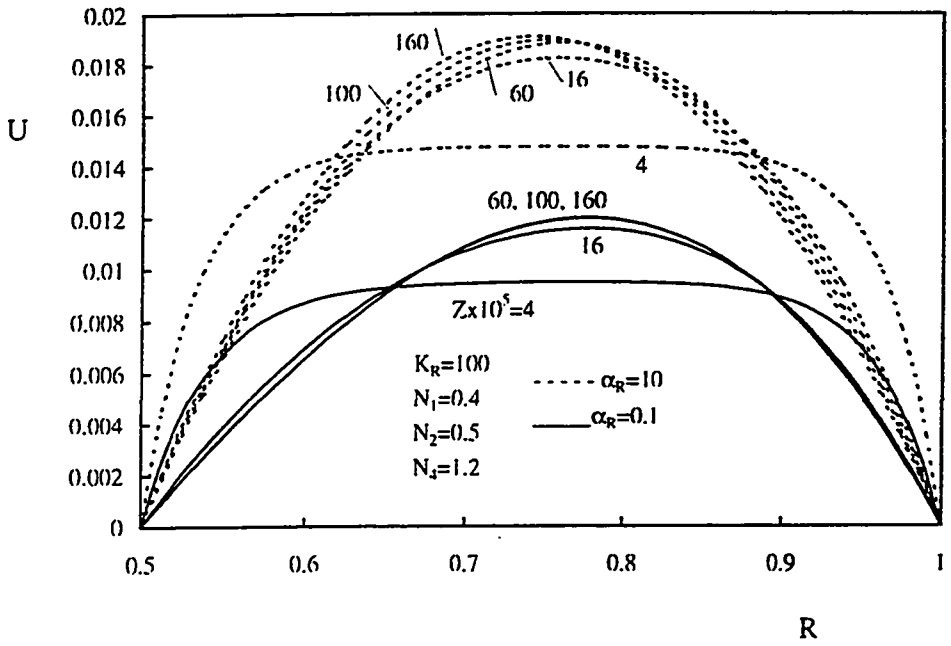

Figure 5.10: Effect of α_R on the developing axial velocity, $t = 0.225, Gr^* = 500$

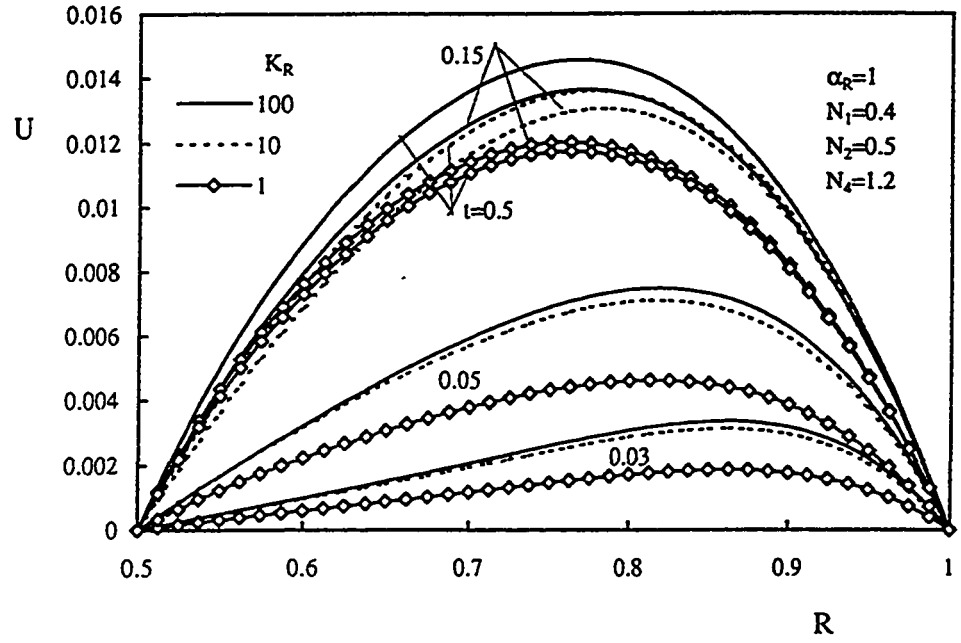

Figure 5.11: Effect of K_R on the variation of the mid-height axial velocity with time, $Gr^* = 10^3, \alpha_R = 1$

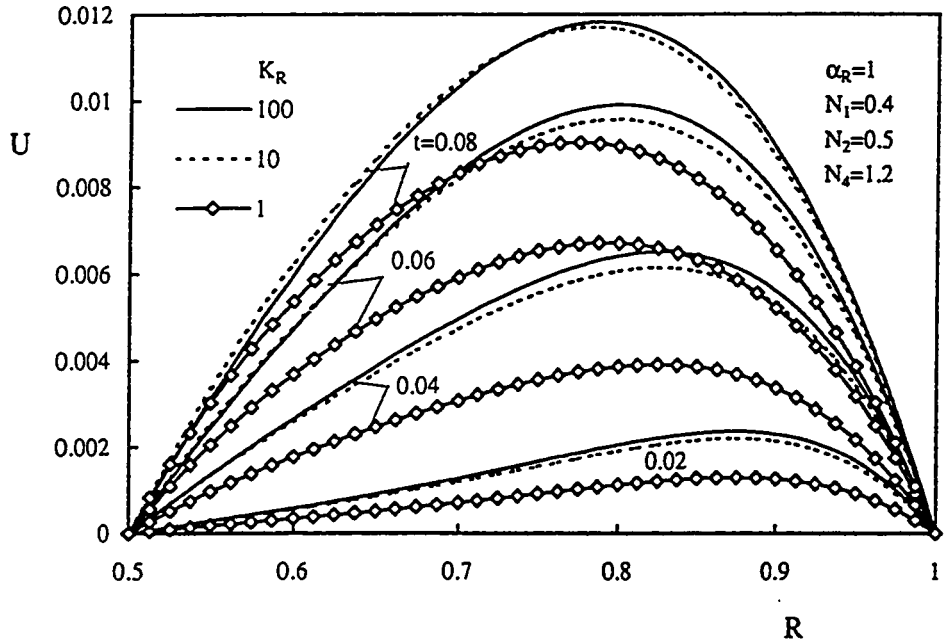

Figure 5.12: Effect of K_R on the variation of the exit axial velocity with time, $Gr^* = 10^3, \alpha_R = 1$

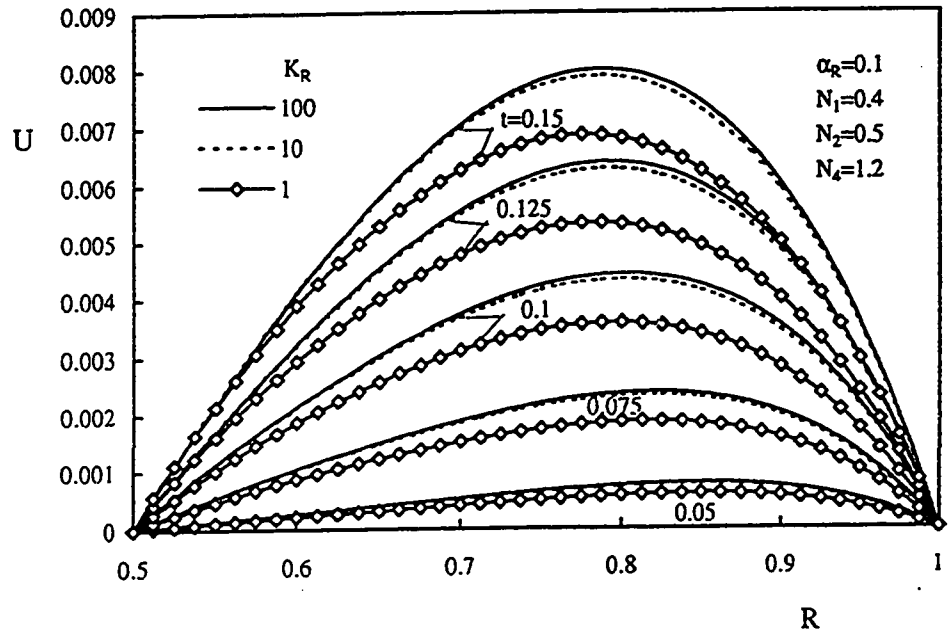

Figure 5.13: Effect of K_R on the variation of the mid-height axial velocity with time, $Gr^* = 10^3, \alpha_R = 0.1$

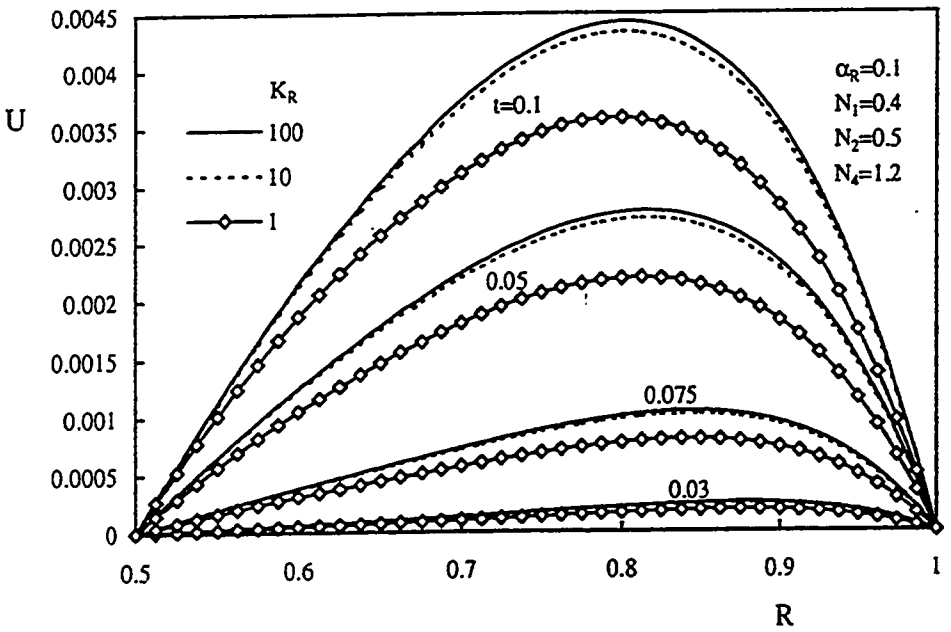

Figure 5.14: Effect of K_R on the variation of the exit axial velocity with time, $Gr^* = 10^3, \alpha_R = 0.1$

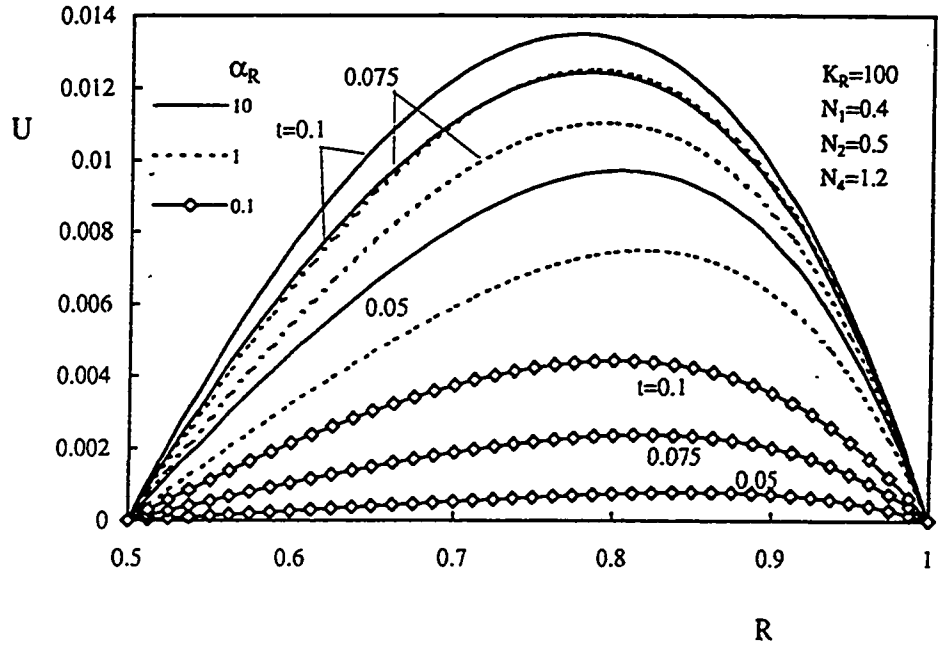

Figure 5.15: Effect of α_R on the variation of the mid-height axial velocity with time, $Gr^* = 10^3, K_R = 100$

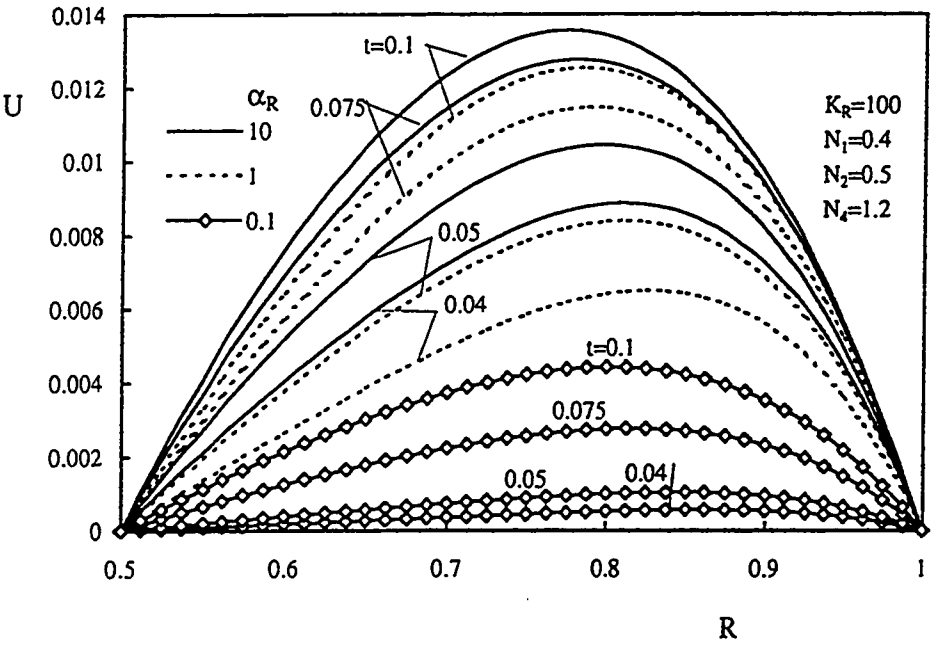

Figure 5.16: Effect of α_R on the variation of the exit axial velocity with time, $Gr^* = 10^3, K_R = 100$

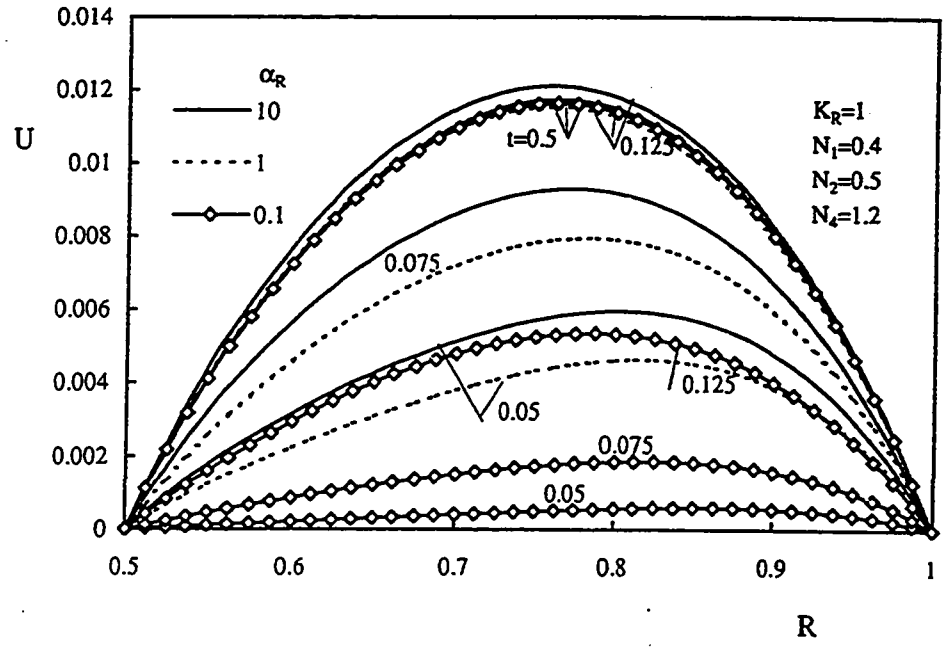

Figure 5.17: Effect of α_R on the variation of the mid-height axial velocity with time, $Gr^* = 10^3, K_R = 1$

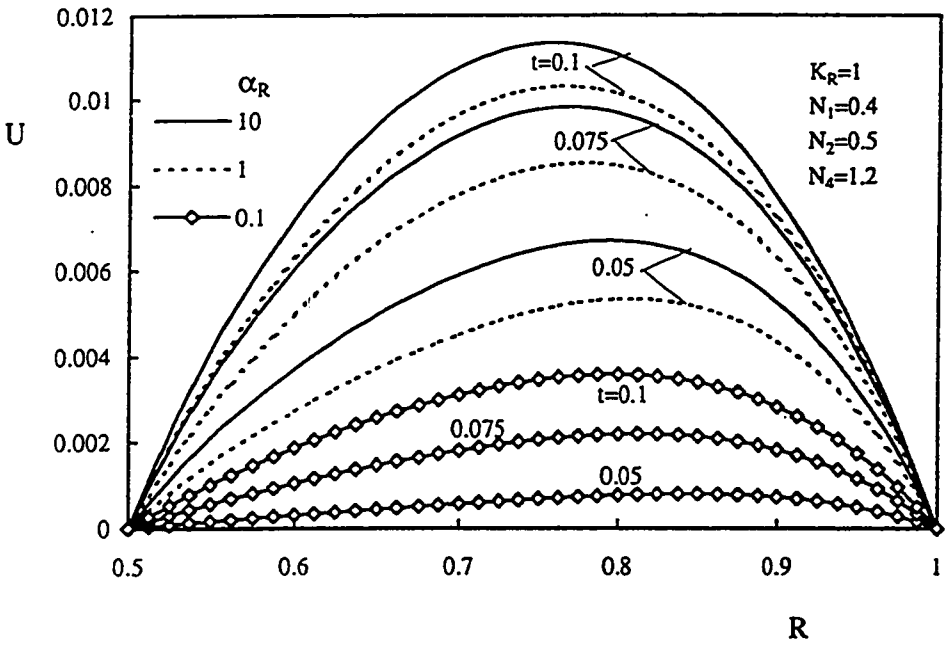

Figure 5.18: Effect of α_R on the variation of the exit axial velocity with time, $Gr^* = 10^3, K_R = 1$

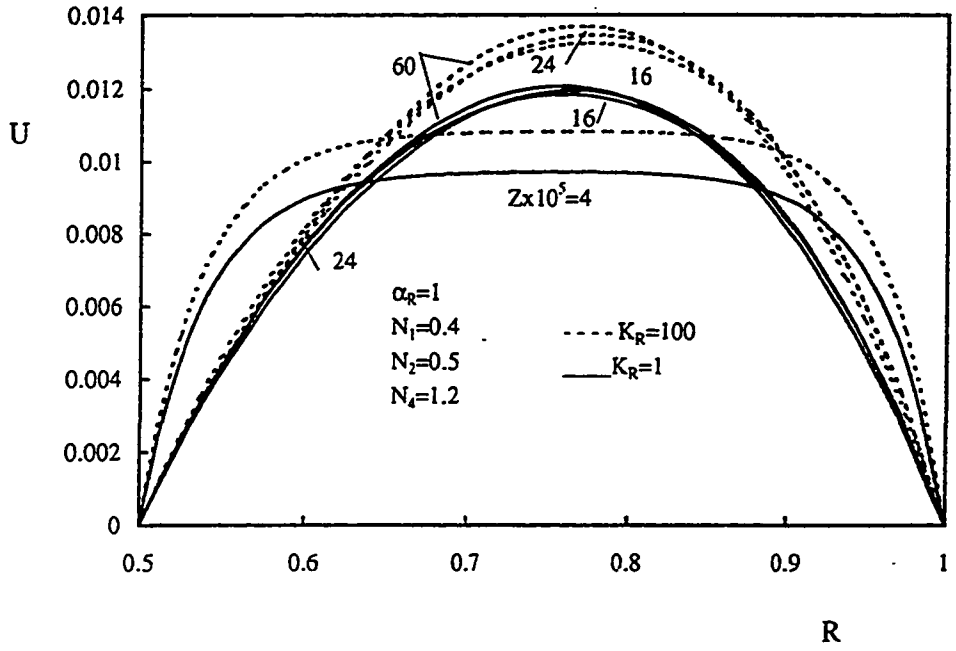

Figure 5.19: Effect of K_R on the developing axial velocity, $t = 0.15, Gr^* = 10^3$

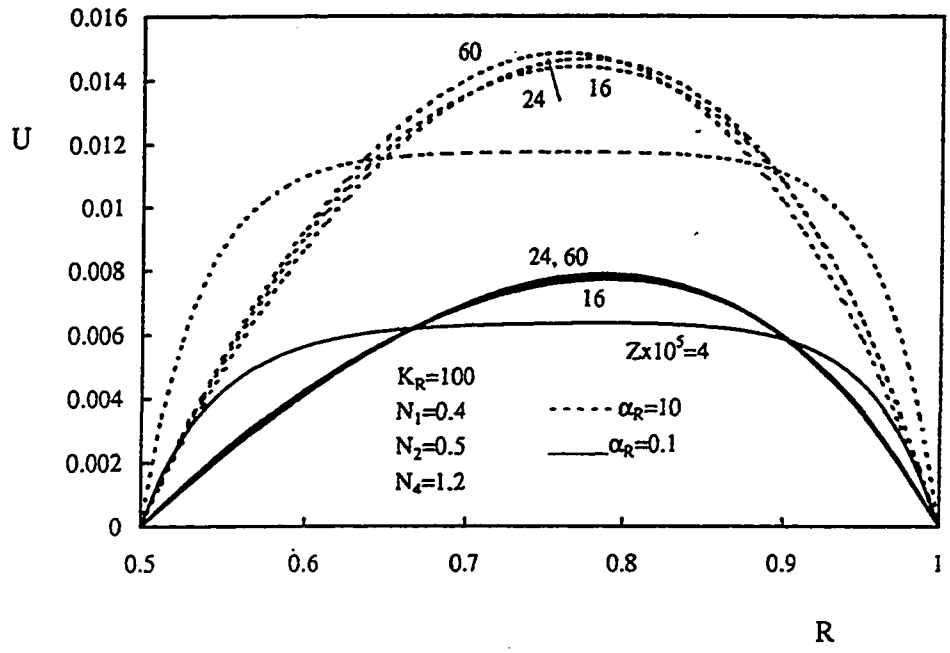

Figure 5.20: Effect of α_R on the developing axial velocity, $t = 0.15, Gr^* = 10^3$

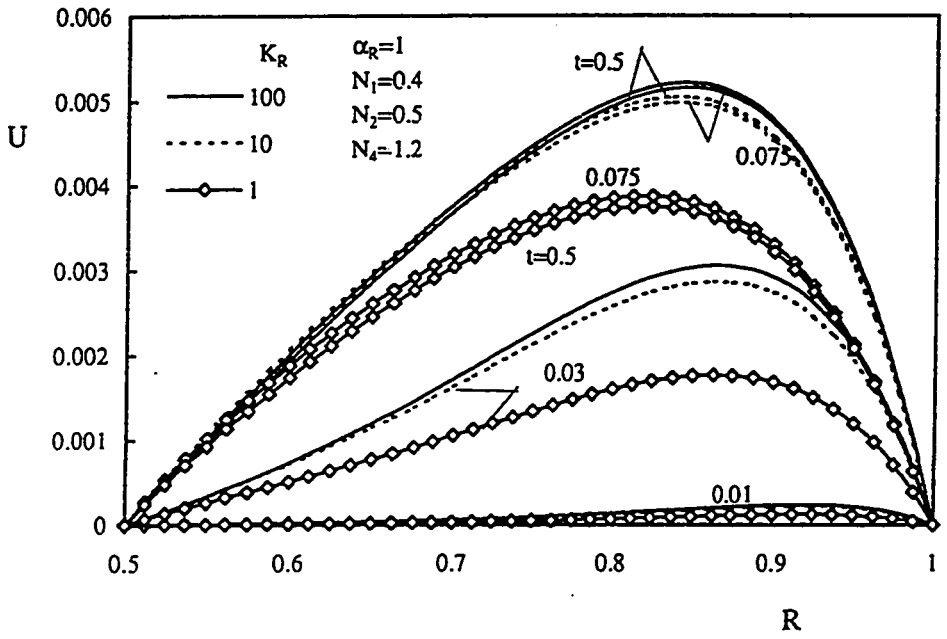

Figure 5.21: Effect of K_R on the variation of the mid-height axial velocity with time, $Gr^* = 10^4, \alpha_R = 1$

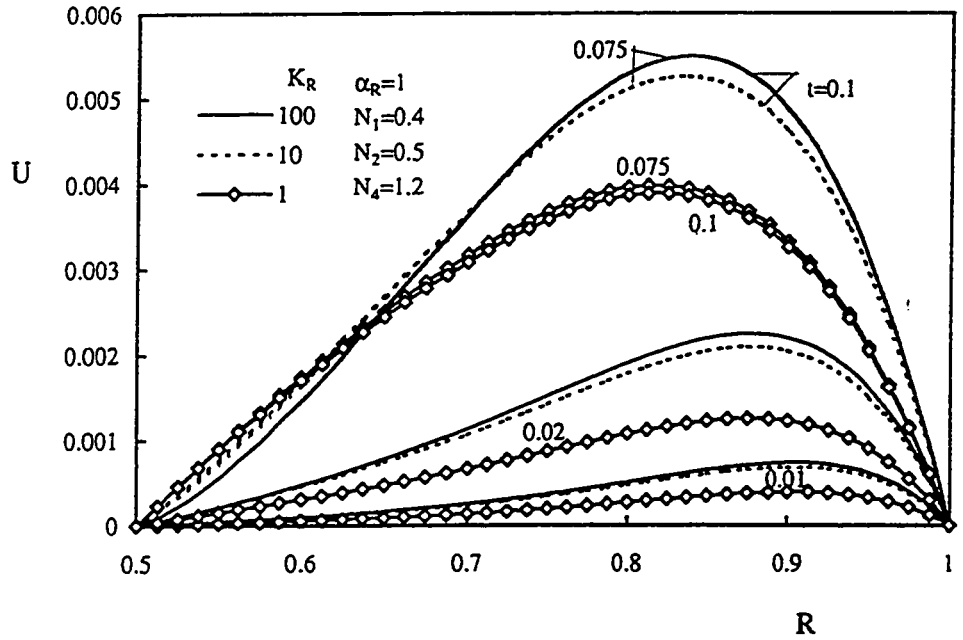

Figure 5.22: Effect of K_R on the variation of the exit axial velocity with time, $Gr^* = 10^4, \alpha_R = 1$

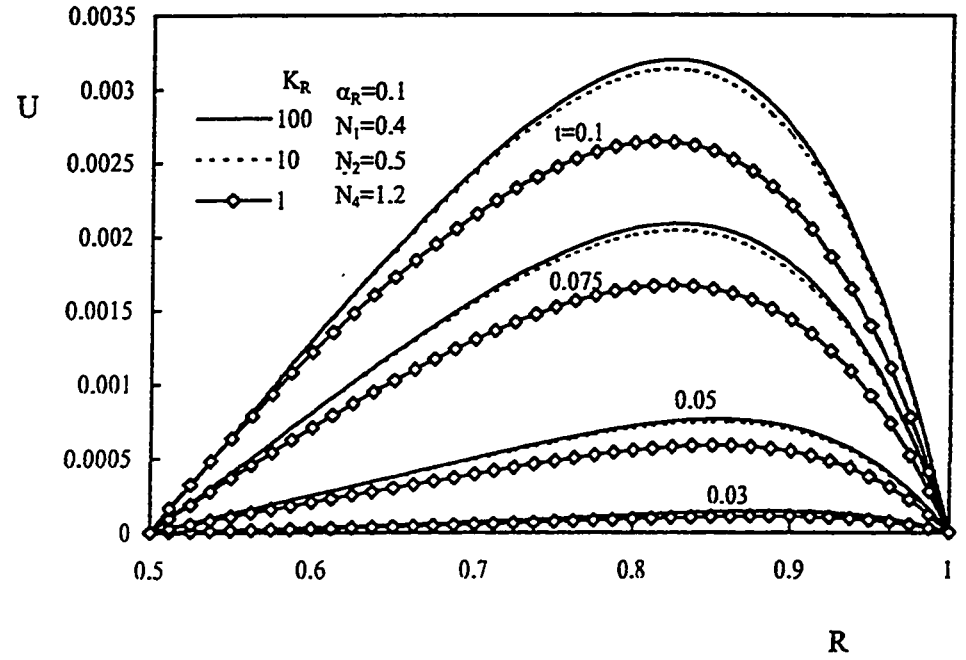

Figure 5.23: Effect of K_R on the variation of the mid-height axial velocity with time, $Gr^* = 10^4, \alpha_R = 0.1$

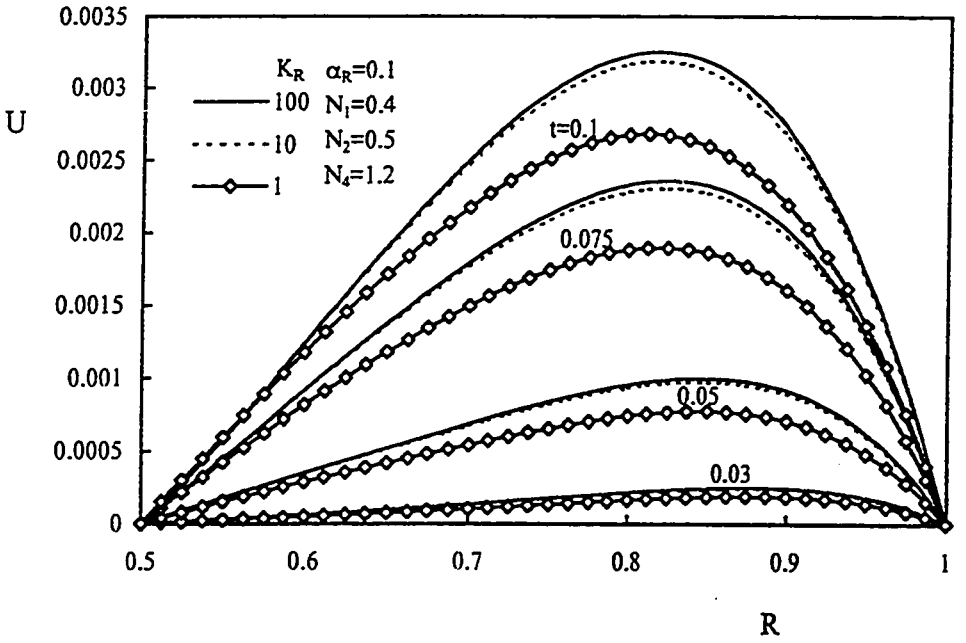

Figure 5.24: Effect of K_R on the variation of the exit axial velocity with time, $Gr^* = 10^4, \alpha_R = 0.1$

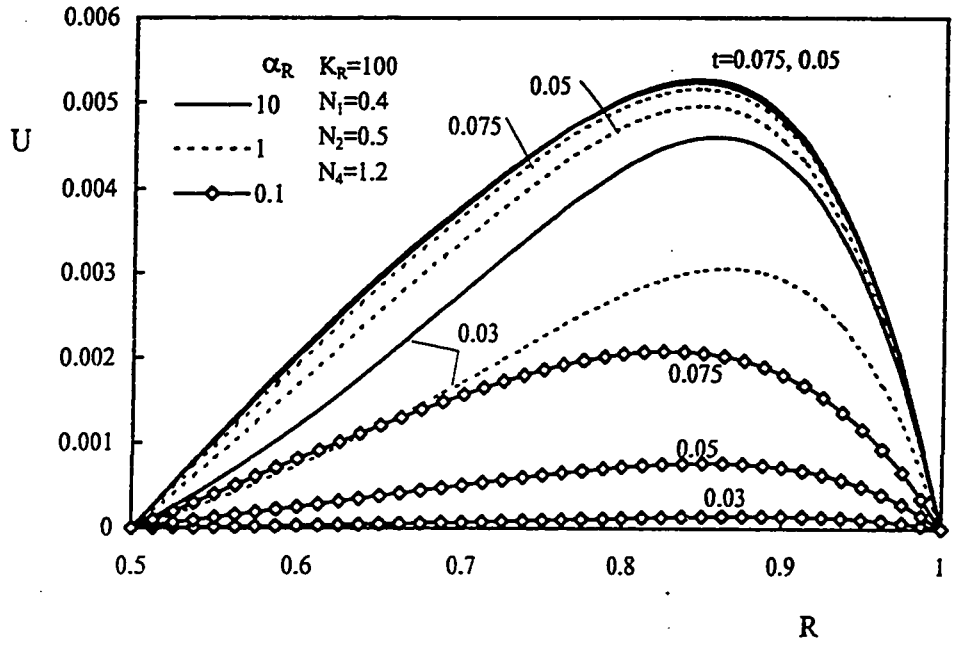

Figure 5.25: Effect of α_R on the variation of the mid-height axial velocity with time, $Gr^* = 10^4, K_R = 100$

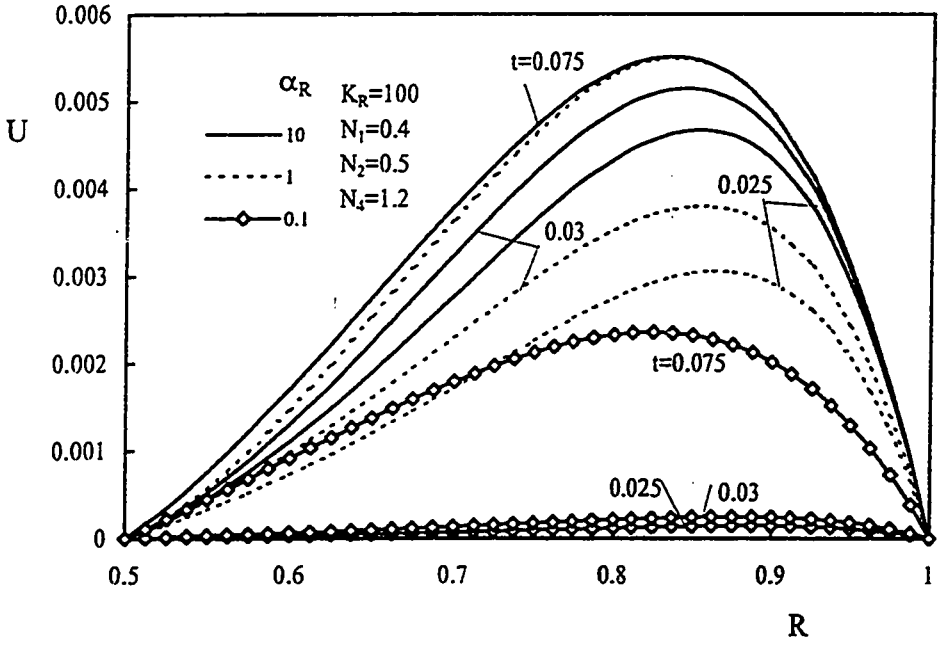

Figure 5.26: Effect of α_R on the variation of the exit axial velocity with time, $Gr^* = 10^4, K_R = 100$

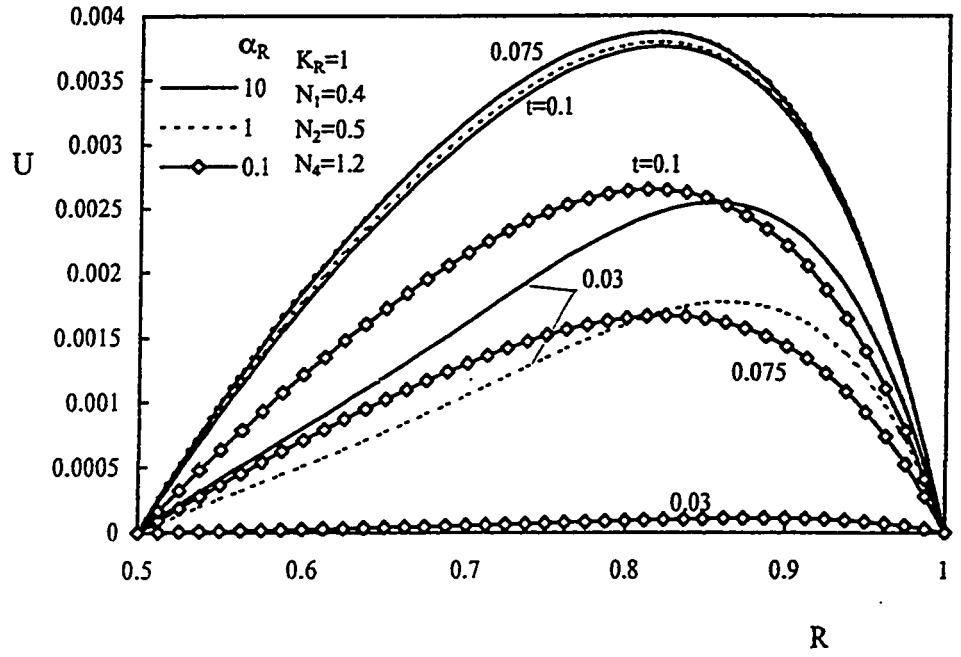

Figure 5.27: Effect of α_R on the variation of the mid-height axial velocity with time, $Gr^* = 10^4, K_R = 1$

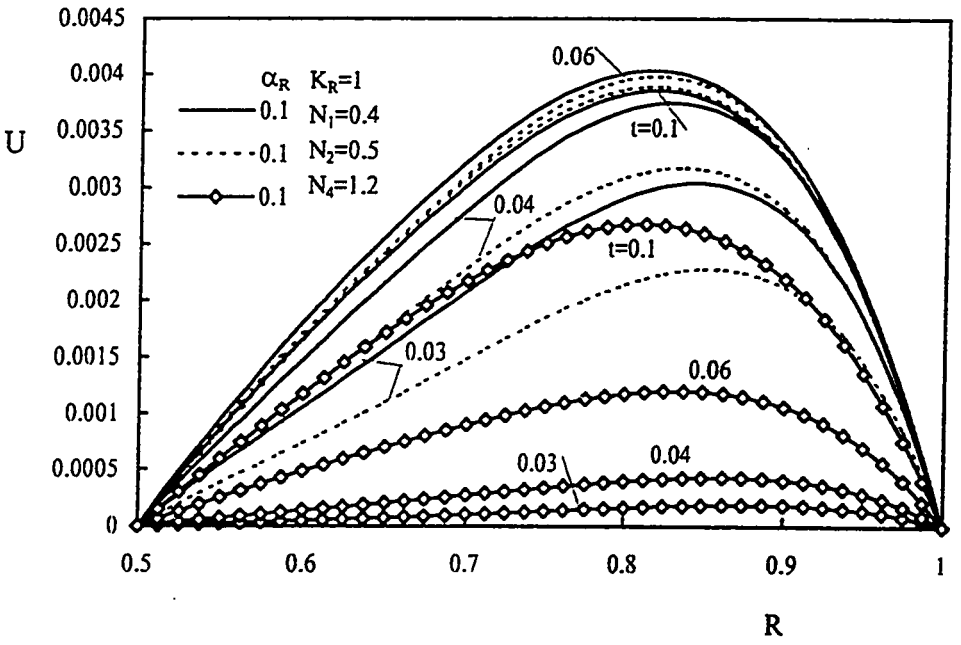

Figure 5.28: Effect of α_R on the variation of the exit axial velocity with time, $Gr^* = 10^4, K_R = 1$

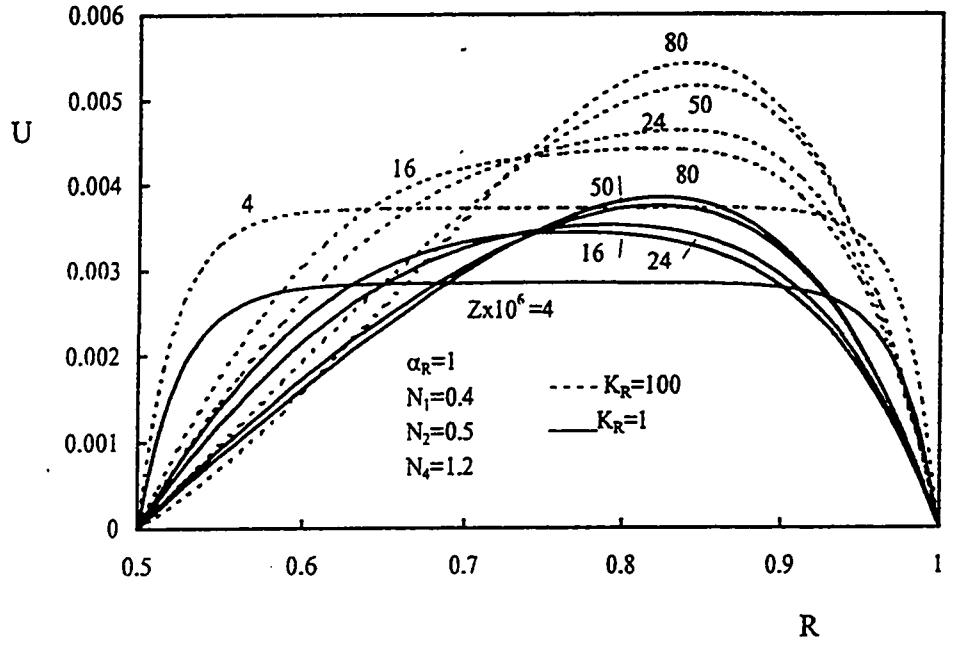

Figure 5.29: Effect of K_R on the developing axial velocity, $t = 0.15, Gr^* = 10^4$

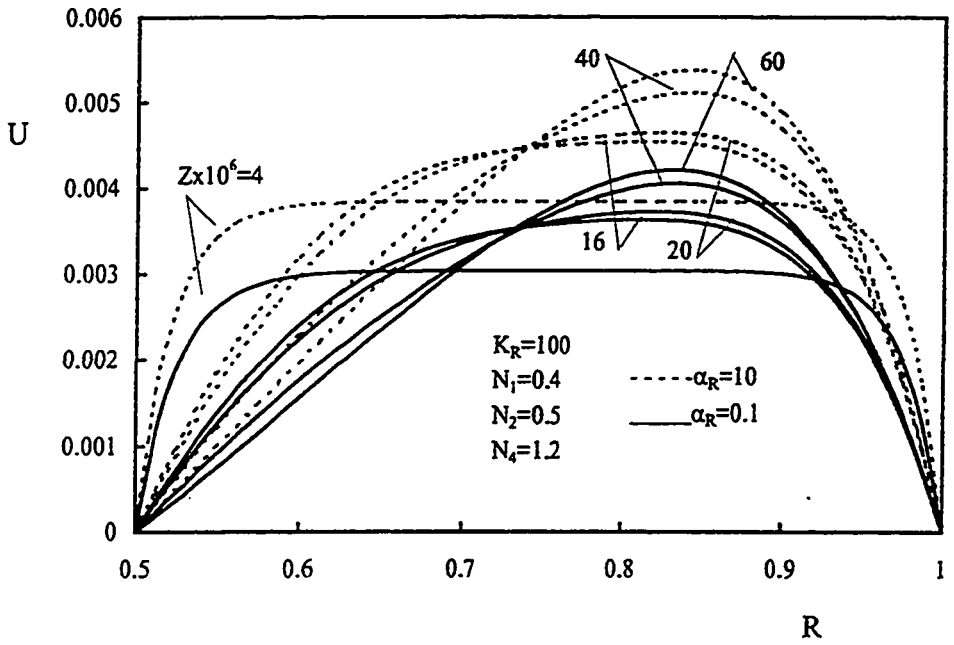

Figure 5.30: Effect of α_R on the developing axial velocity, $t = 0.15, Gr^* = 10^4$

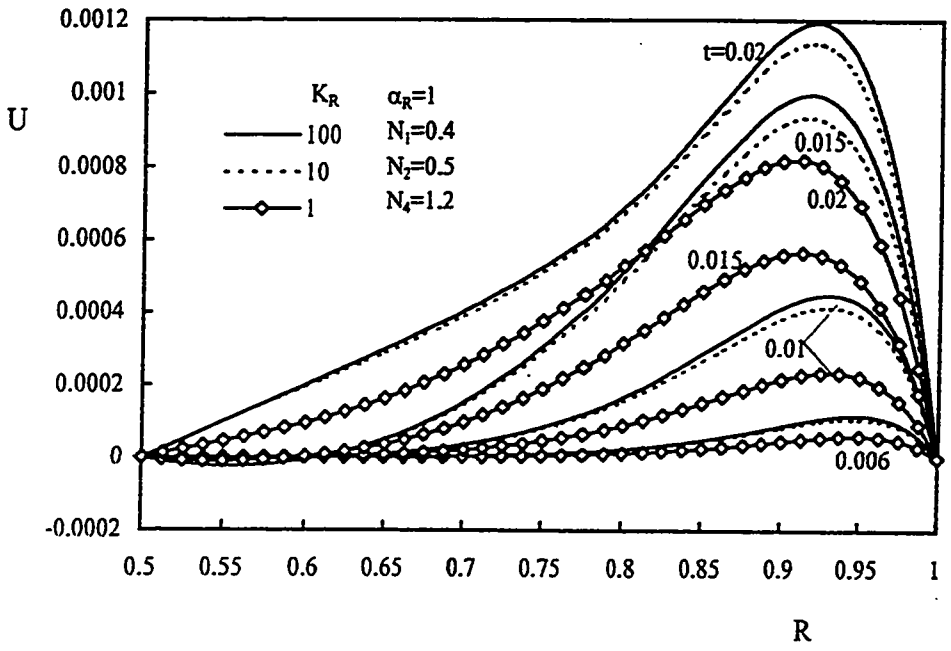

Figure 5.31: Effect of K_R on the variation of the mid-height axial velocity with time, $Gr^* = 10^5, \alpha_R = 1$

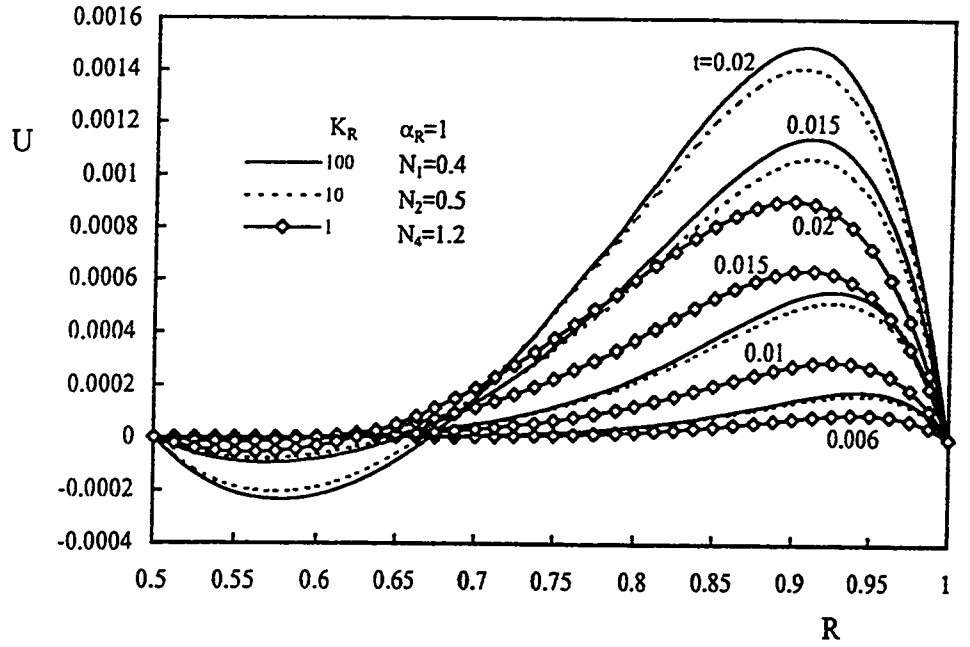

Figure 5.32: Effect of K_R on the variation of the exit axial velocity with time, $Gr^* = 10^5, \alpha_R = 1$

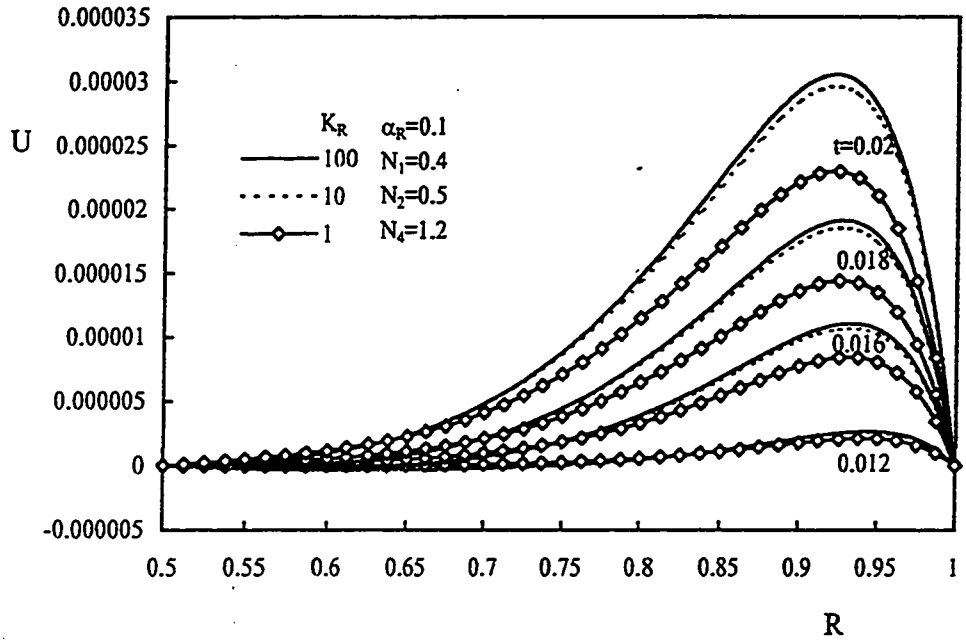

Figure 5.33: Effect of K_R on the variation of the mid-height axial velocity with time, $Gr^* = 10^5, \alpha_R = 0.1$

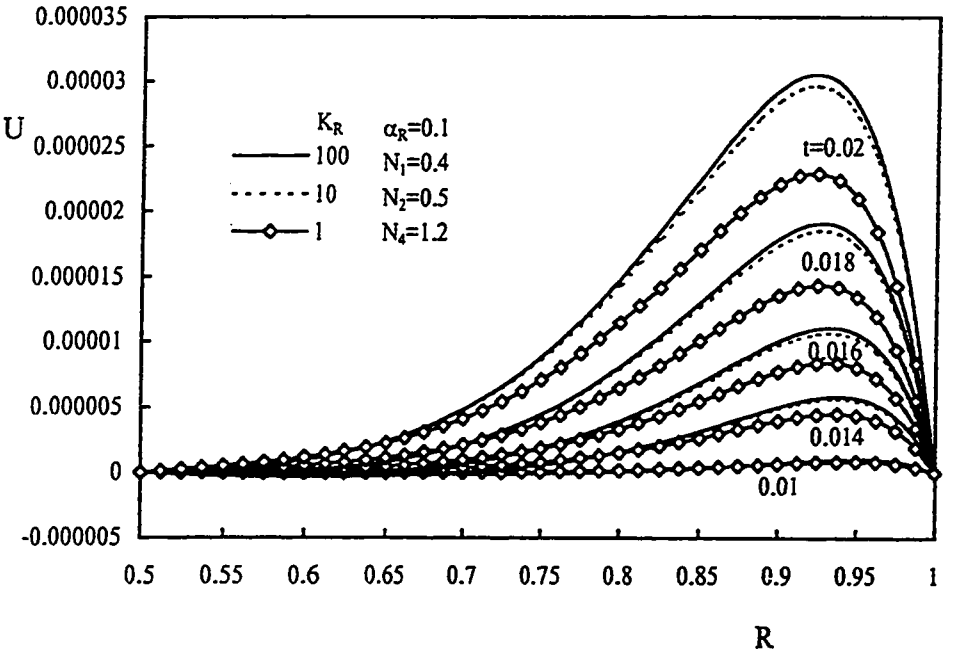

Figure 5.34: Effect of K_R on the variation of the exit axial velocity with time, $Gr^* = 10^5, \alpha_R = 0.1$

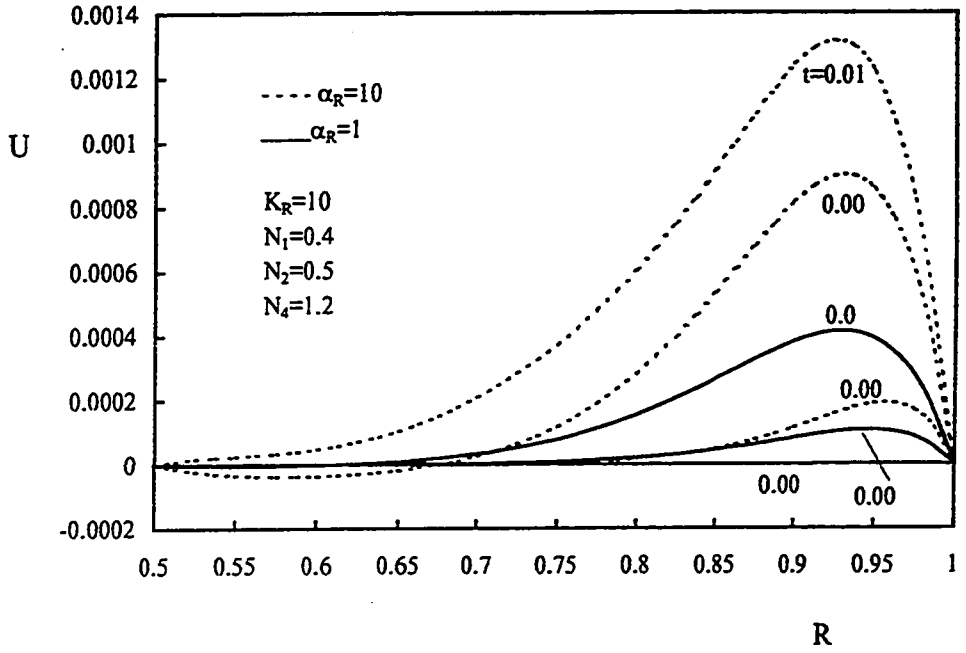

Figure 5.35: Effect of α_R on the variation of the exit axial velocity with time, $Gr^* = 10^5, K_R = 10$

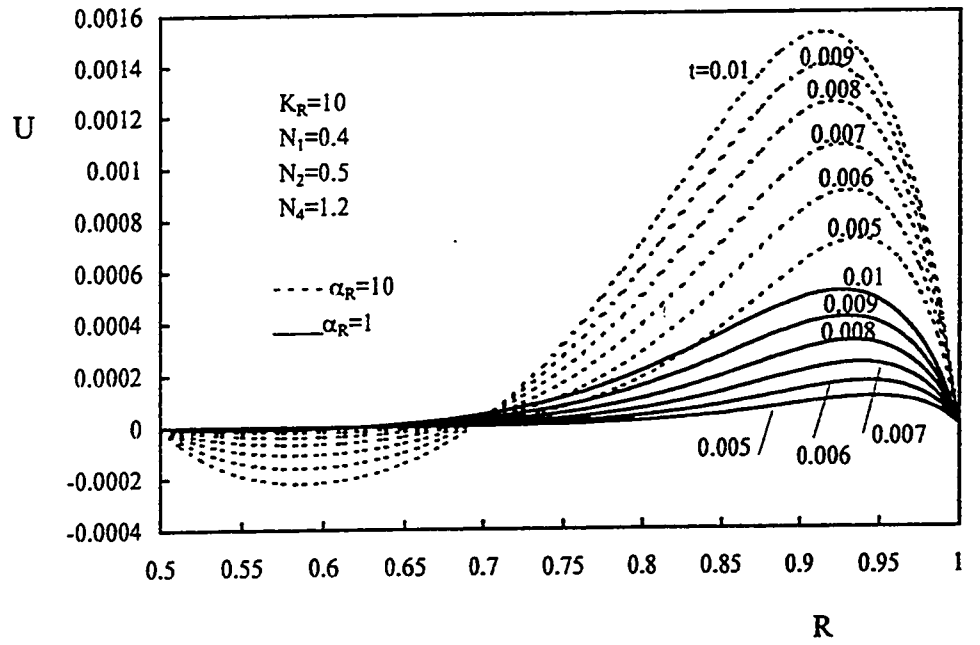

Figure 5.36: Effect of α_R on the variation of the exit axial velocity with time, $Gr^* = 10^5, K_R = 10$

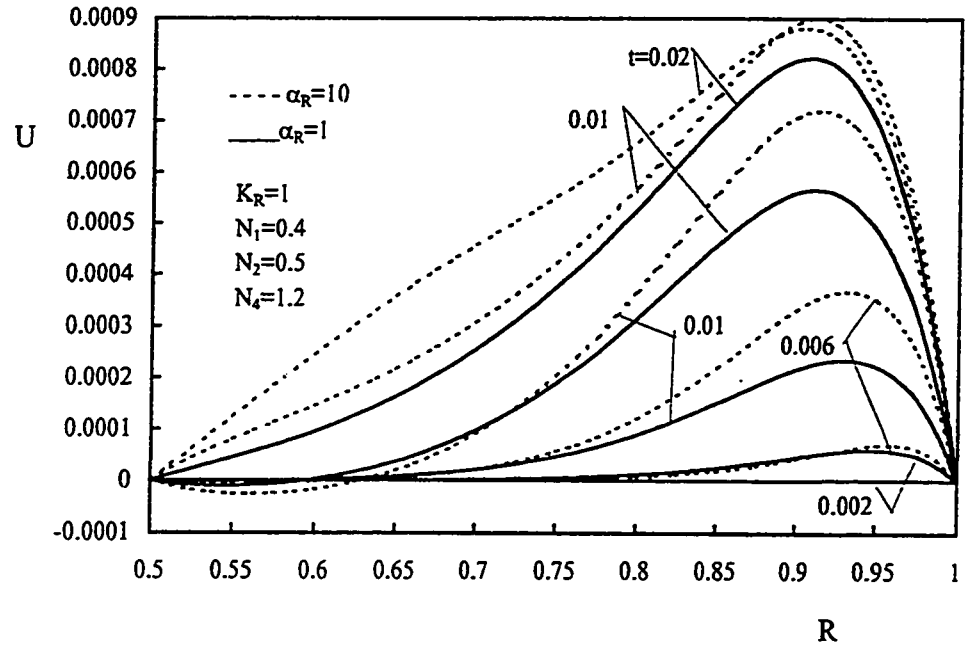

Figure 5.37: Effect of α_R on the variation of the mid-height axial velocity with time, $Gr^* = 10^5, K_R = 1$

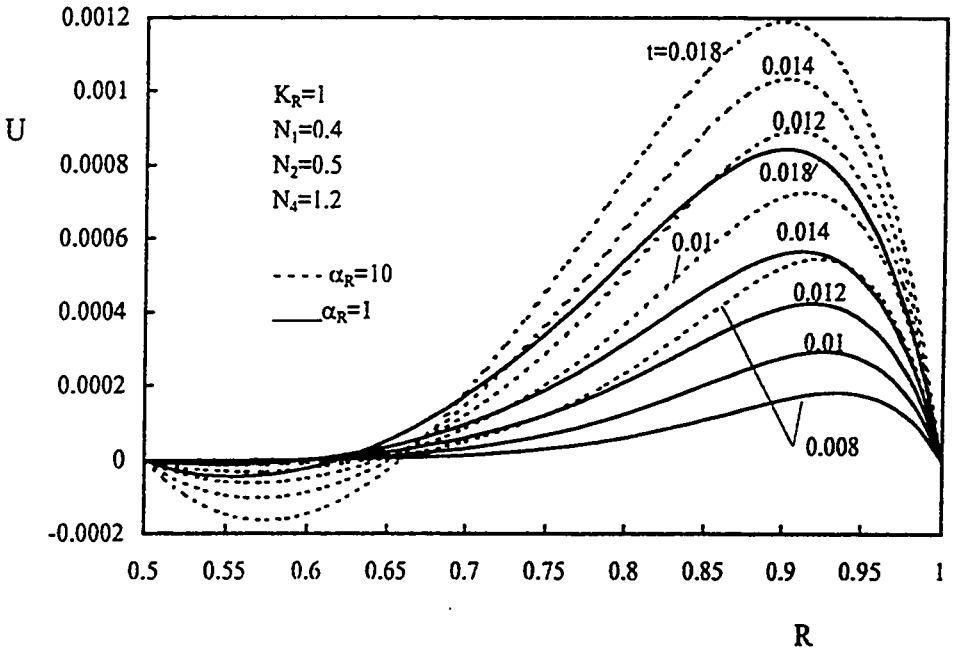

Figure 5.38: Effect of α_R on the variation of the exit axial velocity with time, $Gr^* = 10^5, K_R = 1$

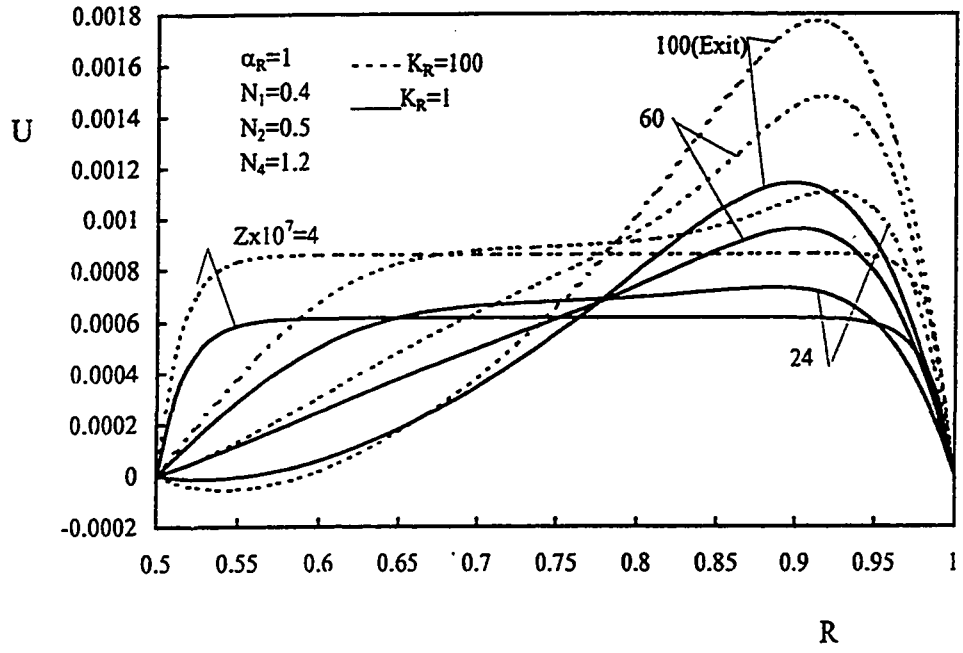

Figure 5.39: Effect of K_R on the developing axial velocity, $t = 0.035, Gr^* = 10^5$

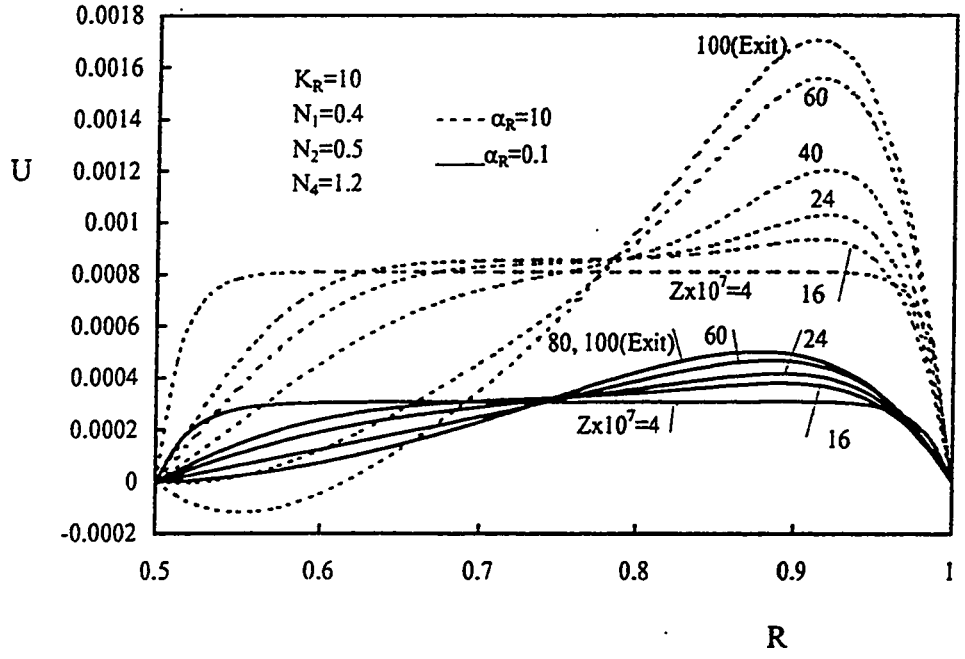

Figure 5.40: Effect of α_R on the developing axial velocity, $t = 0.045, Gr^* = 10^5$

5.3.2 Radial Velocity

Figures 5.41 through 5.66 constitute three groups of figures presenting the effects of K_R and α_R on the radial velocity profile for three values of Gr^*, namely, $Gr^* = 500, 10^4$ *and* 10^5. Each of the first two groups(corresponding to $Gr^* = 500$ *and* 10^4) consists of ten figures. The first four figures in each of these two groups present, for given values of α_R, the effect of K_R on the development with time of the radial velocity profile at the mid-height and exit cross-sections of the annulus. The next four figures in each of these groups present the effect of α_R on the variation with time of the radial velocity profile for given values of K_R at the aforementioned two cross-sections. The ninth figure shows the effect of K_R on the developing radial velocity profile at given values of α_R and time while the tenth figure presents the effect of α_R on the developing radial velocity for given values of K_R and time. However, the last group(which corresponds to $Gr^* = 10^5$) comprises only six figures. This is because, some computer runs for this group showed high numerical instabilities due to the presence of strong flow reversal (i.e., large negative axial velocity near the adiabatic wall) and failed to reach the steady-state conditions(e.g., when $K_R \geq 10$ and $\alpha_R \geq 1$).

Figure 5.41 shows how K_R affects the development with time of the mid-height radial velocity for an annulus of $Gr^* = 500$ and $\alpha_R = 1$. At early time, the small amount of heat conducted through the heated wall to the fluid annular gap induces a small flow rate which moves upwards through the annulus with a small axial velocity. Consequently, this slow flow may approach the fully-developed state in a short axial distance(which may be

shorter than the mid-height of the annulus, i.e., $V \approx 0$ at the mid-height). As time elapses, more heat is conducted into the core region of the annulus increasing the amount of the induced fluid. Hence, the magnitude of the induced flow axial velocity increases and the flow needs larger axial distance to approach the fully-developed state. Thus, the radial velocity at the mid-height cross-section might be larger than zero. For $Gr^* = 500$ and at the mid-height cross section, Fig. 5.41 shows that increasing K_R causes a decrease in the values of the radial velocity component. This is attributed to the increase in the rate of heat transfer to the fluid-annular gap as K_R increases. Consequently, for higher values of K_R, the developing flow has a larger axial velocity(i.e., smaller boundary-layer thickness; $\delta \sim \frac{1}{\sqrt{Re}}$) and hence a smaller mid-height radial velocity. A careful look at Fig. 5.42 reveals that the radial velocity profiles at the exit cross-section have smaller values than those corresponding to the mid-height. This means that the induced flow approaches its fully-developed state as it moves upward. Moreover, as K_R increases, the flow approaches faster the full-development state. In fact, Fig. 5.42 does not include any profile for $K_R = 100$ as for this particular value of K_R the flow has almost reached, for the selected values of time, the fully developed state near the exit cross-section($V \simeq 0$).

Figures 5.43 and 5.44 present the effect of K_R on the variation with time of the radial velocity profile at the mid-height and exit cross-sections for the same annulus under consideration with $\alpha_R = 0.1$. A comparison between Figs. 5.41 and 5.42 and Figs. 5.43 and 5.44, reveals that, for given values of K_R and time, the value of the radial velocity generally increases with α_R. This means that the induced fluid for this particular case, is

still developing and needs larger axial distance to approach the fully developed state. The reason for this behavior is explained in detail hereinafter.

Figures 5.45 through 5.48 show how α_R affects the development with time of the radial velocity profile at the mid-height and exit cross-sections. It is seen in these figures that, generally, for given values of K_R and time, the radial velocity increases with α_R. This is due to the increase in the amount of heat transferred to the fluid compared with that absorbed by the solid wall material. This results in an increase in the buoyancy force, or in other words, an increase in the values of the axial velocity across the annulus. Consequently, the axial distance needed for the flow to approach the fully developed state increases with α_R.

Figure 5.49 presents the effect of K_R on the developing radial velocity as the induced fluid moves upward through the annulus at given values of α_R and time(i.e., development of radial velocity with axial distance if there were a time freeze) while such effect for α_R is shown in Fig. 5.50 for given values of K_R and time. It can be seen from Fig. 5.49, for a given value of Z, as K_R increases the radial velocity decreases, as was mentioned before during the discussion of Figs. 5.41 and 5.42. Moreover, the figure shows that, for the given value of time, the flow corresponding to $K_R = 100$ has almost reached the fully-developed state ($V \simeq 0$) while for $K_R = 1$ the flow is still developing and needs more axial distance to approach the full-development state. Figure 5.50 shows that, for the given time, the radial velocity, at a given axial position, increases with α_R. This means that the

flow needs a larger axial distance to reach its fully developed state. This is attributed, as mentioned before, to the increase in the amount of heat transferred to the fluid.

Similar to the above group of figures, Figs. 5.51 through 5.60 and Figs. 5.61 through 5.66 present another two groups for $Gr^* = 10^4$ *and* 10^5, respectively. It is seen that each of these groups of figures has the same general qualitative characteristics of the first group except that the radial velocity, generally, has large positive values across the annulus. This is because large values of Gr^* represent short annuli which means that the induced flow reaches the exit of the annulus without approaching its fully-developed state.

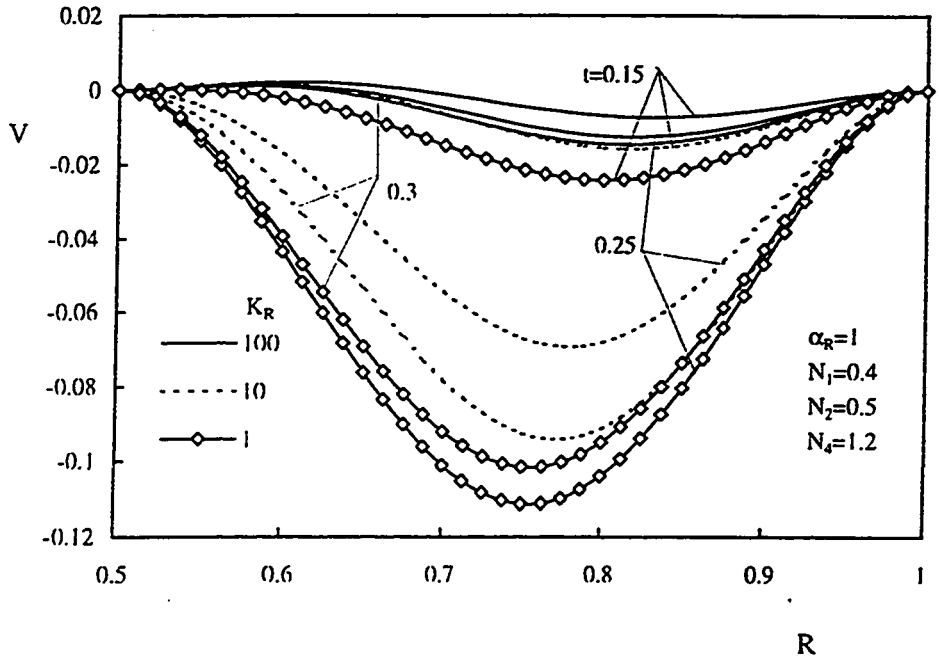

Figure 5.41: Effect of K_R on the variation of the mid-height radial velocity with time, $Gr^* = 500, \alpha_R = 1$

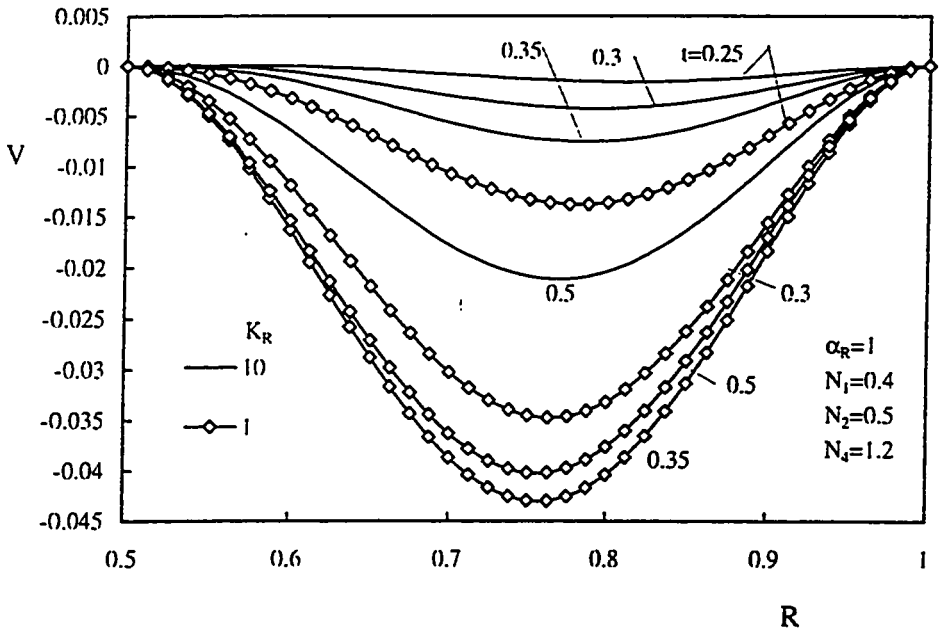

Figure 5.42: Effect of K_R on the variation of the exit radial velocity with time, $Gr^* = 500, \alpha_R = 1$

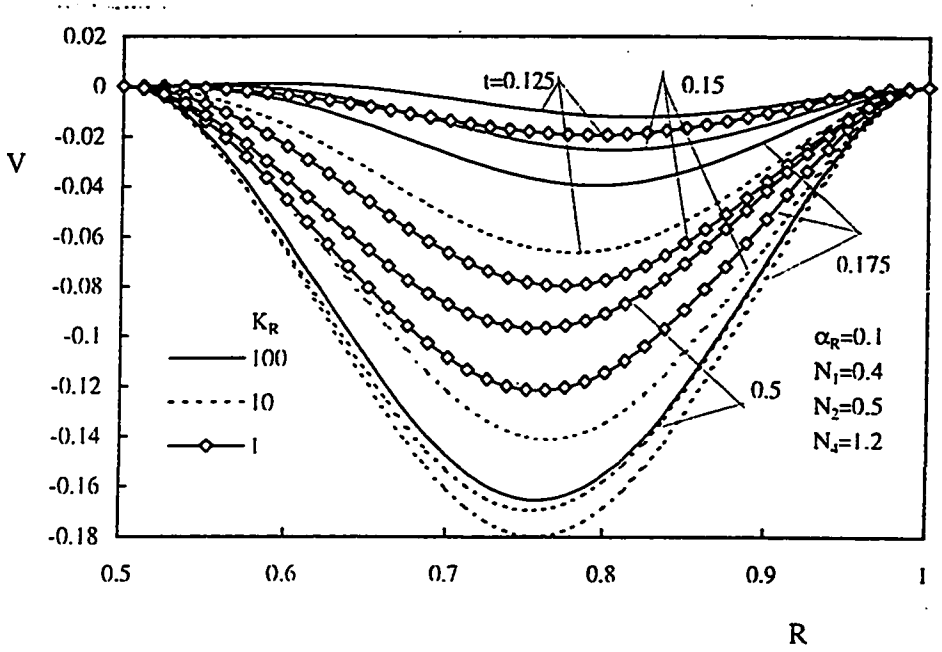

Figure 5.43: Effect of K_R on the variation of the mid-height radial velocity with time, $Gr^* = 500, \alpha_R = 0.1$

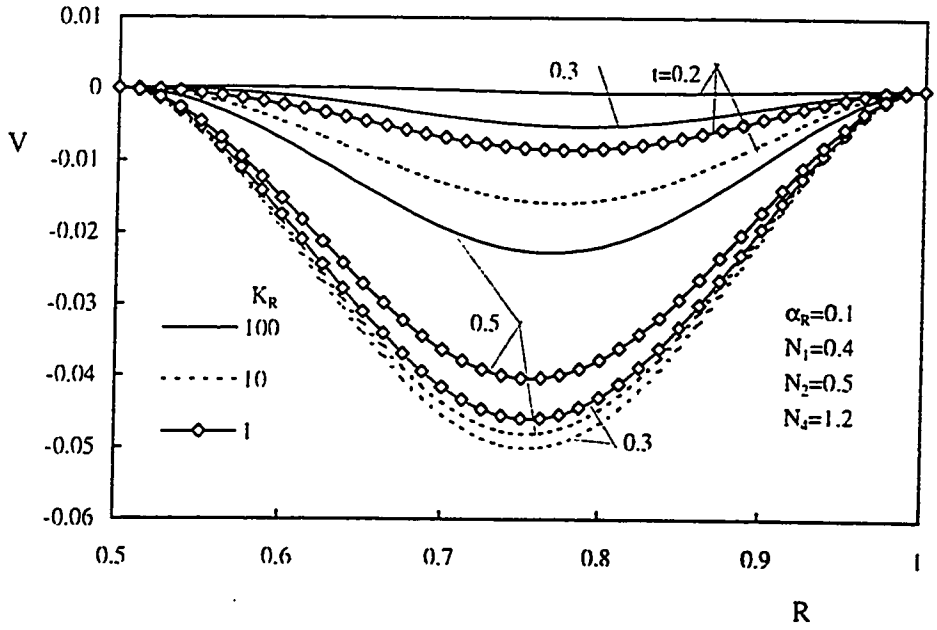

Figure 5.44: Effect of K_R on the variation of the exit radial velocity with time, $Gr^* = 500, \alpha_R = 0.1$

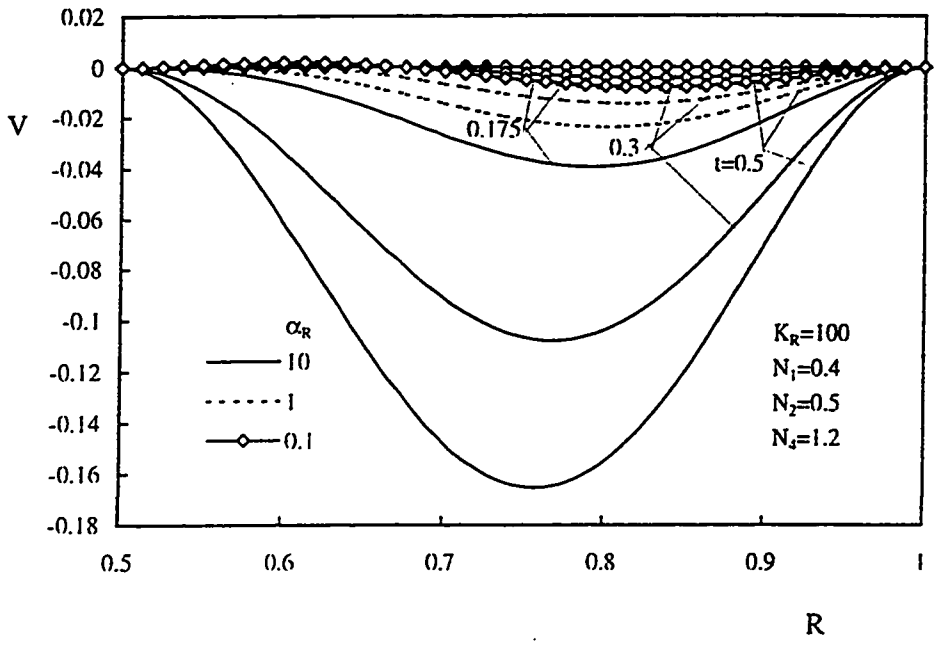

Figure 5.45: Effect of α_R on the variation of the mid-height radial velocity with time. $Gr^* = 500, K_R = 100$

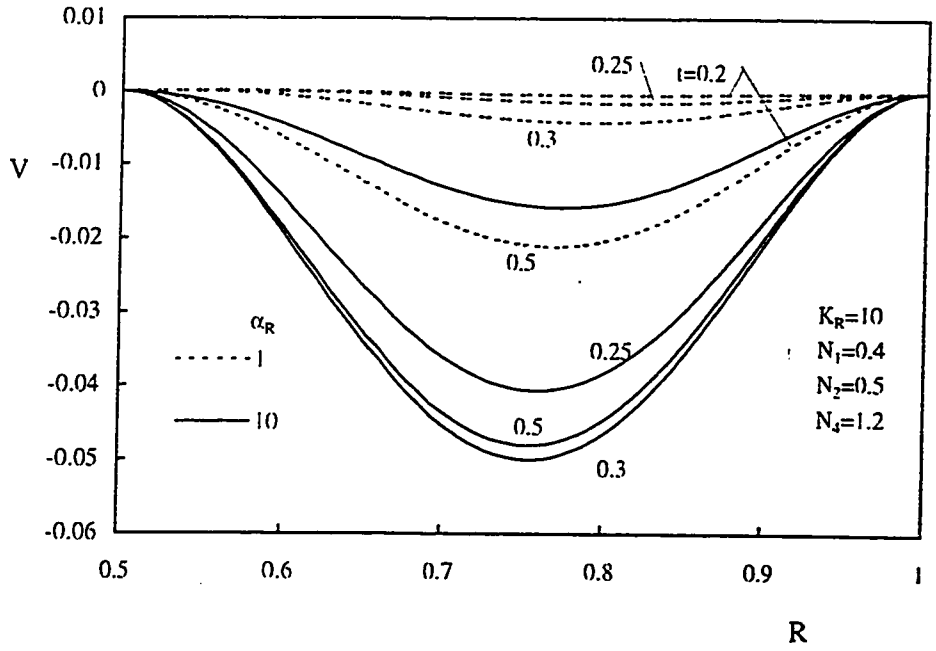

Figure 5.46: Effect of α_R on the variation of the exit radial velocity with time, $Gr^* = 500, K_R = 100$

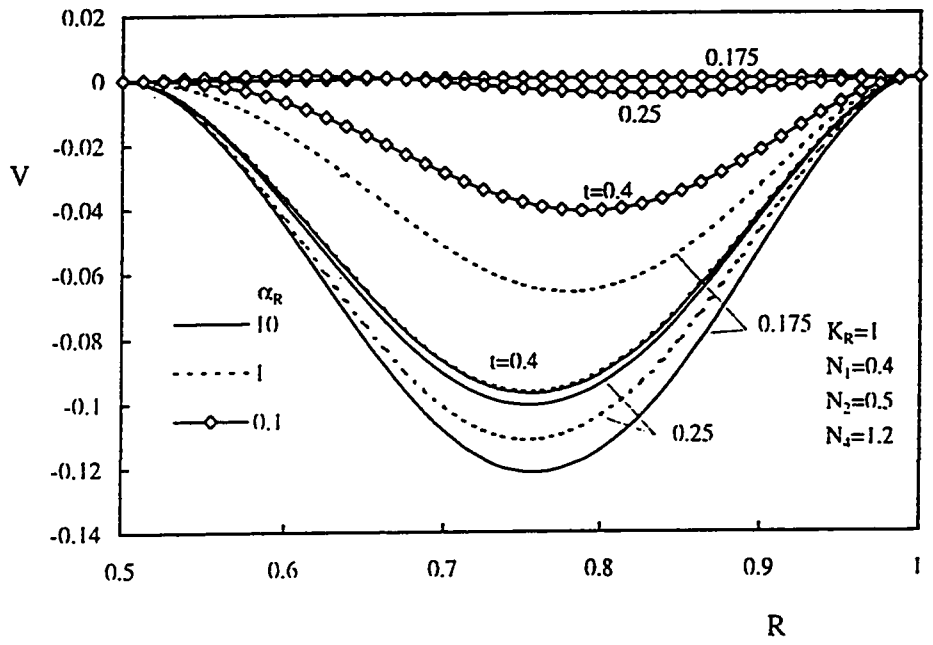

Figure 5.47: Effect of α_R on the variation of the mid-height radial velocity with time, $Gr^* = 500, K_R = 1$

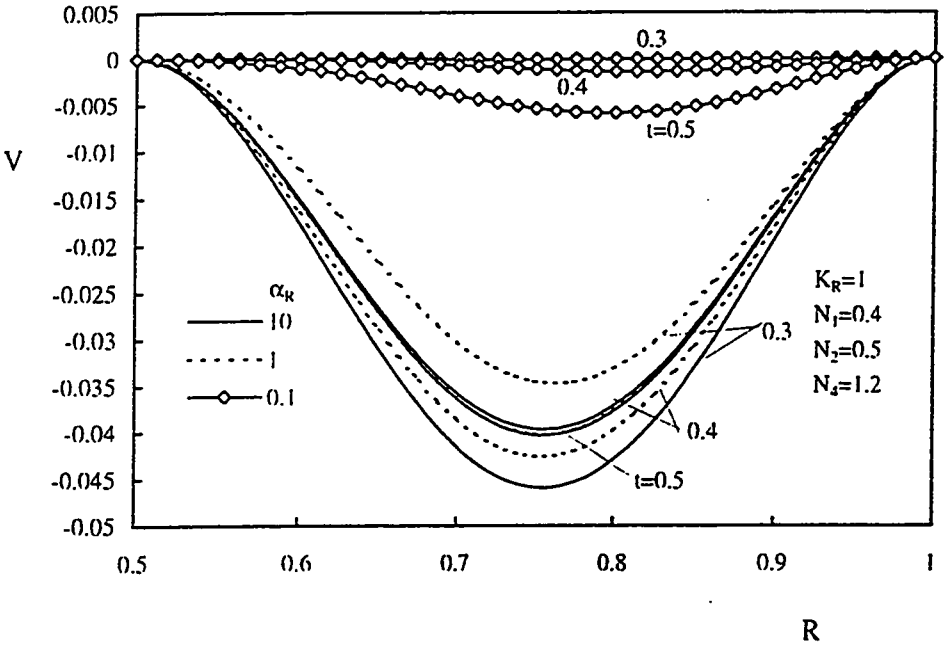

Figure 5.48: Effect of α_R on the variation of the exit radial velocity with time, $Gr^* = 500, K_R = 1$

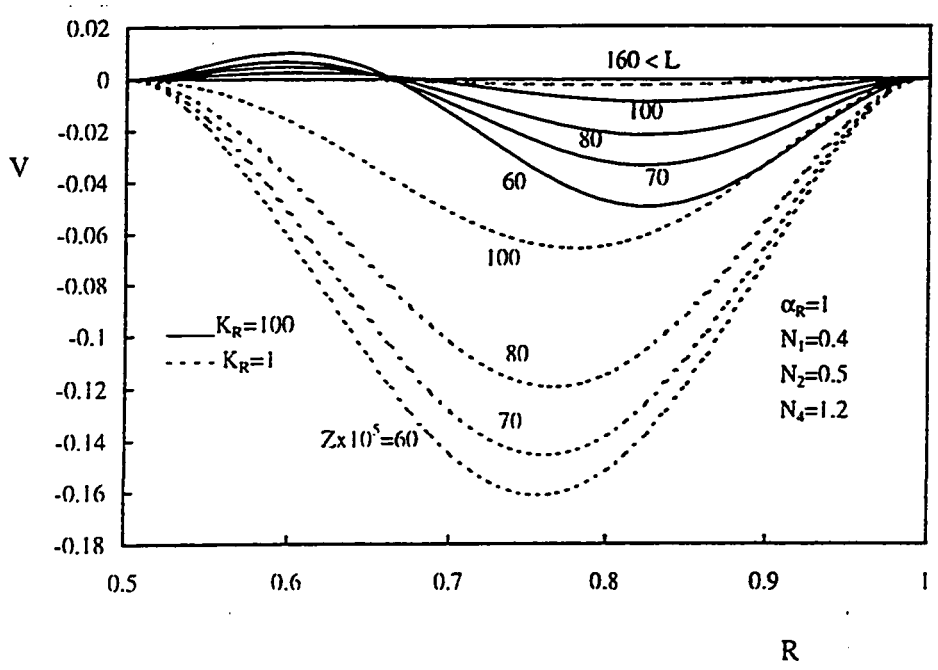

Figure 5.49: Effect of K_R on the developing radial velocity, $t = 0.175, Gr^* = 500$

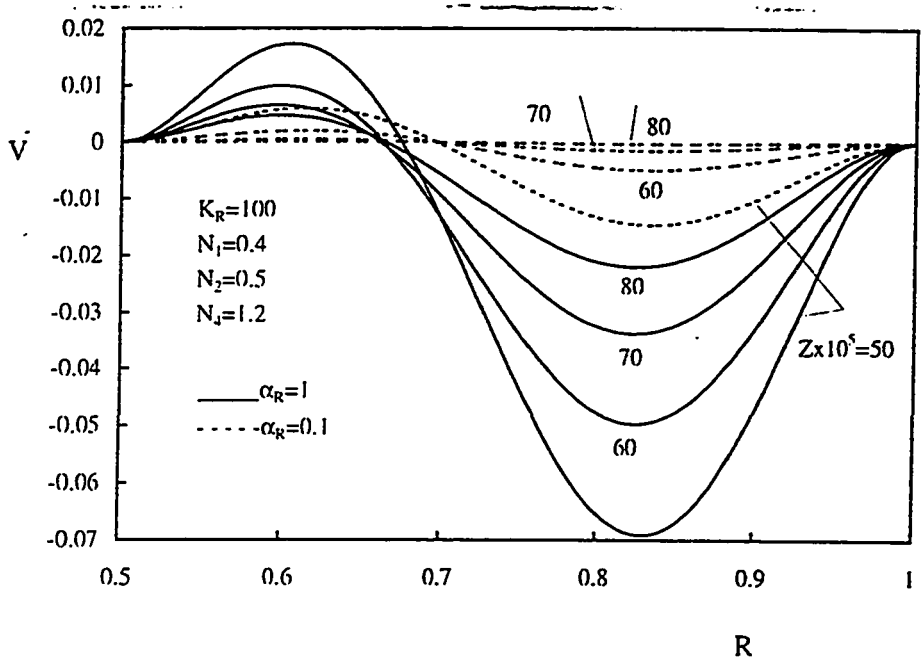

Figure 5.50: Effect of α_R on the developing radial velocity, $t = 0.175, Gr^* = 500$

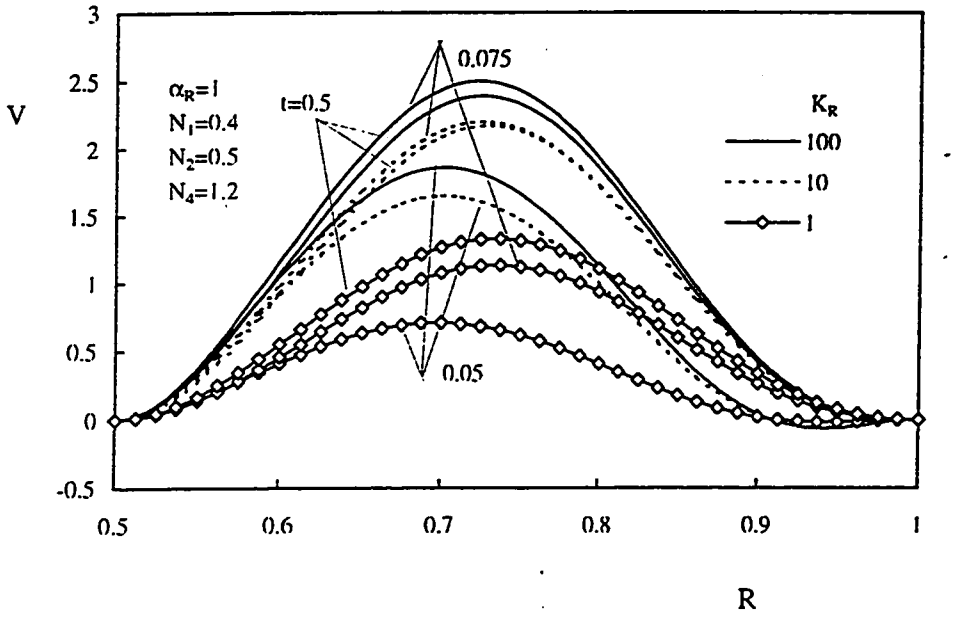

Figure 5.51: Effect of K_R on the variation of the mid-height radial velocity with time, $Gr^* = 10^4, \alpha_R = 1$

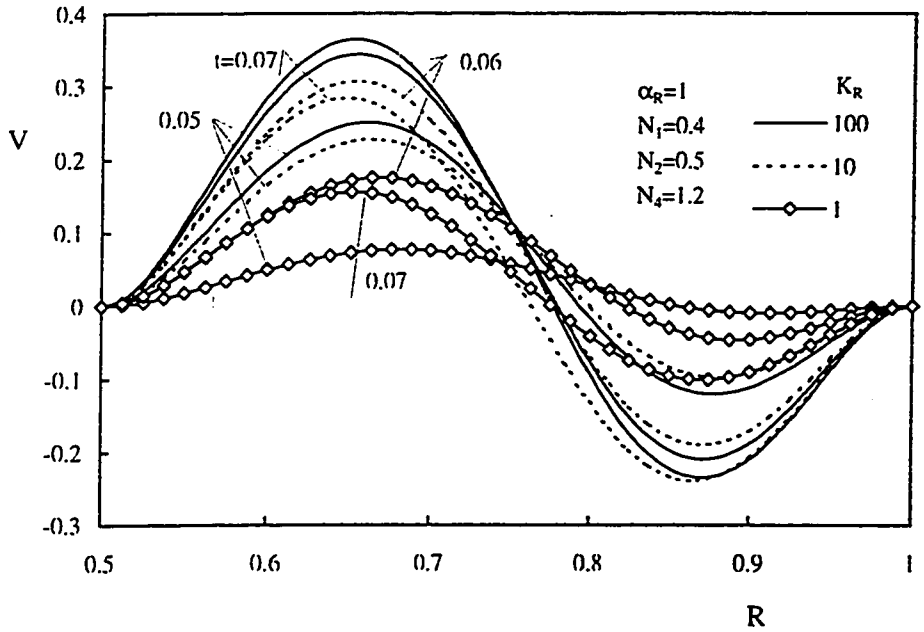

Figure 5.52: Effect of K_R on the variation of the exit radial velocity with time, $Gr^* = 10^4, \alpha_R = 1$

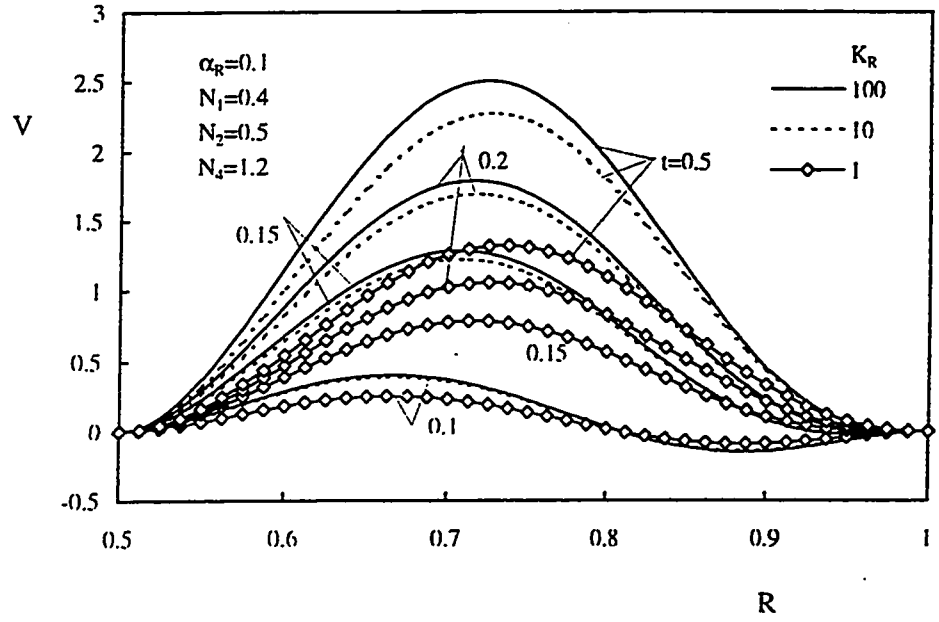

Figure 5.53: Effect of K_R on the variation of the mid-height radial velocity with time, $Gr^* = 10^4, \alpha_R = 0.1$

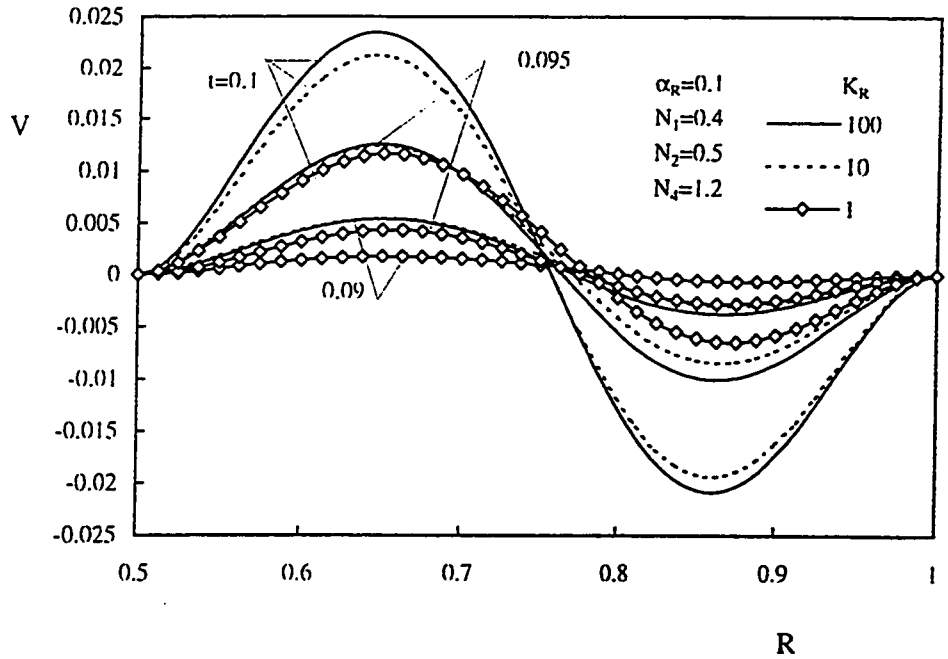

Figure 5.54: Effect of K_R on the variation of the exit radial velocity with time, $Gr^* = 10^4, \alpha_R = 0.1$

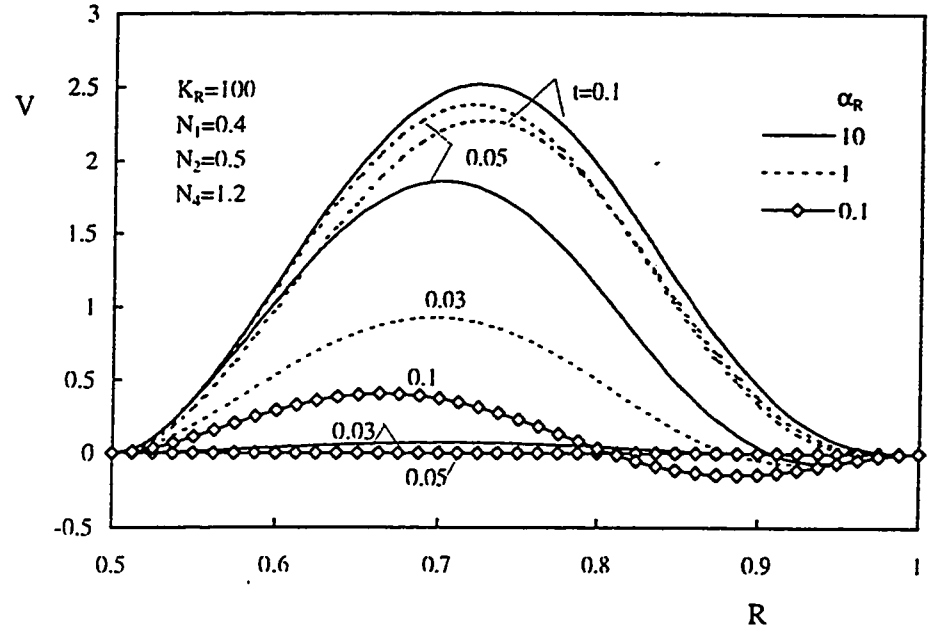

Figure 5.55: Effect of α_R on the variation of the mid-height radial velocity with time, $Gr^* = 10^4$, $K_R = 100$

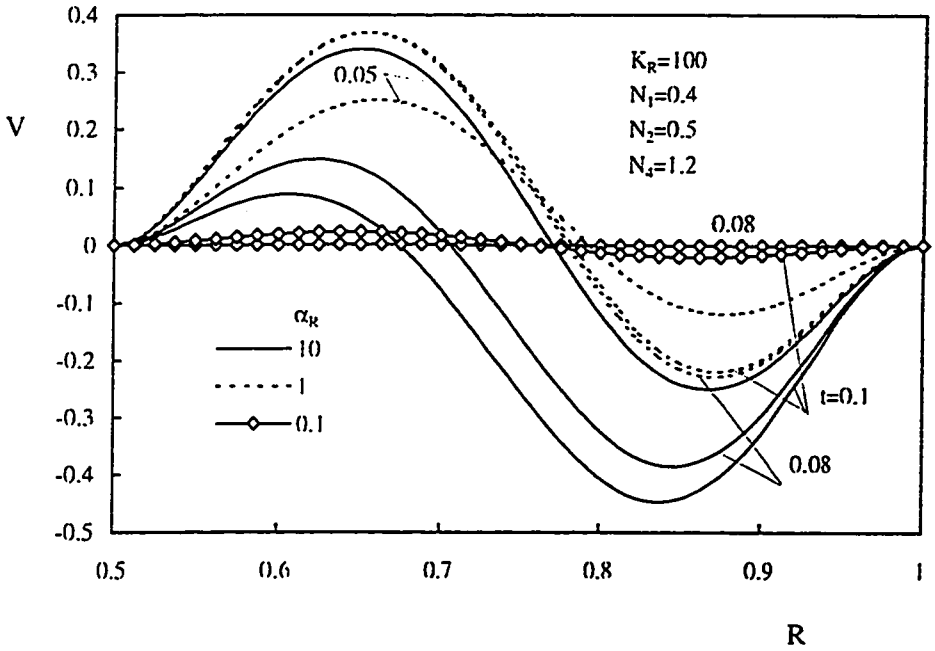

Figure 5.56: Effect of α_R on the variation of the exit radial velocity with time, $Gr^* = 10^4$, $K_R = 100$

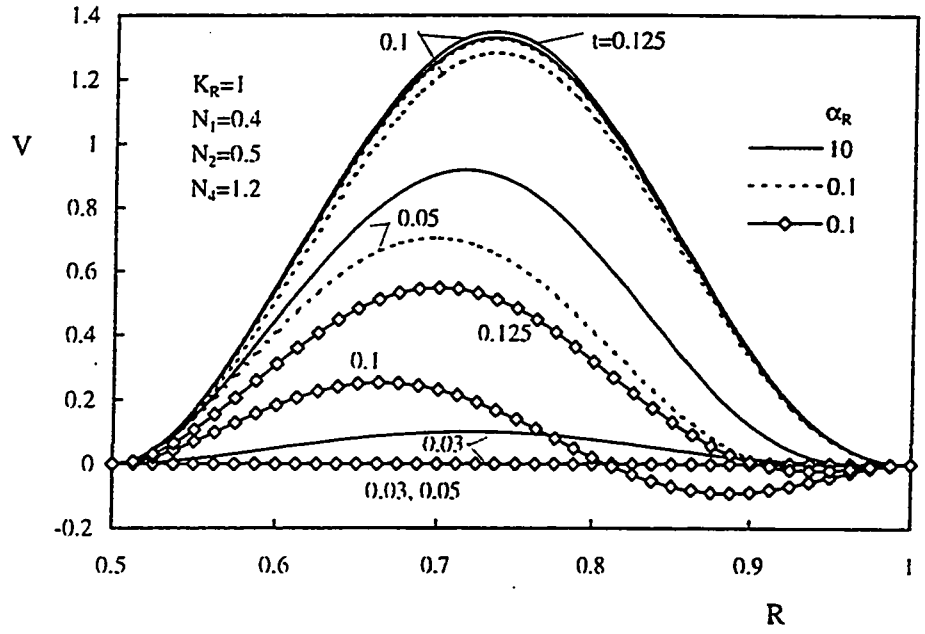

Figure 5.57: Effect of α_R on the variation of the mid-height radial velocity with time, $Gr^* = 10^4, K_R = 1$

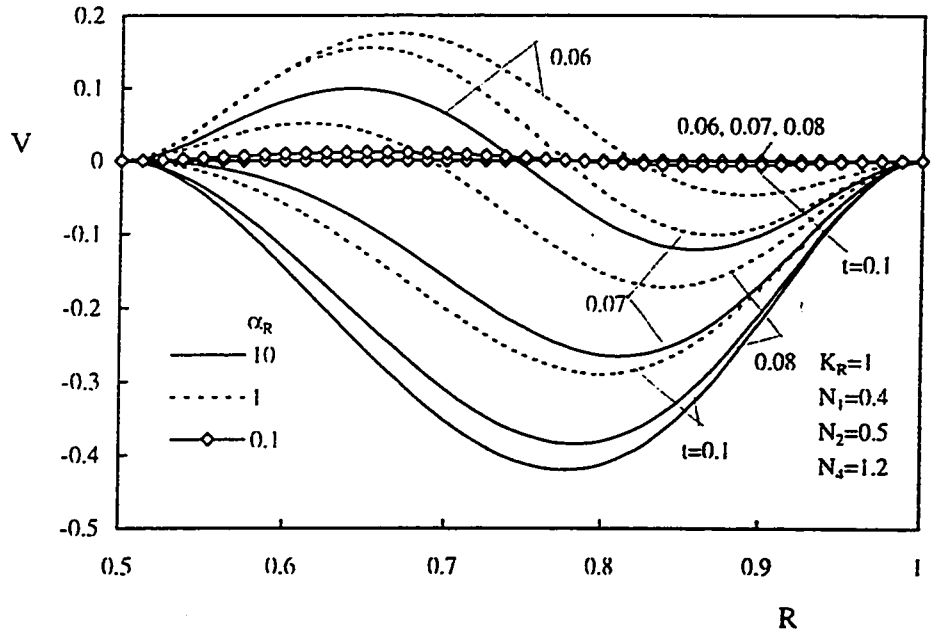

Figure 5.58: Effect of α_R on the variation of the exit radial velocity with time, $Gr^* = 10^4, K_R = 1$

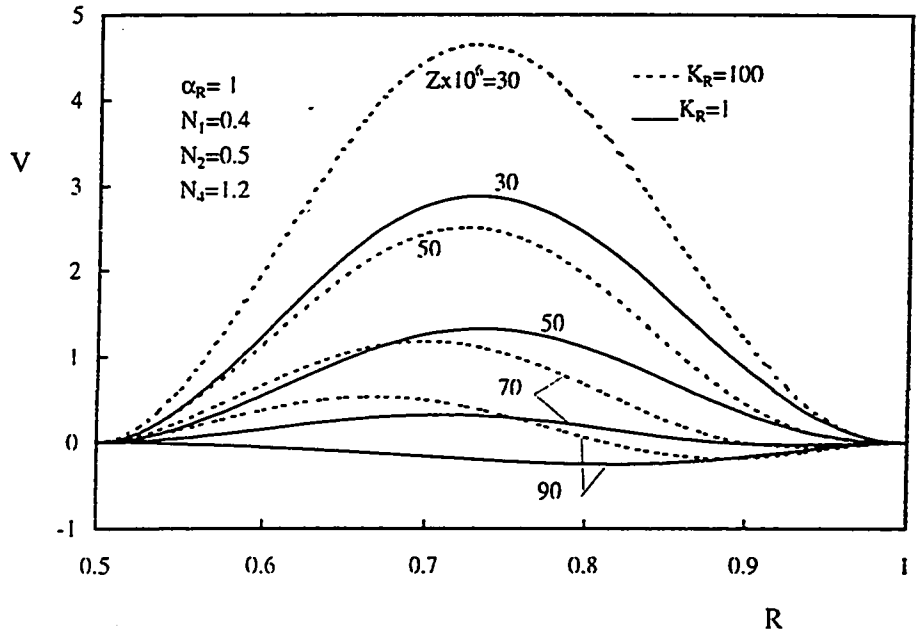

Figure 5.59: Effect of K_R on the developing radial velocity, $t = 0.175, Gr^* = 10^4$

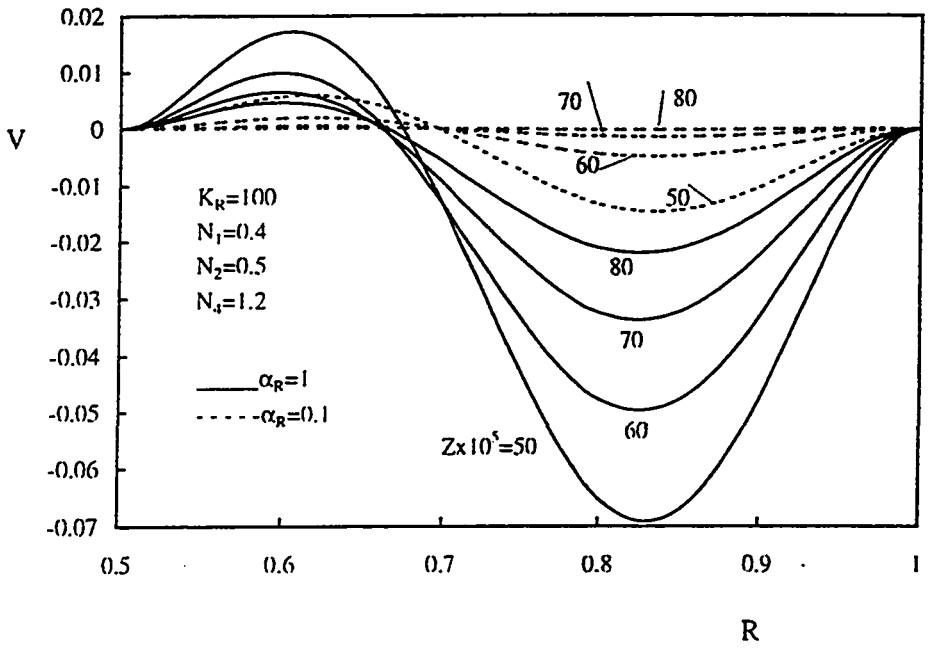

Figure 5.60: Effect of α_R on the developing radial velocity, $t = 0.175, Gr^* = 10^4$

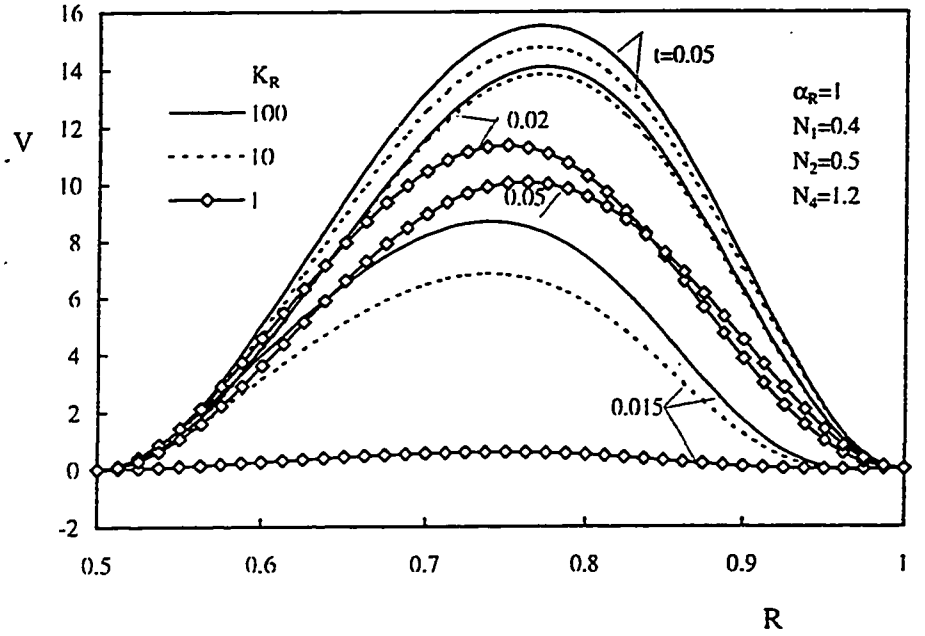

Figure 5.61: Effect of K_R on the variation of the mid-height radial velocity with time, $Gr^* = 10^5, \alpha_R = 1$

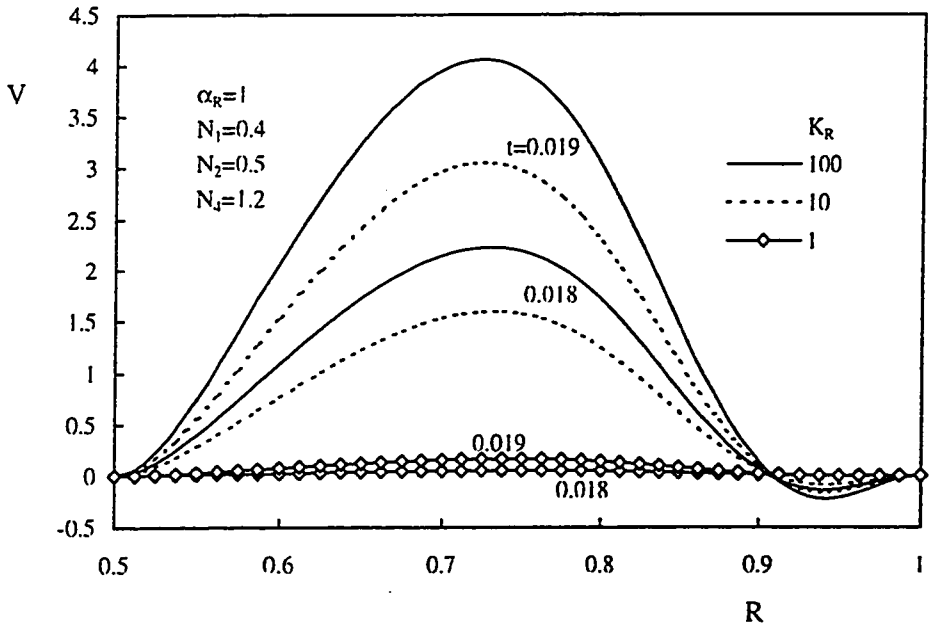

Figure 5.62: Effect of K_R on the variation of the exit radial velocity with time, $Gr^* = 10^5, \alpha_R = 1$

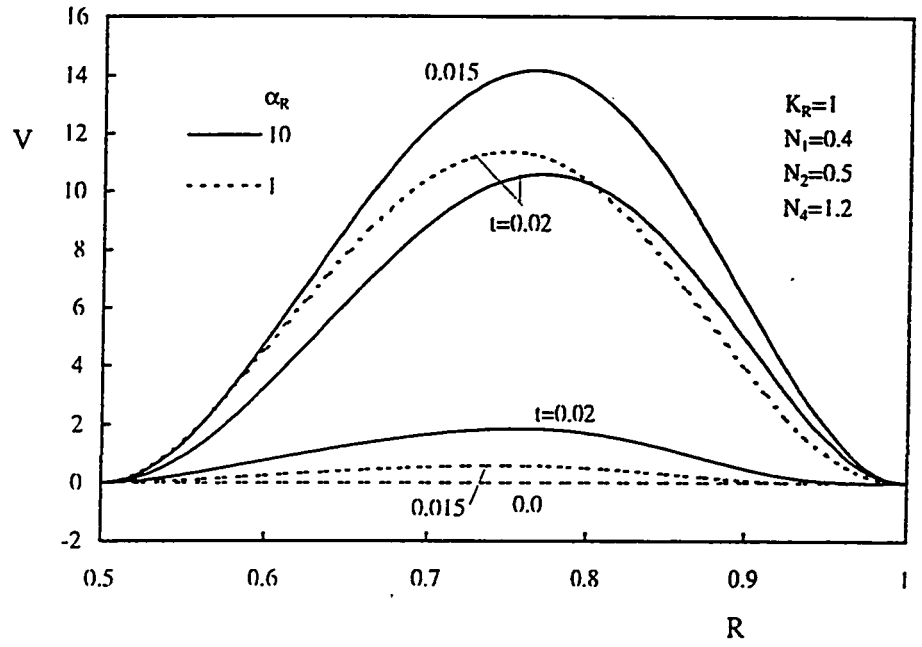

Figure 5.63: Effect of α_R on the variation of the mid-height radial velocity with time, $Gr^* = 10^5, K_R = 1$

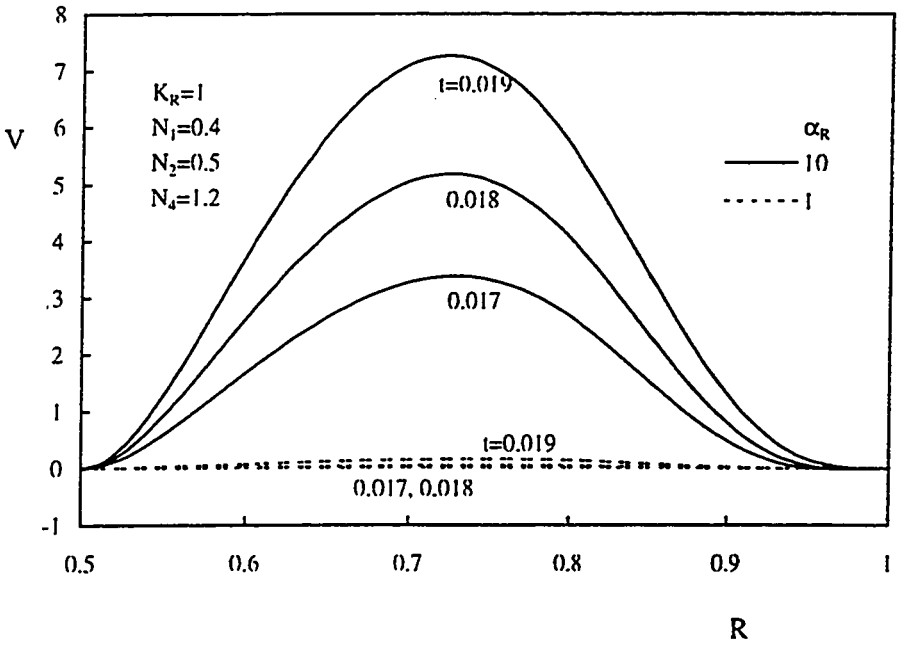

Figure 5.64: Effect of α_R on the variation of the exit radial velocity with time, $Gr^* = 10^5, K_R = 1$

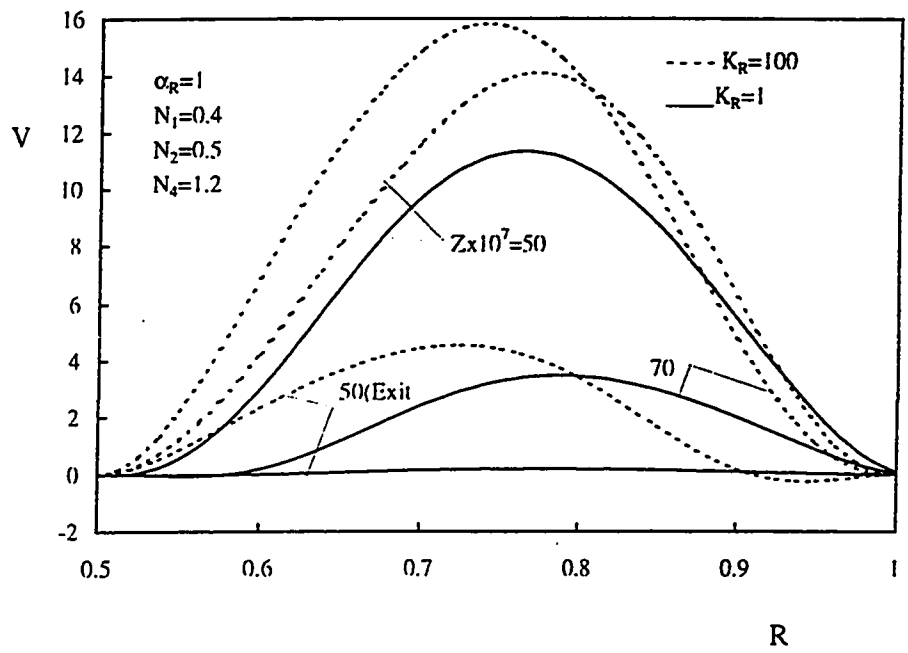

Figure 5.65: Effect of K_R on the developing radial velocity, $t = 0.02, Gr^* = 10^5$

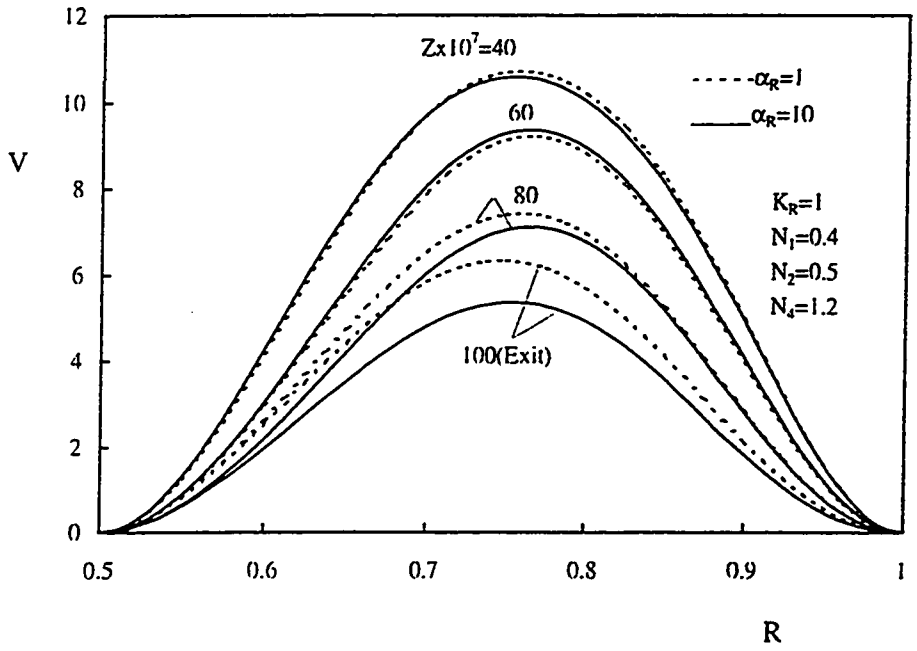

Figure 5.66: Effect of α_R on the developing radial velocity, $t = 0.035, Gr^* = 10^5$

5.3.3 Temperature

In this section, four groups of figures corresponding to $Gr^* = 500, 10^3, 10^4$ *and* 10^5 present the effect of both K_R and α_R on the temperature profiles at different axial positions. Each of the first three groups(corresponding to $Gr^* = 500, 10^3$ *and* 10^4) consists of five pairs of figures. The first two pairs in each of these three groups present, for given values of α_R, the effect of K_R on the development with time of the temperature profile at the mid-height and exit cross-sections of the annulus. The next two pairs in these groups show, for given values of K_R, how α_R affects the development with time of the temperature profile at the aforesaid axial positions. Finally, the last pair shows, for a given value of time, the effects of K_R and α_R on the variation of the temperature profile across the annulus as the induced fluid moves upward through the annulus. On the other hand, the last group(which corresponds to $Gr^* = 10^5$) comprises only three pairs. This is because some computer runs showed numerical instability and failed to obtain any solution as clarified in the preceding sections.

Figure 5.67 shows, for a given α_R, the effect of K_R on the mid-height temperature profile as it develops with time. At early time, a small amount of heat has been transferred through the solid heated wall to the annulus causing only fluid adjacent to the heated wall to warm up while fluid adjacent to the outer surface of the adiabatic inner wall remains cold. As time elapses, more heat is transferred into the fluid-annular gap resulting in an increase in the temperature within the solid wall and across the annulus. As can be seen from Fig. 5.67, in general for a given time, increasing K_R increases the temperature near the heated

wall. This can be attributed to the increase in the rate of heat transfer through the heated wall and consequently the induced fluid as K_R increases. However, near the adiabatic wall, K_R has a reverse effect, i.e., as K_R increases, the temperature near the adiabatic wall decreases. This unexpected effect of K_R on the temperature near the adiabatic wall becomes easily pronounced at large values of time. This behavior of the mid-height temperature profile can be explained by means of Fig. 5.41 which presents the effect of K_R on the development with time of the mid-height radial velocity for the given annulus($Gr^* = 500$, $\alpha_R = 1$). In this figure, it can be seen that the mid-height radial velocity for the smaller value of $K_R(K_R = 1)$ has larger negative magnitudes compared with that corresponding to the larger values of K_R. Accordingly, the amount of heat convected radially towards the adiabatic wall due to transportation by the radial velocity component is larger for the smaller value of K_R. Hence, the temperature near the adiabatic wall has larger magnitudes for smaller values of K_R.

A careful look at temperature profiles shows that, for $K_R = 1$, the temperature profile corresponding to $t = 0.2$ overshoots that corresponding to $t = 0.3$. This phenomenon is called the temperature overshoot; such phenomenon is well known in the field of transient free convection (e.g., [26]). This phenomenon can be explained as follows. At early time, the amount of induced fluid is small; consequently, the coefficient of heat transfer is small and the diffusion dominates the heat transfer process. Hence, the heat transfer process follows the conduction pattern and so the temperature increases to certain values which take into account that the heat removal mechanism by convection is weak. However, as

more heat is conducted to the fluid-annular gap more fluid is sucked. This larger induced fluid absorbs more heat as it sweeps the heated wall with a larger velocity. This leads to an increase in the heat transfer coefficient; hence, the heat removal mechanism by convection becomes strong and the temperature decreases.

Figure 5.68 presents, for a given value of α_R, the effect of K_R on the exit temperature profile as it develops with time. Comparing Figs. 5.67 and 5.68, one can observe that, for a given time(e.g., $t = 0.01$), the temperature profiles(for a given value of K_R) have larger magnitudes at the exit compared with those corresponding to the mid-height cross-section. This is attributed to the more heat that the induced fluid absorbed as it moved upwards through the annulus from the mid-height cross-section till the annulus exit.

For another value of α_R ($\alpha_R = 0.1$) Figs. 5.69 and 5.70 present the effect of K_R on the temperature profiles at the mid-height and the exit as they develop with time in the annulus under consideration. A comparison between Figs. 5.67 and 5.68 and Figs. 5.69 and 5.70 reveals that, for given K_R and time, the temperature values across the annulus at both the mid-height and the exit cross-sections decrease with decreasing α_R. The reason for this is explained hereinafter.

For $K_R = 100$ *and* 1, respectively, Figs. 5.71 through 5.74 present the effect of α_R on the development with time of the temperature profile at the mid-height and exit cross-sections. It is seen from these figures that, for given values of K_R and time, the temperature increases across the annulus as α_R increases. This is attributed to the increase in the thermal diffusivity of the wall material. As mentioned before, the increase in α_R implies a

decrease in the specific heat of the wall material. This leads to an increase in the amount of heat conducted through the heated wall compared with that absorbed by the wall material. Accordingly, this leads to an increase in the value of the temperature across the annulus. Moreover, Figs. 5.71 through 5.74 show that, for a given K_R, the temperature near the adiabatic wall increases with α_R while Figs. 5.67 through 5.70 showed that such temperature decreases as K_R increases. This can be explained by referring to Figs. 5.45 through 5.48 which show, for given values of K_R, the effect of α_R on the development with time of the radial velocity profile at the mid-height and exit cross-sections. It can be seen from these figures that, for given time and K_R, the magnitudes of the radial velocity component increase with α_R. Consequently, for given time and K_R, with the increase in the value of α_R more heat is transported radially towards the cold fluid near the adiabatic wall. This results in the increase in the values of the temperature there as α_R increases.

Figures 5.75 and 5.76 present the effect of K_R and α_R on the development with the axial distance as the induced fluid moves upwards through the annulus at a given time, i.e., if there were a time freeze. It can be seen from Fig. 5.75 that the temperature across the annulus increases with K_R except near the adiabatic wall where the temperature decreases. Also, Fig. 5.76 shows that the values of the temperature all over the annulus cross-section increase with increasing α_R. This confirm the previous discussion on the effect of both these parameters(K_R and α_R) on the variation with time of the mid-height and exit temperature profiles.

Similar to the above group of figures, Figs. 5.77 through 5.86, Figs. 5.87 through 5.96 and Figs. 5.97 through 5.102 present other three groups for $Gr^* = 10^3, 10^4 \; and \; 10^5$, respectively. It can be seen from all these figures that each of these groups has the same general qualitative characteristics of the first group(Figs. 5.67 through 5.76). Moreover, it is seen in Figs. 5.97 through 5.102 which are for large value of Gr^* (10^5) that the temperature near the adiabatic wall at the mid-height and exit cross sections have almost zero value. This is because no heat has been convected from regions near the heated wall towards that near the adiabatic one (see Figs. 5.61 through 5.64). This might cause a flow reversal as explained earlier. Finally, it can be seen from all the presented results that, generally, the temperature across the annulus increases as Gr^* decreases. This is because, smaller values of Gr^* mean longer annuli with smaller hydraulic diameters which mean that the induced fluid has enough axial distance to absorb more heat compared with annuli of larger values of Gr^*. Consequently, as the fluid approaches the exit cross-section the temperature across the annulus increases to a maximum value which can approach the value of $\theta = 1$ if the flow approaches the fully-developed state.

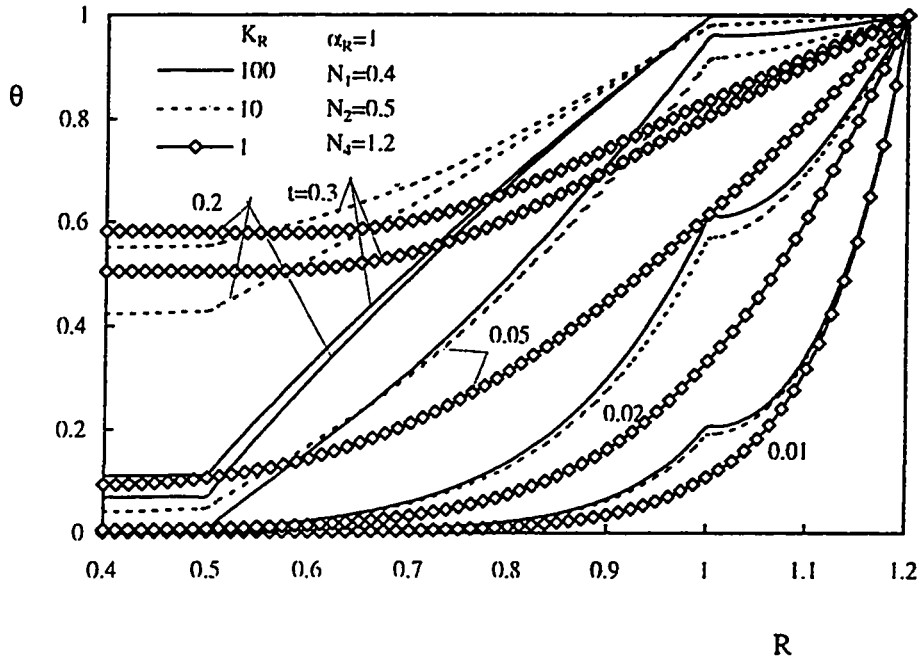

Figure 5.67: Effect of K_R on the variation of the mid-height temperature with time, $Gr^* = 500, \alpha_R = 1$

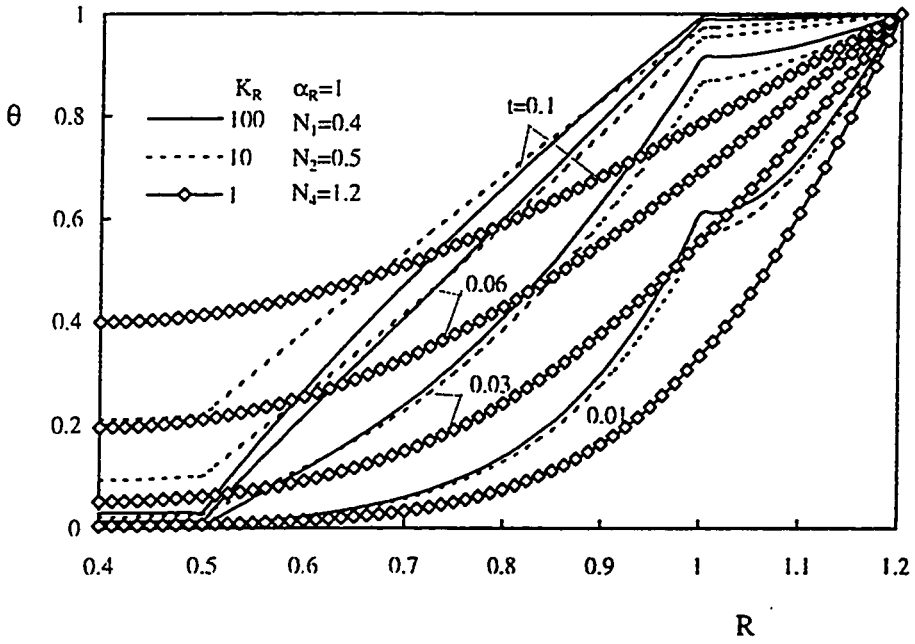

Figure 5.68: Effect of K_R on the variation of the exit temperature with time, $Gr^* = 500, \alpha_R = 1$

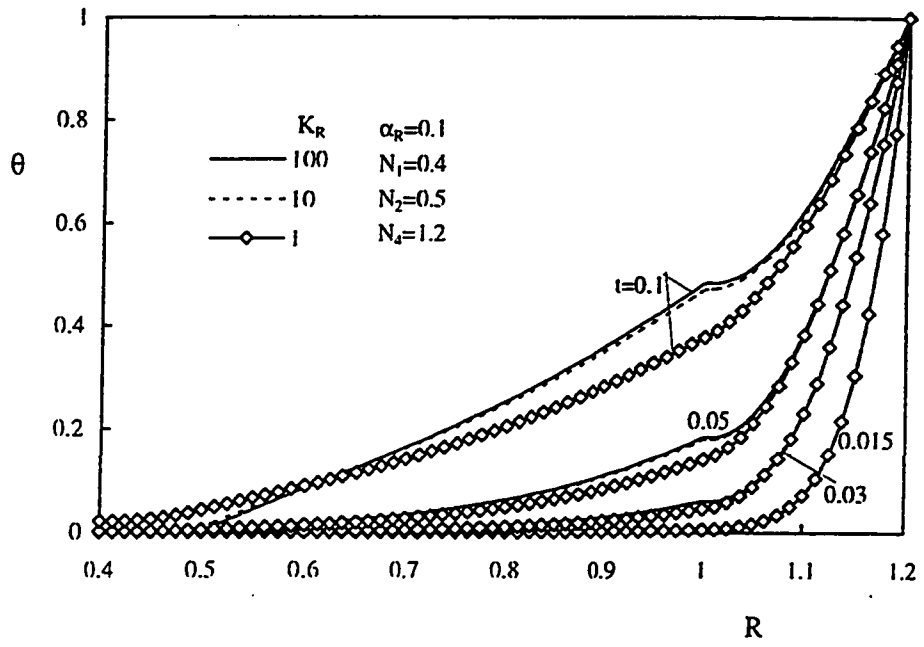

Figure 5.69: Effect of K_R on the variation of the mid-height temperature with time, $Gr^* = 500, \alpha_R = 0.1$

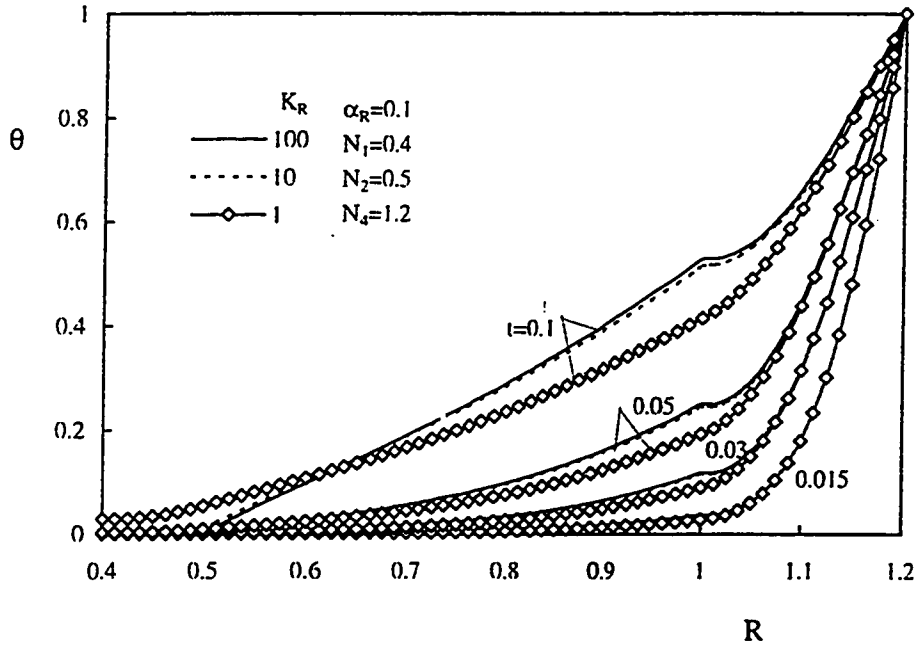

Figure 5.70: Effect of K_R on the variation of the exit temperature with time, $Gr^* = 500, \alpha_R = 0.1$

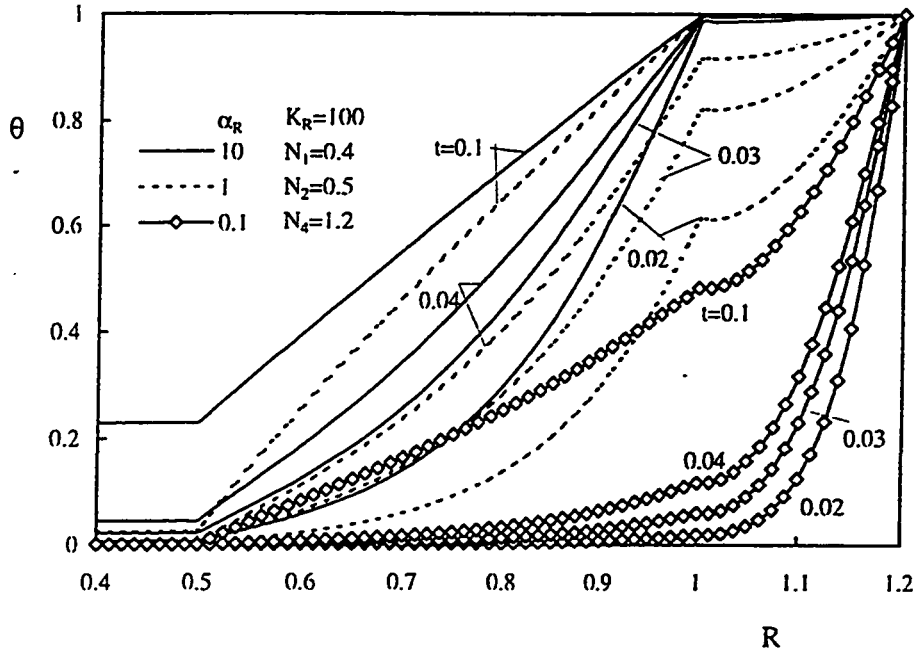

Figure 5.71: Effect of α_R on the variation of the mid-height temperature with time, $Gr^* = 500, K_R = 100$

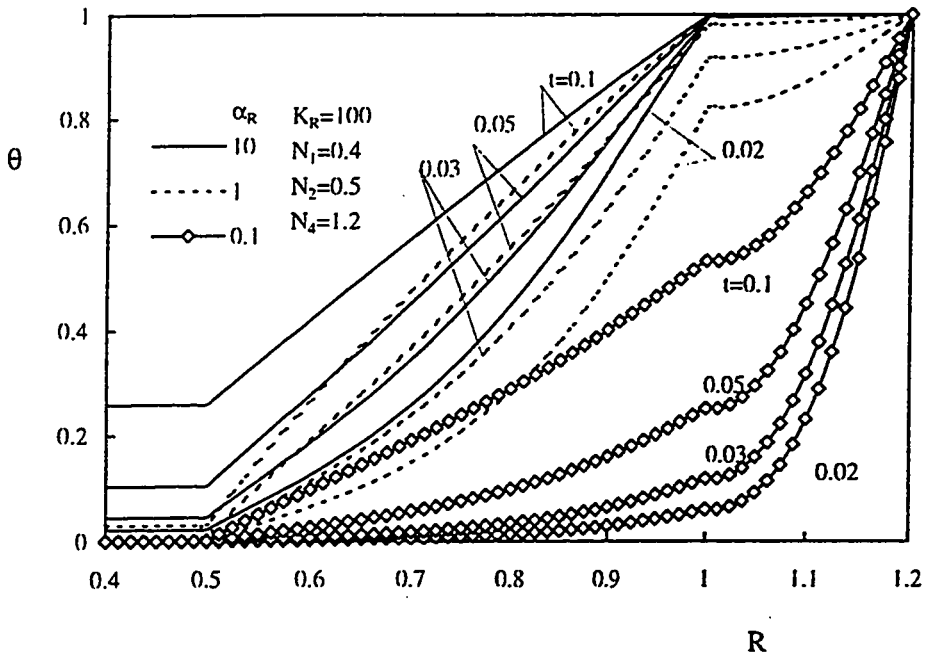

Figure 5.72: Effect of α_R on the variation of the exit temperature with time, $Gr^* = 500, K_R = 100$

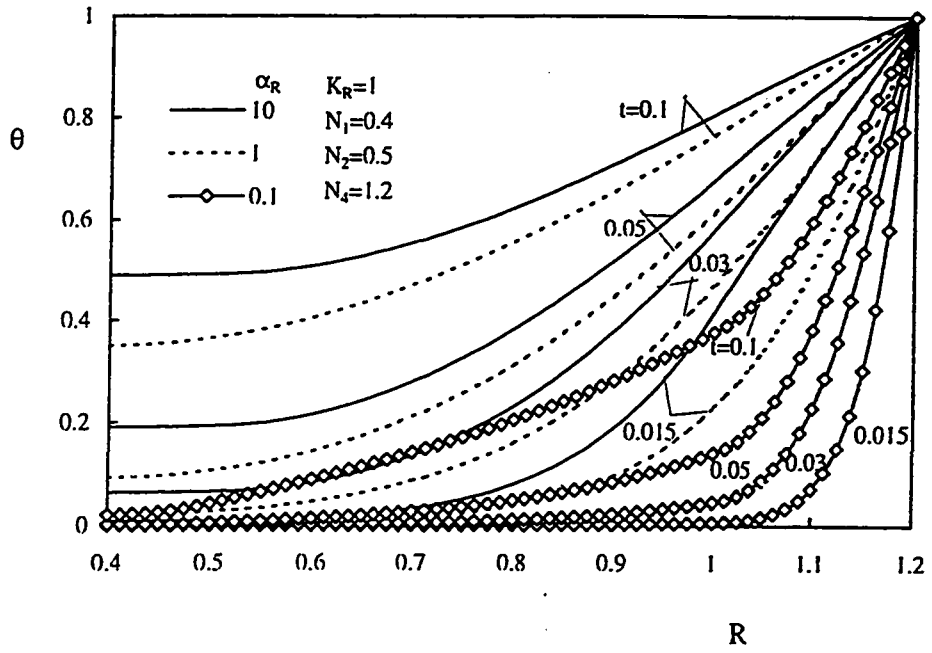

Figure 5.73: Effect of α_R on the variation of the mid-height temperature with time, $Gr^* = 500, K_R = 1$

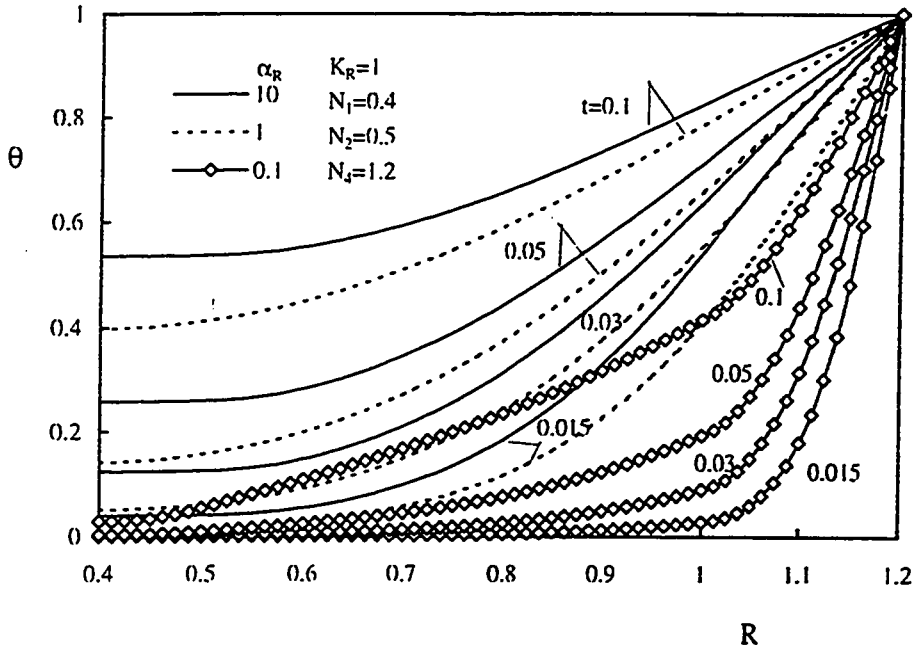

Figure 5.74: Effect of α_R on the variation of the exit temperature with time, $Gr^* = 500, K_R = 1$

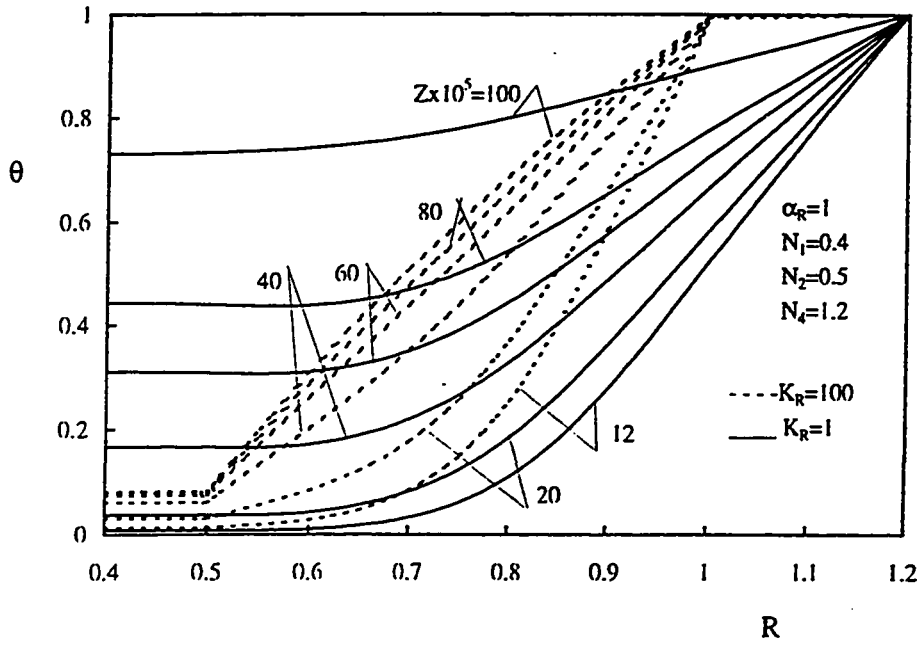

Figure 5.75: Effect of K_R on the temperature distribution at different axial positions, $t = 0.225, Gr^* = 500$

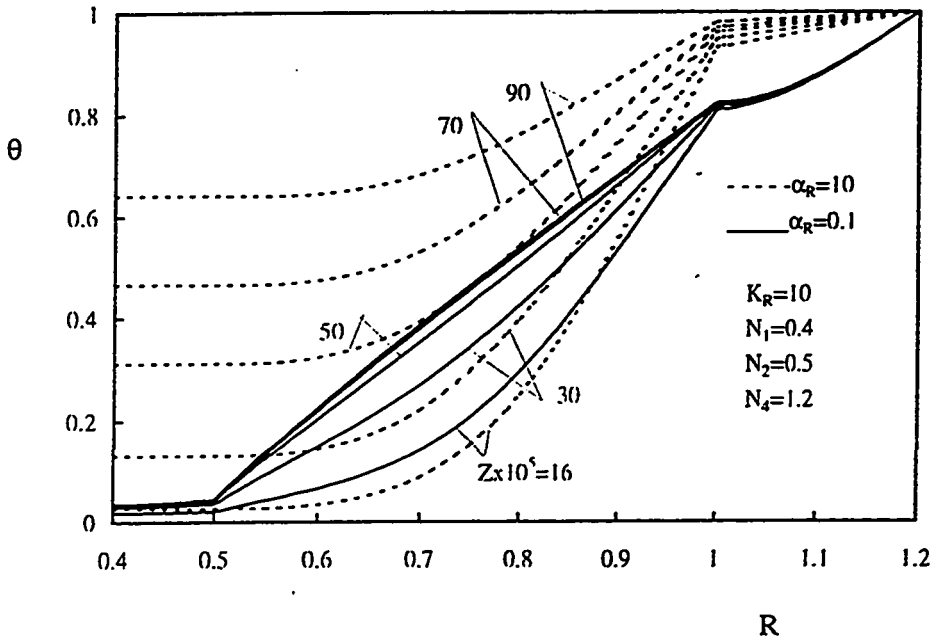

Figure 5.76: Effect of α_R on the temperature distribution at different axial positions, $t = 0.225, Gr^* = 500$

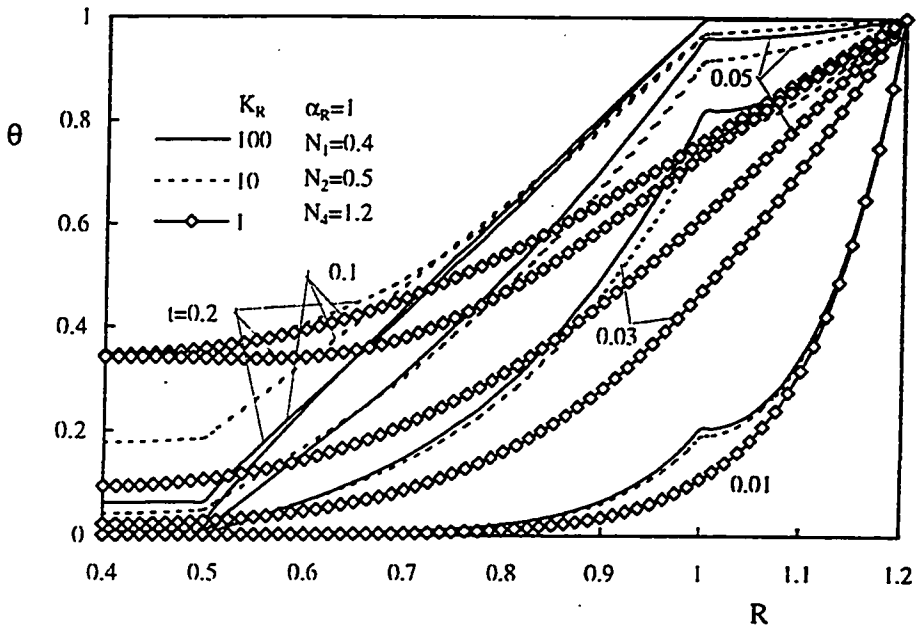

Figure 5.77: Effect of K_R on the variation of the mid-height temperature with time, $Gr^* = 10^3, \alpha_R = 1$

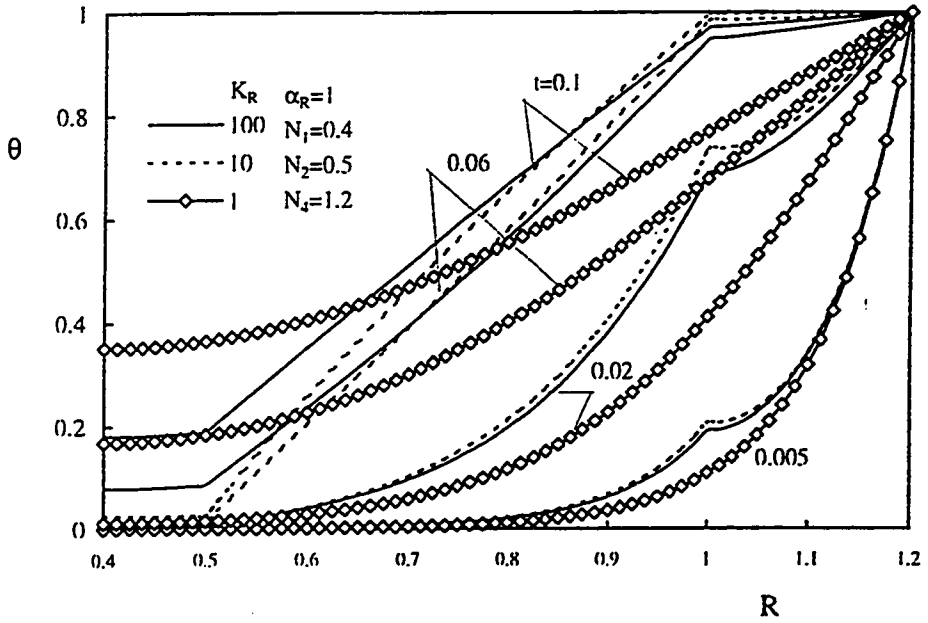

Figure 5.78: Effect of K_R on the variation of the exit temperature with time, $Gr^* = 10^3, \alpha_R = 1$

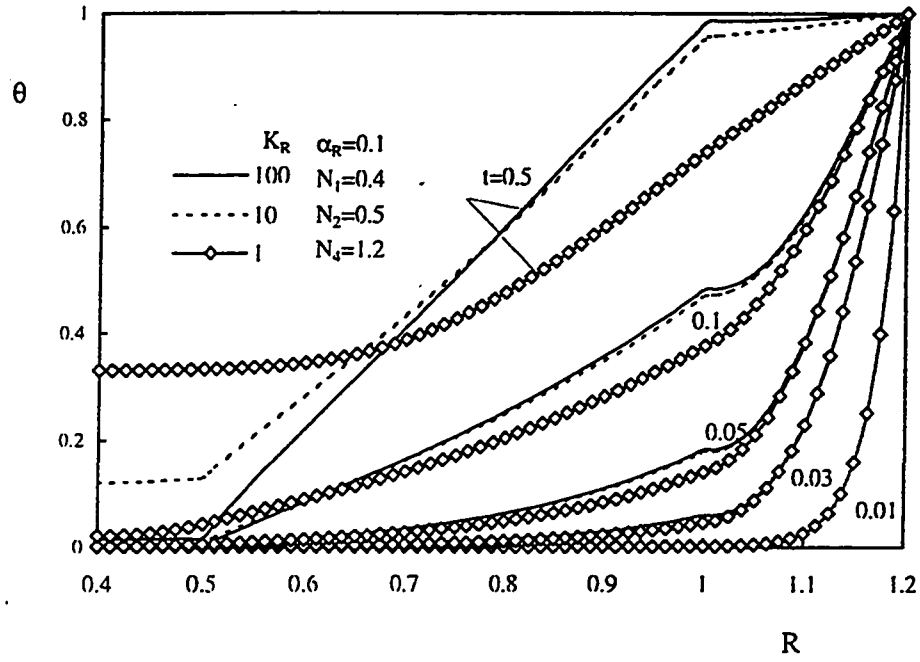

Figure 5.79: Effect of K_R on the variation of the mid-height temperature with time, $Gr^* = 10^3, \alpha_R = 0.1$

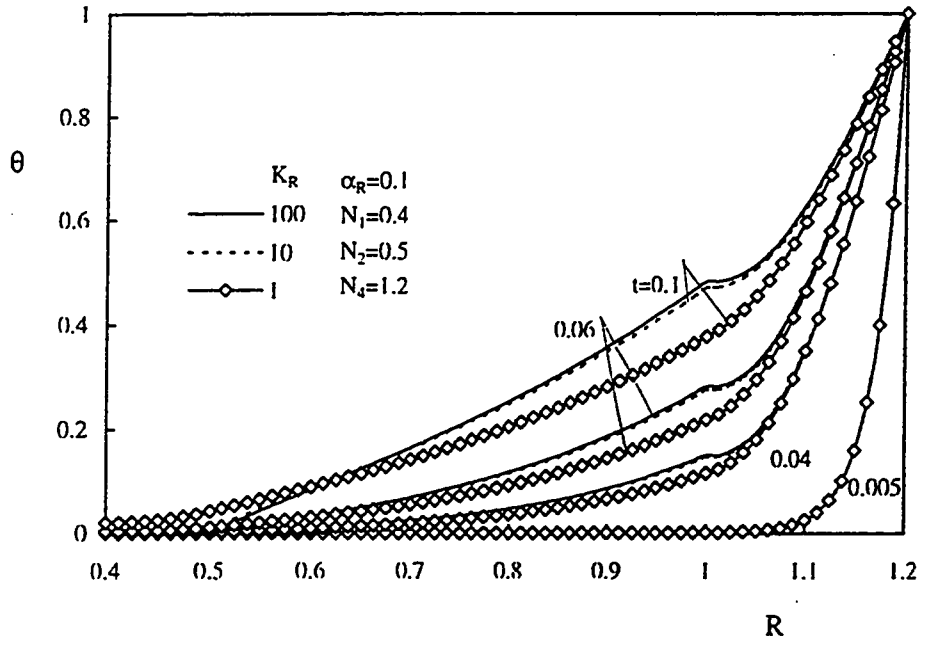

Figure 5.80: Effect of K_R on the variation of the exit temperature with time, $Gr^* = 10^3, \alpha_R = 0.1$

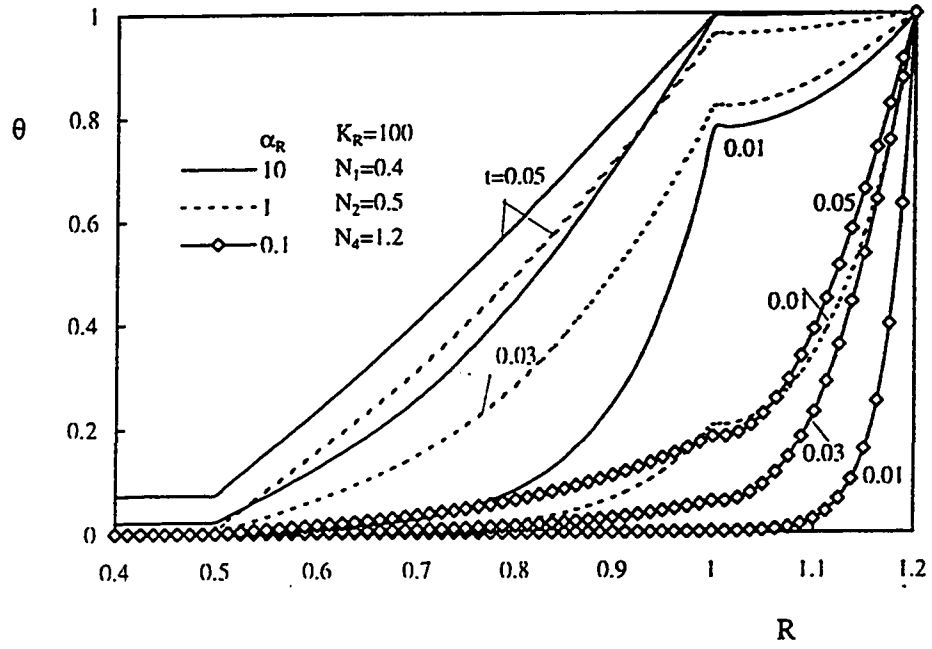

Figure 5.81: Effect of α_R on the variation of the exit temperature with time, $Gr^* = 10^3, K_R = 100$

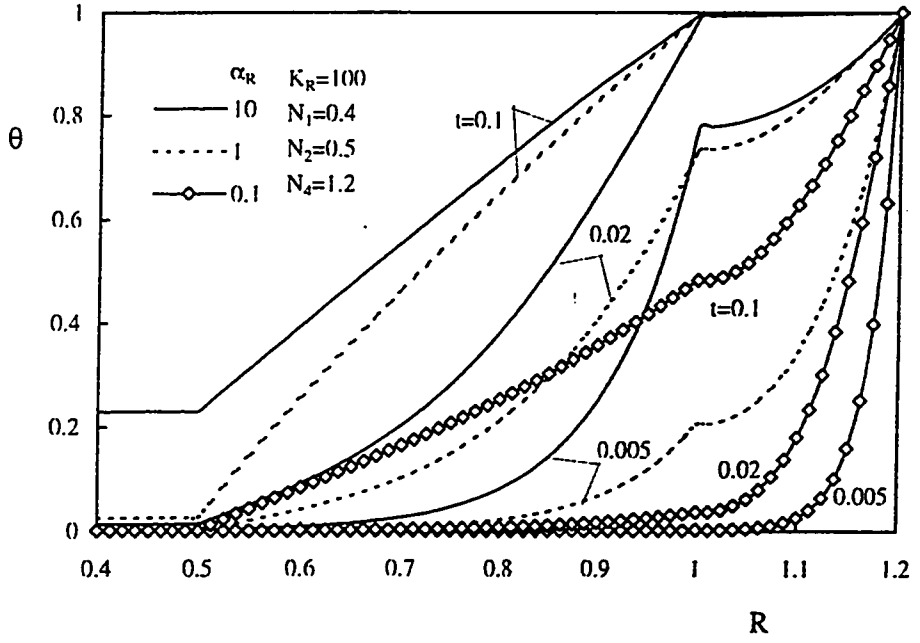

Figure 5.82: Effect of α_R on the variation of the mid-height temperature with time, $Gr^* = 10^3, K_R = 100$

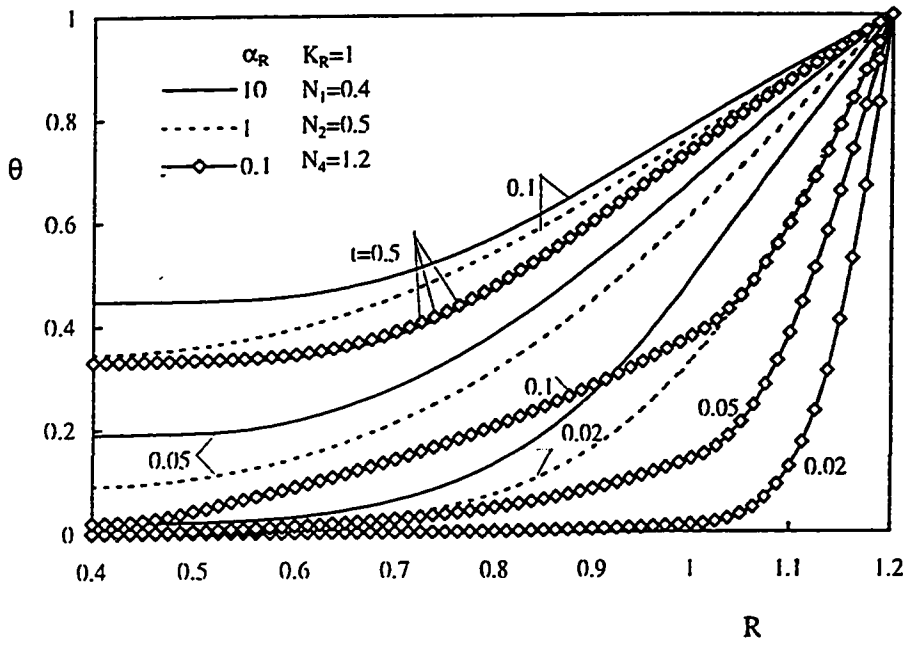

Figure 5.83: Effect of α_R on the variation of the exit temperature with time, $Gr^* = 10^3, K_R = 1$

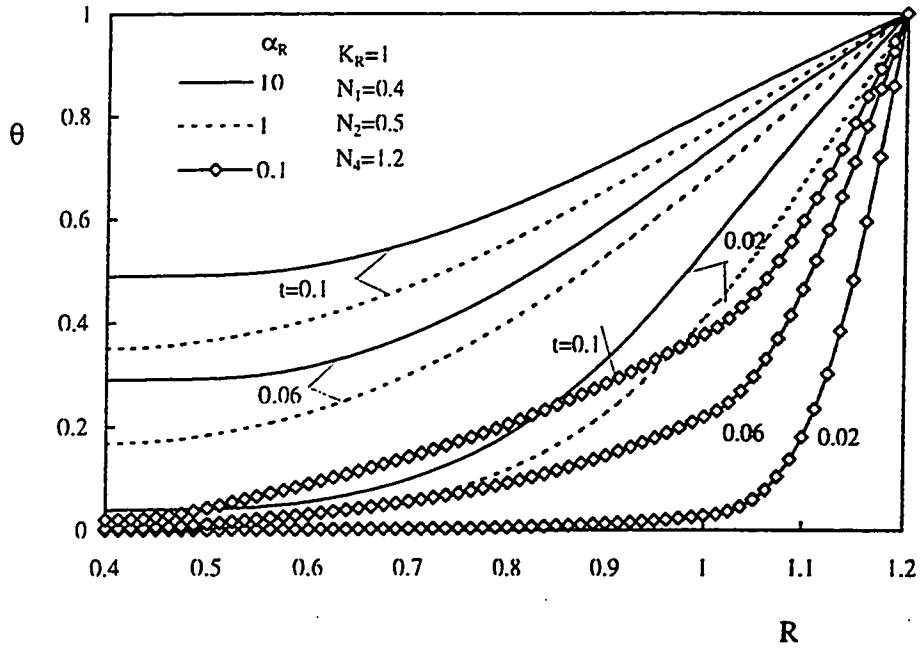

Figure 5.84: Effect of α_R on the variation of the of the mid-height temperature with time, $Gr^* = 10^3, K_R = 1$

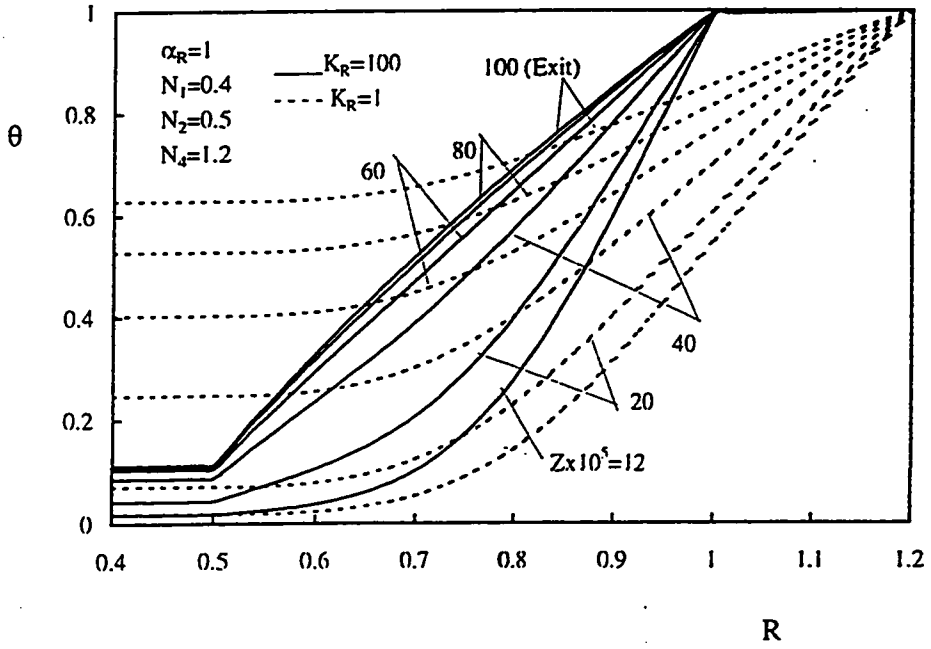

Figure 5.85: Effect of K_R on the temperature distribution at different axial positions, $t = 0.3, Gr^* = 10^3$

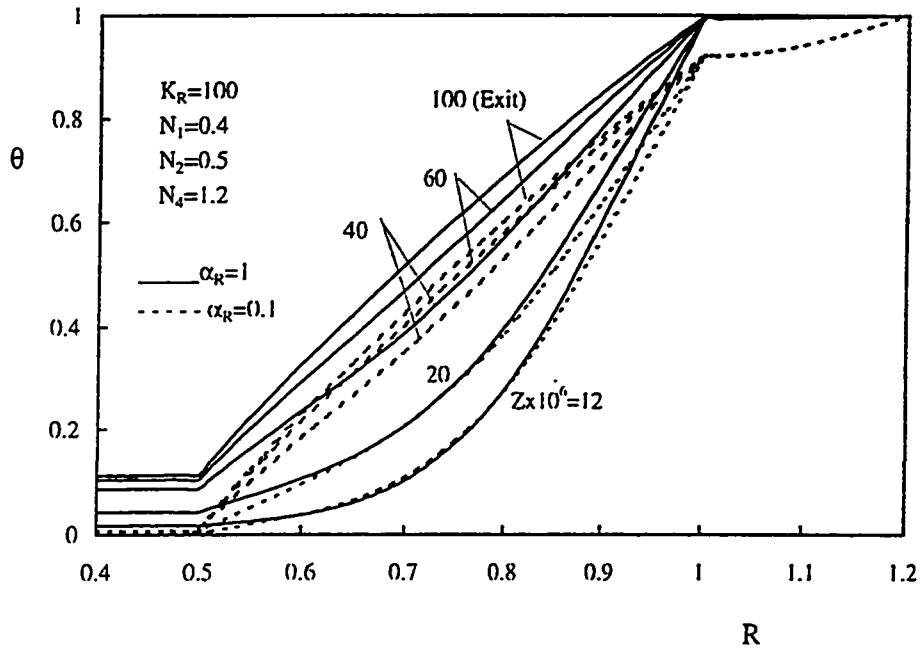

Figure 5.86: Effect of α_R on the temperature distribution at different axial positions,$t = 0.3, Gr^* = 10^3$

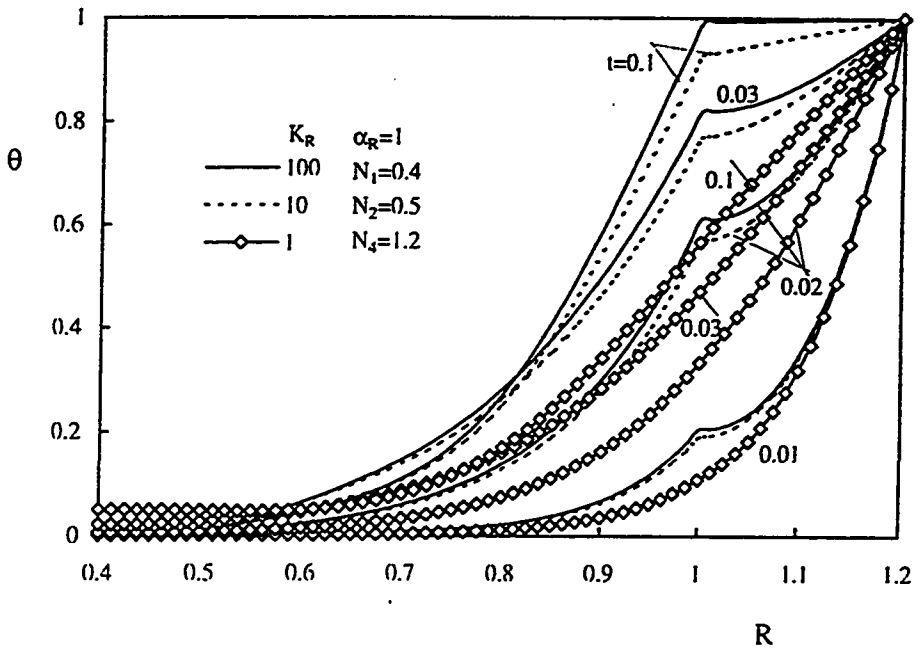

Figure 5.87: Effect of K_R on the variation of the mid-height temperature with time, $Gr^* = 10^4, \alpha_R = 1$

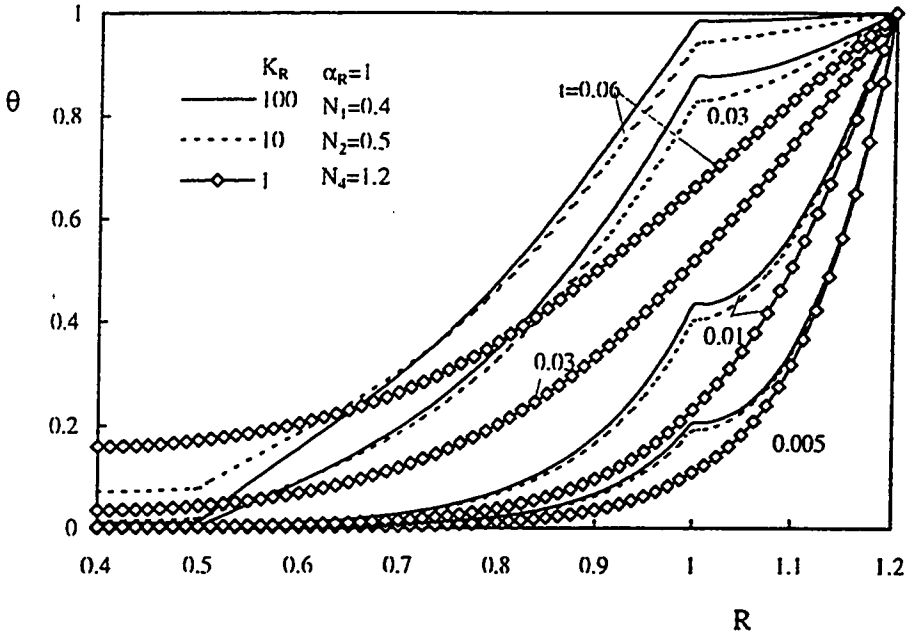

Figure 5.88: Effect of K_R on the variation of the exit temperature with time, $Gr^* = 10^4, \alpha_R = 1$

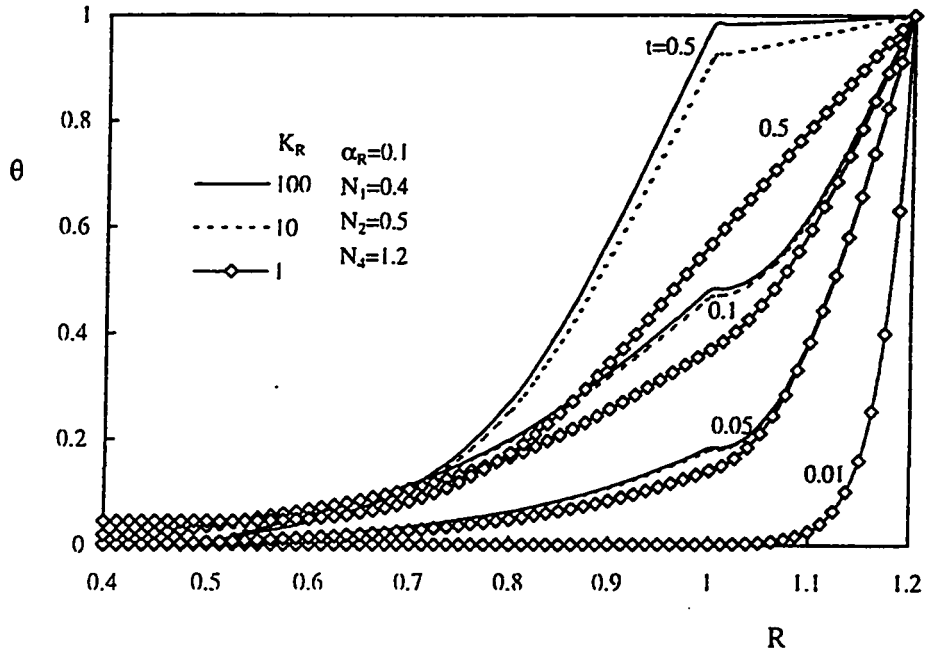

Figure 5.89: Effect of K_R on the variation of the mid-height temperature with time, $Gr^* = 10^4, \alpha_R = 0.1$

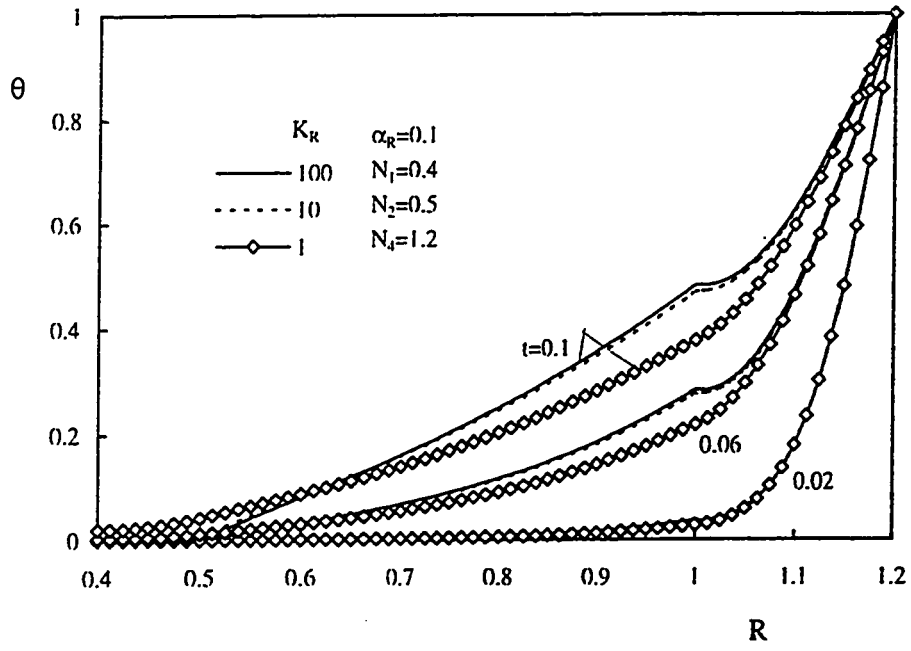

Figure 5.90: Effect of K_R on the variation of the exit temperature with time, $Gr^* = 10^4, \alpha_R = 0.1$

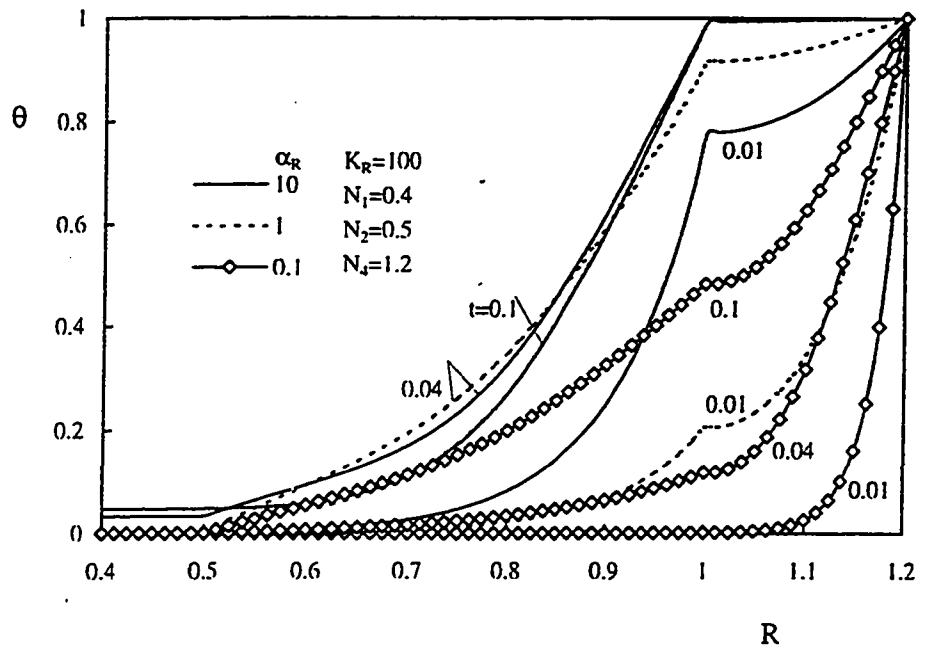

Figure 5.91: Effect of α_R on the variation of the mid-height temperature with time, $Gr^* = 10^4, K_R = 100$

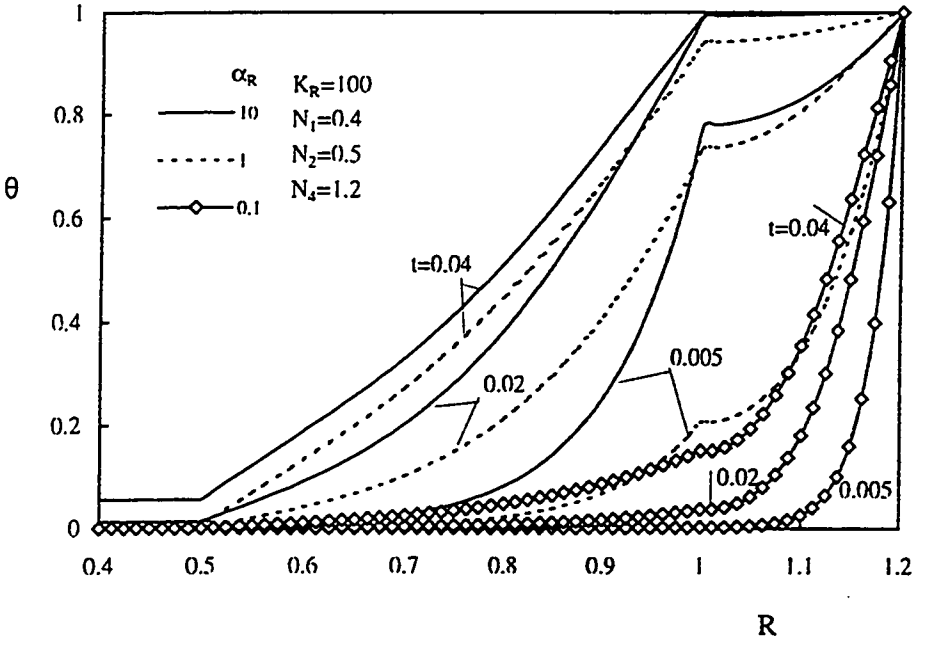

Figure 5.92: Effect of α_R on the variation of the exit temperature with time, $Gr^* = 10^4, K_R = 100$

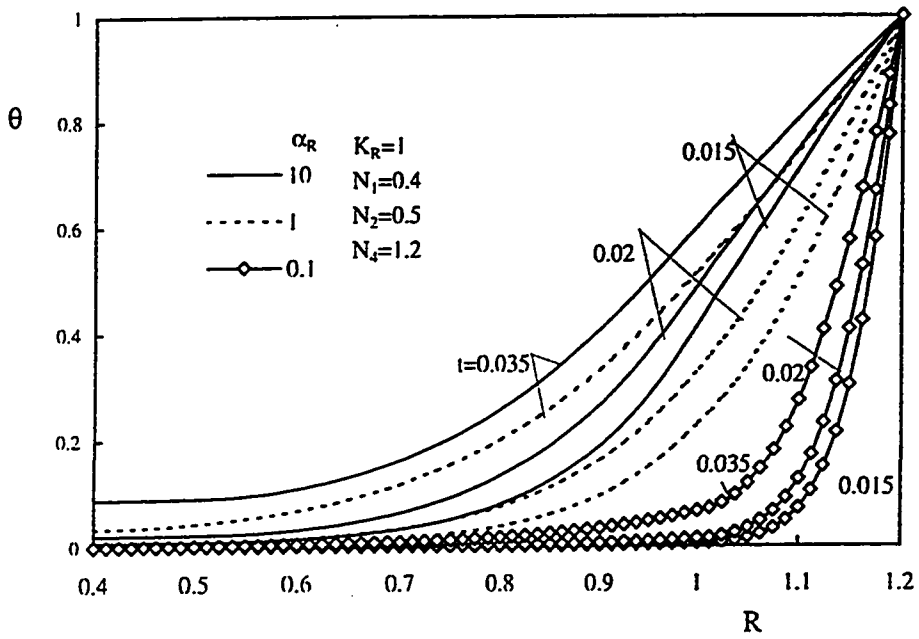

Figure 5.93: Effect of α_R on the variation of the mid-height temperature with time, $Gr^* = 10^4, K_R = 1$

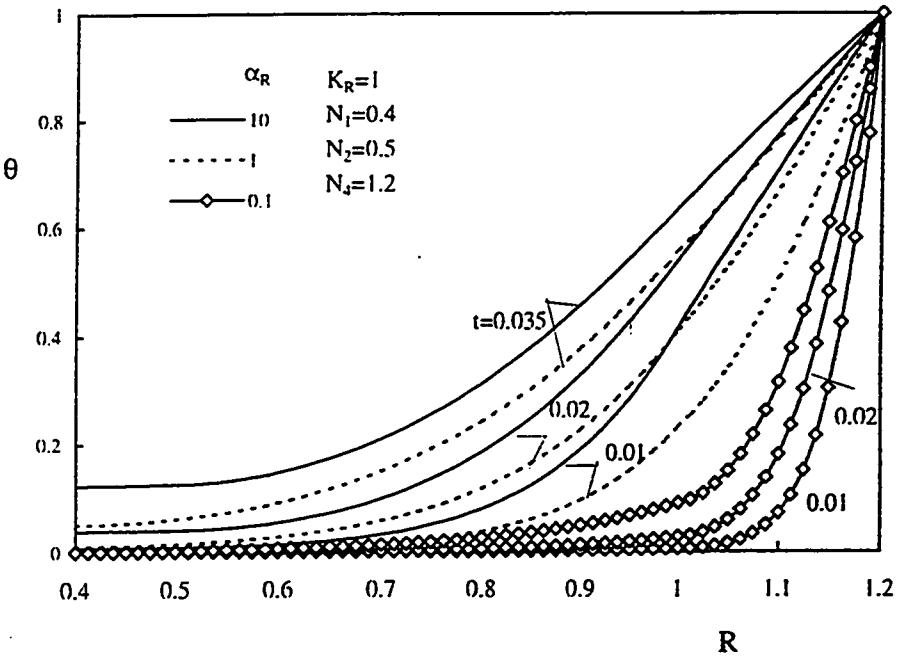

Figure 5.94: Effect of α_R on the variation of the exit temperature with time, $Gr^* = 10^4, K_R = 1$

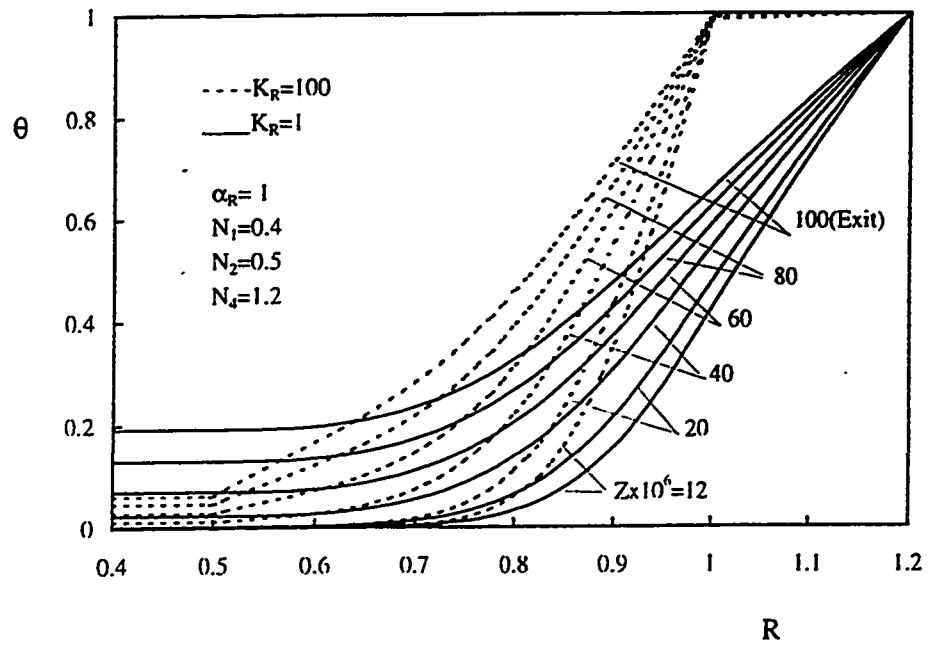

Figure 5.95: Effect of K_R on the temperature distribution at different axial positions, $t = 0.3, Gr^* = 10^4$

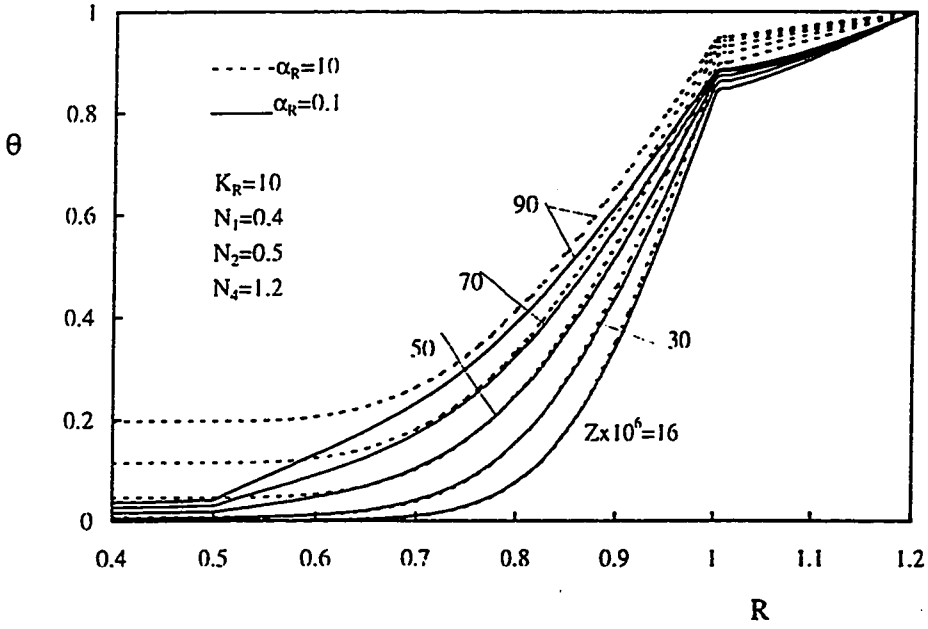

Figure 5.96: Effect of α_R on the temperature distribution at different axial positions, $t = 0.3, Gr^* = 10^4$

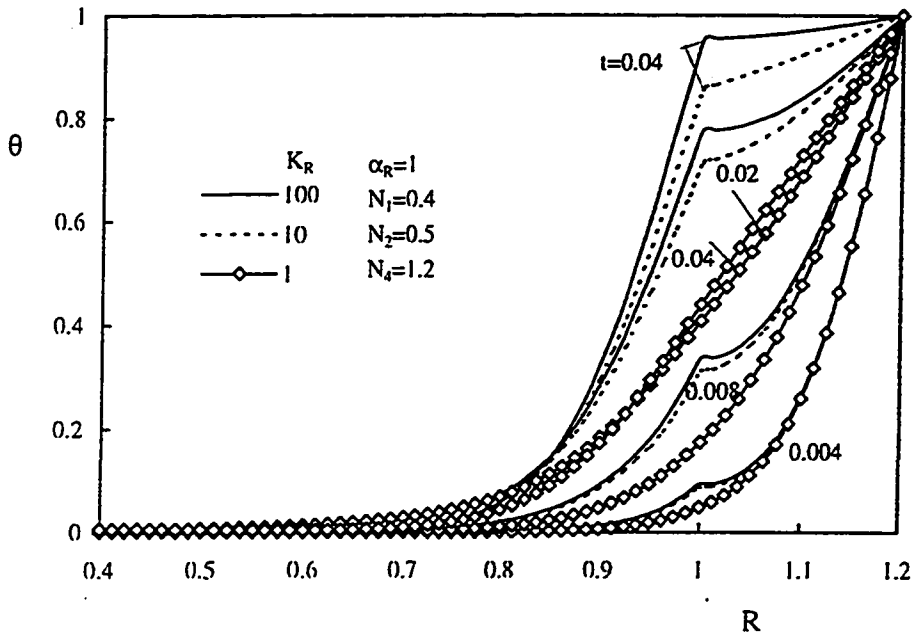

Figure 5.97: Effect of K_R on the variation of the mid-height temperature with time, $Gr^* = 10^5, \alpha_R = 1$

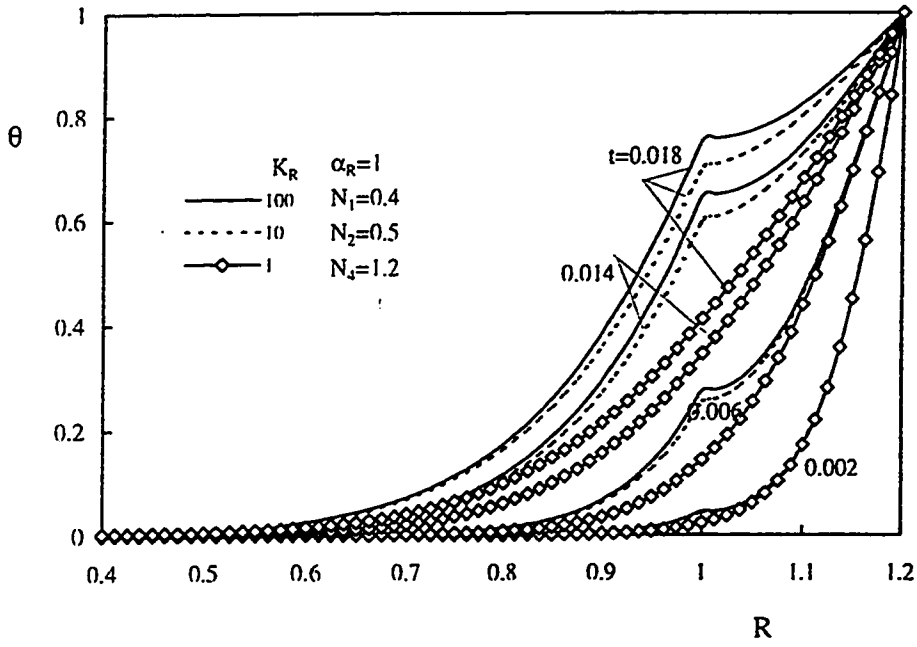

Figure 5.98: Effect of K_R on the variation of the exit temperature with time, $Gr^* = 10^5, \alpha_R = 1$

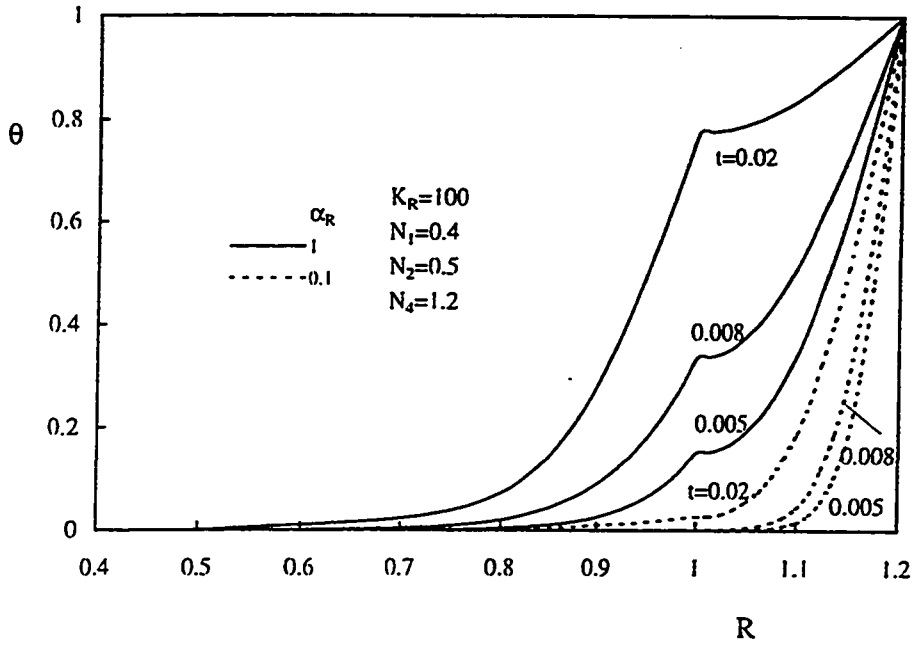

Figure 5.99: Effect of α_R on the variation of the mid-height temperature with time, $Gr^* = 10^5, K_R = 100$

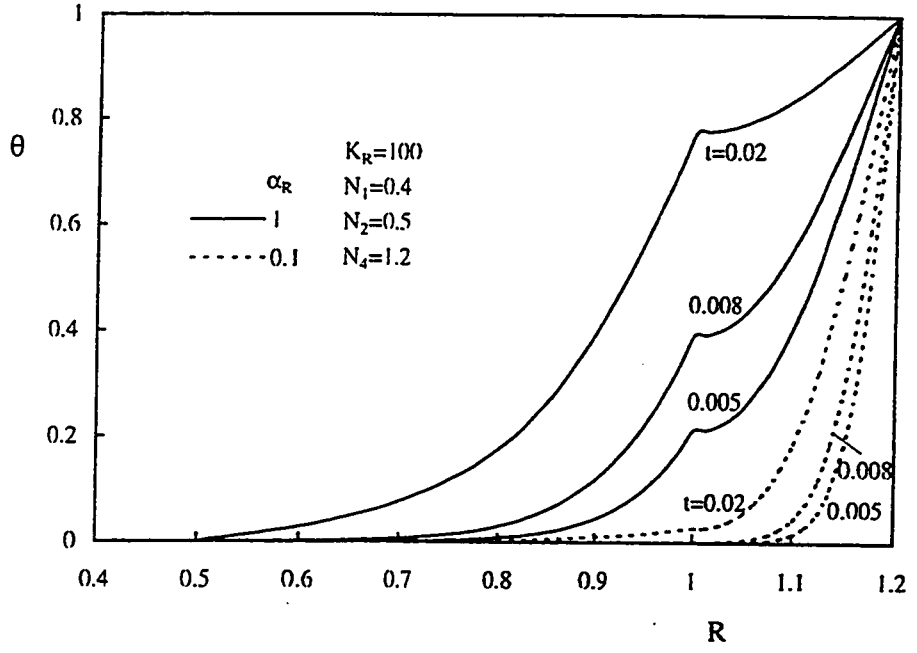

Figure 5.100: Effect of α_R on the variation of the exit temperature with time, $Gr^* = 10^5, K_R = 100$

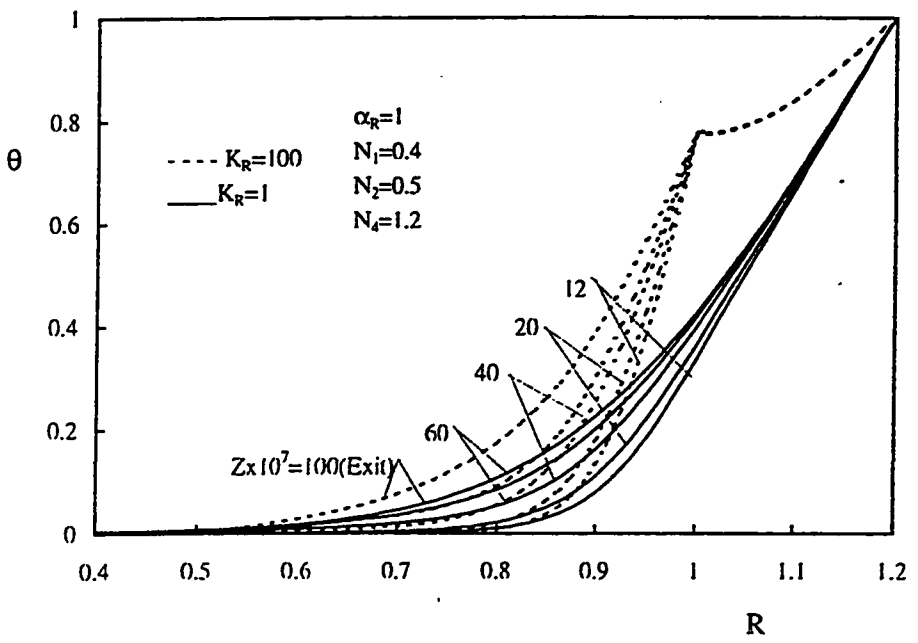

Figure 5.101: Effect of K_R on the temperature distribution at different axial positions.$t = 0.02, Gr^* = 10^5$

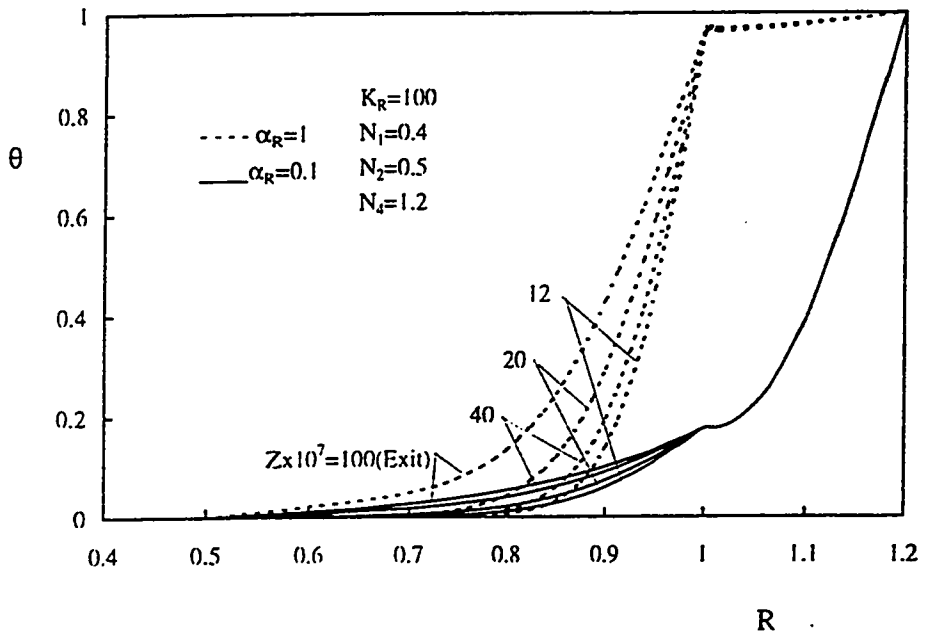

Figure 5.102: Effect of α_R on the temperature distribution at different axial positions, $L = 0.035$, $Gr^* = 10^5$

5.3.4 Adiabatic Surface Temperature

Figures 5.103 through 5.114 constitute three groups of figures present the effect of K_R and α_R on the adiabatic surface temperature at different values of time for three values of Gr^*, namely, $Gr^* = 500, 10^3$ and 10^4. Each group consists of two pairs of figures. The first pair presents, for given values of α_R, the effect of K_R on the adiabatic surface temperature at different values of time while the second pair shows such effect for given values of K_R. For $Gr^* = 500$, Fig. 5.103 presents the effect of K_R on the development with time of the adiabatic surface temperature for $\alpha_R = 1$. At early time, a small amount of heat is transferred to the fluid-annular gap causing a small amount of fluid to be sucked and moves upwards through the annulus. At the annulus entrance, the induced fluid feels the no-slip condition(viscosity effect) and two asymmetrical boundary-layers start to develop along the two fluid-solid interfaces. Consequently, at early time, the radial velocity which transfers heat from regions close to the heated wall towards that near the adiabatic one has a small magnitude; hence, the adiabatic surface temperature has a small value. Moreover, as the amount of the induced fluid is small, the flow reaches the state of thermal saturation after small axial distance. Hence, at this axial distance the adiabatic surface temperature reaches asymptotic value which does not increase with the axial distance. As time elapses, more heat is conducted through the heated wall into the fluid-annular gap causing more fluid to be induced which leads to an increase in the radial velocity (see Fig. 5.41). This means an increase in the amount of heat transferred radially (radial convection) towards the adiabatic wall which leads to an increase in the adiabatic surface temperature along the

annulus height as can be seen from Fig. 5.103. However, it is interesting to observe that, at a given time, as K_R increases the adiabatic surface temperature decreases. This unexpected effect of K_R can be explained by referring to Fig. 5.41 which presents the effect of K_R on the development with time of the mid-height radial velocity for the same values of Gr^* and α_R. In this figure, it can be seen that the radial velocity profiles, at a given value of time, have larger negative values for smaller values of K_R. Hence, the amount of heat convected radially towards the adiabatic wall compared with that absorbed by the induced fluid near the heated wall is larger for smaller values of K_R. Consequently, the adiabatic surface has larger temperatures for lower value of K_R. Similar to Fig. 5.103, Fig. 5.104 presents the effect of K_R on the development with time of the adiabatic surface temperature for another value of α_R, $\alpha_R = 0.1$. Comparing Fig. 5.103 with Fig. 5.104, it is seen that the adiabatic surface temperature along the annulus decreases with the decrease in the value of α_R. This effect of α_R is explained hereinafter.

For $K_R = 100$ and 1, Figs. 5.105 and 5.106 present, respectively, the effect of α_R on the development with time of the adiabatic surface temperature for $Gr^* = 500$. Figure 5.105 shows that, for a given value of K_R, the adiabatic surface temperature increases with α_R. This can be explained by referring to Figs. 5.45 through 5.48(which show the effect of α_R on the development with time of the radial velocity component at the mid-height and exit cross-sections of the annulus). In these figures, it is seen that the radial velocity profiles have larger negative values for larger values of α_R. This means that the amount

of heat convected radially towards the adiabatic wall compared with that absorbed near the heated wall increases with α_R. Hence, the temperature there increases with α_R.

It is worth mentioning that the maximum value for the adiabatic surface temperature that can be attained (at the exit cross-section) is $\theta = 1$ (fully -developed condition) which is the heated surface temperature. It is observed in Figs. 5.103 and 5.105 that, for a given time($t = 0.5$), the the adiabatic surface temperature near the exit cross-section attained values > 0.8 which means that the flow at time ($t \leq 0.5$) reached the annulus exit without reaching the fully-developed state.

Similar to Figs. 5.103 through 5.106, Figs. 5.107 through 5.110 and Figs. 5.111 through 5.114 present another two groups for $Gr^* = 10^3$ and 10^4, respectively. It is seen that each of these two groups has the same general qualitative characteristics of the first group which was for $Gr^* = 500$. Moreover, it is observed that as Gr^* increases the adiabatic surface temperature decreases. This is attributed to the fact that, small values of Gr^* represent long annuli with small hydraulic diameters. Thus the induced fluid has large axial distance to absorb more heat. Moreover, by referring to the figures of the radial velocity for small and large values of Gr^*, it can be seen that for small values of Gr^*, the radial velocity has large negative values, i.e., it transfers heat from regions near the heated wall towards that near the adiabatic one. On the other hand, for large values of Gr^*, the radial velocity component has large positive values, i.e., heat is transferred radially towards the adiabatic wall by only molecular diffusion which is a very weak means compared with the radial convection by the radial velocity. In Fig. 5.113, the adiabatic surface temperature

profiles is drawn only for two values of α_R(10 and 1). This is because for $\alpha_R = 0.1$, the values of the adiabatic surface temperature is very small compared with those corresponding to the presented values of α_R.

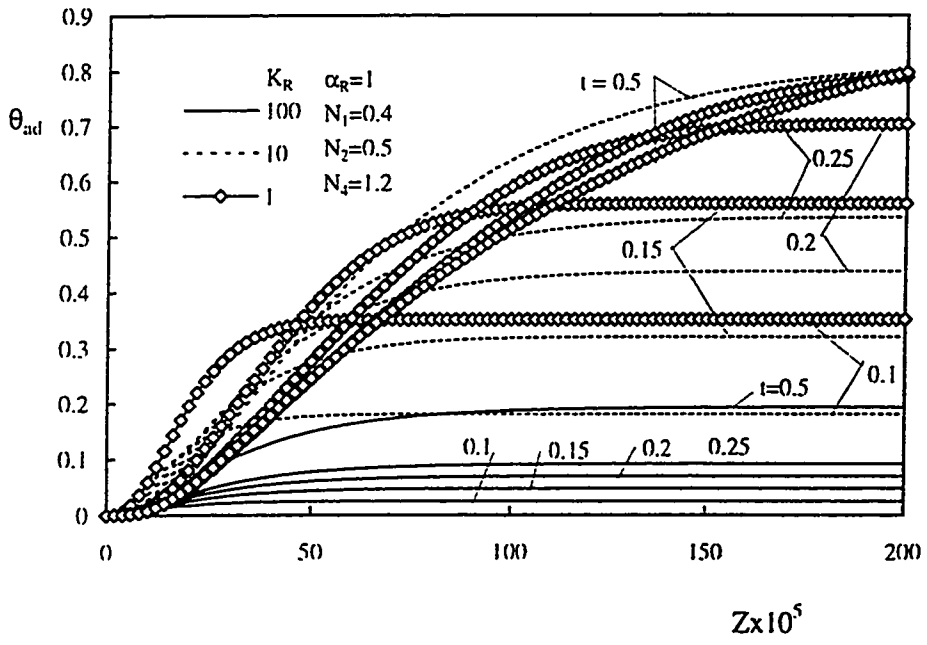

Figure 5.103: Effect of K_R on the variation of the adiabatic surface temperature with time, $Gr^* = 500, \alpha_R = 1$

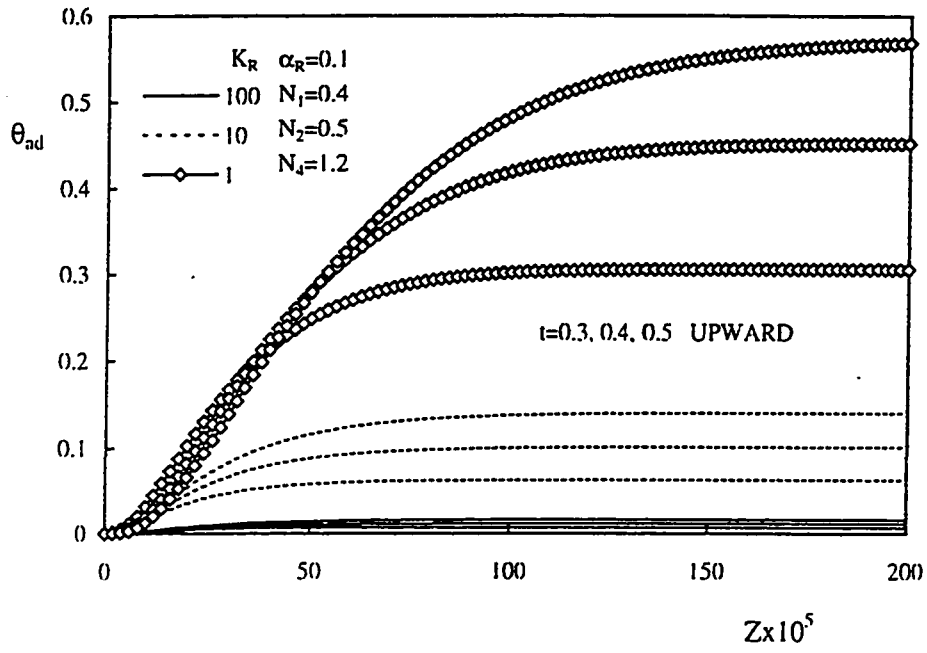

Figure 5.104: Effect of K_R on the variation of the adiabatic surface temperature with time, $Gr^* = 500, \alpha_R = 0.1$

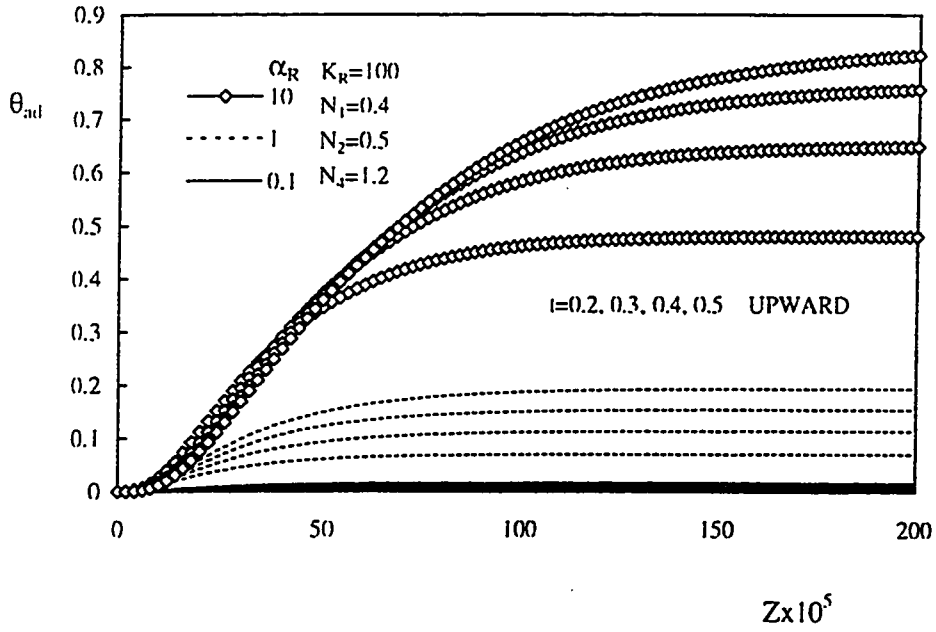

Figure 5.105: Effect of α_R on the variation of the adiabatic surface temperature with time, $Gr^* = 500, K_R = 100$

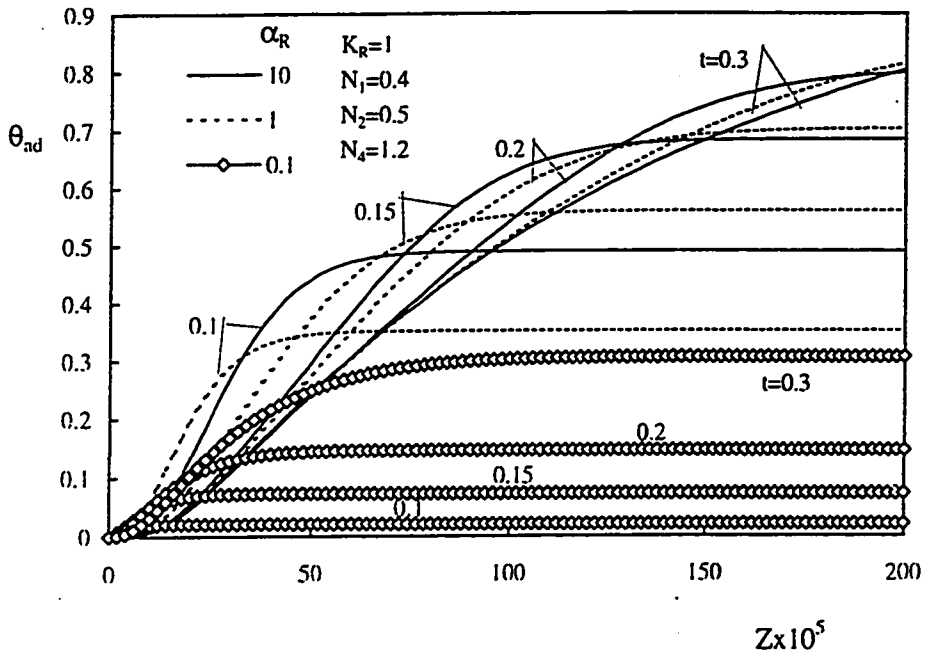

Figure 5.106: Effect of α_R on the variation of the adiabatic surface temperature with time, $Gr^* = 500, K_R = 1$

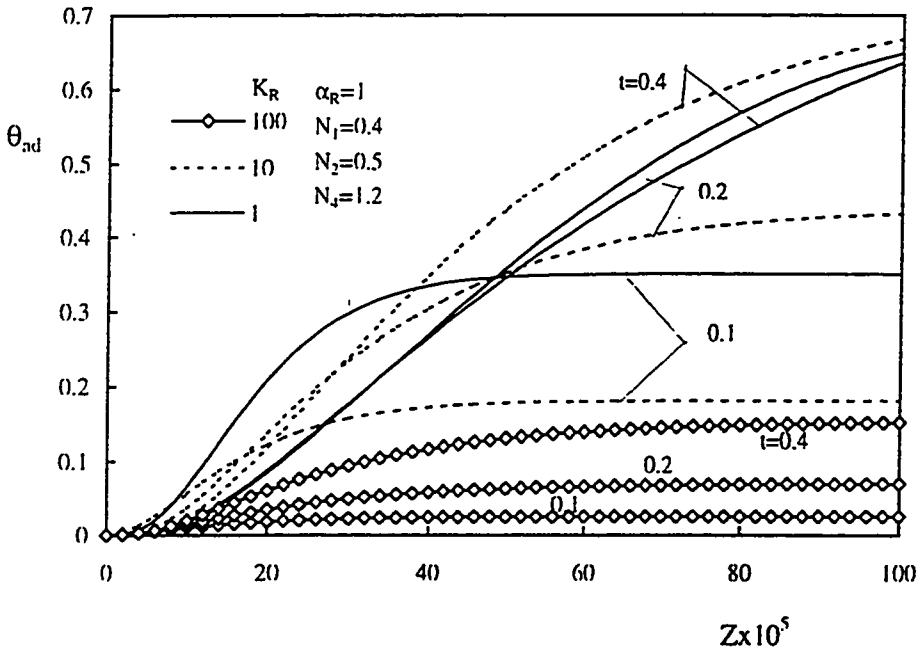

Figure 5.107: Effect of K_R on the variation of the adiabatic surface temperature with time, $Gr^* = 10^3, \alpha_R = 1$

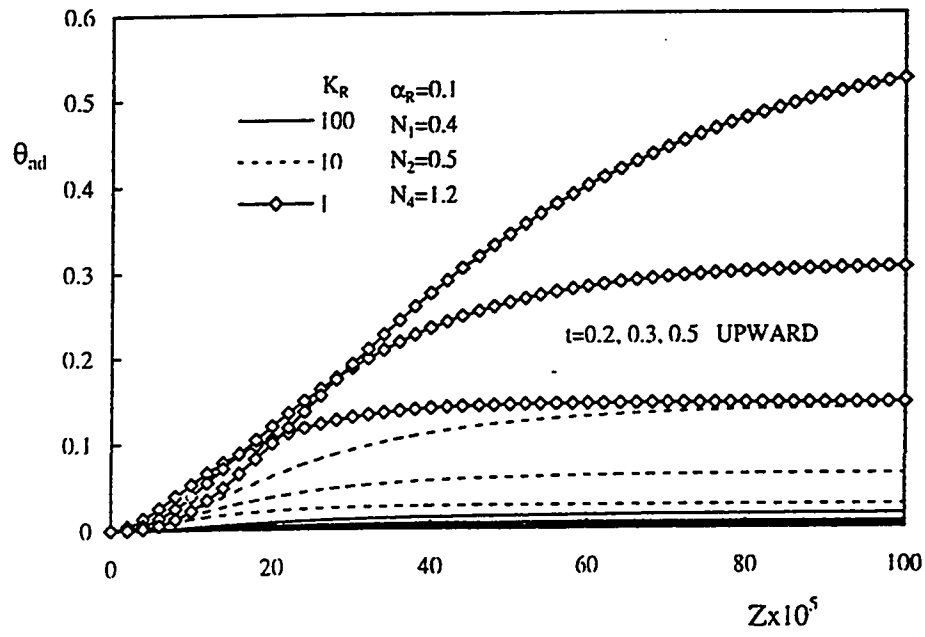

Figure 5.108: Effect of K_R on the variation of the adiabatic surface temperature with time, $Gr^* = 10^3, \alpha_R = 0.1$

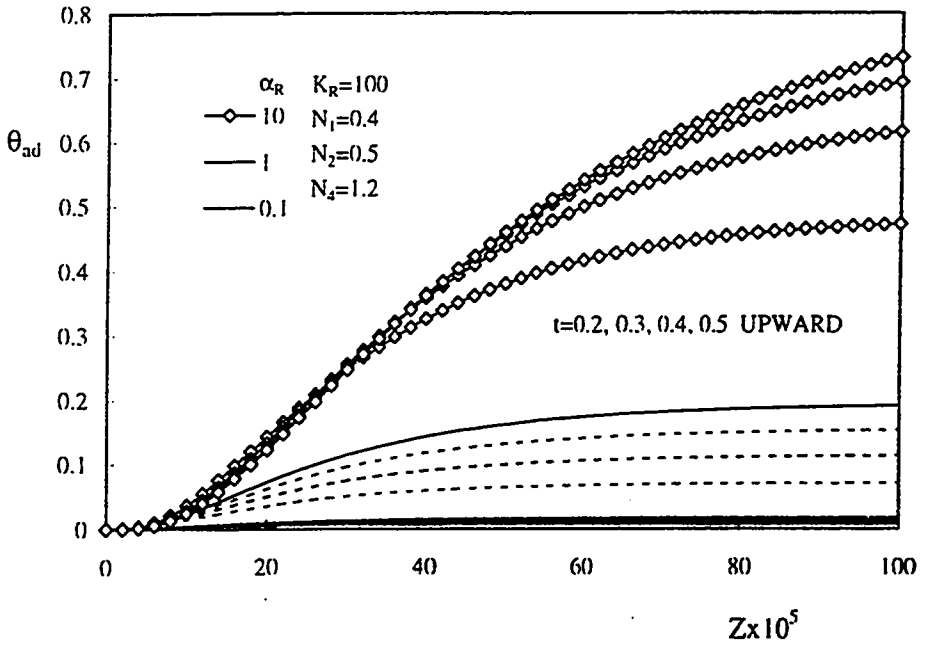

Figure 5.109: Effect of α_R on the variation of the adiabatic surface temperature with time, $Gr^* = 10^3, K_R = 100$

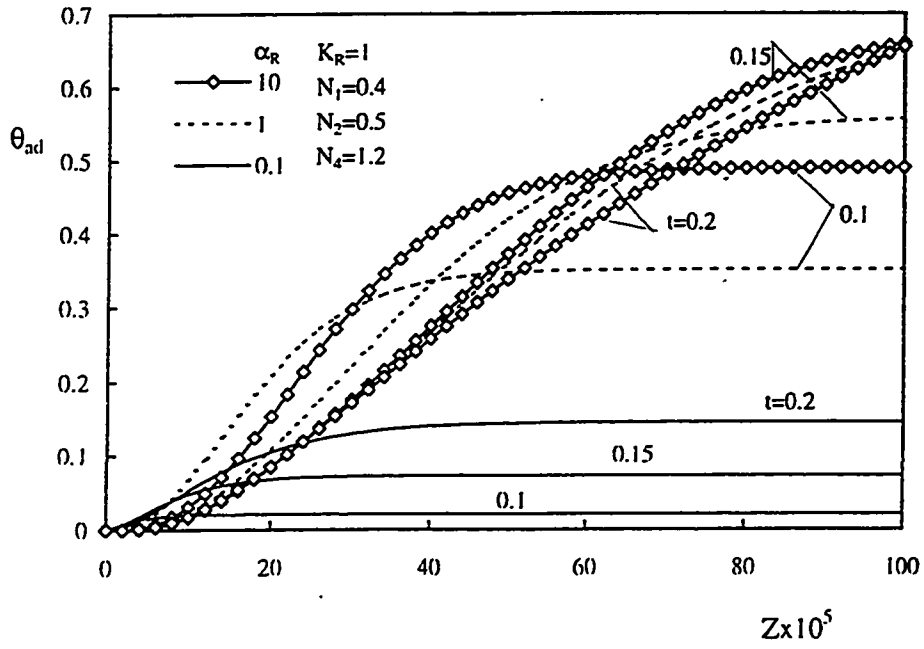

Figure 5.110: Effect of α_R on the variation of the adiabatic surface temperature with time, $Gr^* = 10^3, K_R = 1$

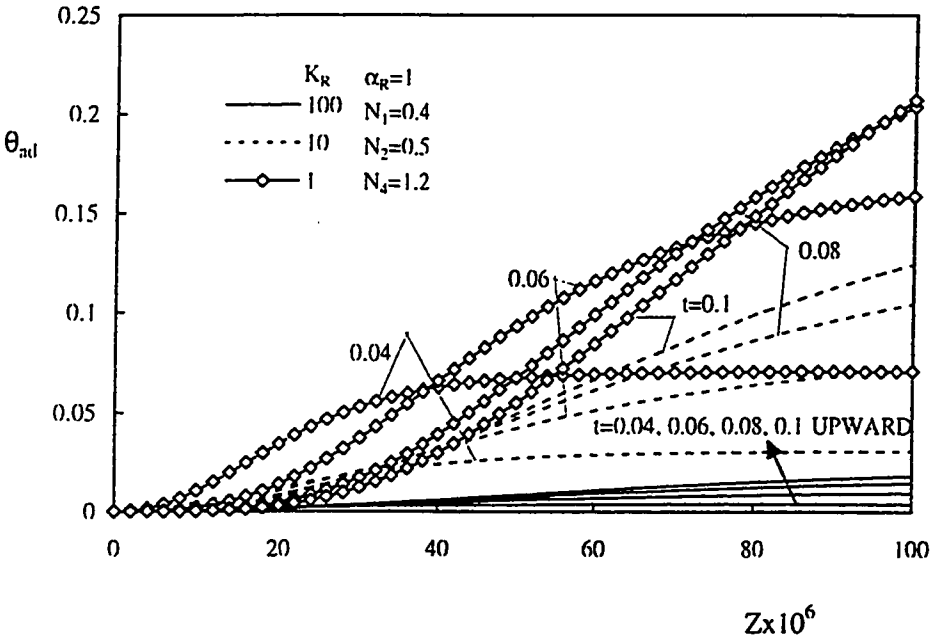

Figure 5.111: Effect of K_R on the variation of the adiabatic surface temperature with time, $Gr^* = 10^4, \alpha_R = 1$

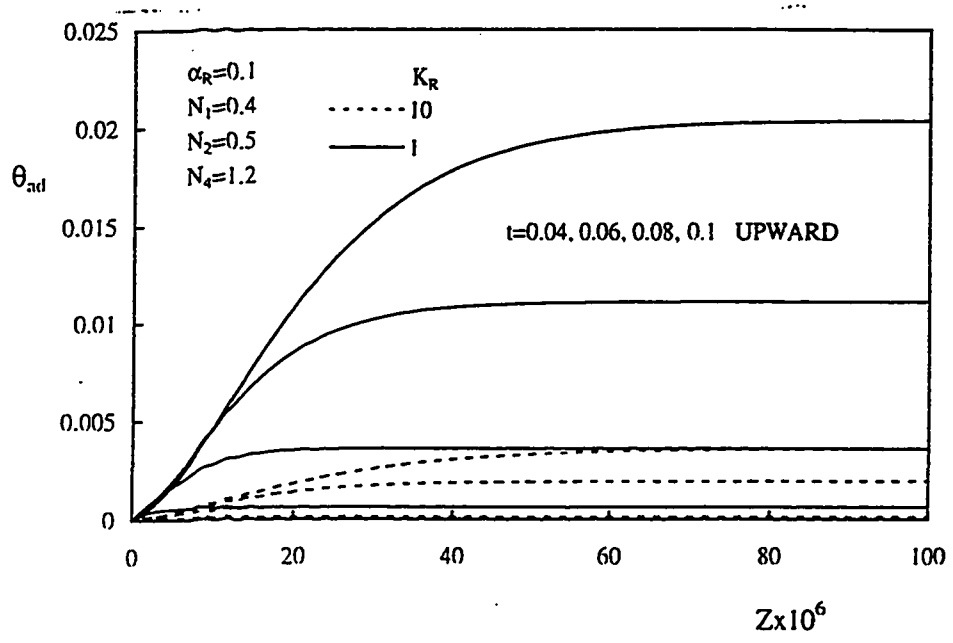

Figure 5.112: Effect of K_R on the variation of the adiabatic surface temperature with time, $Gr^* = 10^4, \alpha_R = 0.1$

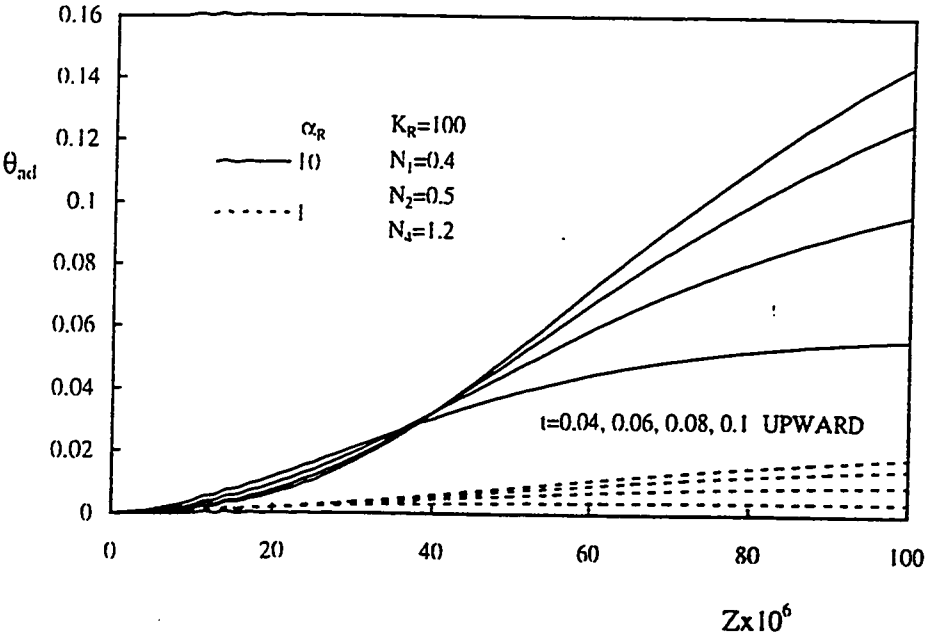

Figure 5.113: Effect of α_R on the variation of the adiabatic surface temperature with time, $Gr^* = 10^4, K_R = 100$

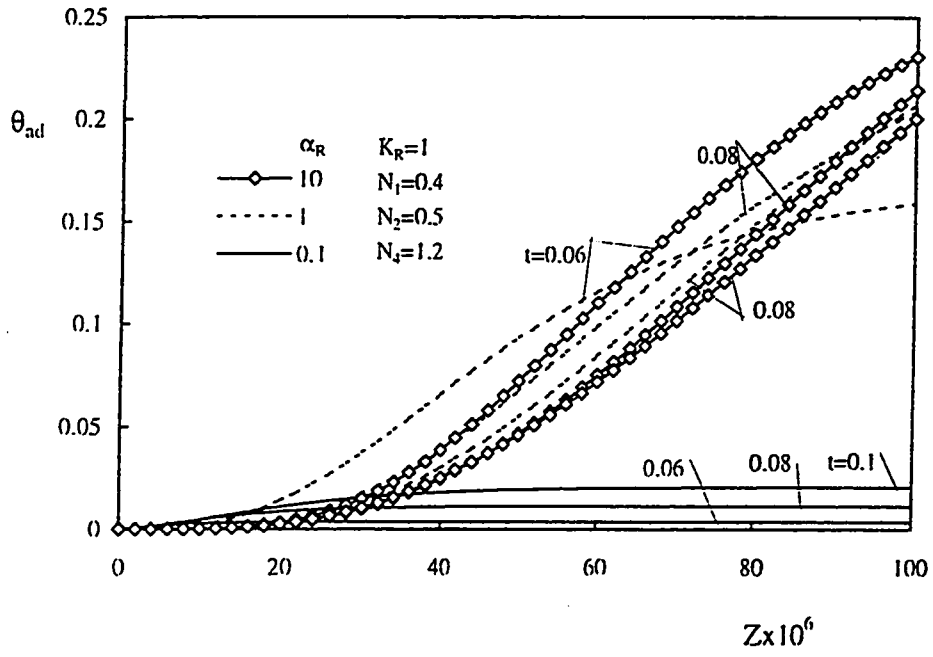

Figure 5.114: Effect of α_R on the variation of the adiabatic surface temperature with time, $Gr^* = 10^4, K_R = 1$

5.3.5 Pressure

Figures 5.115 through 5.126 constitute four groups presenting the effect of K_R and α_R on the development with time of the pressure defect along the annulus. Each group consists of two pairs of figures. The first pair shows, for a given value of α_R, how K_R affects the variation with time of the pressure along the annulus while, for a given value of K_R, the second pair shows such effect for α_R. For a given value of Gr^*, namely, $Gr^* = 500$, Fig. 5.115 presents the effect of K_R on the development with time of the pressure defect along the annulus for $\alpha_R = 1$. For a given time, the pressure decreases from the value $(-\frac{1}{2}U_o^2)$ at the entrance of the annulus to a minimum value and then increases again to reach zero at the annulus exit. This behavior of the pressure can be explained as follows. Near the entrance, the induced fluid absorbs small amount of heat and hence, the buoyancy force has a small magnitude compared with the viscous force (wall and fluid friction). Consequently, the viscous force overcomes the buoyancy force and as a result the pressure decreases with the axial distance(Z). As the flow moves upwards through the annulus , it absorbs more heat and the buoyancy force develops more until it becomes equal to the friction force at the axial position where the pressure is minimum. As the fluid keeps moving upwards and absorbs more heat, the buoyancy force increases more and hence, the pressure increases. Moreover, as time elapses, the fluid near the entrance of the annulus absorbs more heat and consequently the buoyancy force increases. This means an increase in the axial velocity which results in an increase in the friction force. Hence, the point at which the pressure is minimum is shifted upwards far from the entrance. In general, it is seen in Fig. 5.115

that, for a given value of time, increasing K_R increases the pressure defect. This can be attributed to the increase in the rate of heat transfer through the heated wall into the fluid-annular gap. This gives rise to more induced fluid with larger axial velocity which increases the friction and hence decreases the pressure.

For another value of α_R, namely, $\alpha_R = 0.1$, Fig. 5.116 presents the effect of K_R on the variation with time of the pressure defect along the annulus. Comparing Figs. 5.115 and 5.116, it can be seen that, for given values of time and K_R, the pressure defect profile along the annulus has smaller negative values for the smaller value of α_R. The explanation for this is mentioned in the following paragraph..

For $K_R = 100$, 10 and 1, Figures 5.117 and 5.118 present, respectively, the effect of α_R on the variation with time of the pressure defect along the annulus. From these two figures, it is seen that, the pressure defect increases (has large negative values) with increasing α_R. As mentioned before, since $\alpha_R = K_R \frac{\rho_f C_f}{\rho_s C_s}$, hence for a given K_R, the increase in the value of α_R implies a decrease in the value of the specific heat of the solid wall material. Consequently, for a given value of time, increasing the value of α_R increases the amount of heat conducted through the heated wall into the fluid as compared with that absorbed by the wall. This results in an increase in the buoyancy force which means more induced fluid with larger axial velocity. Consequently, the friction increases and as a results the pressure defect increases. On the other hand, for a given value of time, decreasing α_R decreases this amount of conducted heat to the fluid and hence reduces the buoyancy

force which leads to a decrease in the amount of the induced fluid and its axial velocity. Accordingly, the friction decreases and as a result the pressure defect decreases.

Similar to the above group of figures, Figs. 5.119 through 5.122 and Figs. 5.123 through 5.126 present another two groups for $Gr^* = 10^3$ and 10^3, respectively. It can be seen that Figs. 5.119 through 5.126 have the same general qualitative characteristics of Figs. 5.115 through 5.122 and nothing more can be discussed here. Moreover, with a careful look at all the presented results, it is easily observed that, as Gr^* decreases the pressure defect increases. This is because as Gr^* decreases the annulus height increases causing more heat to be conducted through the heated wall into the fluid-annular gap. This gives rise to the buoyancy force which means an increase in the induced fluid with larger axial velocity. Hence, the friction increases and thus the pressure defect increases. In some of the presented results for $Gr^* = 10^4$, it can be seen that, some pressure profiles intersects each other. This is due to the presence of the flow reversal at that period of time.

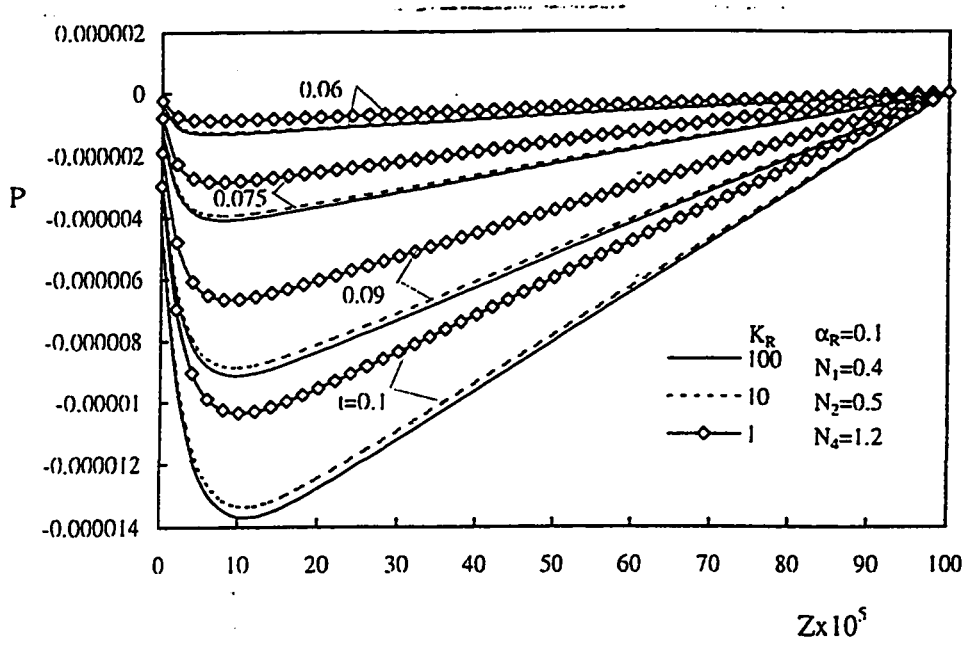

Figure 5.115: Effect of K_R on the variation of the pressure with time, $Gr^* = 500, \alpha_R = 1$

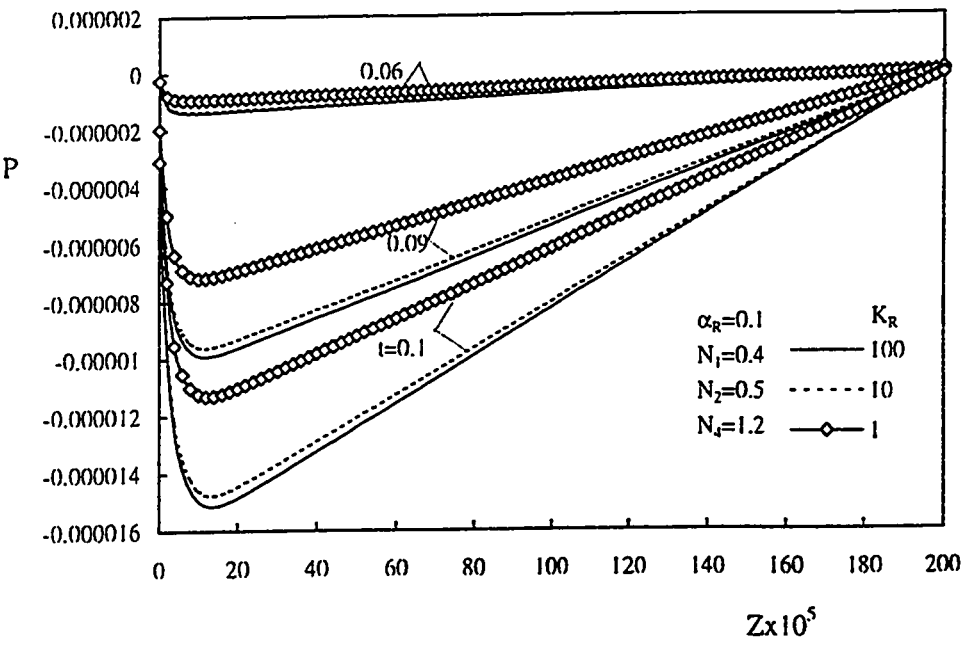

Figure 5.116: Effect of K_R on the variation of the pressure with time, $Gr^* = 500, \alpha_R = 0.1$

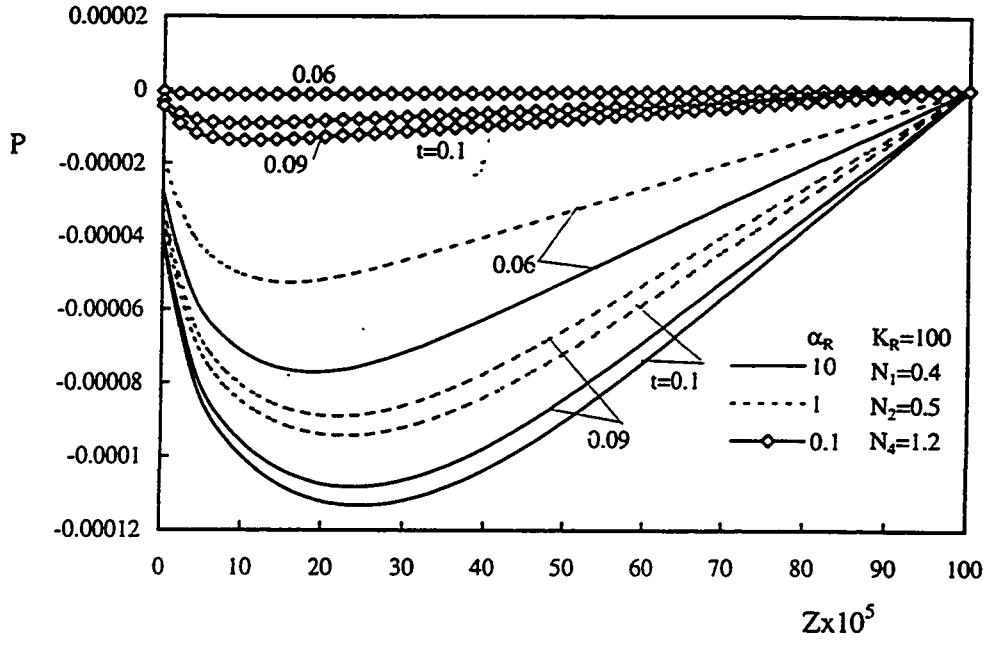

Figure 5.117: Effect of α_R on the variation of the pressure with time, $Gr^* = 500, K_R = 100$

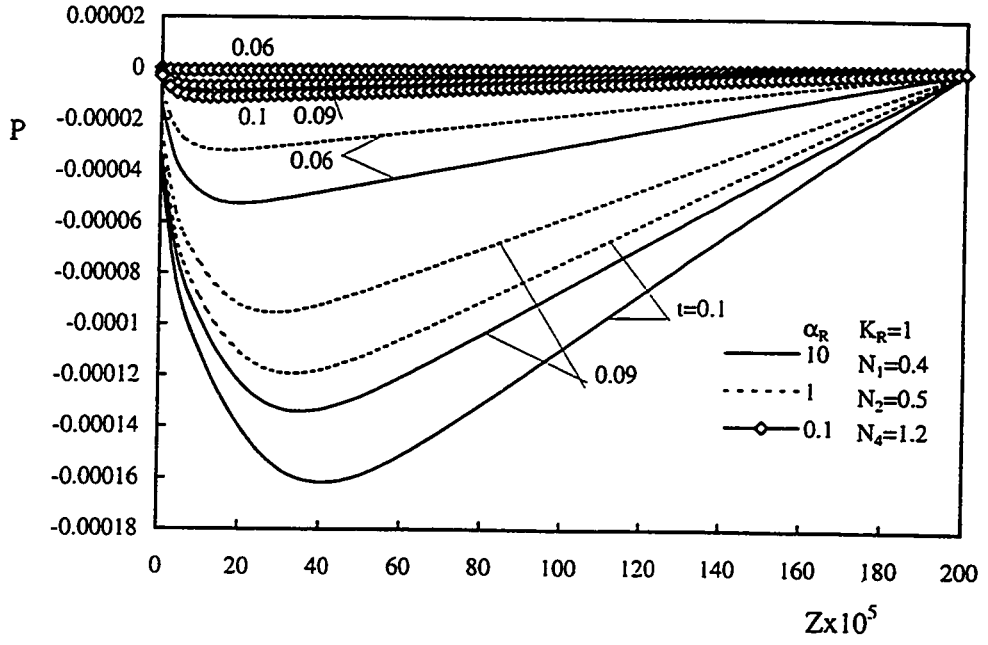

Figure 5.118: Effect of α_R on the variation of the pressure with time, $Gr^* = 500, K_R = 1$

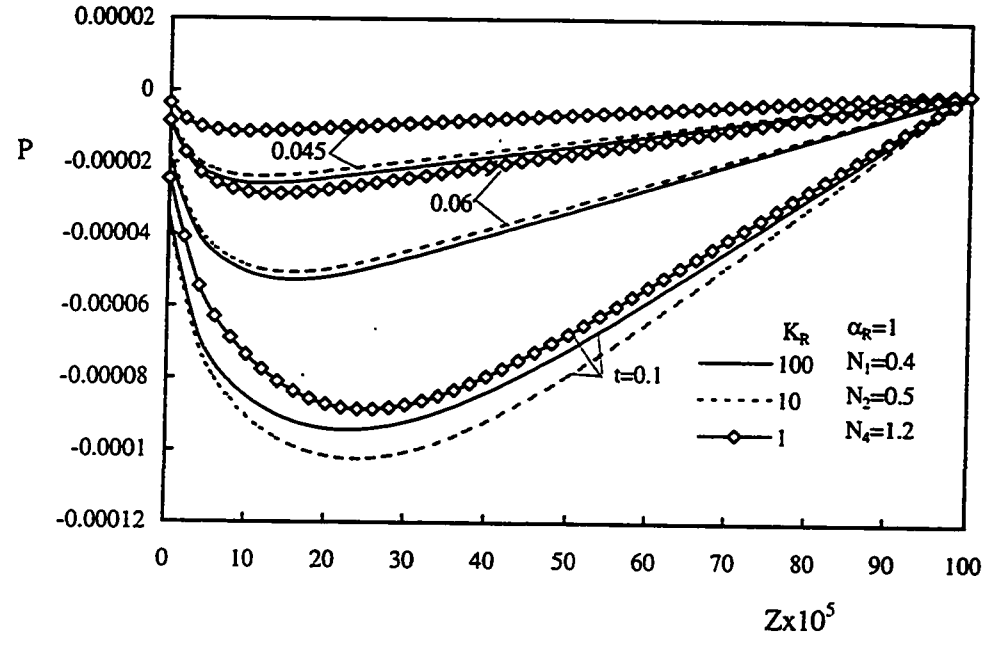

Figure 5.119: Effect of K_R on the variation of the pressure with time, $Gr^* = 10^3, \alpha_R = 1$

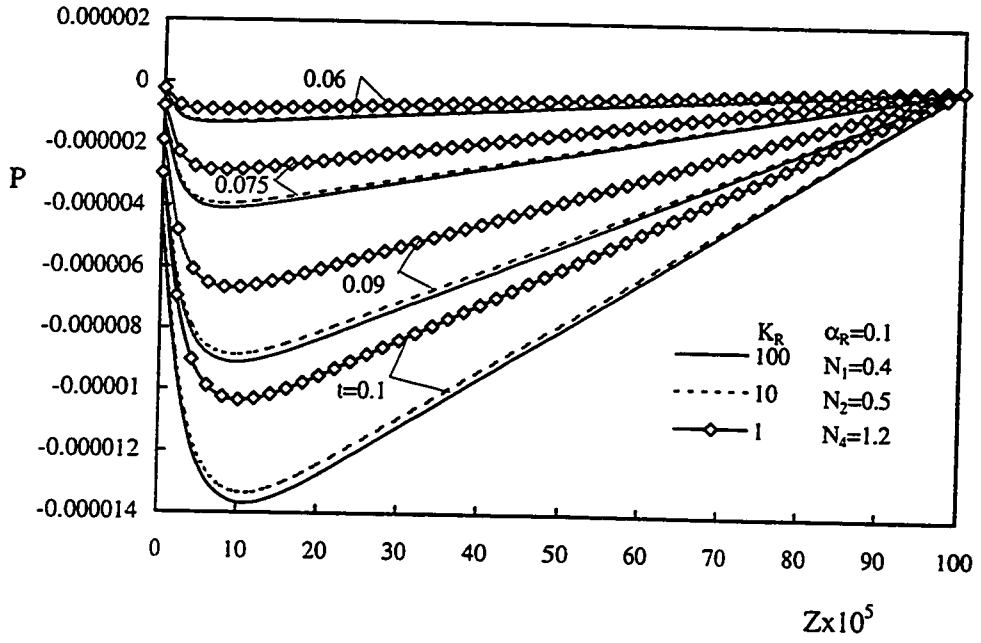

Figure 5.120: Effect of K_R on the variation of the pressure with time, $Gr^* = 10^3, \alpha_R = 0.1$

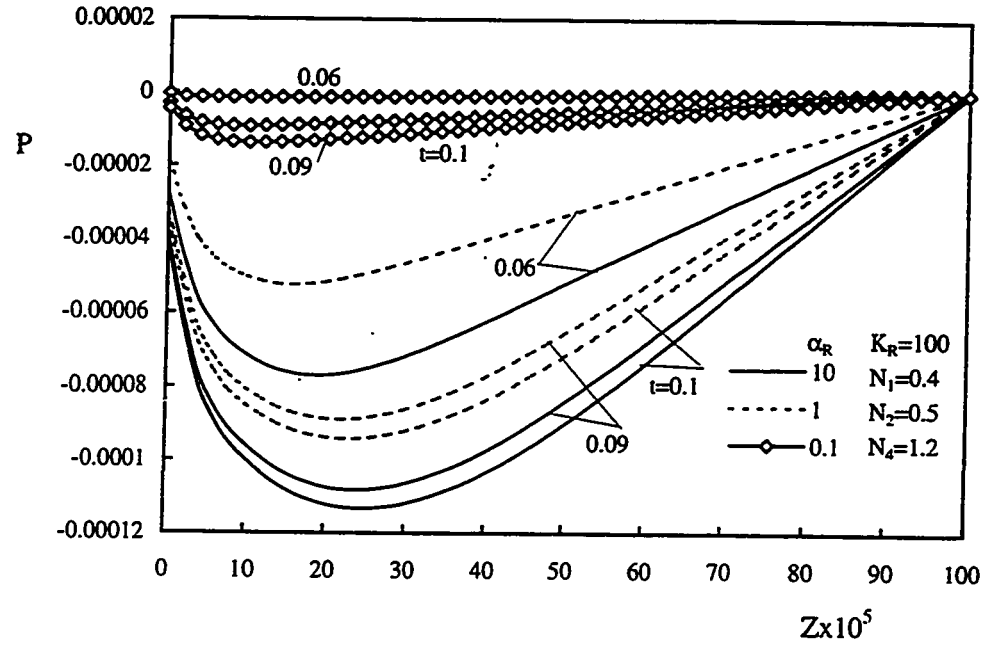

Figure 5.121: Effect of α_R on the variation of the pressure with time, $Gr^* = 10^3, K_R = 100$

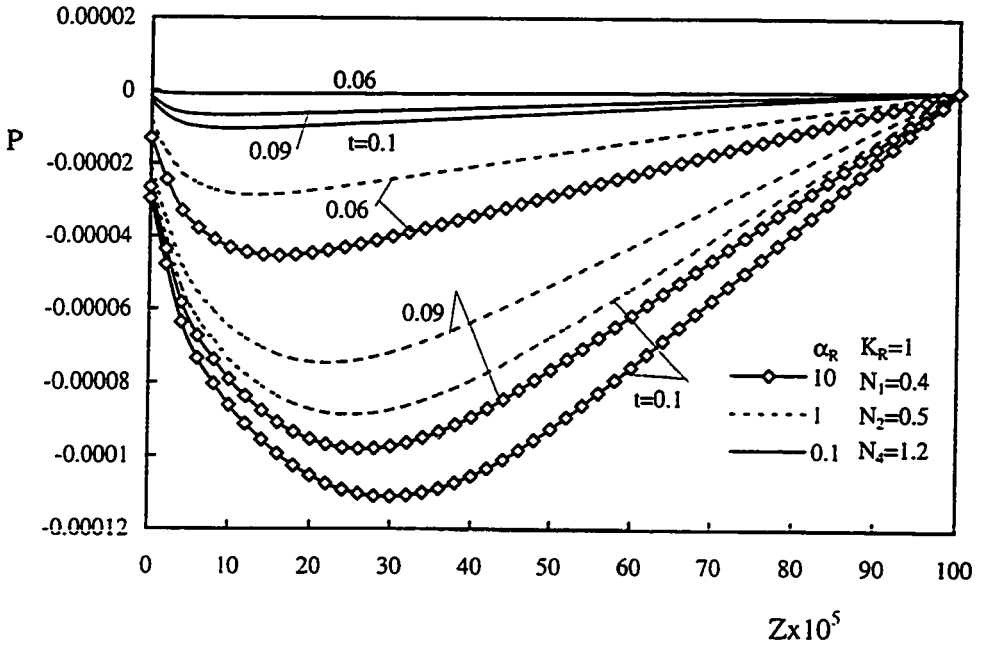

Figure 5.122: Effect of α_R on the variation of the pressure with time, $Gr^* = 10^3, K_R = 1$

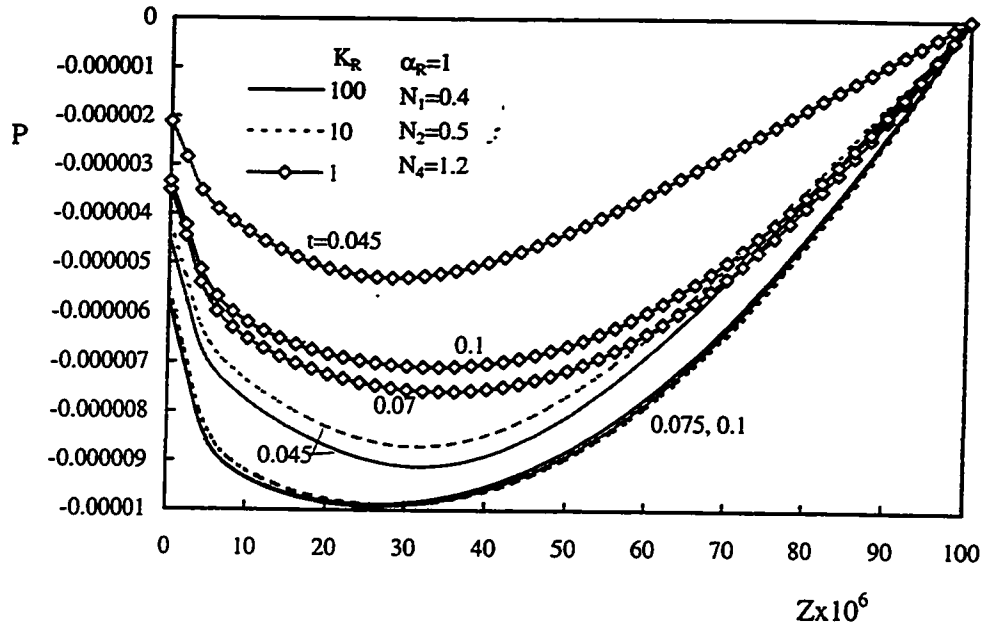

Figure 5.123: Effect of K_R on the variation of the pressure with time, $Gr^* = 10^4, \alpha_R = 1$

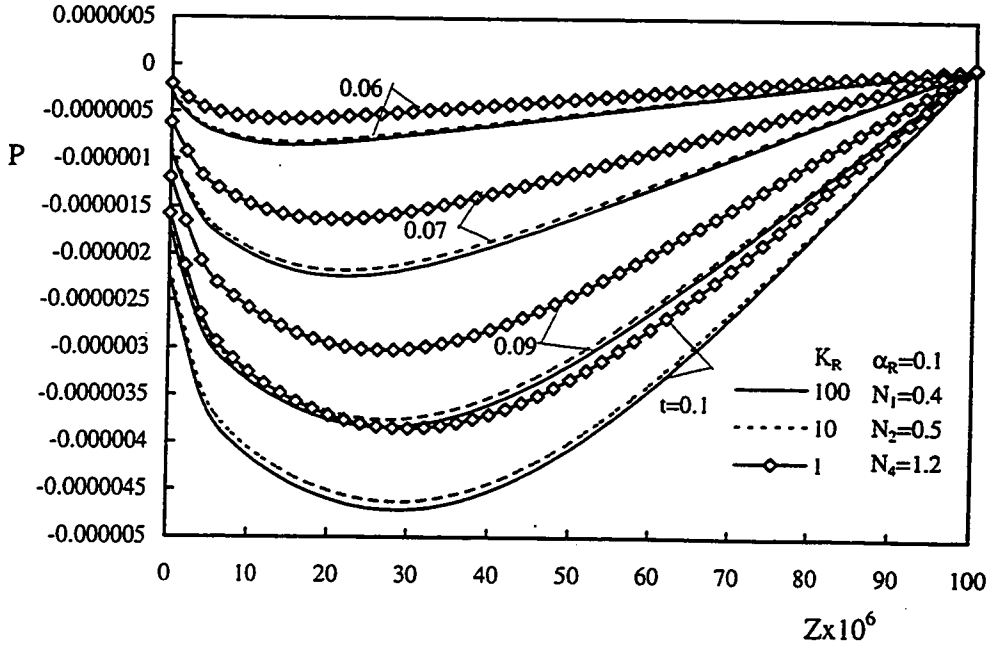

Figure 5.124: Effect of K_R on the variation of the pressure with time, $Gr^* = 10^4, \alpha_R = 0.1$

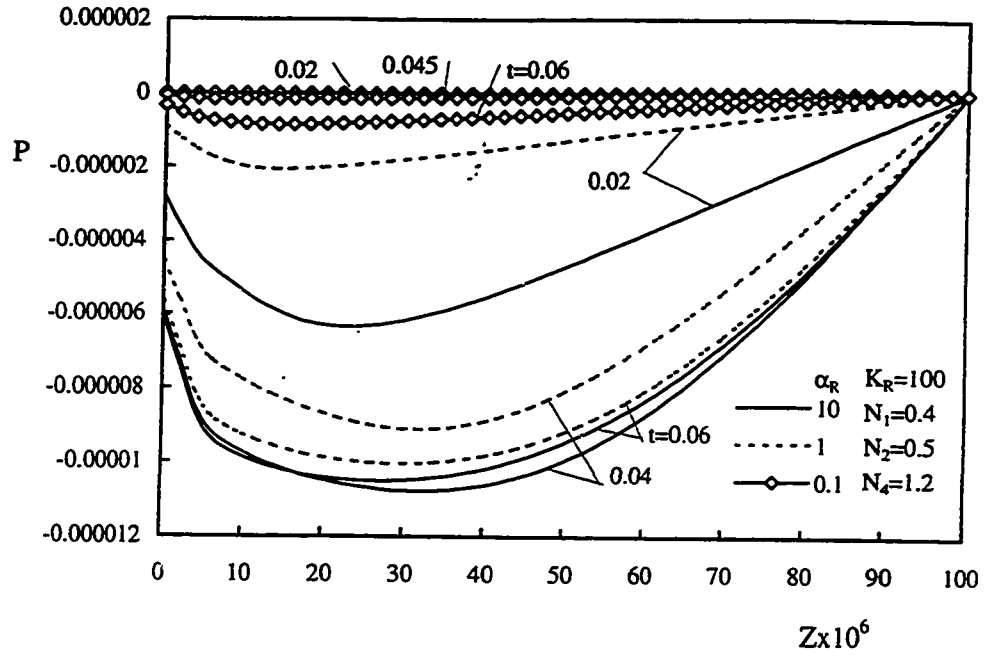

Figure 5.125: Effect of α_R on the variation of the pressure with time, $Gr^* = 10^4, K_R = 100$

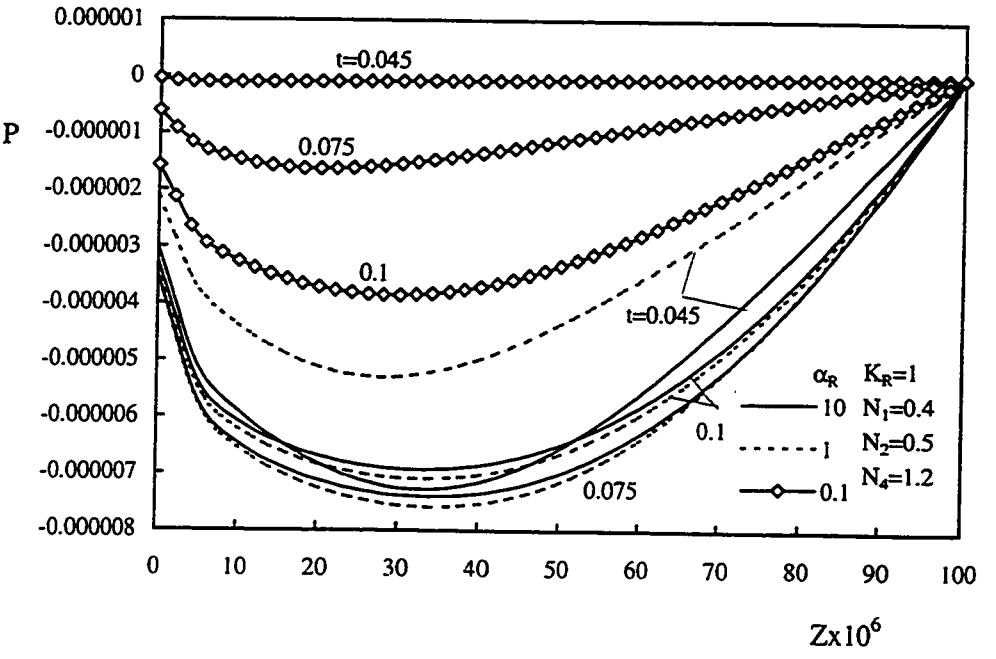

Figure 5.126: Effect of α_R on the variation of the pressure with time, $Gr^* = 10^4, K_R = 1$

5.3.6 Mixing-Cup Temperature

Figures 5.127 through 5.142 constitute four groups of plots presenting the effect of K_R on the variation with time of the mixing-cup temperature at different axial positions for four given values of Gr^*, namely, $Gr^* = 500, 10^3, 10^4$ and 10^5. Each of these groups consists of two pairs of figures. The first pair in each of these groups presents the effect of K_R on the variation with time of the mixing-cup temperature at different values of Z for given values of α_R. The second pair shows, for given values of K_R, the effect of α_R on the development with time of the mixing-cup temperature at different axial positions.

Figure 5.127 shows how K_R affects the development with time of the mixing-cup temperature at different axial positions for $Gr^* = 500$ and $\alpha_R = 1$. At early time, the small amount of fluid that is sucked under the chimney effect absorbs the heat conducted through the heated wall to the fluid-annular gap. As time elapses, more fluid is sucked which sweeps the heated wall with larger axial velocity. This results in an increase in the amount of heat absorbed and thus the mixing-cup temperature increases. It is easily seen in Fig. 5.127 that, at a given axial position, the mixing-cup temperature increases with time to a maximum value and then decreases to its steady-state value. This phenomenon is attributed to the temperature overshoot phenomenon that has been discussed before. Moreover, the effect of K_R on the mixing-cup temperature is pronounced. It is seen that, for a given time, increasing K_R results in an increase in the value of the mixing-cup temperature at any given axial position. In fact, increasing K_R means an increase in the rate of heat conducted through the heated wall to the fluid-annular gap and hence the heat absorbed by the induced

fluid increases which means an increase in the mixing-cup temperature. It is interesting to observe that, for all the presented values of K_R, the mixing-cup temperature, at early times (until say $t = 0.1$) and for the given different axial positions, has the same value but as time elapses its value differs with the axial distance. This can be explained as follows. At early time, a small amount of fluid is induced and as it moves upwards washing the heated wall, it warms up by absorbing the heat coming from the wall. After some axial distance the fluid became saturated, i.e., it does not has any more capacity to absorb more heat. Consequently, it continues moving upwards with the same amount of heat absorbed and the mixing-cup temperature that has been attained at earlier distance. It is worth mentioning that the maximum value for the the mixing-cup temperature that the fluid can attain is $\theta_m = 1$ for the fully-developed state. It is seen in Fig. 5.127 that the mixing-cup temperature at the exit has attained a value $(1 > \theta_m > 0.9)$ which means that the flow reached the exit of the annulus without reaching the fully-developed state.

Similar to Fig. 5.127, Fig. 5.128 presents the effect of K_R on the development with time of the mixing-cup temperature for $\alpha_R = 0.1$. Comparing Figs. 5.127 and 5.128, it is seen that, for a given value of K_R, the values of the mixing-cup temperature decreases with the decrease in α_R. This effect of α_R is discussed hereinafter.

For $K_R = 100$ and 1, respectively, Figs. 5.129 and 5.130 present the effect of α_R on the development with time of the mixing-cup temperature at different axial positions. It can be seen from these two figures that the mixing-cup temperature increases with the increase in the value of α_R. This can be explained by referring to the definition of α_R. Since

$\alpha_R = K_R \frac{\rho_f C_f}{\rho_s C_s}$, hence for a given value of K_R, the increase in α_R implies a decrease in the value of the specific heat of the solid wall material. This leads to an increase in the amount of heat conducted through the heated wall compared with that absorbed by the wall material; this results in an increase in the buoyancy force. This means an increase in the amount of the induced fluid and hence an increase in the amount of the heat absorbed; consequently, the mixing-cup temperature increases.

Similar to the above group of figures, Figs. 5.131 through 5.134, Figs. 5.135 through 5.138 and 5.139 through 5.142 present another three groups of figures for $Gr^* = 10^3, 10^4$ and 10^5, respectively. It can be seen that all these figures have the same general qualitative characteristics as those of $Gr^* = 500$ except that the mixing-cup temperature reaches the steady state in a shorter time and also the overshoot phenomenon appears at a shorter time. In fact, larger values of Gr^* represent shorter annuli with larger hydraulic diameter and larger temperature difference. Hence, as Gr^* increases the amount of the induced fluid decreases and due to the large temperature difference, the flow develops, with time, faster. Consequently, the overshoot phenomenon appears at earlier time compared with annuli of smaller values of Gr^*, i.e., larger height ($L = \frac{1}{Gr^*}$). It can be seen in Figs. 5.139 and 5.141 that the mixing-cup temperature profiles near the exit(for $K_R = 100$) are distorted. This is because of the existence of flow reversal at such time and position. Also, Fig. 5.141 comprises only two values of α_R(1 and 0.1). This is because for $\alpha_R = 10$, strong back flow occurred and caused numerical instability.

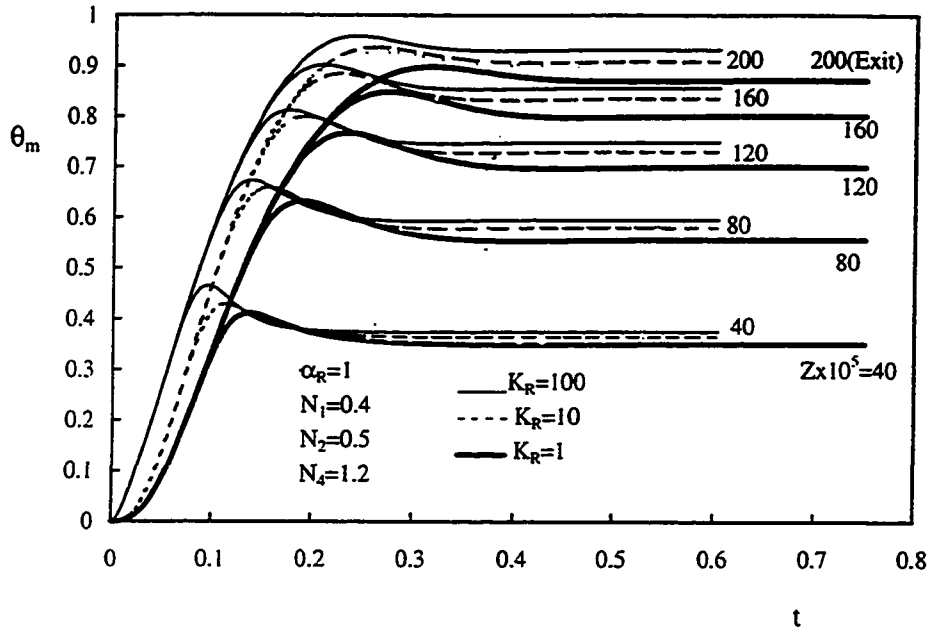

Figure 5.127: Effect of K_R on the variation with time of the mixing-cup temperature at different axial positions, $Gr^* = 500, \alpha_R = 1$

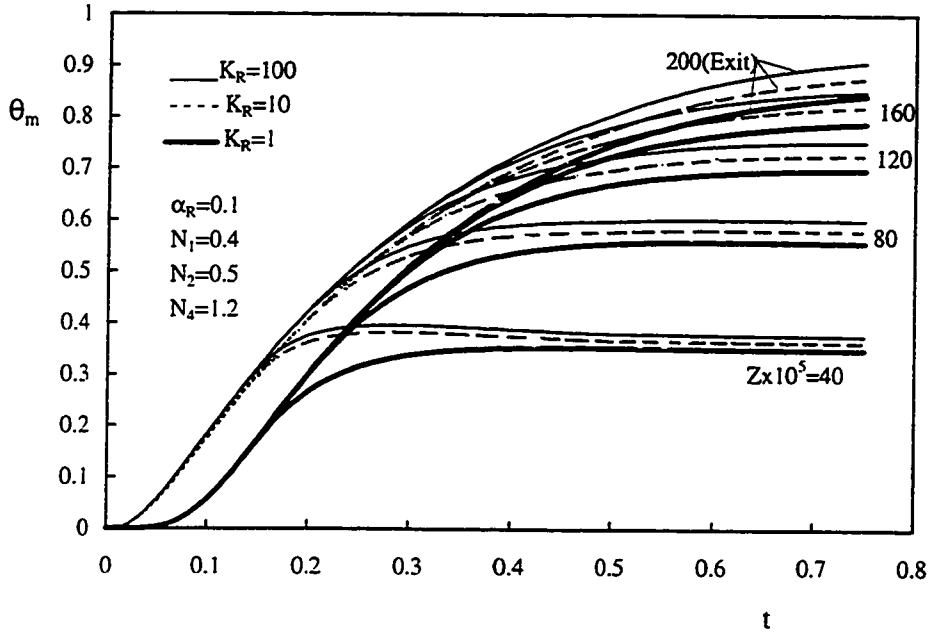

Figure 5.128: Effect of K_R on the variation with time of the mixing-cup temperature at different axial positions, $Gr^* = 500, \alpha_R = 0.1$

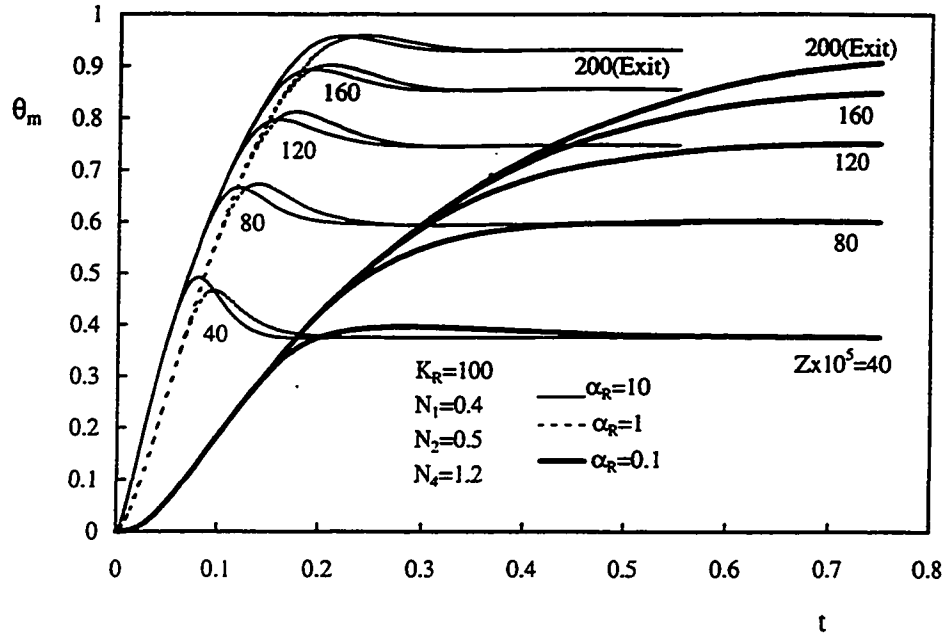

Figure 5.129: Effect of α_R on the variation with time of the mixing-cup temperature at different axial positions, $Gr^* = 500, K_R = 100$

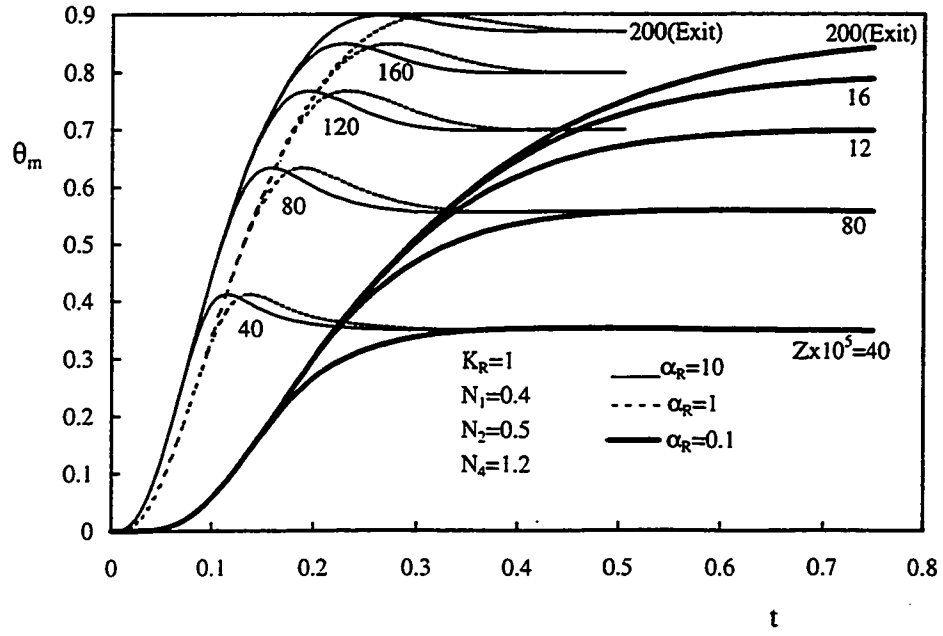

Figure 5.130: Effect of α_R on the variation with time of the mixing-cup temperature at different axial positions, $Gr^* = 500, K_R = 1$

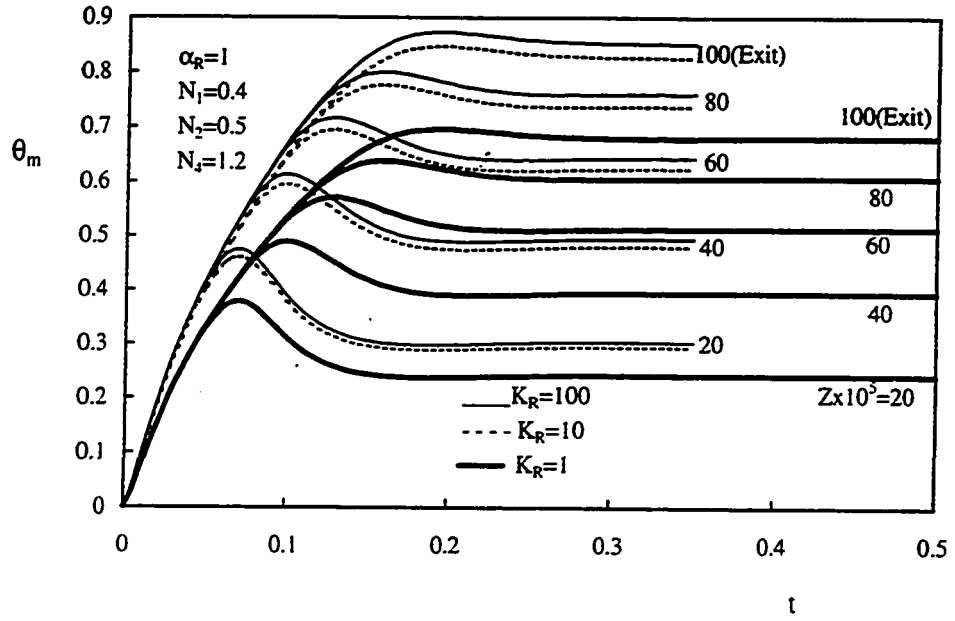

Figure 5.131: Effect of K_R on the variation with time of the mixing-cup temperature at different axial positions, $Gr^* = 10^3, \alpha_R = 1$

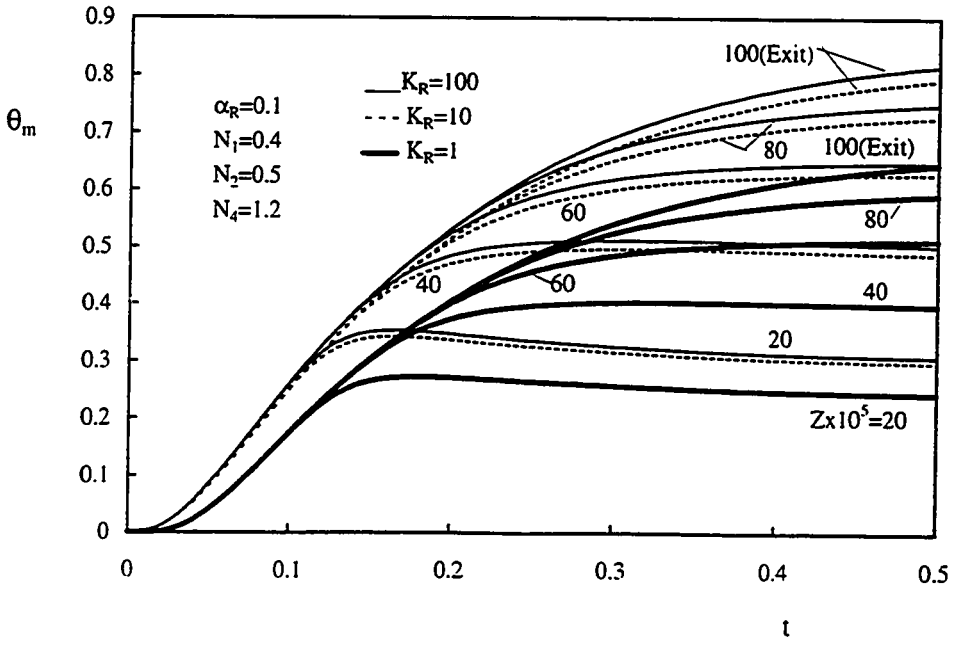

Figure 5.132: Effect of K_R on the variation with time of the mixing-cup temperature at different axial positions, $Gr^* = 10^3, \alpha_R = 0.1$

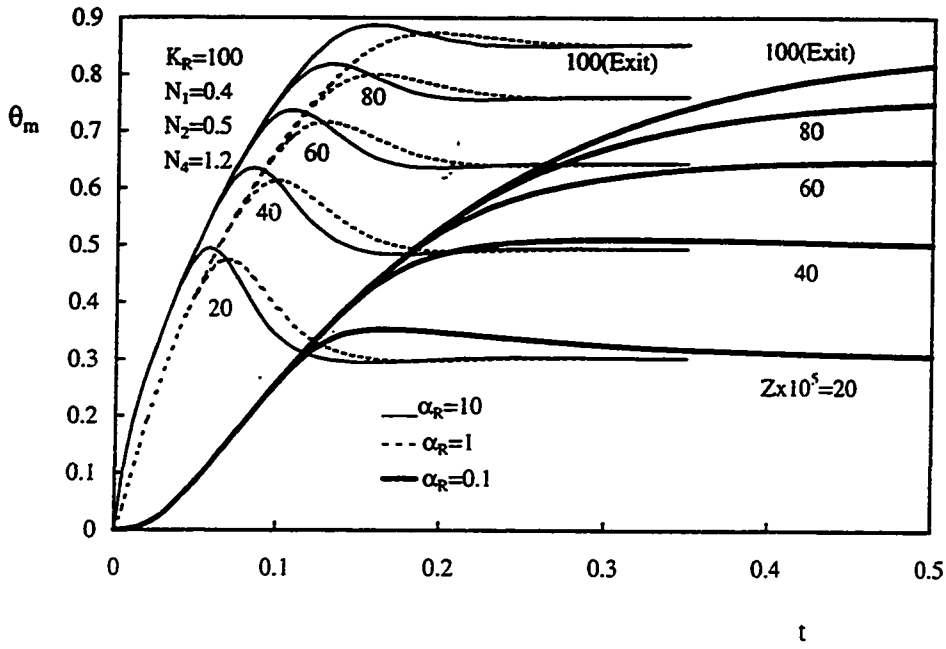

Figure 5.133: Effect of α_R on the variation with time of the mixing-cup temperature at different axial positions, $Gr^* = 10^3, K_R = 100$

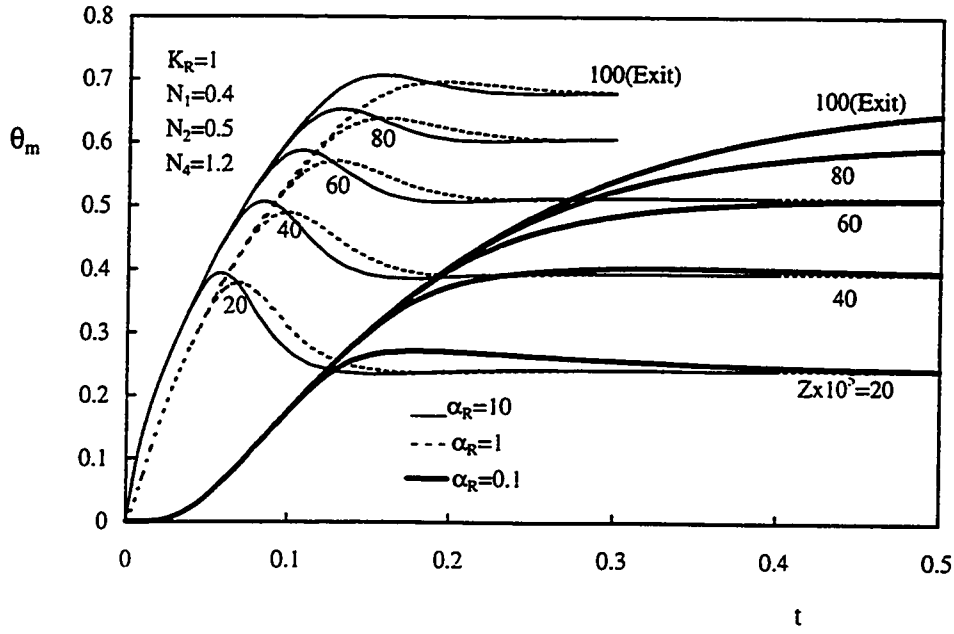

Figure 5.134: Effect of α_R on the variation with time of the mixing-cup temperature at different axial positions, $Gr^* = 10^3, K_R = 1$

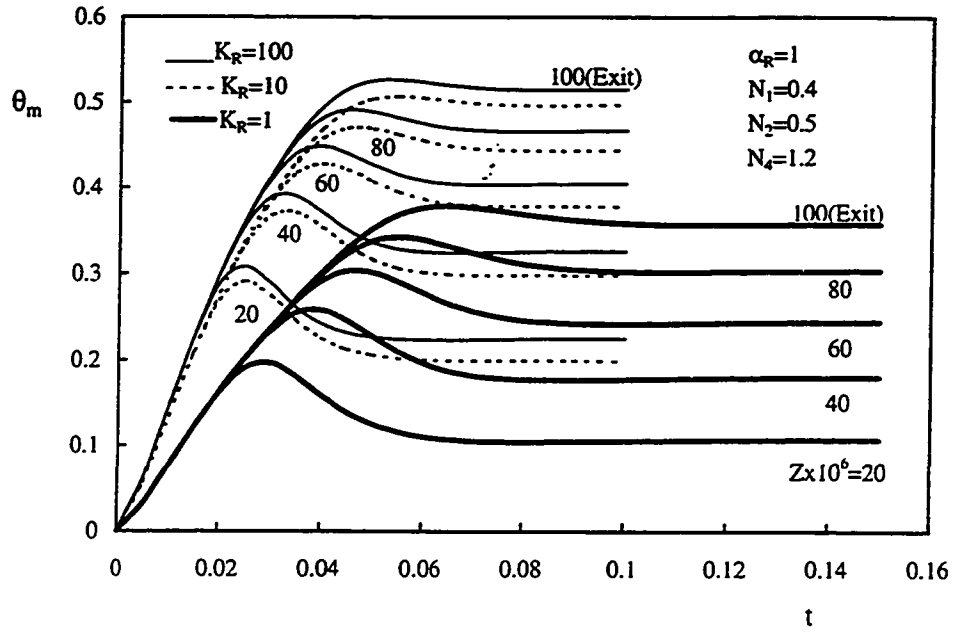

Figure 5.135: Effect of K_R on the variation with time of the mixing-cup temperature at different axial positions, $Gr^* = 10^4, \alpha_R = 1$

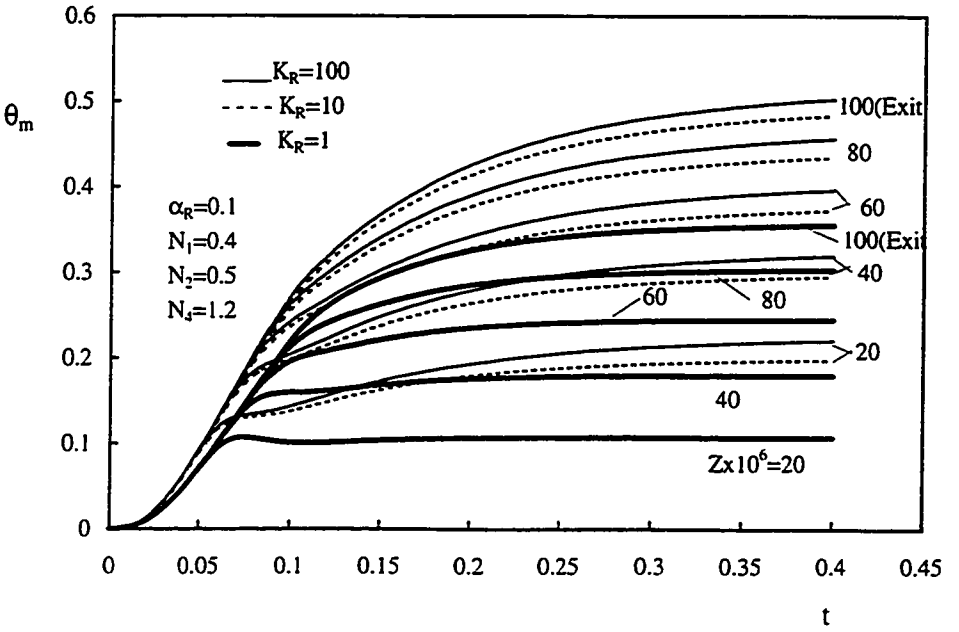

Figure 5.136: Effect of K_R on the variation of the mixing-cup temperature at different axial positions, $Gr^* = 10^4, \alpha_R = 0.1$

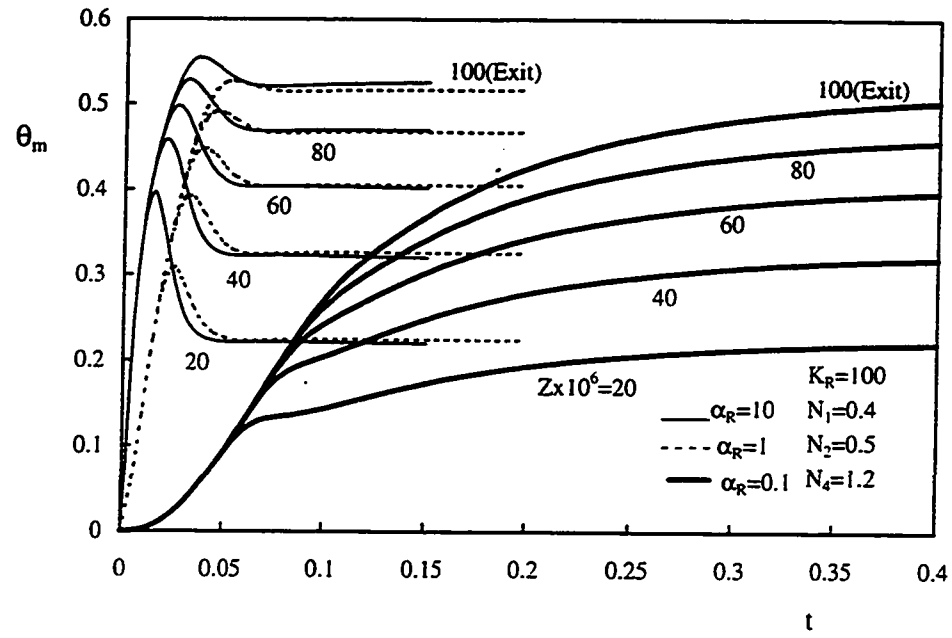

Figure 5.137: Effect of α_R on the variation with time of the mixing-cup temperature at different axial positions, $Gr^* = 10^4, K_R = 100$

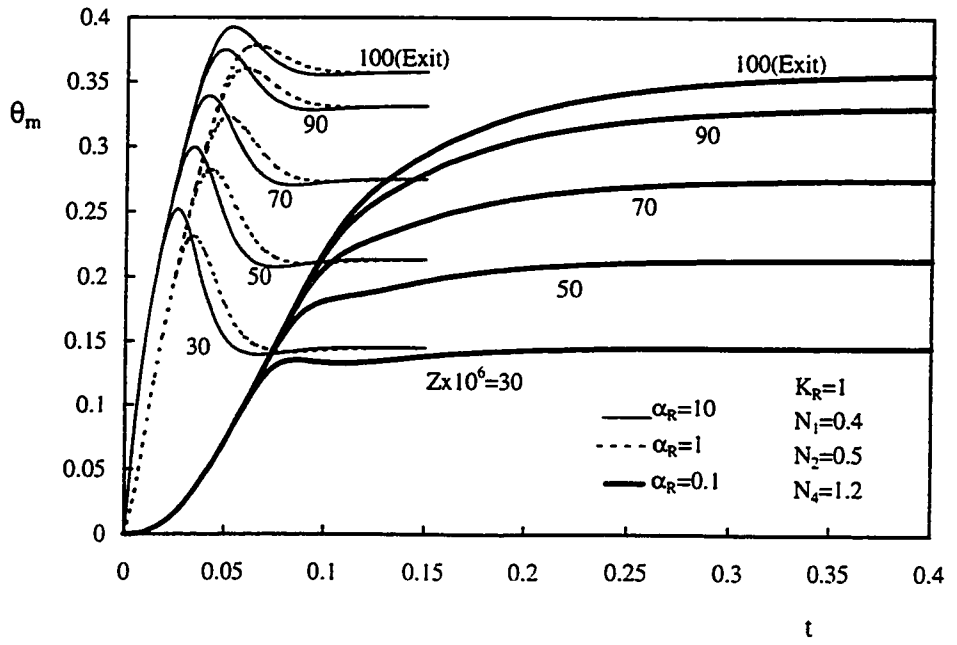

Figure 5.138: Effect of α_R on the variation with time of the mixing-cup temperature at different axial positions, $Gr^* = 10^4, K_R = 1$

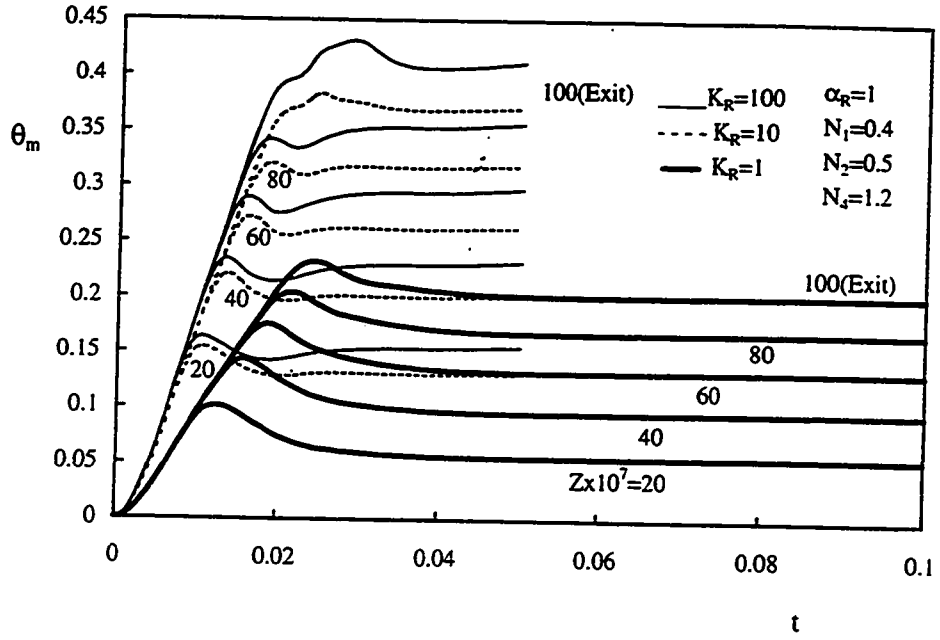

Figure 5.139: Effect of K_R on the variation with time of the mixing-cup temperature at different axial positions, $Gr^* = 10^4, \alpha_R = 1$

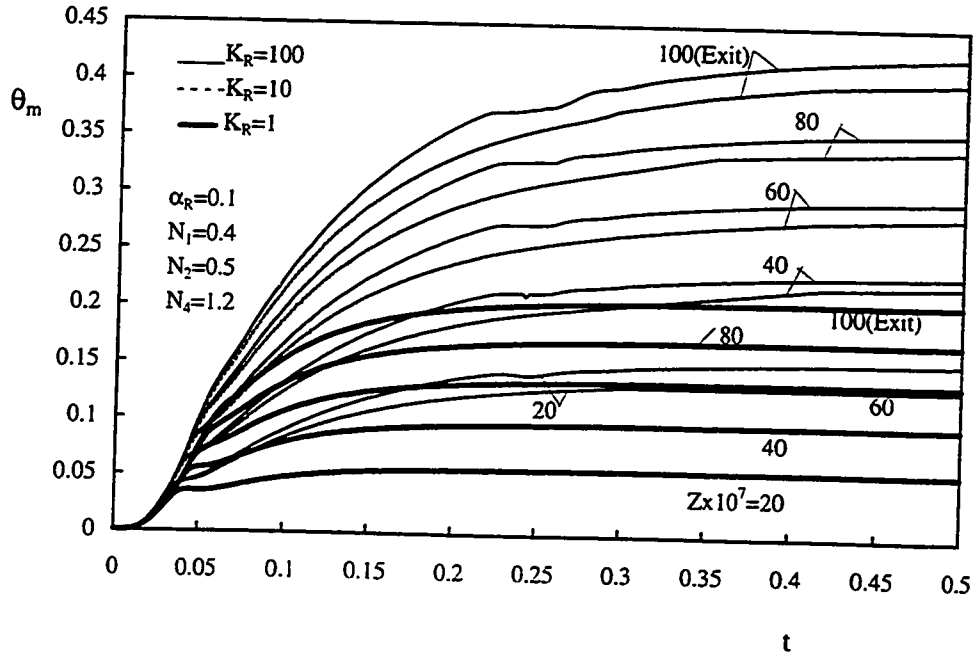

Figure 5.140: Effect of K_R on the variation with time of the mixing-cup temperature at different axial positions, $Gr^* = 10^5, \alpha_R = 0.1$

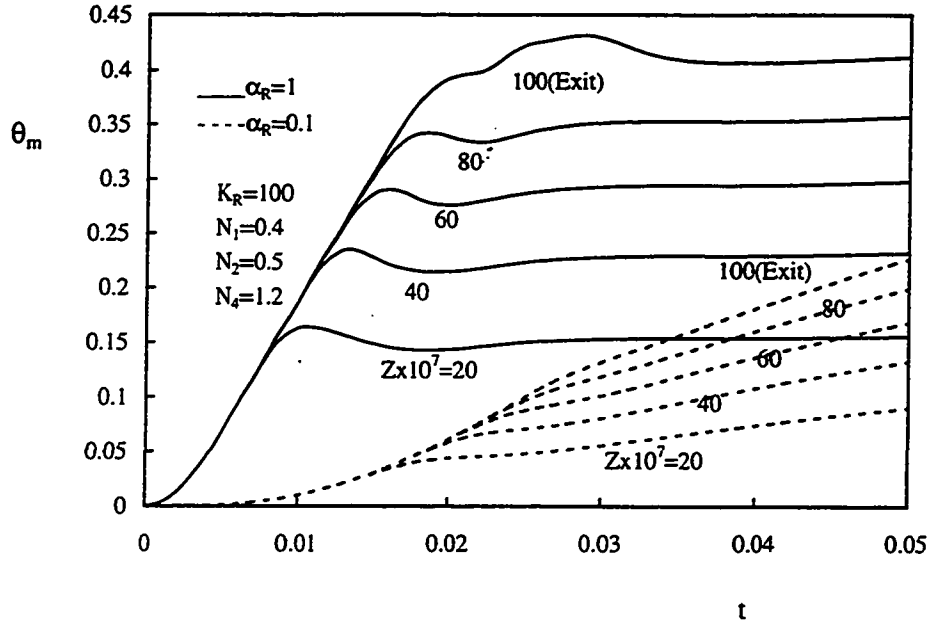

Figure 5.141: Effect of K_R on the variation with time of the mixing-cup temperature at different axial positions, $Gr^* = 10^5$, $K_R = 100$

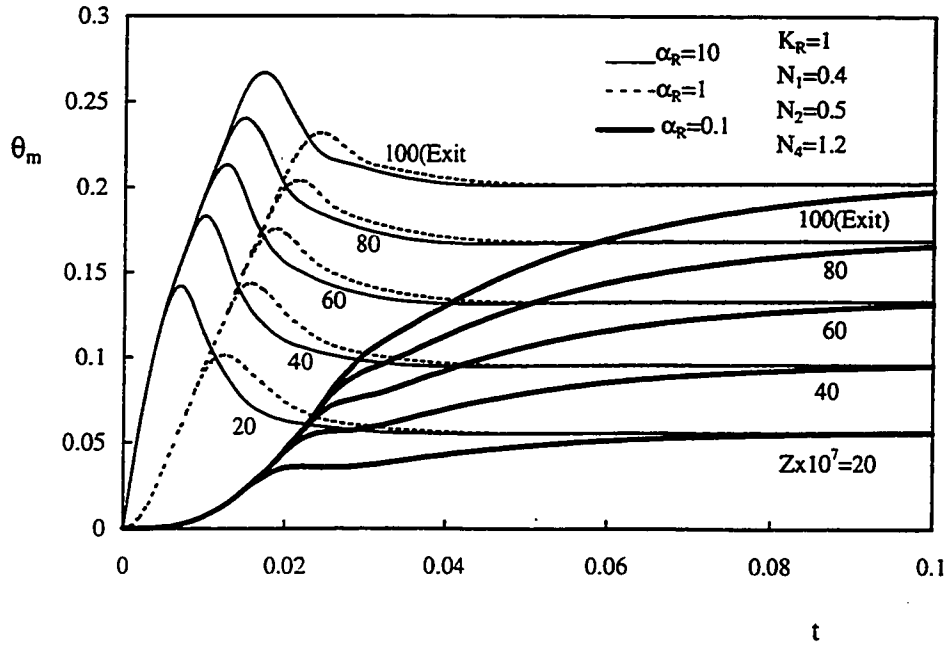

Figure 5.142: Effect of α_R on the variation with time of the mixing-cup temperature at different axial positions, $Gr^* = 10^5$, $K_R = 1$

5.3.7 Heat Absorbed

Figures 5.143 through 5.158 constitute four groups of plots presenting the effect of K_R on the development with time of the heat absorbed at different axial positions for four given values of Gr^*, namely, $Gr^* = 500, 10^3, 10^4$ *and* 10^5. Each of these groups consists of two pairs of figures. The first pair in each of these groups presents the effect of K_R on the variation with time of the heat absorbed at different axial positions for given values of α_R, namely, $\alpha_R = 1$ *and* 0.1. The second pair of these figures presents the effect of α_R on the variation with time of the heat absorbed at different axial positions for given values of K_R, namely, $K_R = 100$ *and* 1.

Figure 5.143 shows the effect of K_R on the development with time of the heat absorbed at different axial positions for an annulus of $Gr^* = 500$ and $\alpha_R = 1$. At early time, a small amount of fluid is induced due to chimney effect as a small buoyancy force is created in the fluid-annular gap. This small sucked fluid absorbs the heat conducted through the heated wall to the fluid-annular gap. As time elapses, the buoyancy force develops more as the rate of heat transfer through the heated wall to the fluid increases. This leads to the increase in the amount of the induced flow rate which sweeps the heated wall with a larger axial velocity; consequently, the heat absorbed increases. It can be easily seen from Fig. 5.143 that the heat absorbed, at a given axial position, increases to a maximum value and then decreases to its steady-state value. This phenomenon is attributed to the temperature overshoot phenomenon that has been discussed before. Moreover, Fig. 5.143 shows that, at a given axial position, the heat absorbed increases with the increase in the value of

K_R. Since, $K_R = \frac{K_s}{K_f}$, the increase in K_R implies an increase in the thermal conductivity of the solid wall material(as $K_f = const.$). Hence, increasing K_R leads to an increase in the rate of heat transfer through the heated wall to the fluid-annular gap.

For $\alpha_R = 0.1$, Fig. 5.144 presents the effect of K_R on the development with time of the heat absorbed at different axial positions. Comparing Fig. 5.143 with Fig. 5.144, it can be easily seen that the heat absorbed decreases with the decrease in the value of α_R. Moreover, it is seen that all the heat absorbed profiles for all values of K_R do not show any effect for the temperature overshoot. The reason for this effect of α_R is discussed in detail hereinafter.

For $K_R = 100$ *and* 1, Figs. 5.145 and 5.146 present, respectively, the effect of α_R on the development with time of the heat absorbed at different axial positions. It is seen from these two figures that the heat absorbed increases with the increase in the value of α_R. Since, $\alpha_R = K_R \frac{\rho_f C_f}{\rho_s C_s}$, the increase in the value of α_R implies a decrease in the specific heat of the solid wall material. Hence, increasing the value of α_R increases the amount of heat conducted through the heated wall to the fluid compared with that absorbed by the wall. This leads to an increase in the buoyancy force which means an increase in the amount of the induced flow rate. This induced fluid sweeps the heated wall with larger axial velocity and hence absorbs more heat. On the other hand, decreasing α_R implies an increase in the specific heat of the solid wall material. This leads to a decrease in the amount of heat conducted through the heated wall compared with that absorbed by it. Thus, the conduction effect is weak in this case and the overshoot phenomenon is suppressed.

Similar to the above group of figures, Figs. 5.147 through 5.150 present another group of plots presenting the effect of K_R and α_R on the development with time of the heat absorbed at different axial positions for another value of Gr^*, viz., $Gr^* = 10^3$ while such effect is presented in Figs. 5.151 through 5.154 and Figs. 5.155 through 5.158 for $Gr^* = 10^4$ and 10^5, respectively. It is easily observed that these groups of plots have the same general qualitative characteristics of Figs. 5.143 through 5.146 except that the heat absorbed profiles reach the steady state in a shorter time and also the overshoot phenomenon appears at a shorter time. In fact, larger values of Gr^* represent shorter annuli with larger hydraulic diameter and larger temperature difference. Hence, as Gr^* increases the amount of the induced fluid decreases and due to the large temperature difference, the flow develops, with time, faster. Consequently, the overshoot phenomenon appears at earlier time compared with an annuli of smaller values of Gr^*, i.e., larger height ($L = \frac{1}{Gr^*}$). In Fig. 5.155, it is seen that the heat absorbed profiles near the exit(for $K_R \geq 10$) are distorted. This is because of the existence of flow reversal at that time and position. Also, Fig. 5.157 comprises only two values of α_R(1 and 0.1) and is drawn for $K_R = 10$ instead of $K_R = 100$. This is because for the computer runs corresponding to $K_R \geq 10$ and $\alpha_R \geq 1$, strong back flow occurred and caused numerical instability.

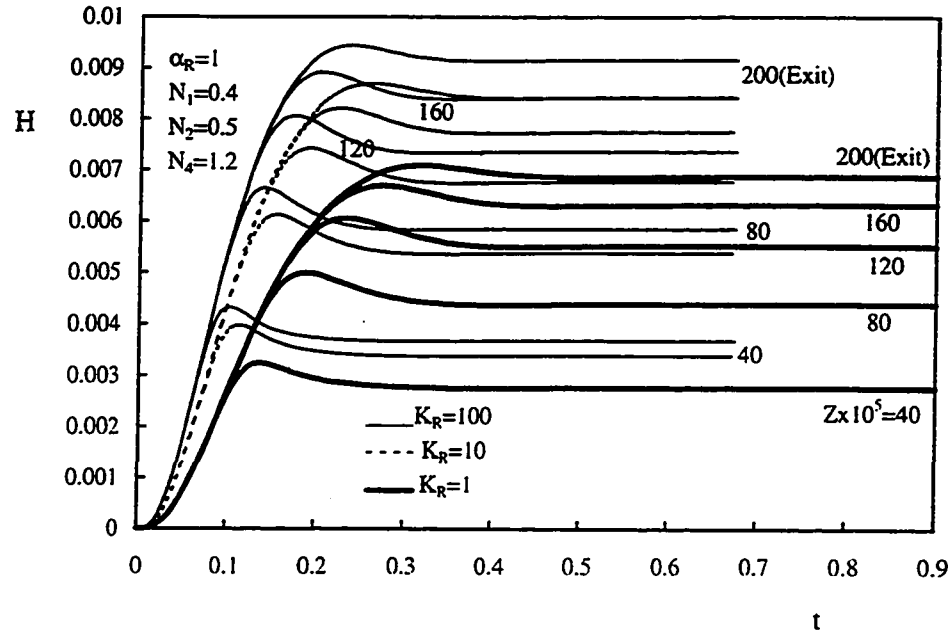

Figure 5.143: Effect of K_R on the development with time of the heat absorbed at different axial positions, $Gr^* = 500, \alpha_R = 1$

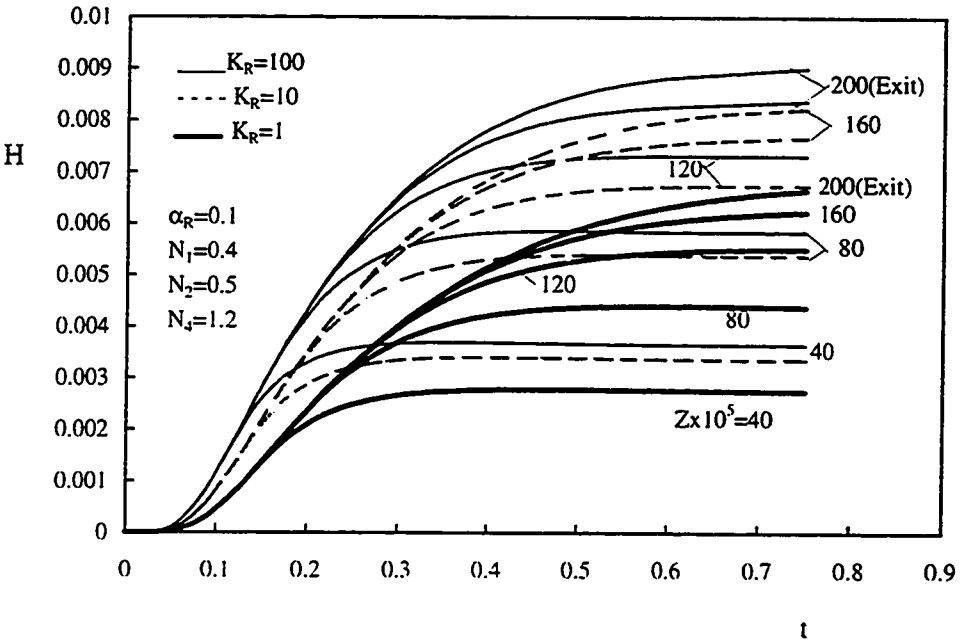

Figure 5.144: Effect of K_R on the development with time of the heat absorbed at different axial positions, $Gr^* = 500, \alpha_R = 0.1$

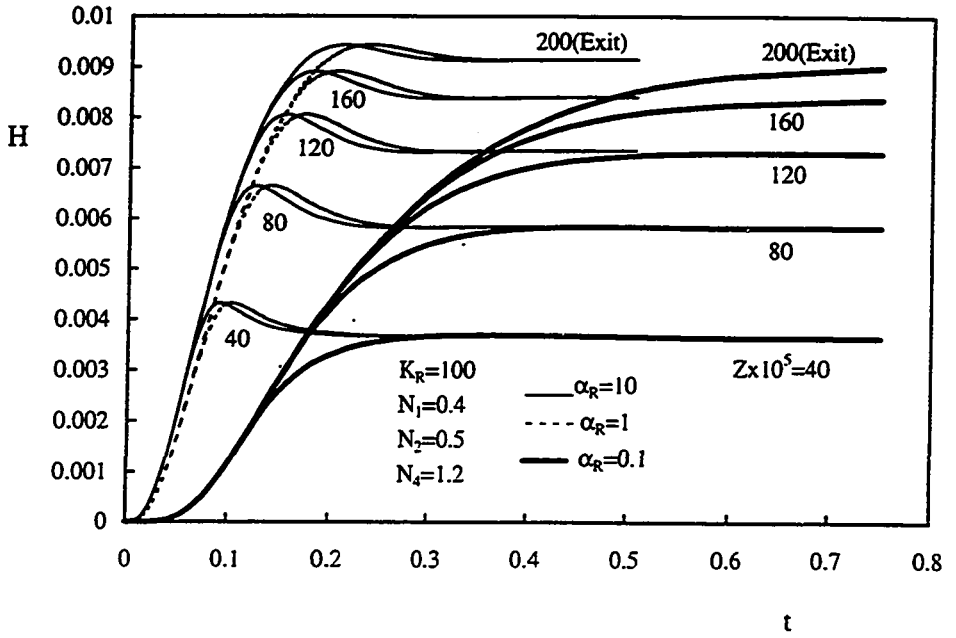

Figure 5.145: Effect of α_R on the development with time of the heat absorbed at different axial positions, $Gr^* = 500, K_R = 100$

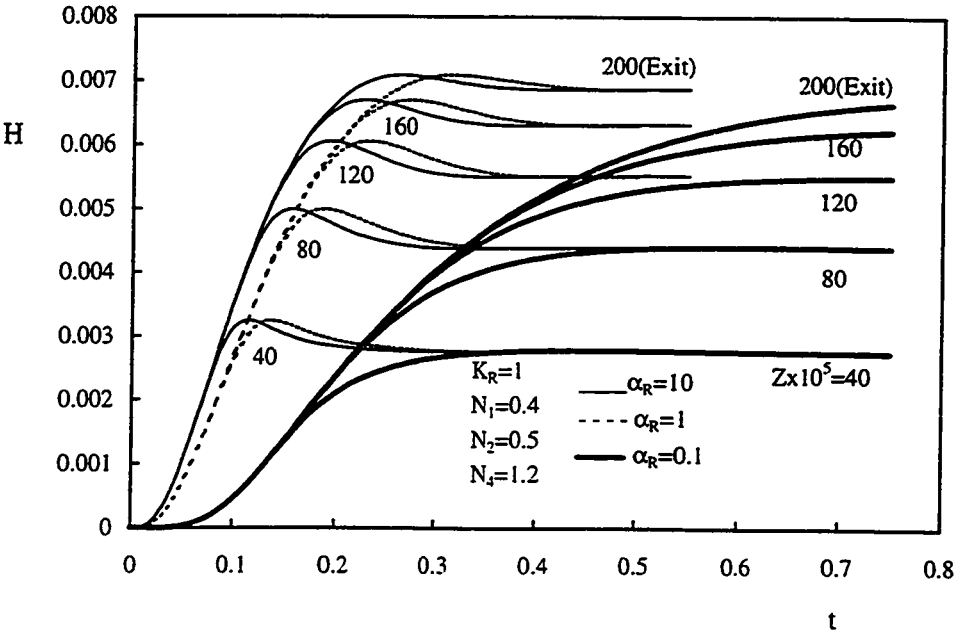

Figure 5.146: Effect of α_R on the development with time of the heat absorbed at different axial positions, $Gr^* = 500, K_R = 1$

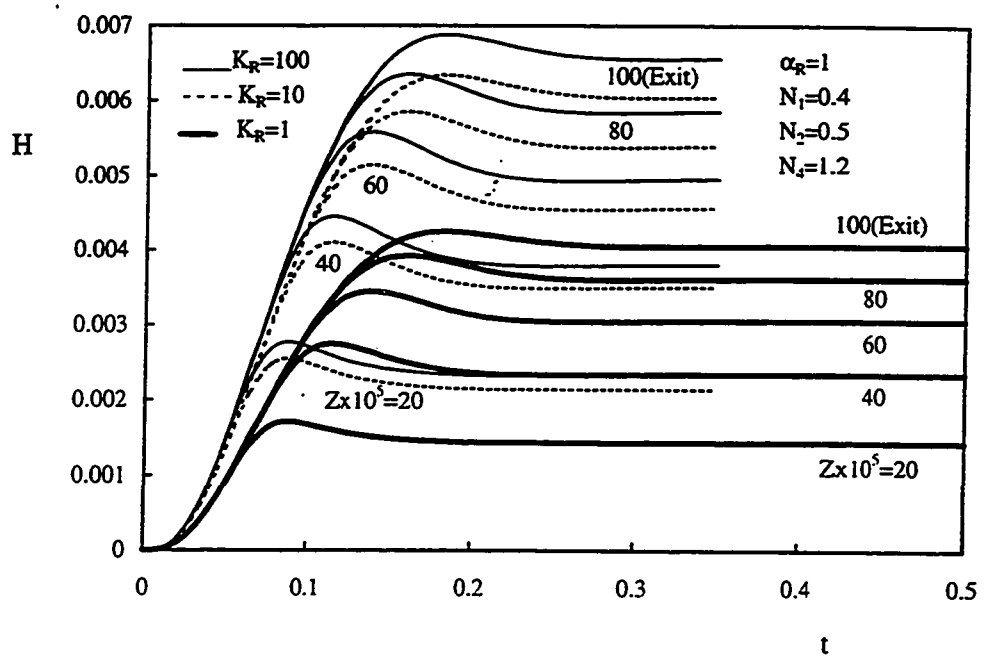

Figure 5.147: Effect of K_R on the development with time of the heat absorbed at different axial positions, $Gr^* = 10^3, \alpha_R = 1$

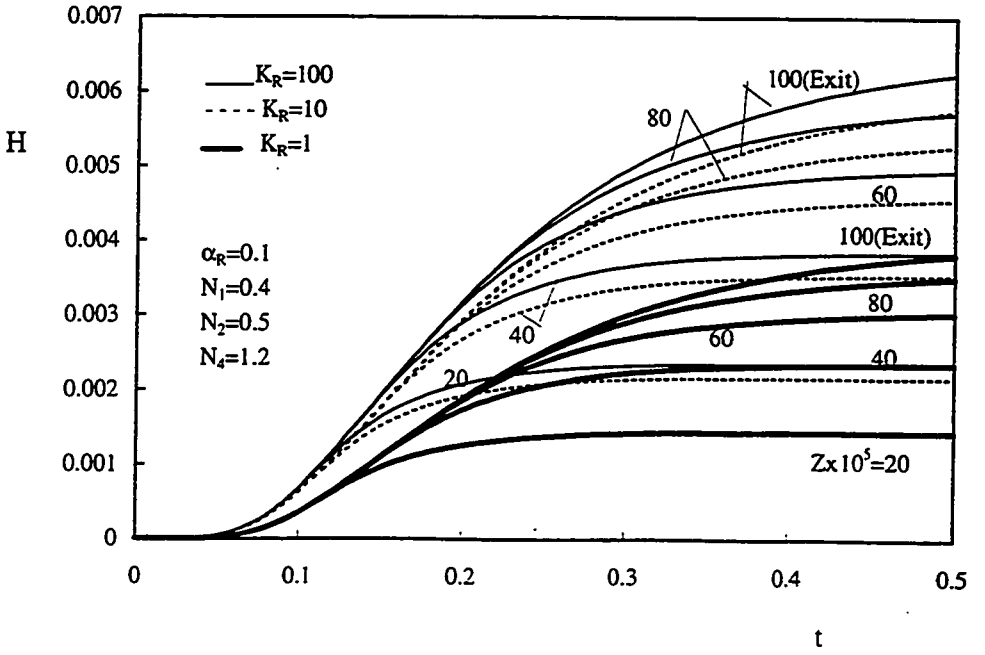

Figure 5.148: Effect of K_R on the development with time of the heat absorbed at different axial positions, $Gr^* = 10^3, \alpha_R = 0.1$

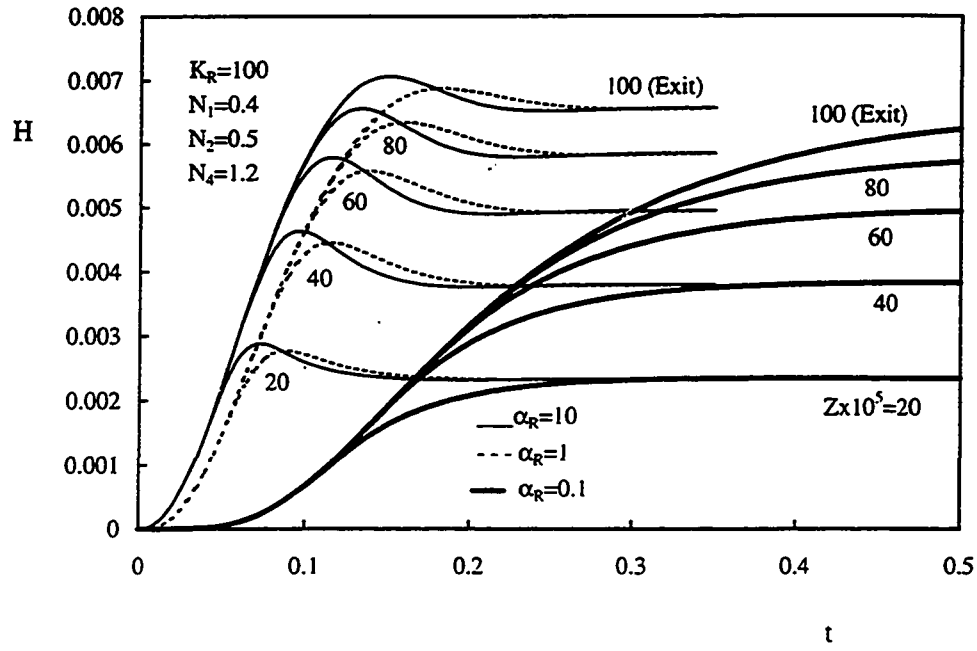

Figure 5.149: Effect of α_R on the development with time of the heat absorbed at different axial positions, $Gr^* = 10^3, K_R = 100$

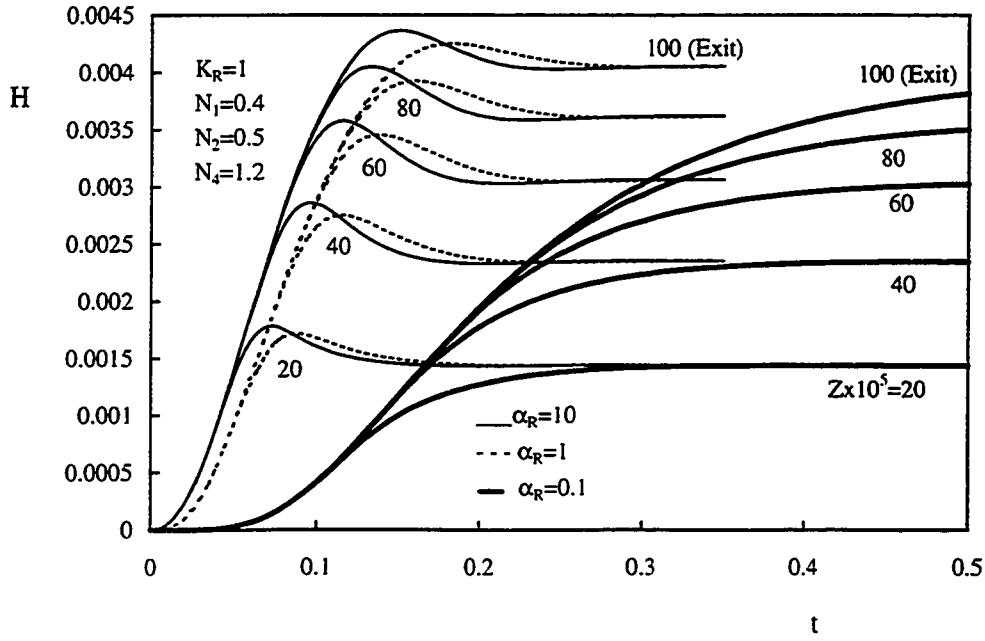

Figure 5.150: Effect of α_R on the development with time of the heat absorbed at different axial positions, $Gr^* = 10^3, K_R = 1$

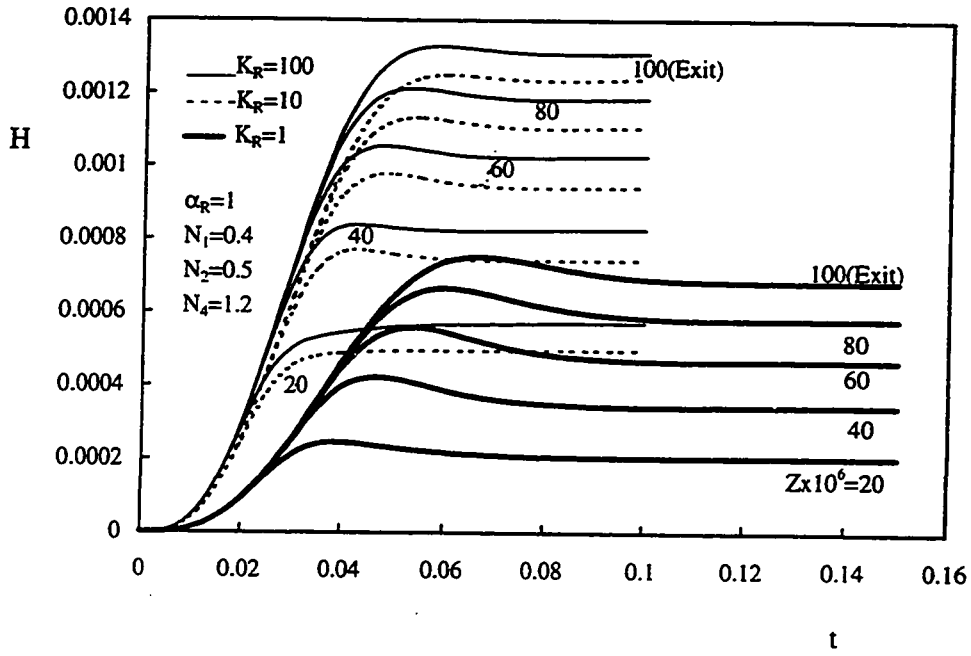

Figure 5.151: Effect of K_R on the development with time of the heat absorbed at different axial positions, $Gr^* = 10^4, \alpha_R = 1$

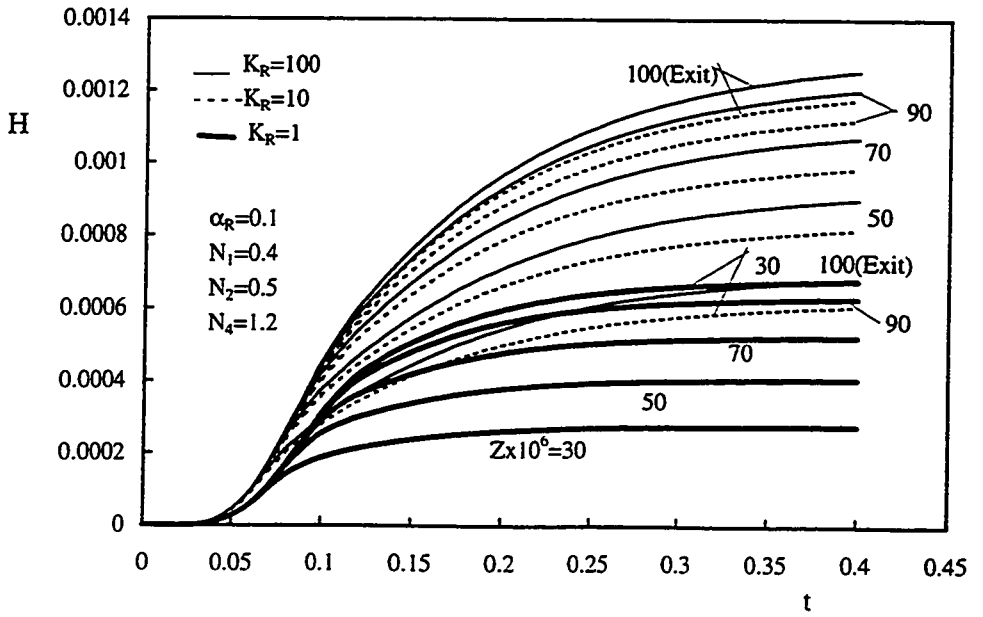

Figure 5.152: Effect of K_R on the development with time of the heat absorbed at different axial positions, $Gr^* = 10^4, \alpha_R = 0.1$

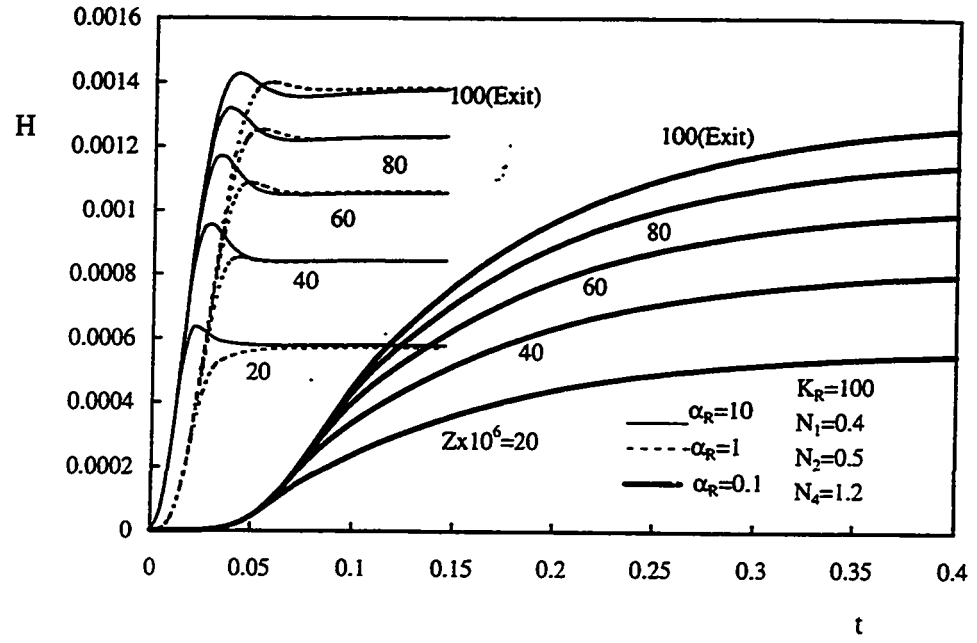

Figure 5.153: Effect of α_R on the development with time of the heat absorbed at different axial positions, $Gr^* = 10^4, K_R = 100$

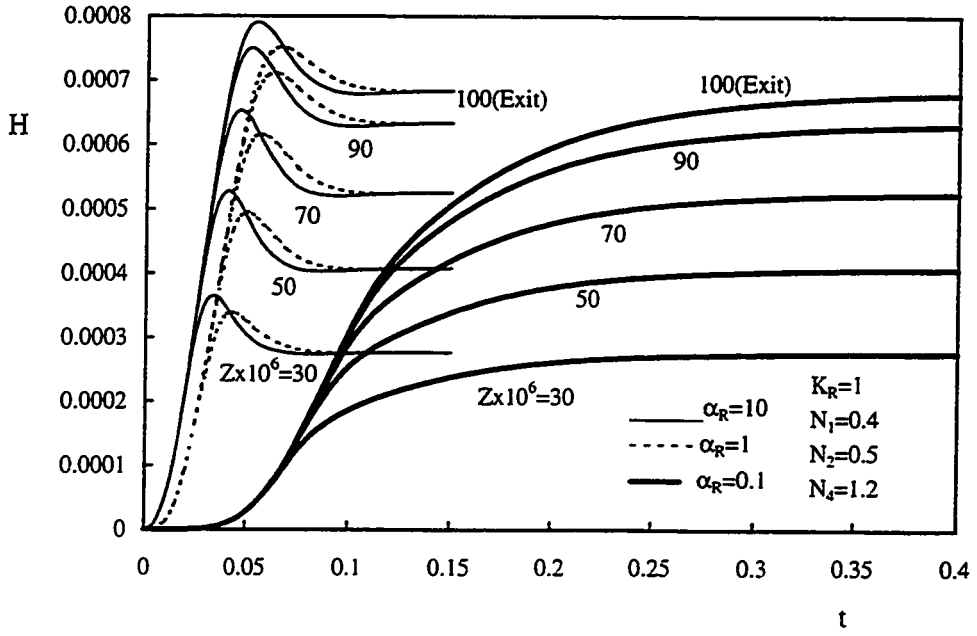

Figure 5.154: Effect of α_R on the development with time of the heat absorbed at different axial positions, $Gr^* = 10^4, K_R = 1$

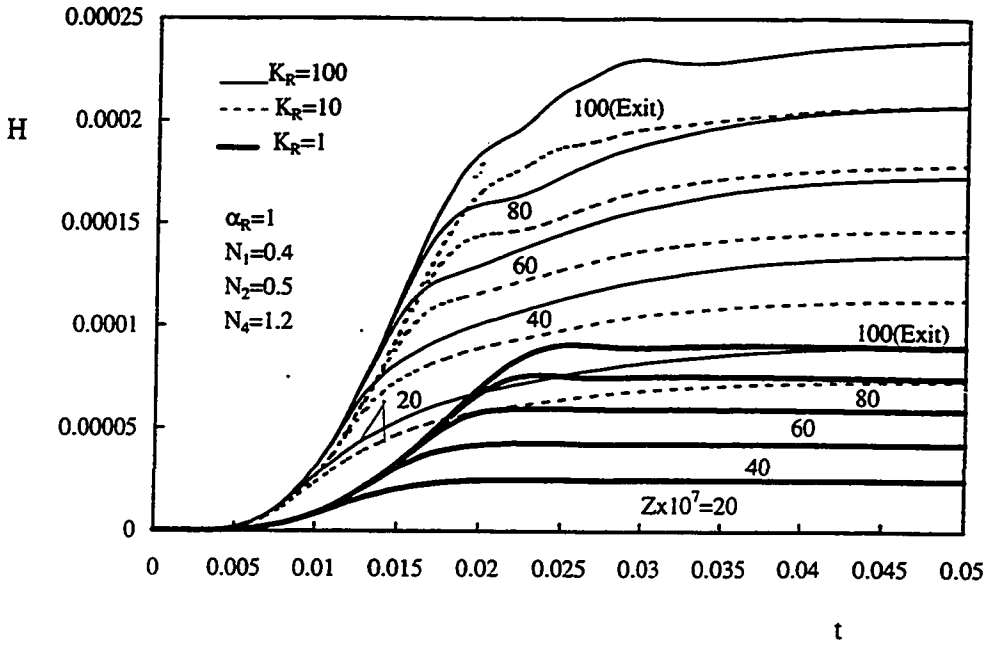

Figure 5.155: Effect of K_R on the development with time of the heat absorbed at different axial positions, $Gr^* = 10^5, \alpha_R = 1$

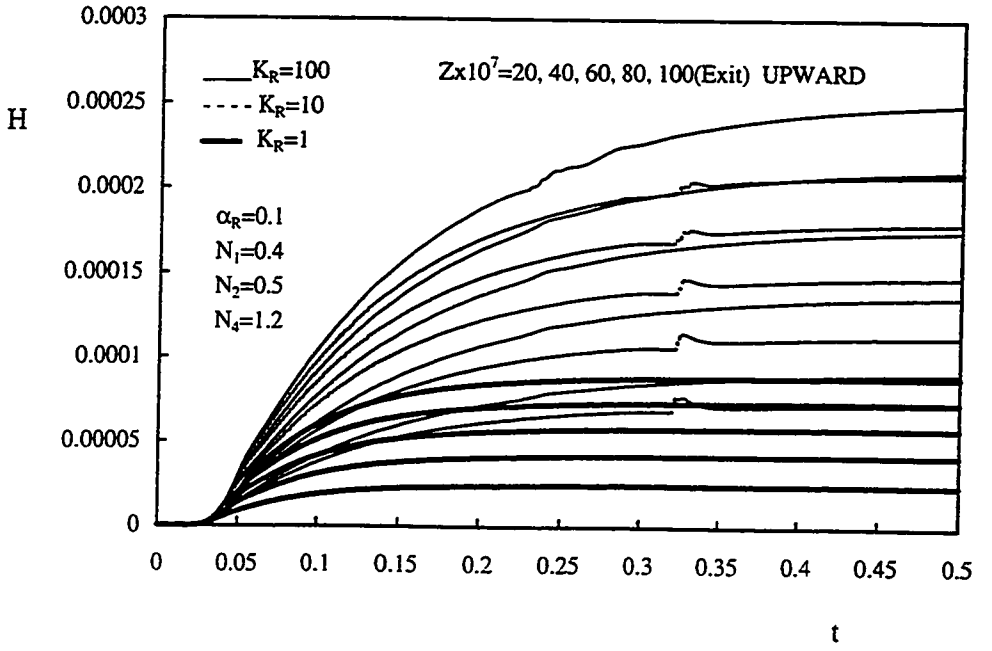

Figure 5.156: Effect of K_R on the development with time of the heat absorbed at different axial positions, $Gr^* = 10^5, \alpha_R = 0.1$

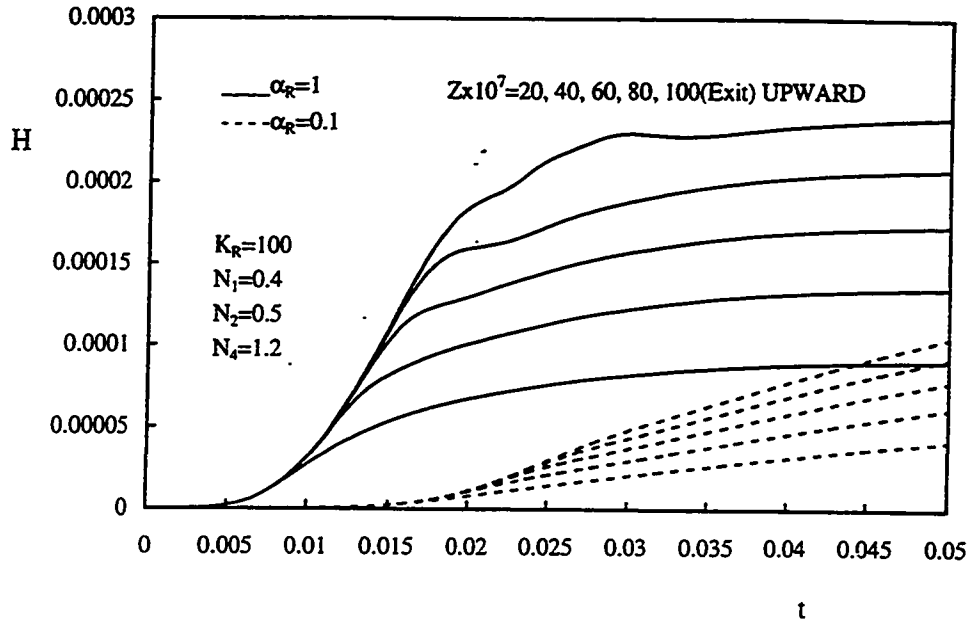

Figure 5.157: Effect of α_R on the development with time of the heat absorbed at different axial positions, $Gr^* = 10^5, K_R = 100$

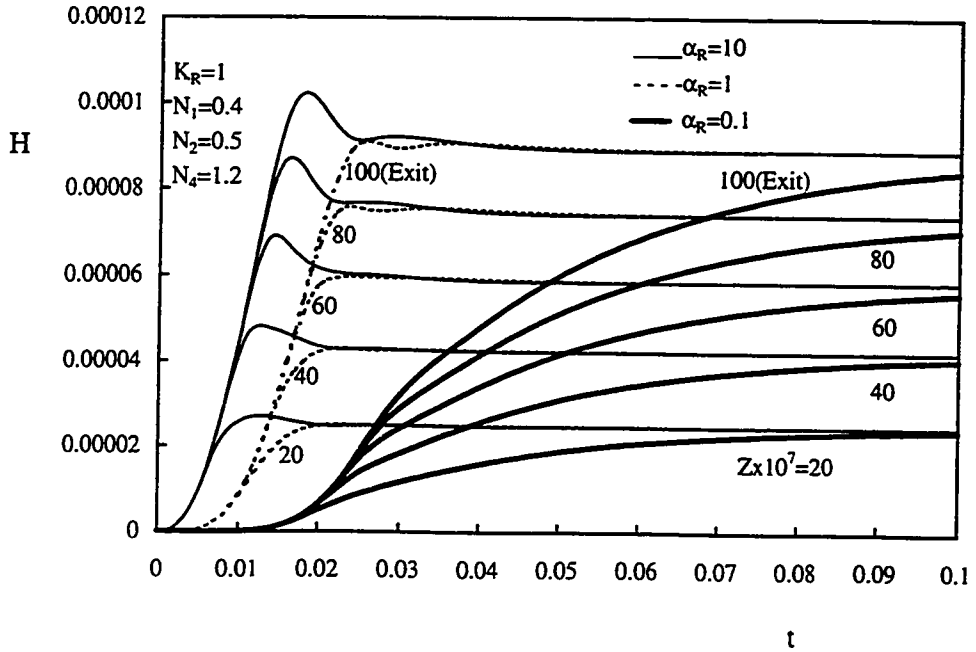

Figure 5.158: Effect of α_R on the development with time of the heat absorbed at different axial positions, $Gr^* = 10^5, K_R = 1$

5.3.8 Induced Flow Rate

Figures 5.159 through 5.172 constitute four groups of plots presenting the effect of K_R and α_R on the induced flow rate for four given values of Gr^*, viz., $Gr^* = 500, 10^3, 10^4$ *and* 10^5. Each of these groups consists of four figures. The first two figures in each group present the effect of K_R on the development with time of the induced flow rate at a given value of α_R while the two following figures present the effect of α_R on the induced flow rate for given values of K_R.

Figure 5.159 presents the effect of K_R on the development with time of the induced flow rate for an annulus of $Gr^* = 500$ and $\alpha_R = 1$. At early time, a small amount of heat is transferred radially through the heated wall to the fluid-annular gap. This creates a small buoyancy force which causes a small quantity of fluid to be sucked through the fluid-annular gap. As time elapses, more heat is transferred causing an increase in the buoyancy force and as a direct result, the induced flow rate increases. The process continues in the transient mode until it achieves the steady-sate conditions. It can be seen from Fig. 5.159 that, for a given α_R, increasing K_R causes an increase in the amount of the induced flow rate. In fact, as $K_R = \frac{K_s}{K_f}$, the increase in the magnitude of K_R means an increase in the thermal conductivity of the solid wall material. Hence, increasing K_R results in an increase in the rate of heat transfer through the heated wall to the fluid-annular gap. Consequently, the buoyancy force increases causing more fluid to be sucked. Moreover, it is easily observed that each of the flow rate profiles increases to a maximum value and then decreases

to its steady-sate value. This is attributed to the temperature overshoot phenomenon that has been discussed before.

For another value of α_R, namely, $\alpha_R = 0.1$, Fig. 5.160 presents the effect of K_R on the development with time of the induced flow rate. Comparing Figs. 5.159 and 5.160, it can be seen that increasing α_R increases the induced flow rate. This is explained in details hereinafter.

For $K_R = 100$ and 1, respectively, Figs. 5.161 and 5.162 present the effect of α_R on the development with time of the induced flow rate for the same value of Gr^*. It can be seen from these two figures that, for given time less than the steady-state value, increasing α_R causes generally an increase in the amount of the induced flow rate. This is attributed, as mentioned before, to the increase in the amount of heat transfer to the fluid annular-gap compared with that absorbed by the wall material. However, Fig. 5.161 shows that for $\alpha_R = 1000$, the induced flow rate has a value close to that corresponding to $\alpha_R = \infty$ for which the wall thermal resistance is neglected. Thus, for an annulus of the same value of Gr^* with negligible thermal resistance, the results of the present case($K_R = 100$ and $\alpha_R = 1000$) can be used with a maximum error of 1.35%.

For another value of Gr^*, namely, $Gr^* = 10^3$, Figures 5.163 through 5.166 show the effect of K_R and α_R on the development with time of the induced flow rate while such effect is presented in Figs. 5.167 through 5.170 and Figs. 5.171 through 5.174 for $Gr^* = 10^4$ and 10^5, respectively. It can be seen from this figures that they have the same qualitative characteristics as the figures belonging to $Gr^* = 500$. However, as Gr^* increases(shorter

annuli), the error percentage of the present results for $\alpha_R = 1000$ compared with that of the conventional case, in which the wall thermal resistance is neglected) increases. For $Gr^* = 10^3$, the error is 1.95% while for $Gr^* = 2.35\%$.

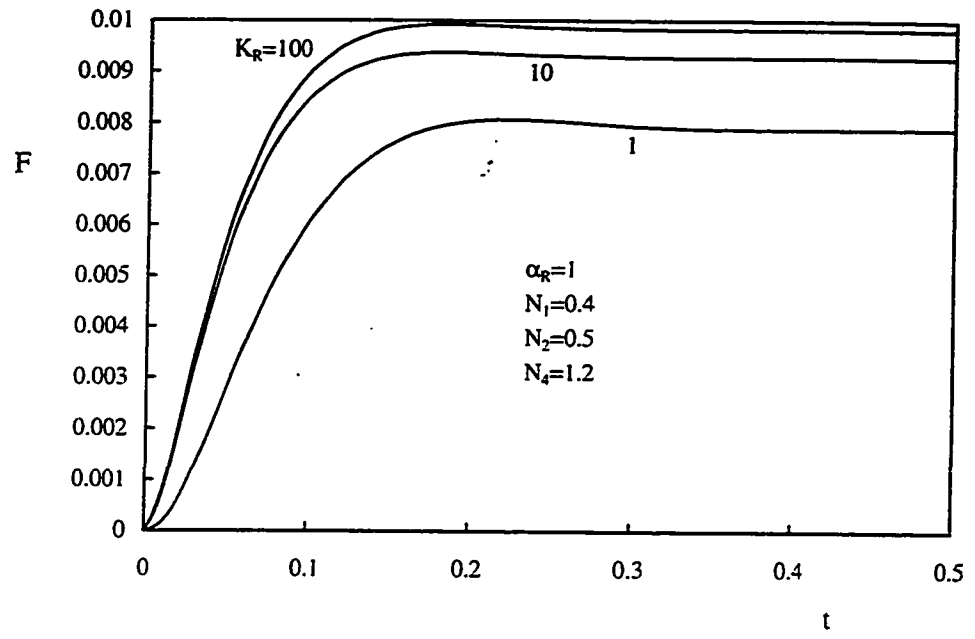

Figure 5.159: Effect of K_R on the induced flow rate, $Gr^* = 500, \alpha_R = 1$

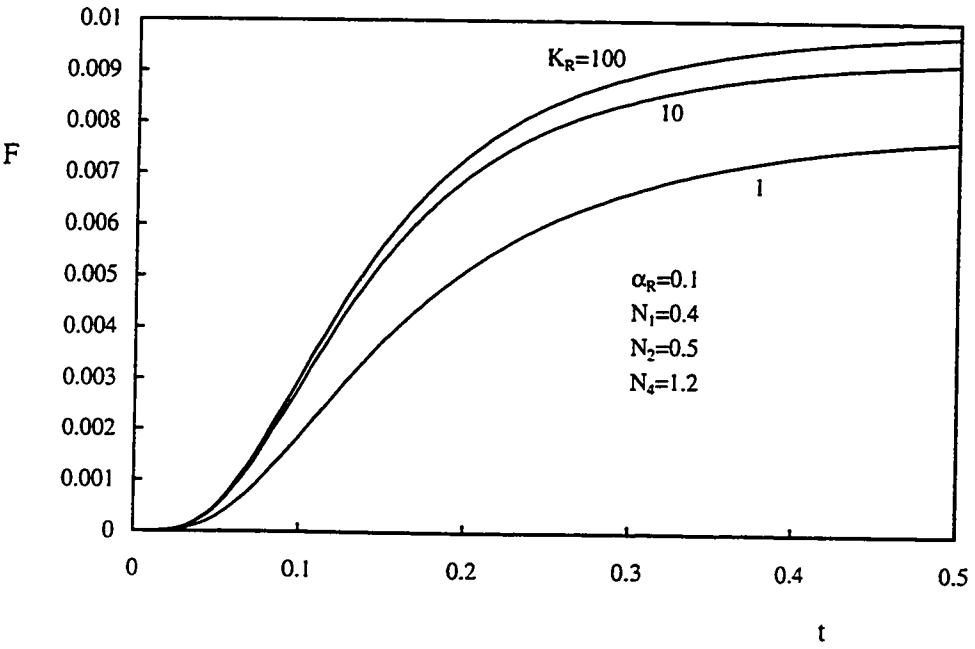

Figure 5.160: Effect of K_R on the induced flow rate, $Gr^* = 500, \alpha_R = 0.1$

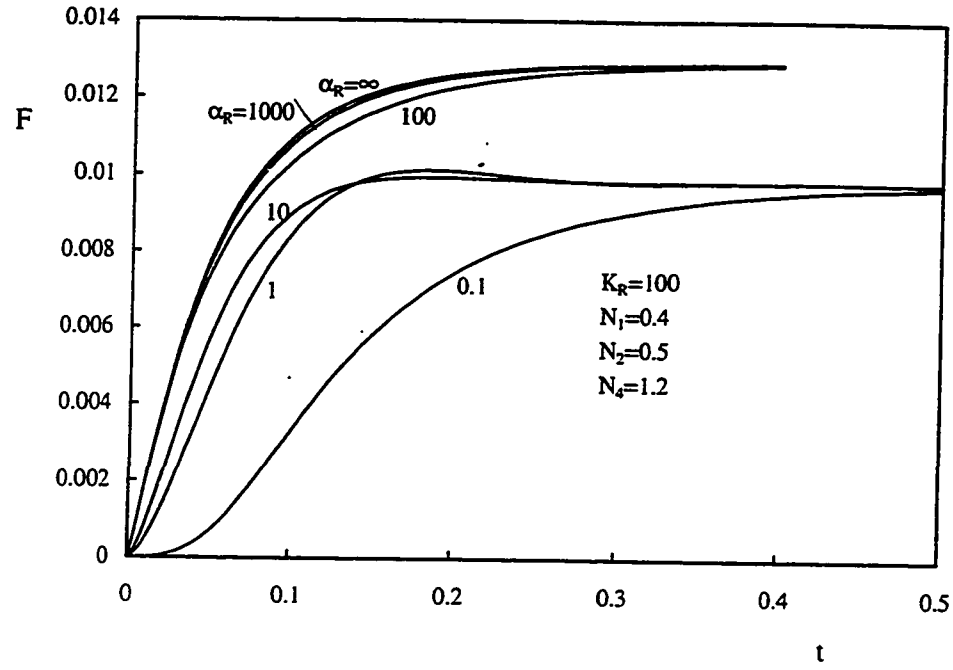

Figure 5.161: Effect of α_R on the induced flow rate, $Gr^* = 500, K_R = 100$

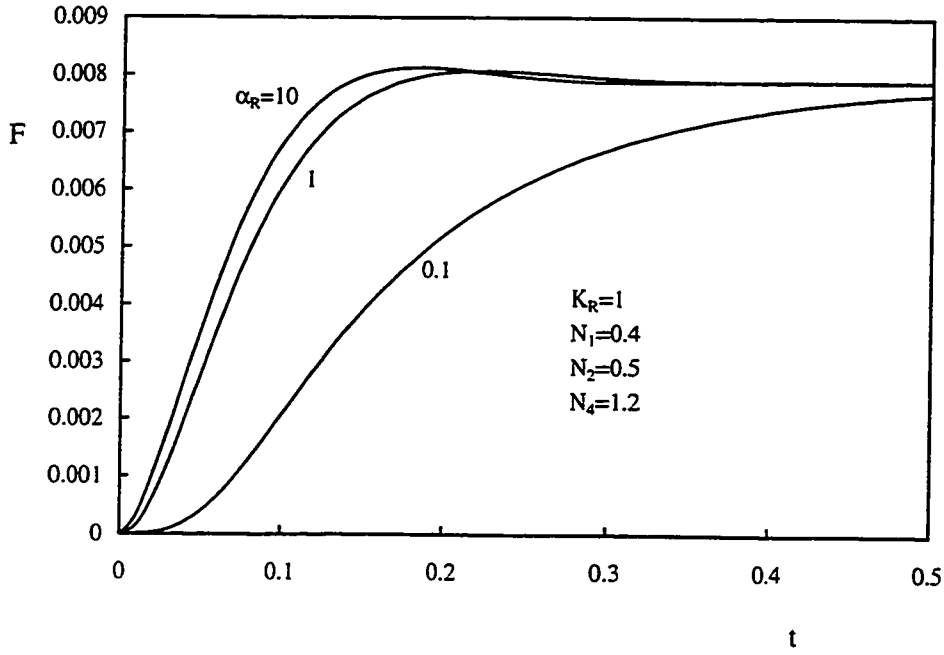

Figure 5.162: Effect of α_R on the induced flow rate, $Gr^* = 500, K_R = 1$

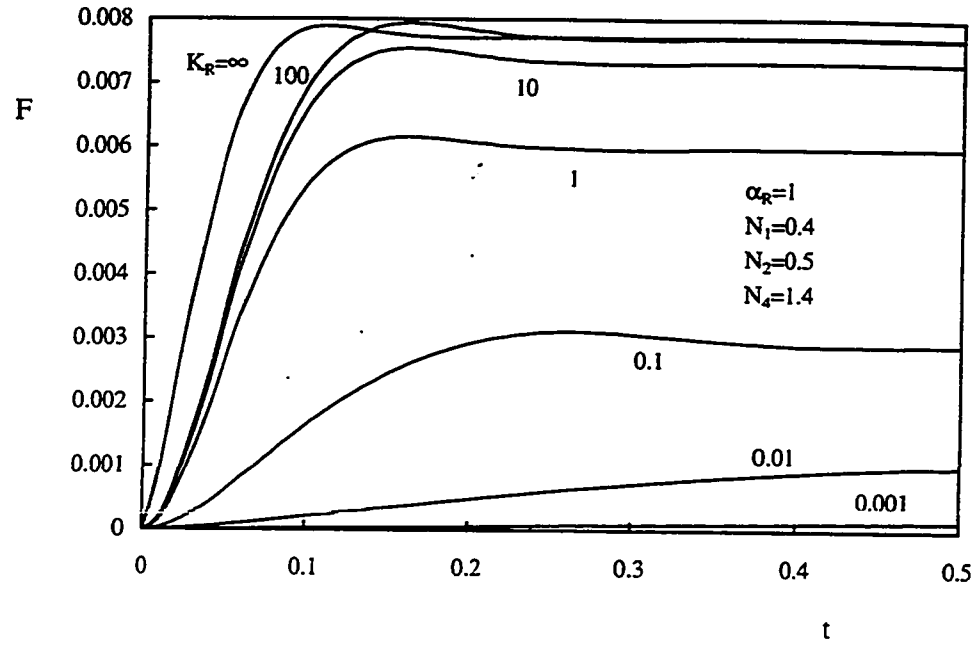

Figure 5.163: Effect of K_R on the induced flow rate, $Gr^* = 10^3, \alpha_R = 1$

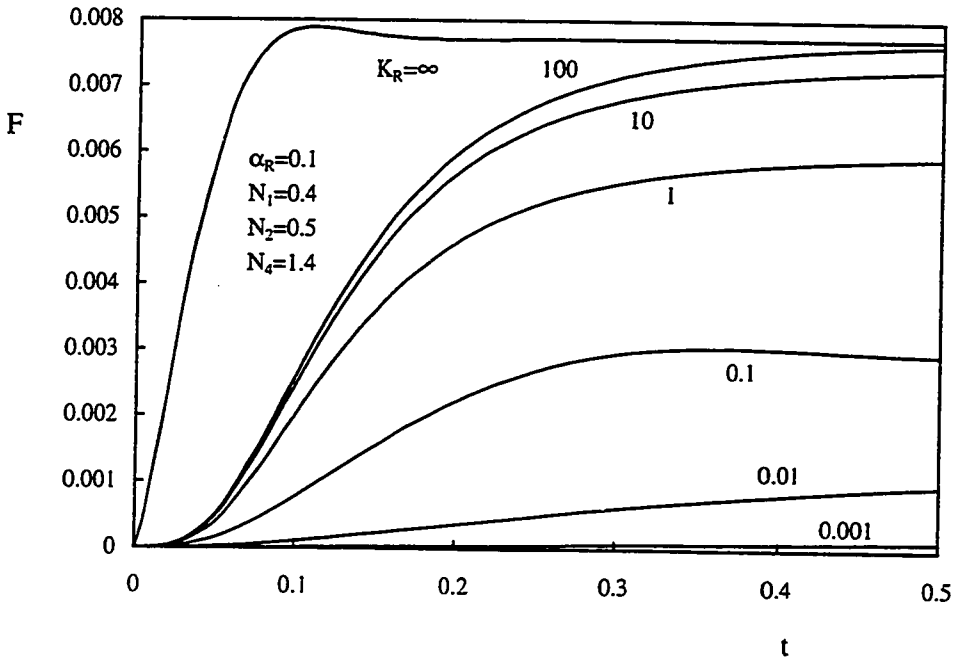

Figure 5.164: Effect of K_R on the induced flow rate, $Gr^* = 10^3, \alpha_R = 0.1$

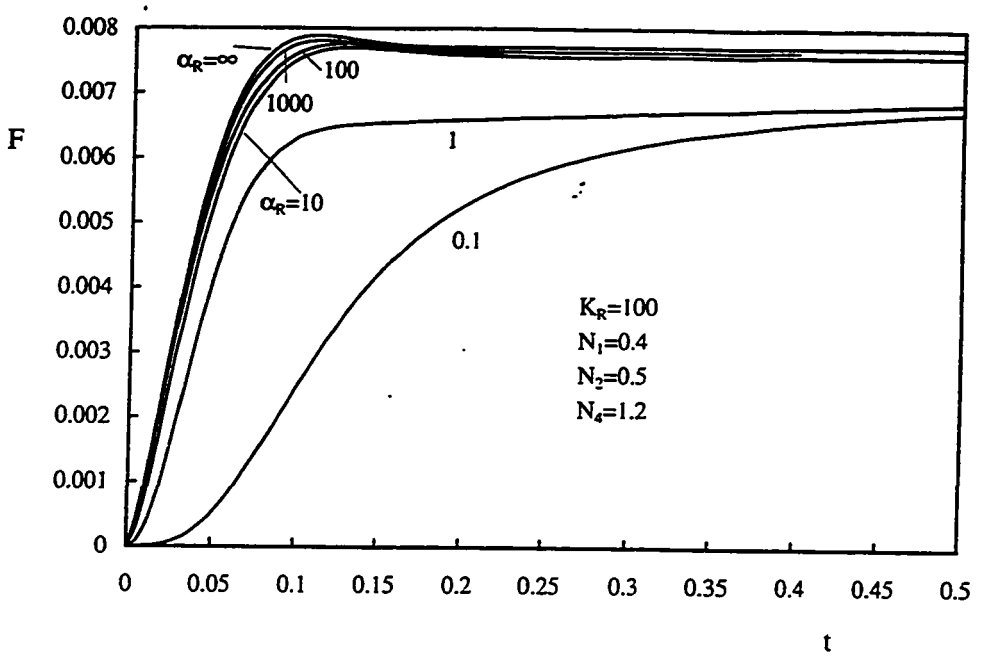

Figure 5.165: Effect of α_R on the induced flow rate, $Gr^* = 10^3, K_R = 100$

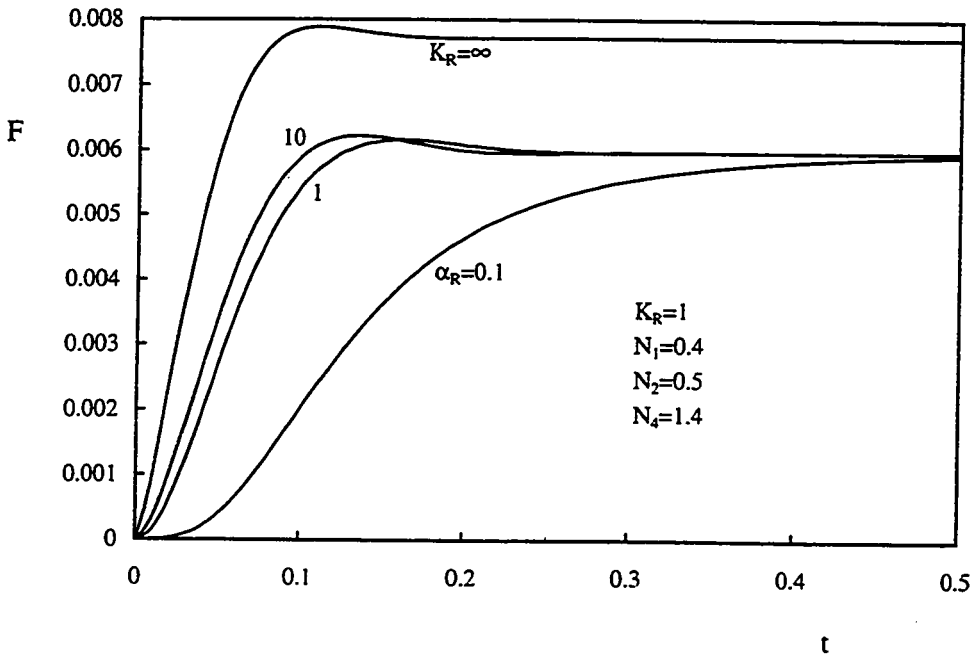

Figure 5.166: Effect of α_R on the induced flow rate, $Gr^* = 10^3, K_R = 1$

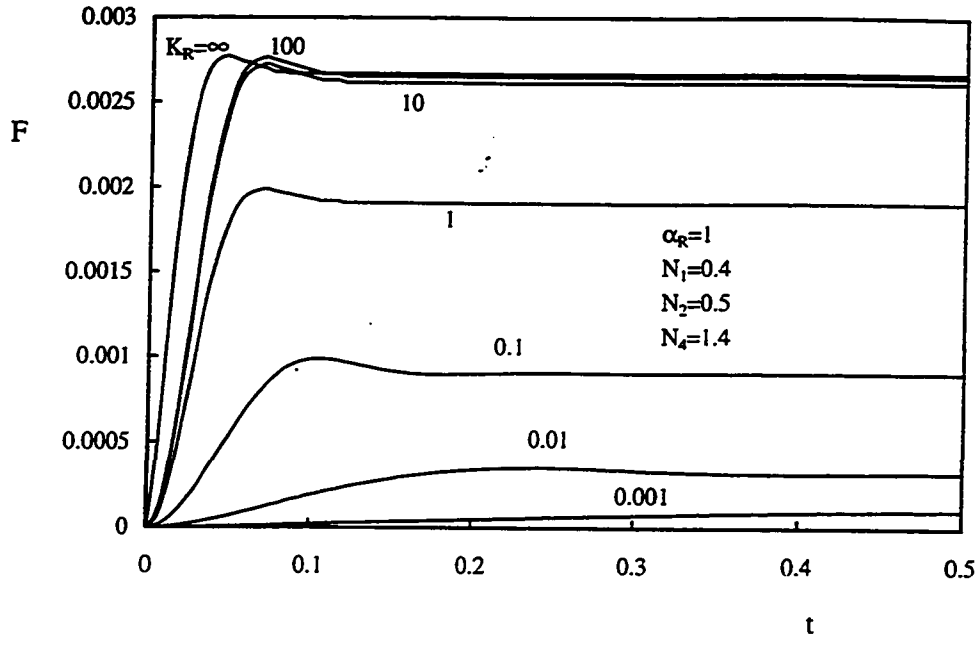

Figure 5.167: Effect of K_R on the indued flow rate, $Gr^* = 10^4, \alpha_R = 1$

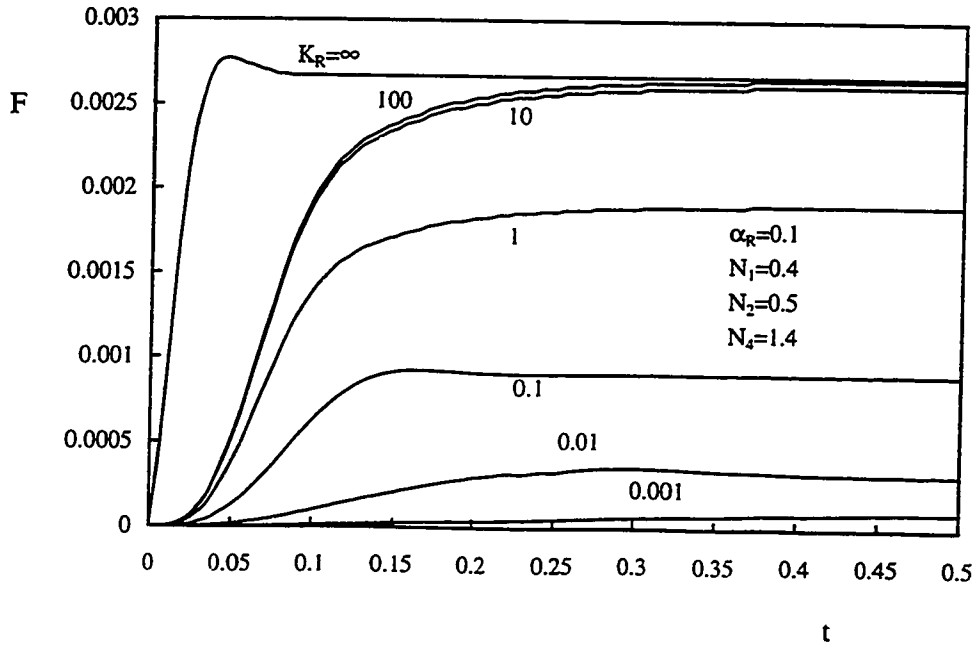

Figure 5.168: Effect of K_R on the induced flow rate, $Gr^* = 10^4, \alpha_R = 0.1$

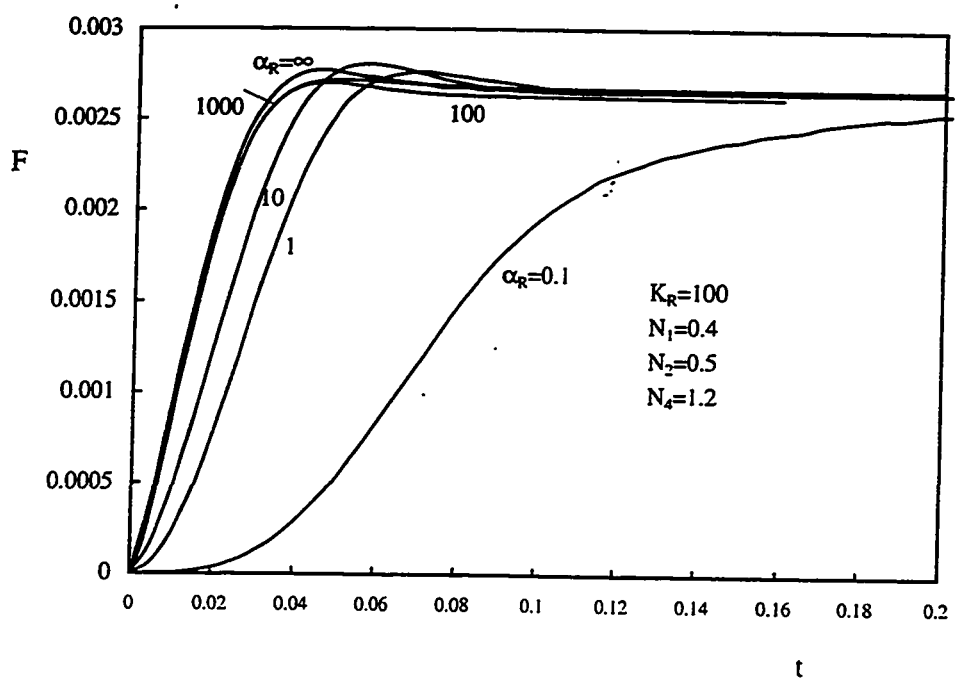

Figure 5.169: Effect of α_R on the induced flow rate, $Gr^* = 10^4, K_R = 100$

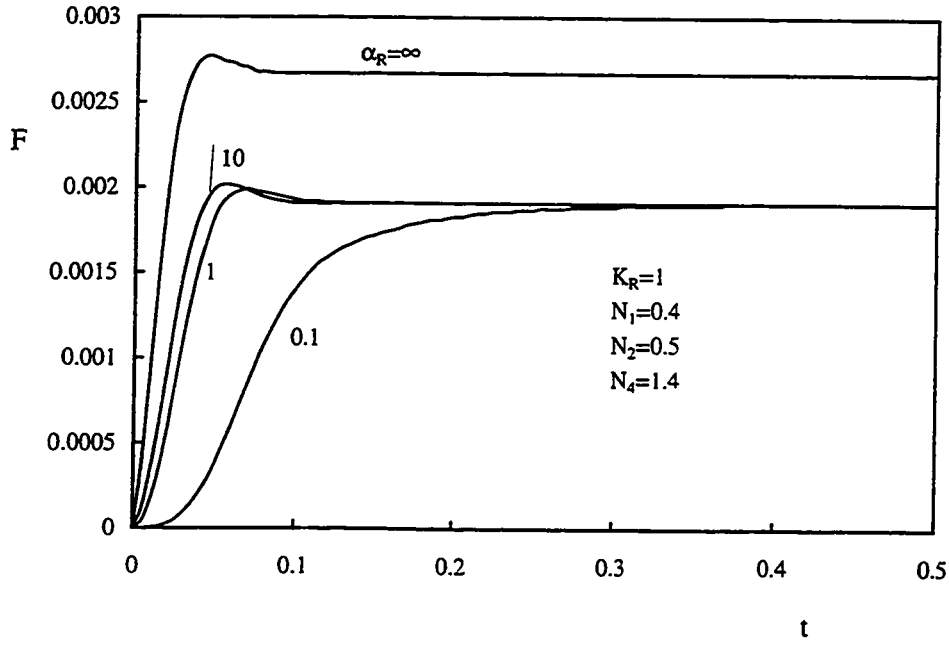

Figure 5.170: Effect of α_R on the induced flow rate, $Gr^* = 10^4, K_R = 1$

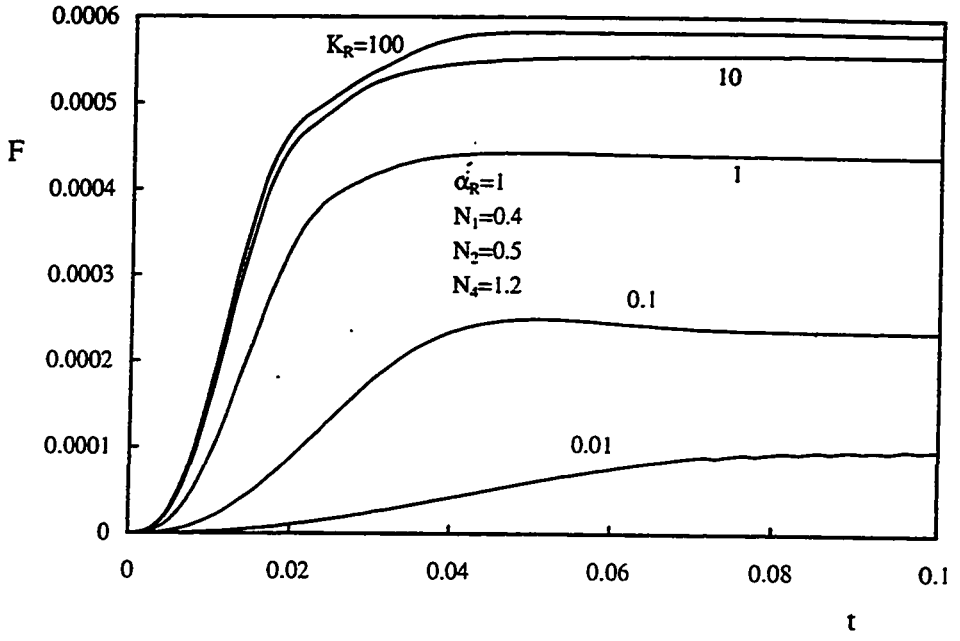

Figure 5.171: Effect of K_R on the induced flow rate, $Gr^* = 10^5, \alpha_R = 1$

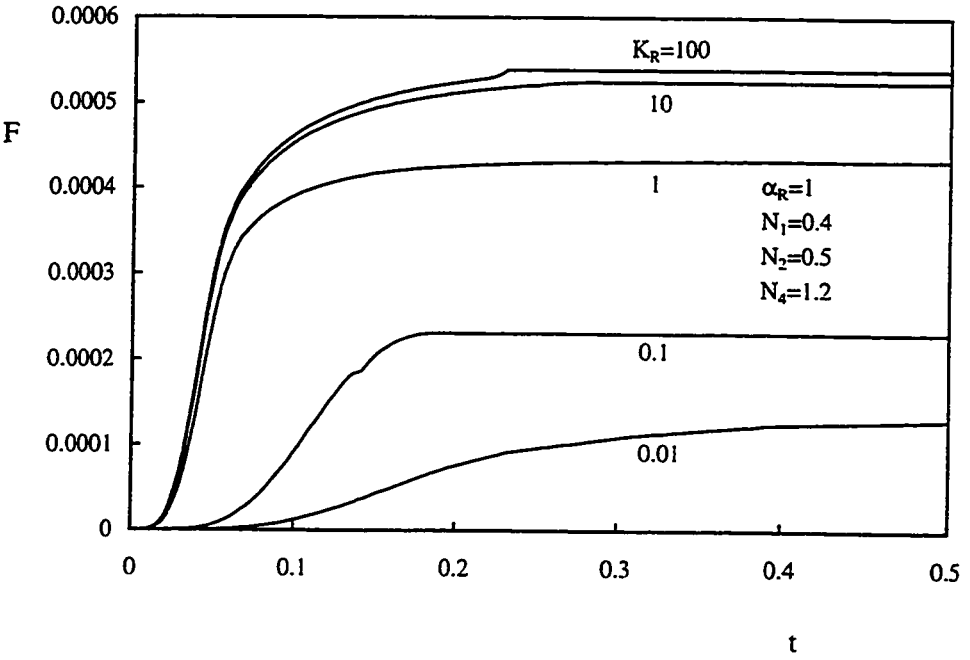

Figure 5.172: Effect of K_R on the induced flow rate, $Gr^* = 10^5, \alpha_R = 0.1$

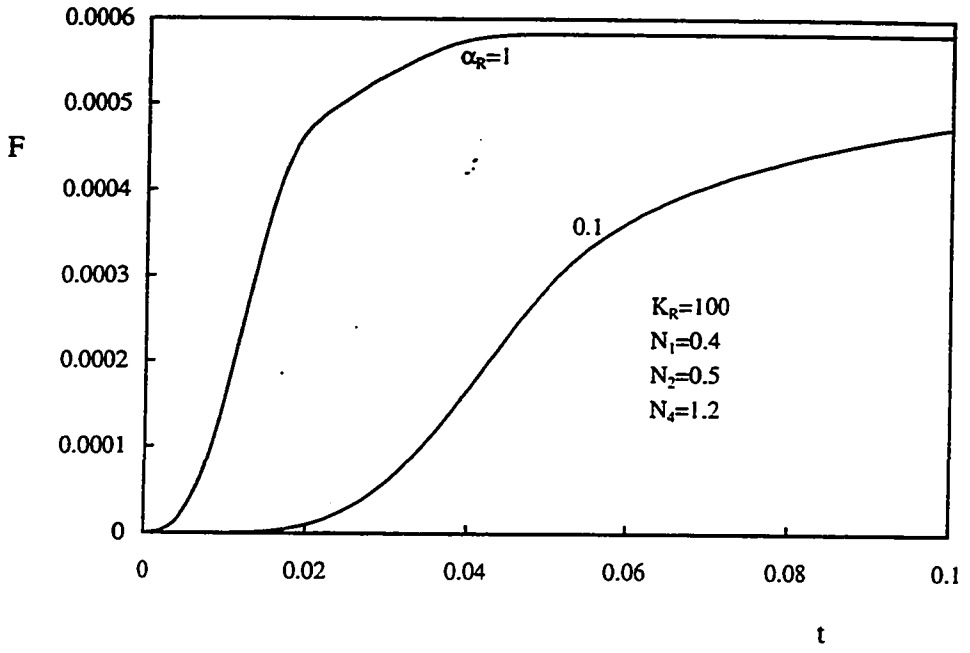

Figure 5.173: Effect of α_R on the induced flow rate, $Gr^* = 10^5$, $K_R = 100$

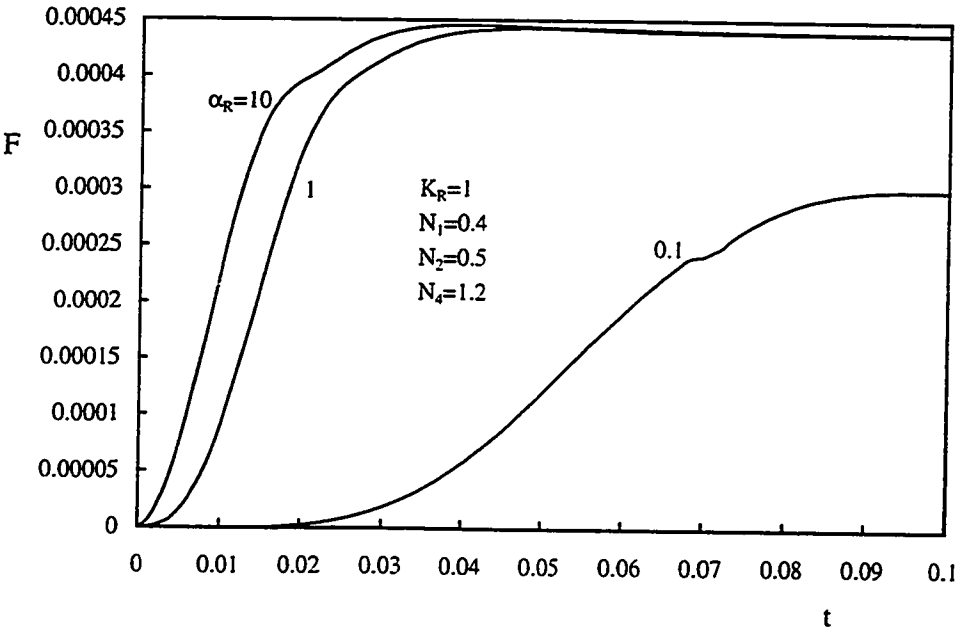

Figure 5.174: Effect of α_R on the induced flow rate, $Gr^* = 10^5$, $K_R = 1$

5.3.9 Steady-State Time

Table 5.1 presents the effects of both K_R and α_R on the time required to reach the steady-state conditions for the four selected values of Gr^*. It is seen from this table that, for given values of K_R and α_R, the steady-state time increases with the decrease in Gr^*. This is because as Gr^* decreases, the annulus height increases. Hence, the time required to reach the steady-state conditions increases. Moreover, for a given value of Gr^*, the steady-state time decreases with the increase in K_R(for a given α_R) and α_R(for a given K_R). This can be attributed to the increase in the rate of heat transferred to the fluid-annular gap through the heated wall with the increase in the values of K_R and α_R. This causes the buoyancy force to develop faster with time.

Gr^*	α_R	K_R		
		100	10	1
500	10	0.280	0.305	0.345
	1	0.301	0.323	0.371
1000	10	0.204	0.231	0.250
	1	0.221	0.252	0.271
10^4	10	0.083	0.103	0.113
	1	0.101	0.111	0.123
	0.1	0.453	0.461	0.522
10^5	10	*	*	0.061
	1	0.051	0.056	0.066
	0.1	0.231	0.252	0.302

TABLE 5.1: Effect of K_R and α_R on the time required to reach the steady-state conditions for different values of Gr^*, K_R and α_R

(*) means numerical instability occurred due to existence of flow reversal

CHAPTER 6

RESULTS OF THE STEADY-STATE CASE

6.1 INTRODUCTION

In this chapter, the physical steady characteristics of the induced flow and the most important pertinent engineering parameters are presented. The numerical solutions were carried out after choosing the controlling parameters Pr, N_1, N_2, N_3, N_4, and K_R. The computations were carried out for only one value of Prandtl number, namely, $\mathrm{Pr} = 0.7$, in a fluid annulus of radius ratio $N_2 = 0.5$, having solid boundaries of $N_1 = 0.4$, and $N_4 = 1.2$. The fluid annulus radius ratio $N_2 = 0.5$ was chosen as it represents a typical annular geometry with its value of 0.5 far enough from unity ($N_2 = 1$) which represents the case of parallel plate channels. Moreover, the value of $N_2 = 0.5$ is common between the present case and the conventional problem which has been solved by El-Shaarawi and Sarhan [23]; consequently, comparisons between the two cases can be made. Also, the solid boundaries radius ratios N_1 and N_4 were chosen to give wall thicknesses sufficient enough to clarify

the conjugate heat transfer effect. Thus the results to be presented in this chapter focus on the effects of both K_R on the induced flow characteristics and its engineering parameters.

6.2 Results

6.2.1 Axial Velocity

Figures 6.1 through 6.8 constitute four groups presenting the effect of K_R on the developing axial velocity profile for four given values of Gr^*, viz., $Gr^* = 500, 10^3, 10^4$ *and* 10^5. Each group consists of two figures, each figure presents the effect of K_R on the developing axial velocity profile. For a given $Gr^* = 500$, Fig. 6.1 shows that the inlet uniform velocity profile is changing as the flow moves upward through the annulus into a profile similar to the fully-developed one. In fact, small values of Gr^* indicate long annuli with small hydraulic diameters and small temperature differences. Accordingly, for such annuli, the inlet flat velocity profile has enough distance to approach the fully-developed shape. Moreover, the increase in the value of K_R gives rise, at a given axial position, to the developing axial velocity component. As explained in the previous chapter, the increase in K_R means an increase in the rate of heat transferred through the heated thick wall to the fluid-annular gap. Hence, the buoyancy force increases resulting in an increase in the magnitude of the axial velocity component. With further increase in the value of K_R, Fig. 6.2 shows that the difference between two axial velocity profiles (corresponding

to two selected value of K_R), at a given position, becomes more pronounced. Indeed, with $K_R \geqslant 100$, the flow characteristics becomes nearer to the conventional case in which the wall thermal resistance is very small and hence its effect can be neglected. This latter case was investigated by El–Shaarawi and Sarhan [23]. A comparison, for the induced flow rate and some engineering parameters, between the case under consideration and the conventional case is presented at the end of this chapter.

Similar to Figs. 6.1 and 6.2, Figs. 6.3 and 6.4 present the effect of K_R on the developing axial velocity profile for $Gr^* = 10^3$ while such effect is shown in Figs. 6.5 and 6.6 and Figs. 6.7 and 6.8 for $Gr^* = 10^4$ and 10^5, respectively. It can be seen that Figs. 6.3 through 6.8 have the same general qualitative characteristics of Figs. 6.1 and 6.2 except that the developing velocity profiles have a peak shifted towards the heated wall. As mentioned in the previous chapter, large values of Gr^* represents short annuli with large hydraulic diameter and large temperature difference. Consequently, as can be seen from Figs. 6.7 and 6.8 (which are for $Gr^* = 10^5$), the inlet uniform velocity profile is changing as the flow moves upwards into a profile indicating remarkably high velocities near the heated wall. This type of velocity distribution is akin to that beside a single vertical flat plate in free convection. Moreover, the phenomenon of the flow reversal near the adiabatic wall is also pronounced.

Figures 6.9 through 6.12 present the effect of K_R on the exit and mid-height axial velocity profiles for the four given values of Gr^*, namely, $Gr^* = 500, 10^3, 10^4$ *and* 10^5, respectively. As can be seen from these four figures, the difference between the values of

the axial velocity component, for a given K_R, at the exit and the mid-height axial positions is small for small values of $Gr^*(\leq 1000)$. This means that, for small values of Gr^*, the developing flow at the mid-height position is very near to the fully-developed state. On the other hand, this difference increases as Gr^* increases. Moreover, the developing axial velocity profile, for large values of Gr^*, is still far from the shape of the fully-developed one. This means that the induced fluid erupts from the annulus without reaching the fully-developed state.

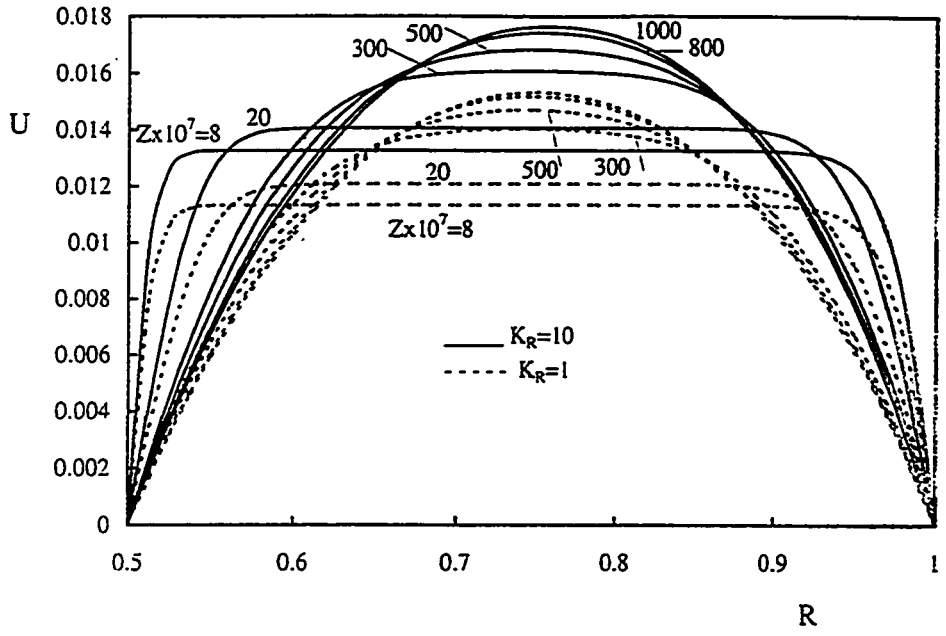

Figure 6.1: Effect of K_R on the developing axial velocity, $Gr^* = 500$, $K_R = 10\&1$

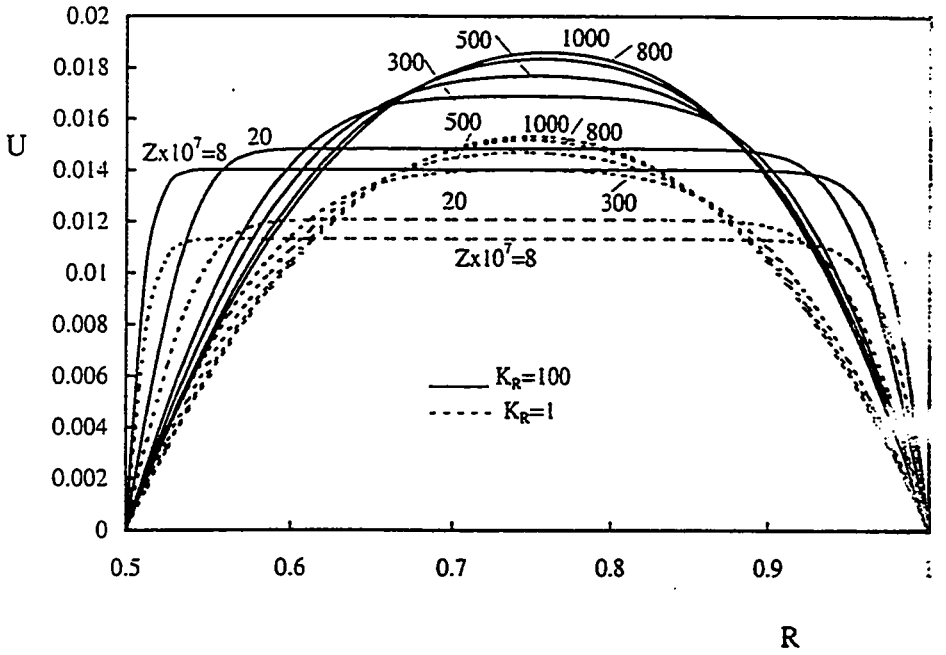

Figure 6.2: Effect of K_R on the developing axial velocity, $Gr^* = 500$, $K_R = 100, \&1$

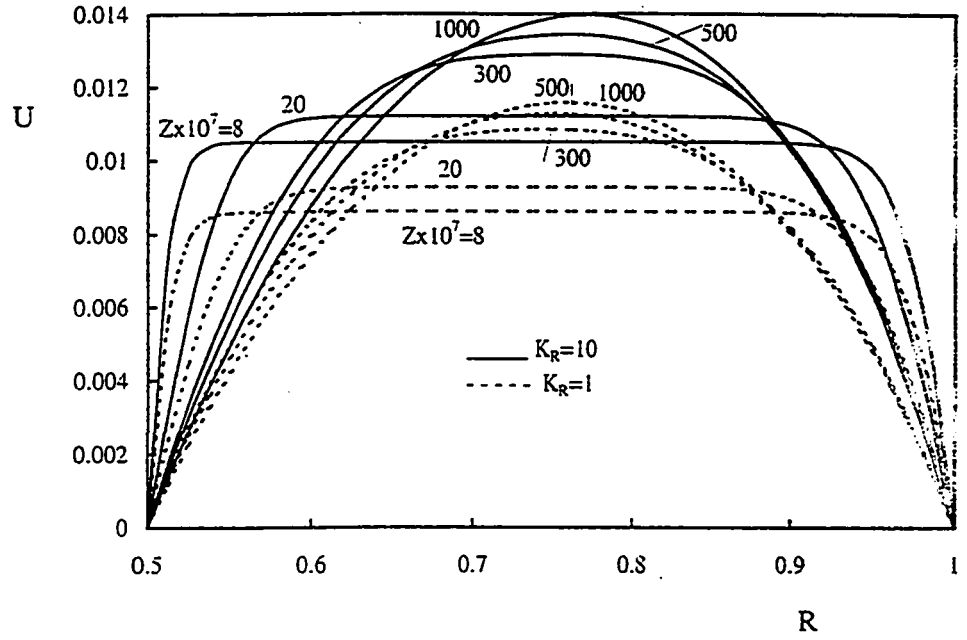

Figure 6.3: Effect of K_R on the developing axial velovity. $Gr^* = 10^3$. $K_R = 10\&1$

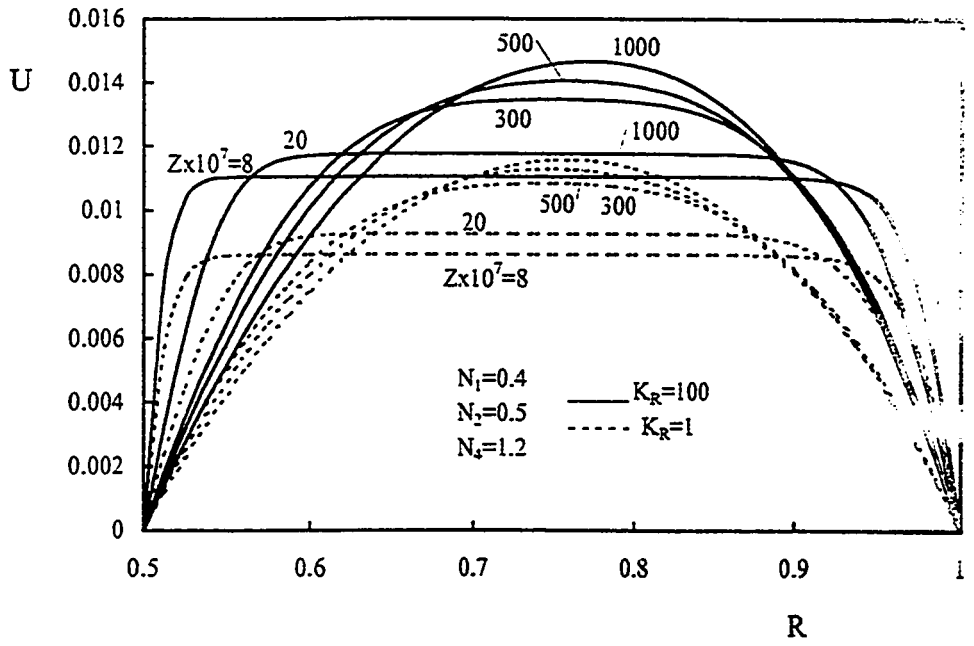

Figure 6.4: Effect of K_R on the developing axial velovity, $Gr^* = 10^3$. $K_R = 100\&1$

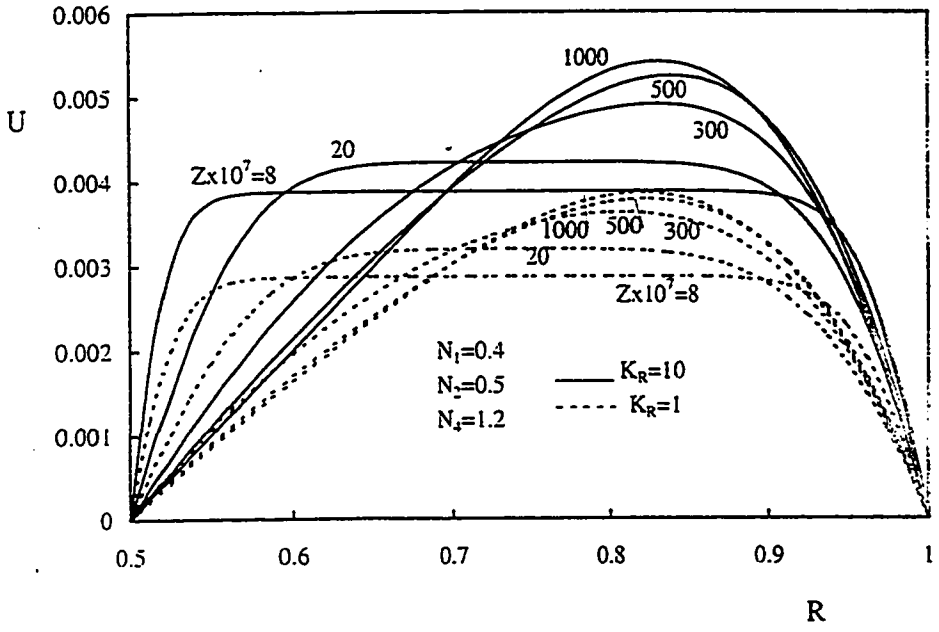

Figure 6.5: Effect of K_R on the developing axial velovity, $Gr^* = 10^4$, $K_R = 10\&1$

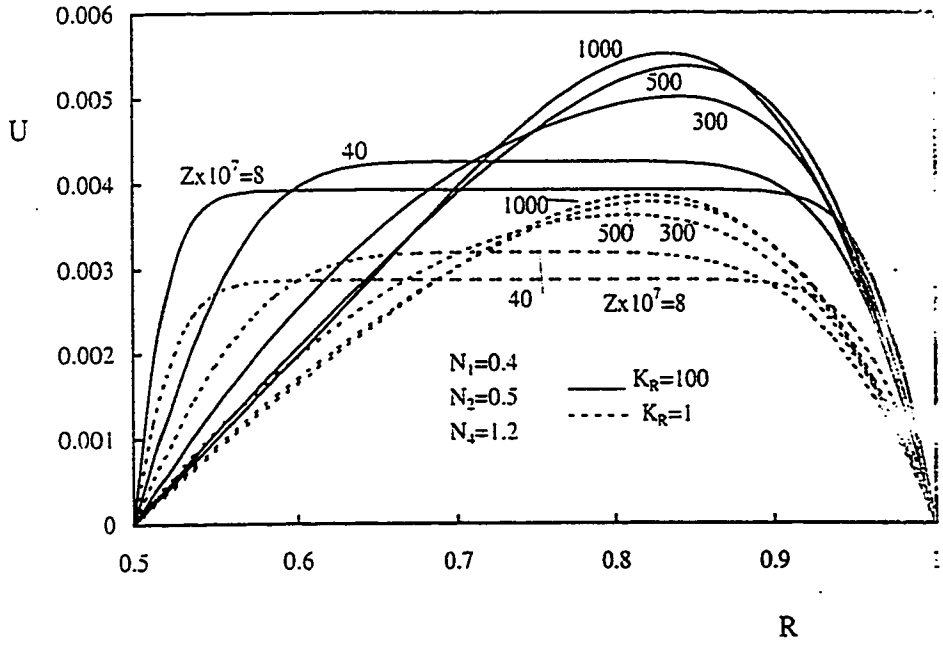

Figure 6.6: Effect of K_R on the developing axial velovity, $Gr^* = 10^4$, $K_R = 100\&1$

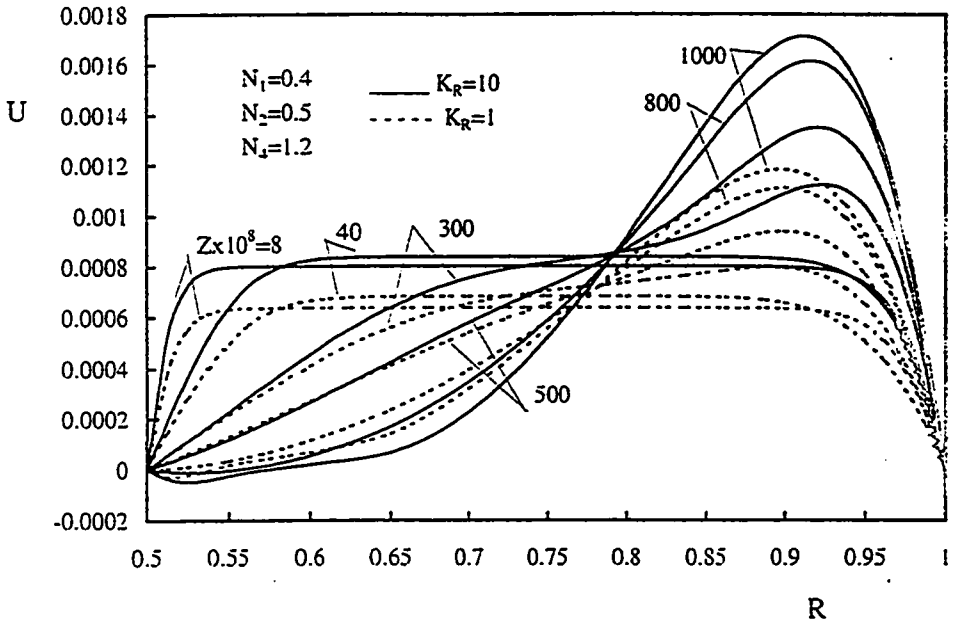

Figure 6.7: Effect of K_R on the developing axial velovity, $Gr^* = 10^5$, $K_R = 10\&1$

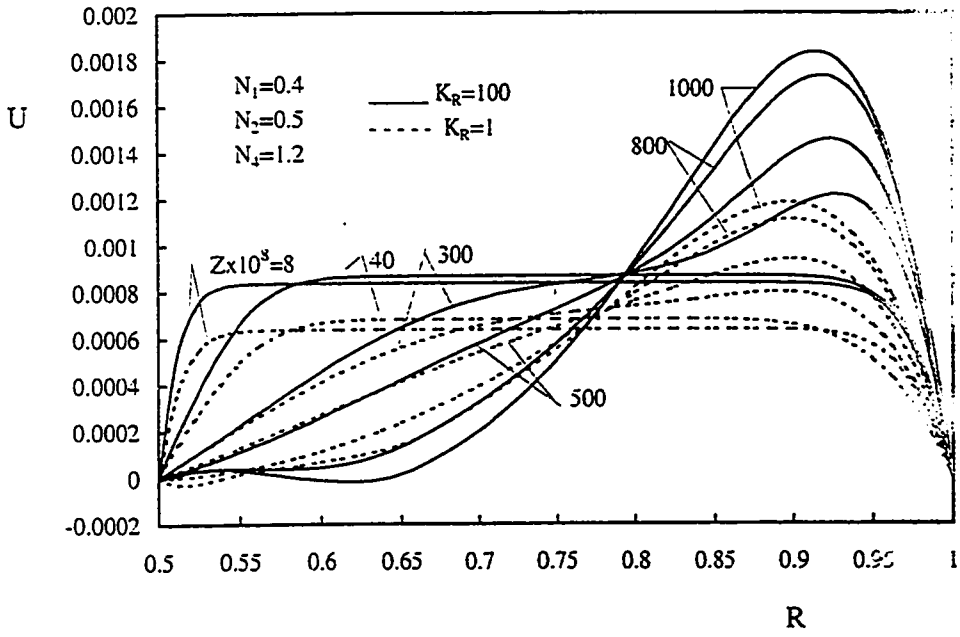

Figure 6.8: Effect of K_R on the developing axial velovity, $Gr^* = 10^5$, $K_R = 100\&1$

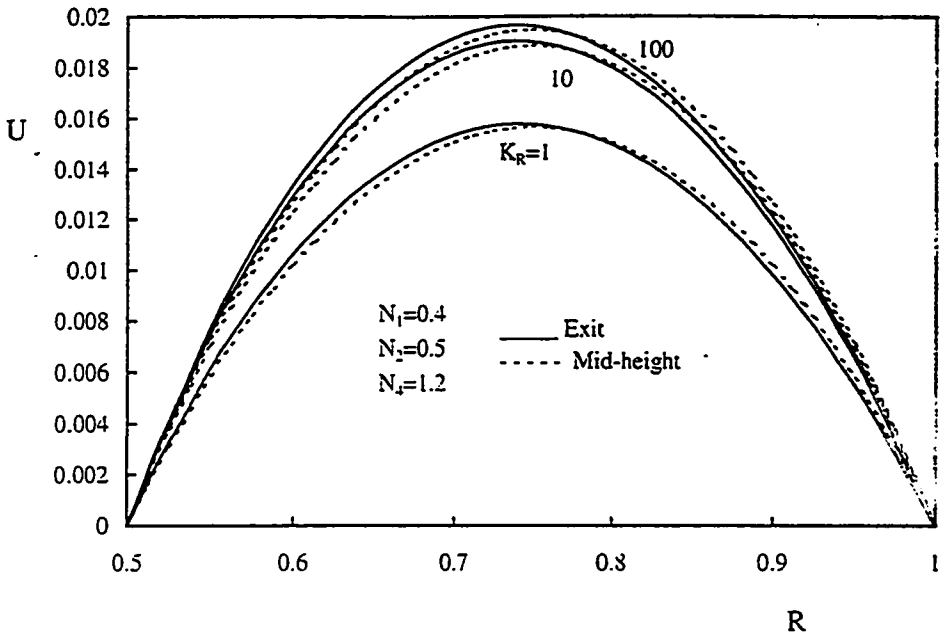

Figure 6.9: Effect of K_R on the axial velocity at the exit and the mid-height cross-sections, $Gr^* = 500$

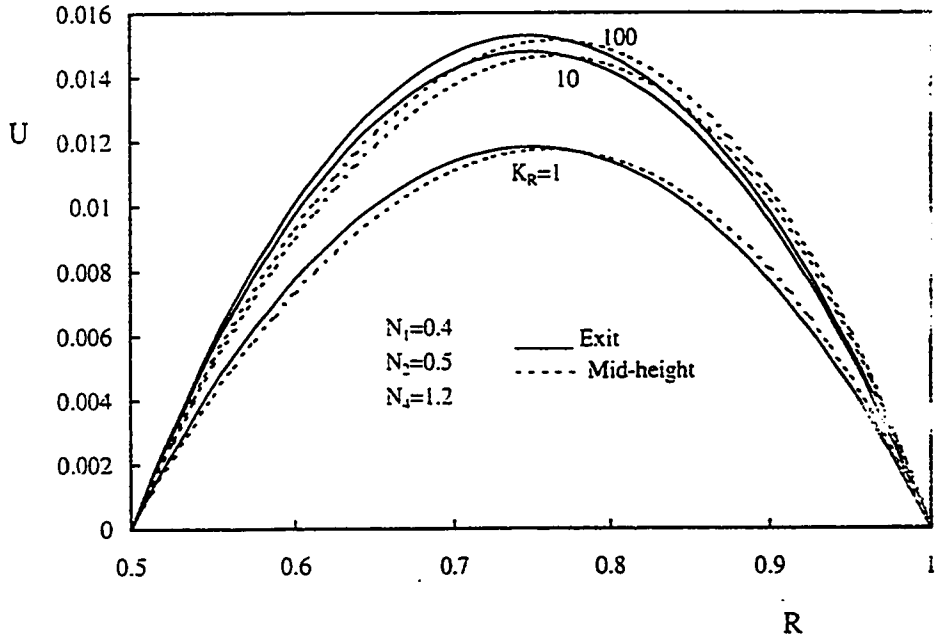

Figure 6.10: Effect of K_R on the axial velocity at the exit and the mid-height cross-sections, $Gr^* = 10^3$

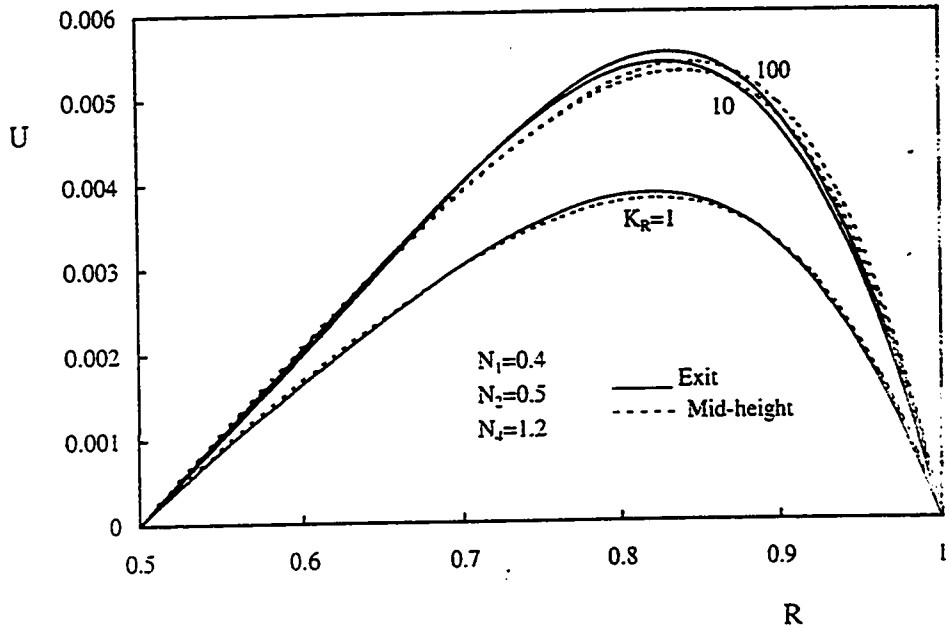

Figure 6.11: Effect of K_R on the axial velocity at the exit and the mid-height cross-sections, $Gr^* = 10^4$

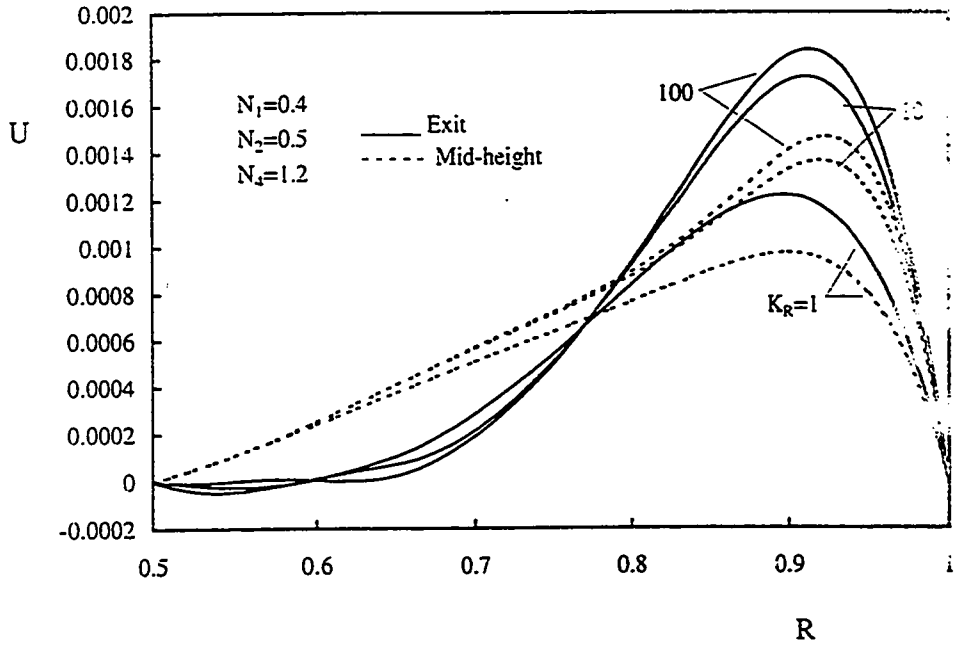

Figure 6.12: Effect of K_R on the axial velocity at the exit and the mid-height cross-sections, $Gr^* = 10^5$

6.2.2 Radial velocity

Figures 6.13 through 6.20 constitute four groups presenting the effect of K_R on the radial velocity profile as the flow develops through the annulus for four given values of $Gr^* = 500, 10^3, 10^4$ *and* 10^5, respectively. Each group consists of two figures and each figure presents the effect of K_R on the developing radial velocity profile. As can be seen from these figures, the heat transferred through the heated thick wall produces negative radial velocity near the heated outer wall. On the other hand, the positive axial velocity near the heated wall engenders a positive radial velocity(from the inner wall towards the outer wall). As can be seen from Fig. 6.13, the increase in K_R leads to an increase in the radial velocity component. In fact, increasing K_R results in an increase in the amount of the induced flow rate. Hence, this induced flow rate washes the heated wall with larger axial velocity which decreases the rate of axial growth of the boundary-layer thickness (as $\delta = \frac{1}{\sqrt{\mathrm{Re}}}$). However, to make up the induced flow near the heated outer wall, the positive radial velocity increases, at the same axial position, with the increase in K_R. .With further increase in K_R, the difference between the two radial velocity profiles, at a given axial position, becomes more pronounced, as shown in Fig. 6.14. Moreover, as Gr^* increases, this difference becomes more easily pronounced as for large values of Gr^*(short annuli) the flow erupts from the annuli exit without reaching the fully-developed state.

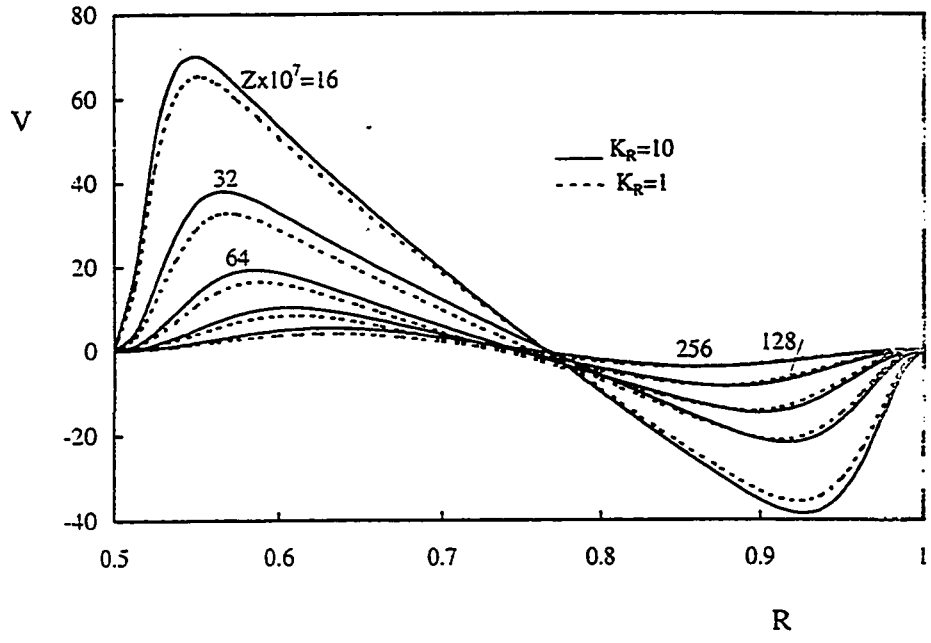

Figure 6.13: Effect of K_R on the developing radial velocity, $Gr^* = 500$, $K_R = 10\&1$

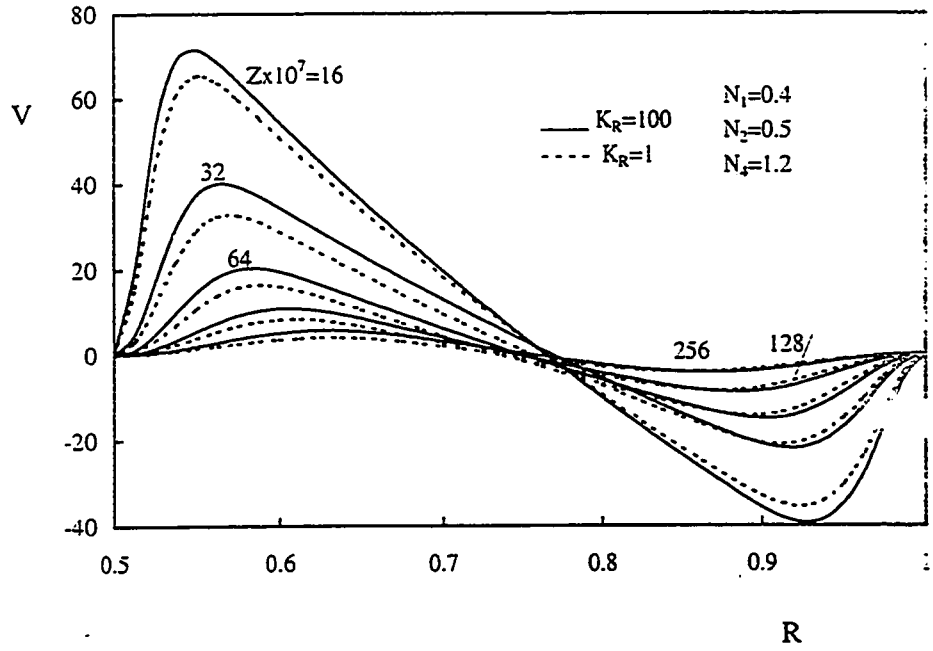

Figure 6.14: Effect of K_R on the developing radial velocity, $Gr^* = 500$, $K_R = 100\&1$

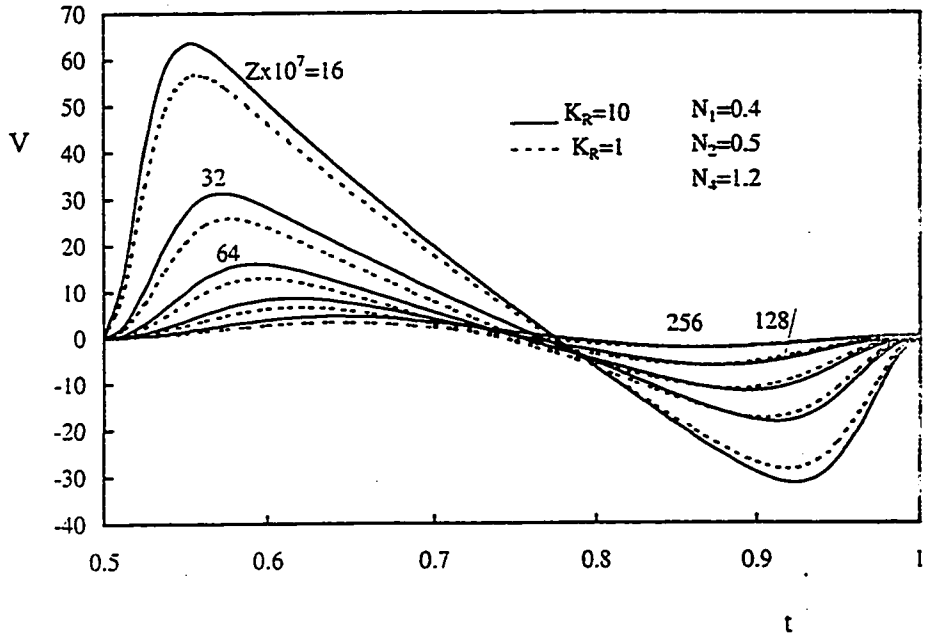

Figure 6.15: Effect of K_R on the developing radial velovity. $Gr^* = 10^3$, $K_R = 10\&1$

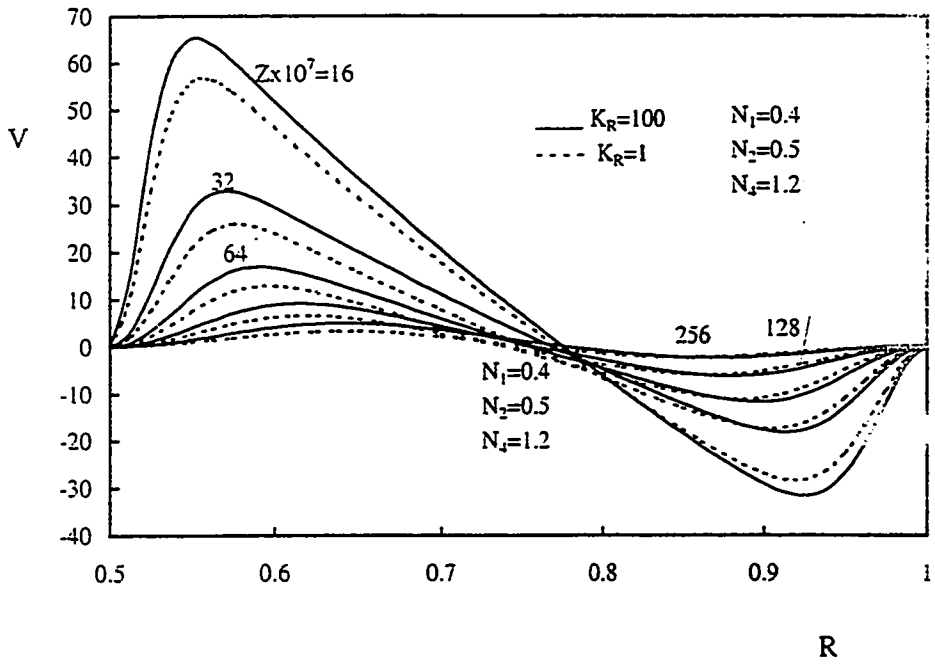

Figure 6.16: Effect of K_R on the developing radial velovity, $Gr^* = 10^3$, $K_R = 100\&1$

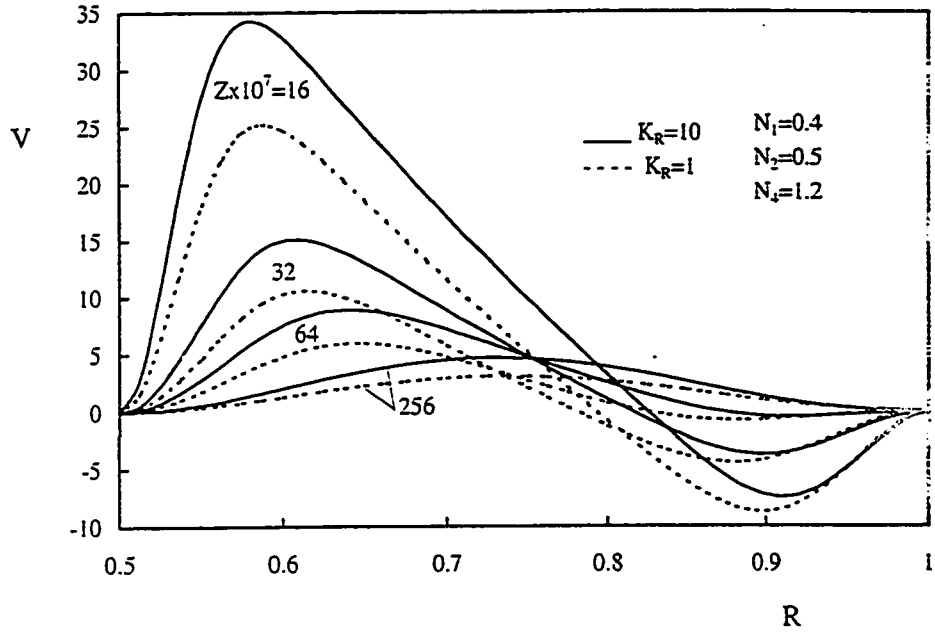

Figure 6.17: Effect of K_R on the developing radial velovity, $Gr^* = 10^4$, $K_R = 10\&1$

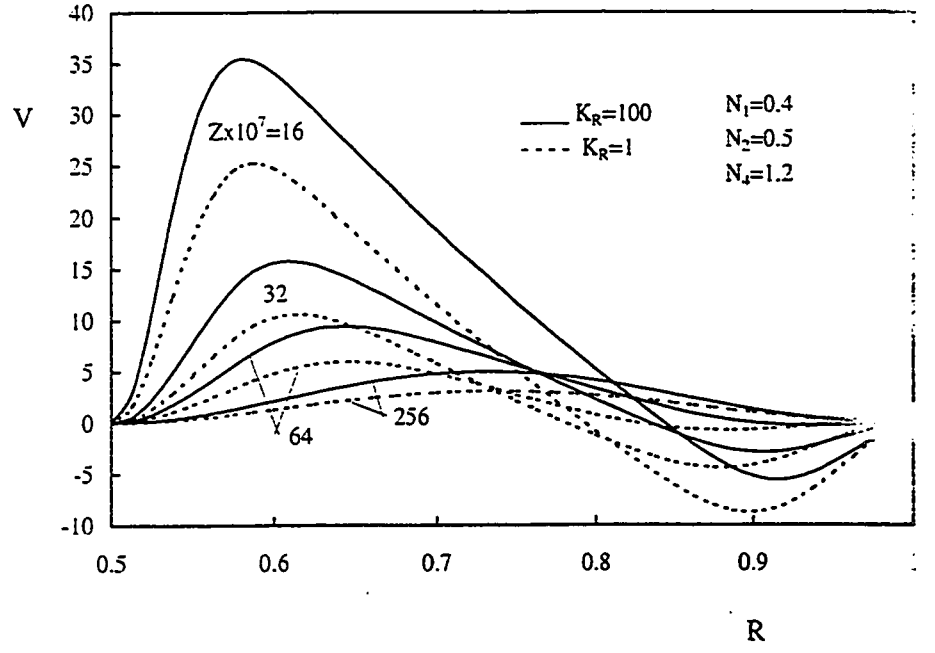

Figure 6.18: Effect of K_R on the developing radial velovity, $Gr^* = 10^4$, $K_R = 100\&1$

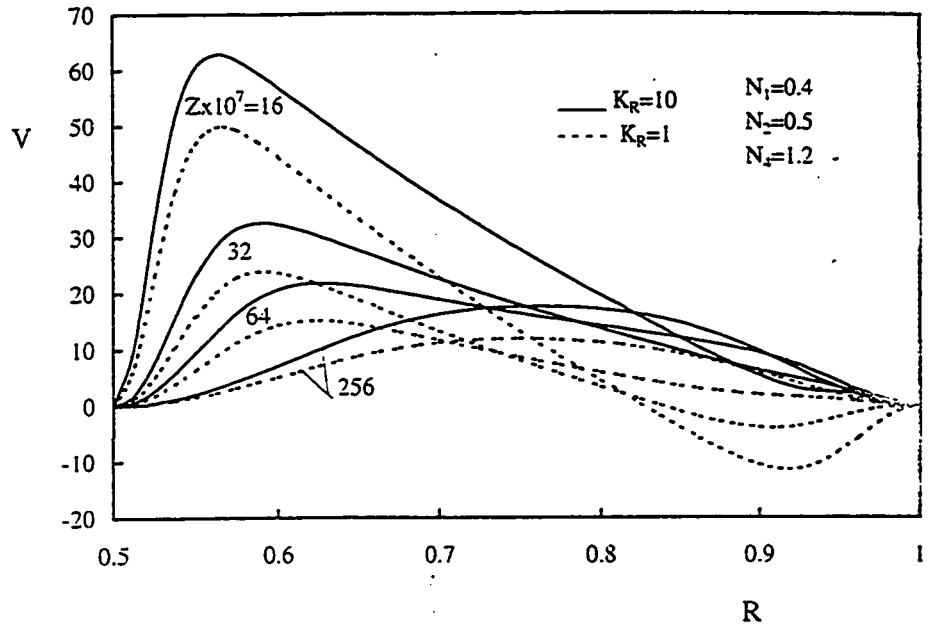

Figure 6.19: Effect of K_R on the developing radial velovity, $Gr^* = 10^5$, $K_R = 10\&1$

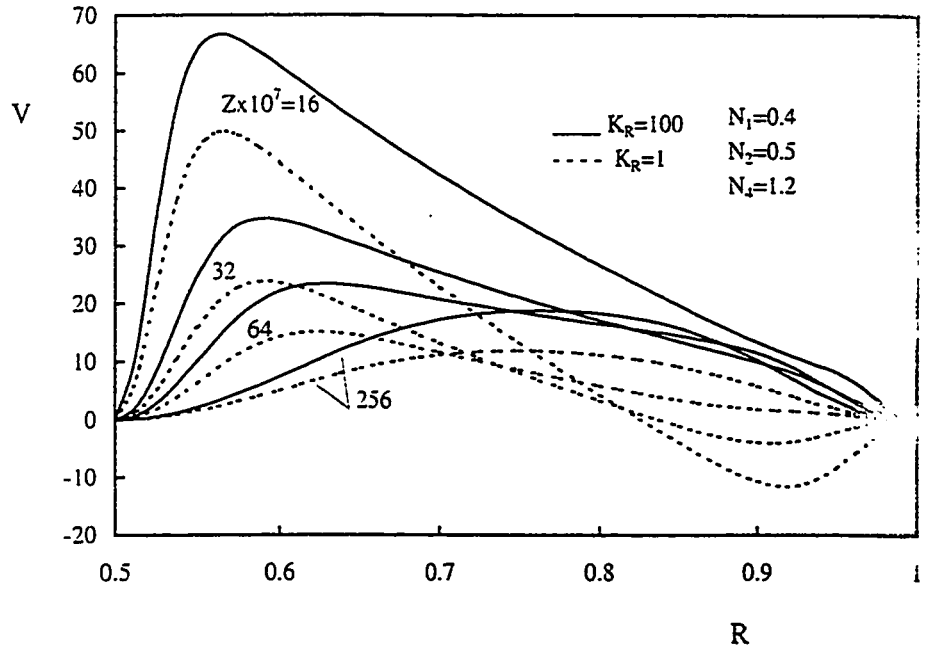

Figure 6.20: Effect of K_R on the developing radial velovity, $Gr^* = 10^5$, $K_R = 100\&1$

6.2.3 Temperature

Figures 6.21 through 6.28 constitute four groups presenting the effect of K_R on the radial temperature distribution for the four given values of Gr^*, viz., $Gr^* = 500, 10^3, 10^4$ *and* 10^5. Each group consists of two figures, each figure describes the temperature distribution across the annulus as the induced flow develops through the annulus. For a given $Gr^* = 500$, Fig. 6.21 shows that the induced fluid near the inlet cross-section started to feel the heat penetrated through the heated thick wall(the outer tube wall) to the fluid-annular gap. As the fluid moves upward, its temperature increases as it absorbs more heat. It is seen in Fig. 6.21 that the induced fluid has reached the exit cross-section of the annulus with temperature lower than the fully-developed value($\theta = 1$). This means that the flow erupts from the annulus without reaching the fully-developed state. Moreover, it is seen that the increase in K_R produces an increase in the temperature at a given axial position. In fact, the increase in K_R means an increase in the rate of heat transferred through the heated solid wall to the fluid region. Consequently, this results in an increase in the induced fluid which washes the heated wall with larger axial velocity. Hence, more heat is absorbed by the fluid as it moves upwards through the annulus. With further increase in K_R, the difference between the temperature profiles at a given location becomes more pronounced as can seen in Fig. 6.22.

Similar to Figs. 6.21 and 6.22, Figs. 6.23 and 6.24 present the effect of K_R on the radial temperature distribution as the flow develops through the annulus of $Gr^* = 10^3$ while such effect is shown in Figs. 6.25 and 6.26 and Figs. 6.27 and 6.28 for $Gr^* = 10^4$ and

10^5, respectively. It is seen that Figs. 6.23 through 6.28 have in general the same qualitative characteristics of Figs. 6.21 and 6.22 except that as Gr^* increases, the temperature decreases. This is because as Gr^* decreases, the annulus height increases causing more buoyancy or chimney effect with more fluid being sucked. Also, it is seen in Figs. 6.27 and 6.28 that the temperature has physically unrealistic values,at some axial positions, near the adiabatic wall. This is due to the existing of the flow reversal at that axial position.

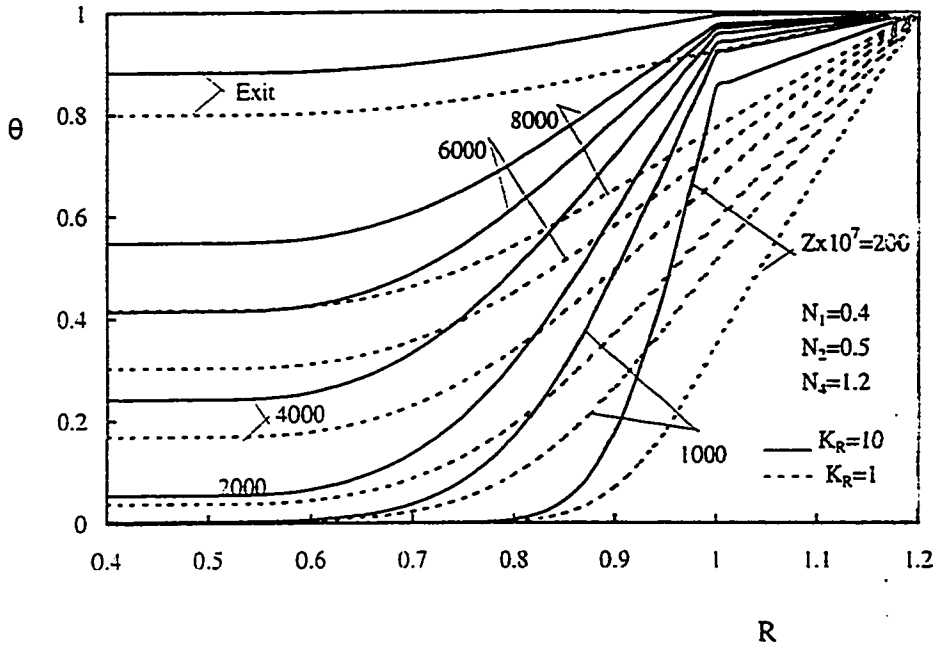

Figure 6.21: Effect of K_R on the temperature distribution at different axial positions, $Gr^* = 500, K_R = 10\&1$

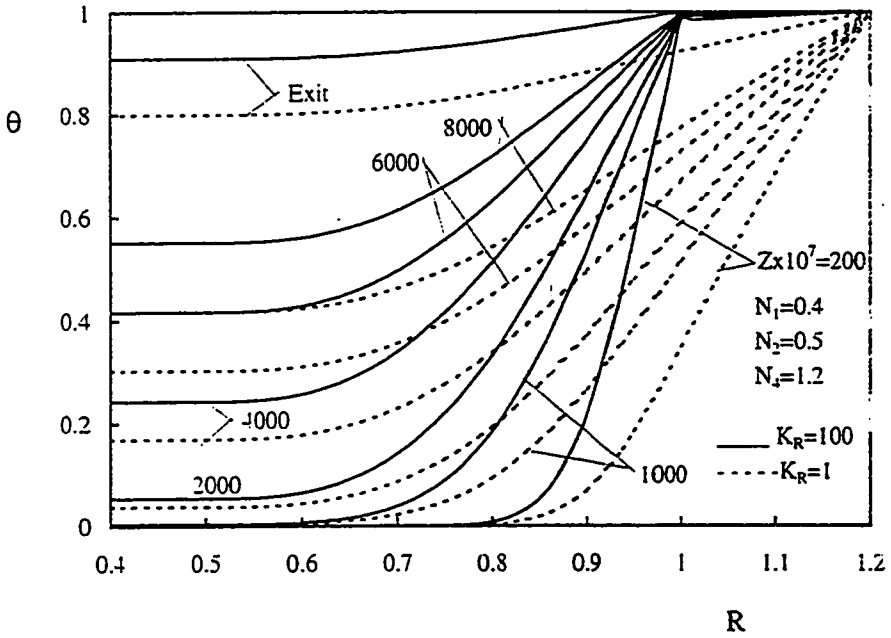

Figure 6.22: Effect of K_R on the temperature distribution at different axial positions, $Gr^* = 500, K_R = 100\&1$

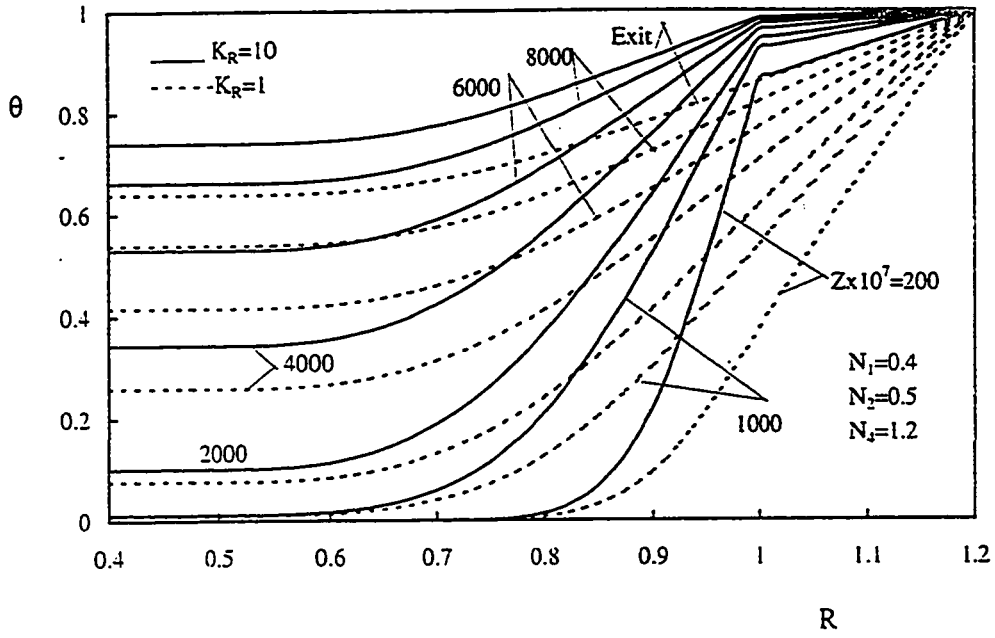

Figure 6.23: Effect of K_R on the temperature distribution at different axial positions, $Gr^* = 10^3, K_R = 10\&1$

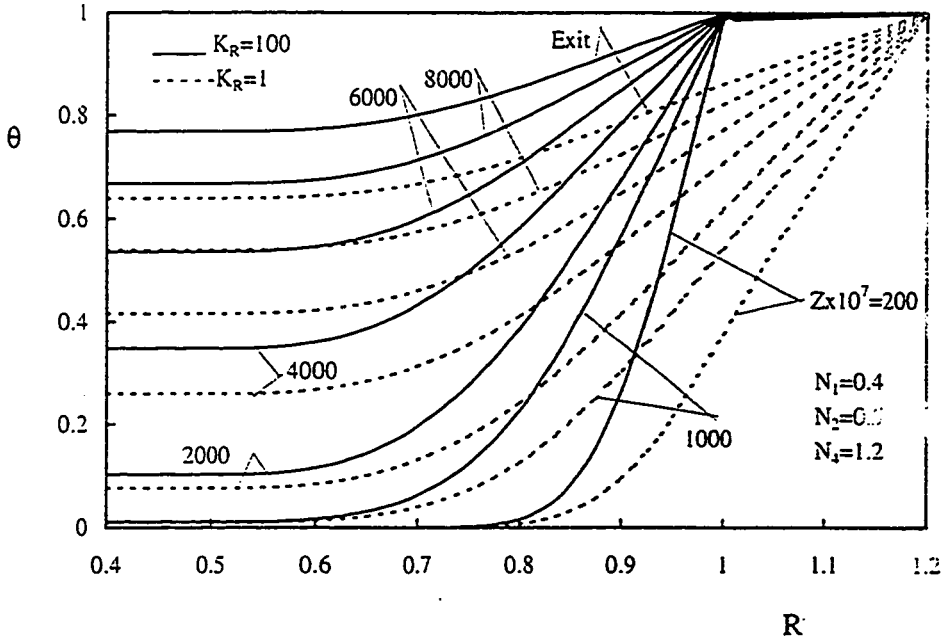

Figure 6.24: Effect of K_R on the temperature distribution at different axial positions, $Gr^* = 10^3, K_R = 100\&1$

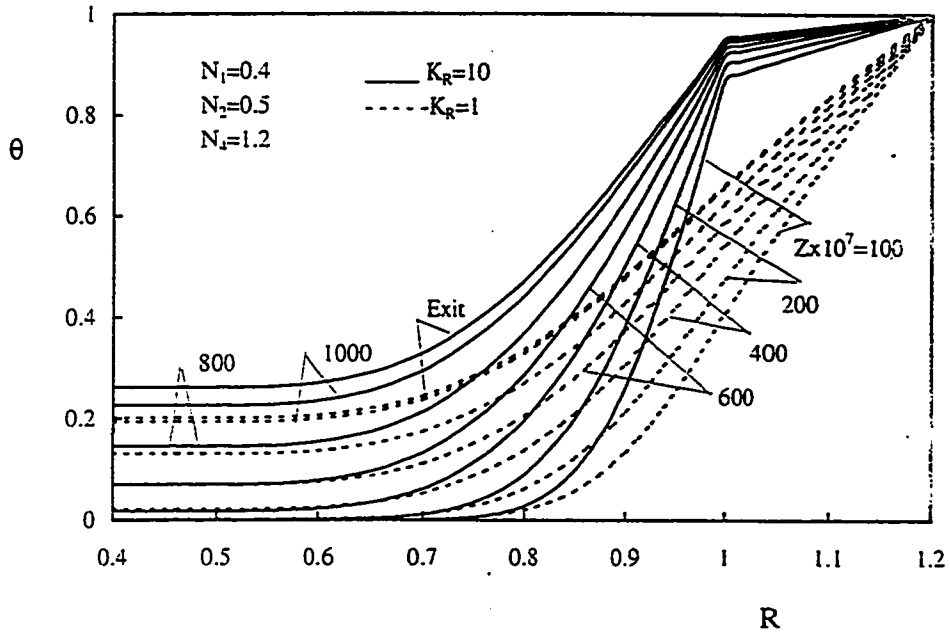

Figure 6.25: Effect of K_R on the temperature distribution at different axial positions, $Gr^* = 10^4, K_R = 10\&1$

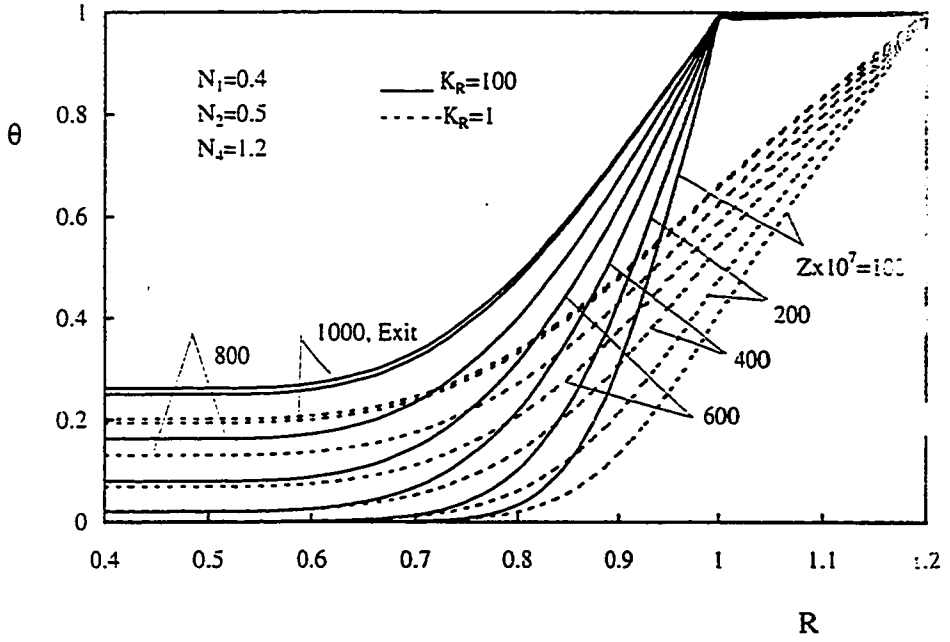

Figure 6.26: Effect of K_R on the temperature distribution at different axial positions, $Gr^* = 10^4, K_R = 100\&1$

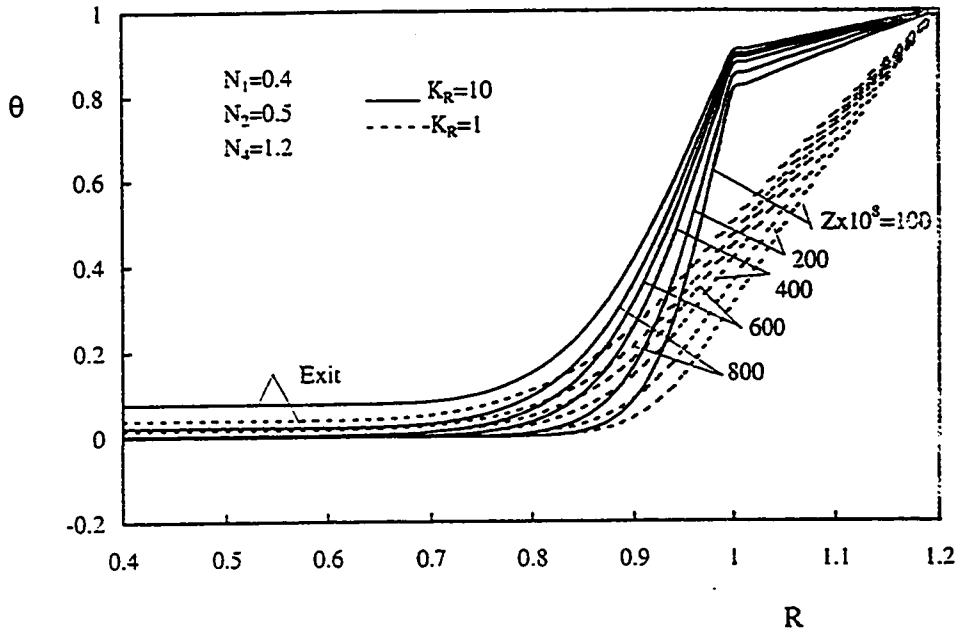

Figure 6.27: Effect of K_R on the temperature distribution at different axial positions, $Gr^* = 10^5, K_R = 10\&1$

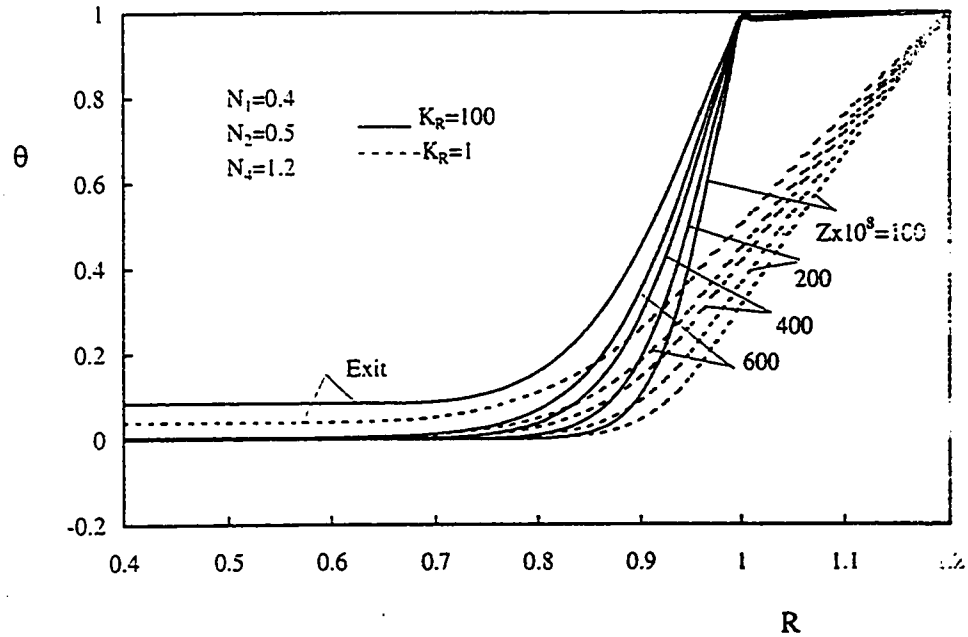

Figure 6.28: Effect of K_R on the temperature distribution at different axial positions, $Gr^* = 10^5, K_R = 100\&1$

6.2.4 Adiabatic Surface Temperature

Figures 6.29 through 6.32 present the effect of K_R on the adiabatic surface temperature as the induced fluid moves upwards through the annulus for the four given values of Gr^*, viz., $Gr^* = 500, 10^3, 10^4$ *and* 10^5, respectively. As can be seen from these figures, near the annulus entrance the induced fluid has just started to feel the heat transferred radially through the heated outer tube wall. As part of this heat is transferred radially by diffusion and radial convection(by radial velocity), the adiabatic wall absorbs this heat and warms up. As the fluid moves further upward and absorbs more heat, the adiabatic surface temperature increases more. In general, it is seen from the four given figures that, as Gr^* decreases, the adiabatic surface temperature at the exit cross-section increases. This is due to the increase in the chimney effect as small values of Gr^* represent long annuli. Finally, it is seen in Fig. 6.32, which shows the effect of K_R on the adiabatic surface temperature for $Gr^* = 10^5$, that the adiabatic temperature profiles (for the three values of K_R) are smooth along the annulus till before the exit cross-section, then they have been distorted. This large distortion which is physically unrealistic is due to the presence of flow reversal at this axial distance.

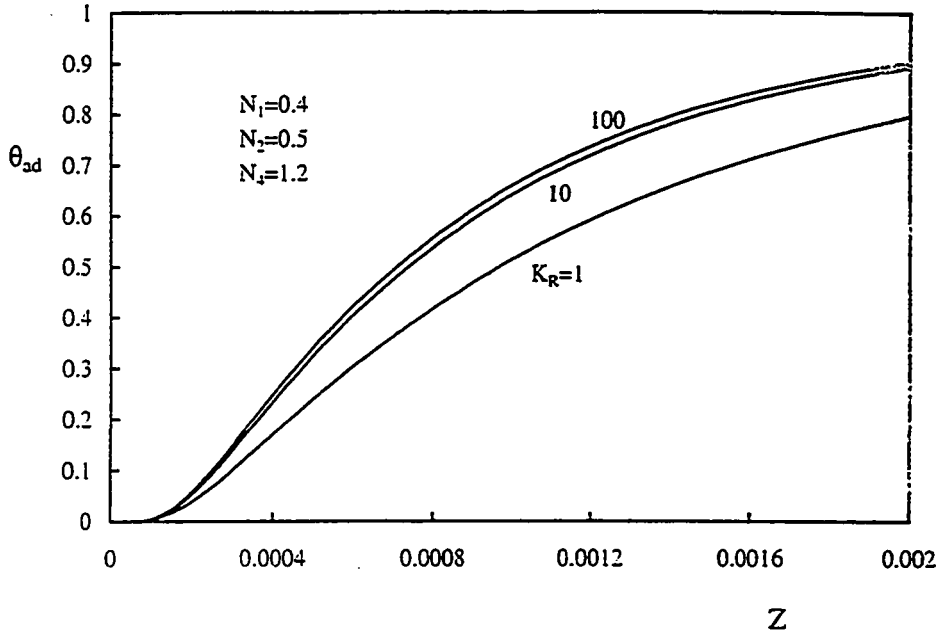

Figure 6.29: Effect of K_R on the adiabatic surface temperature, $Gr^* = 500$

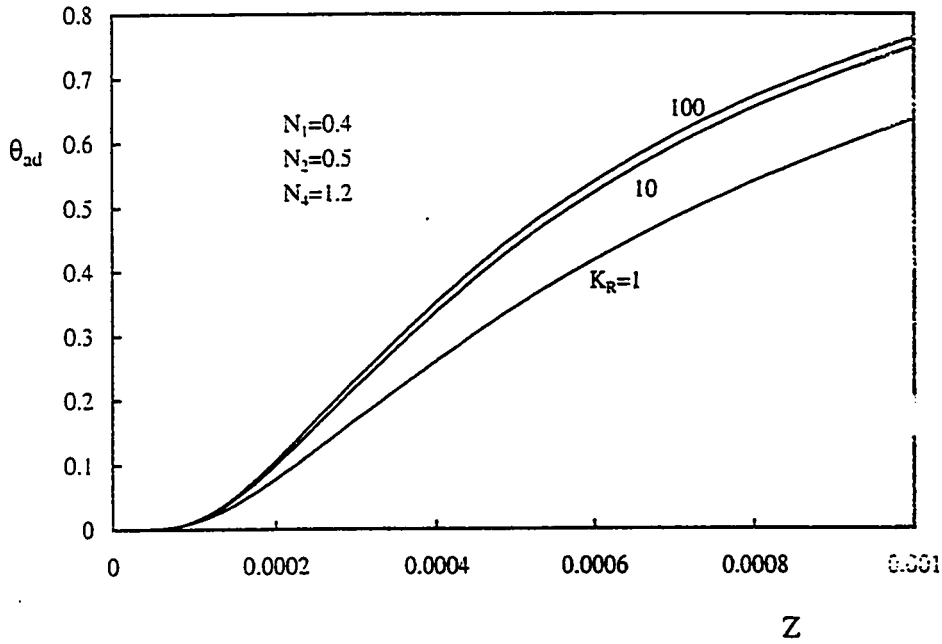

Figure 6.30: Effect of K_R on the adiabatic surface temperature, $Gr^* = 10^3$

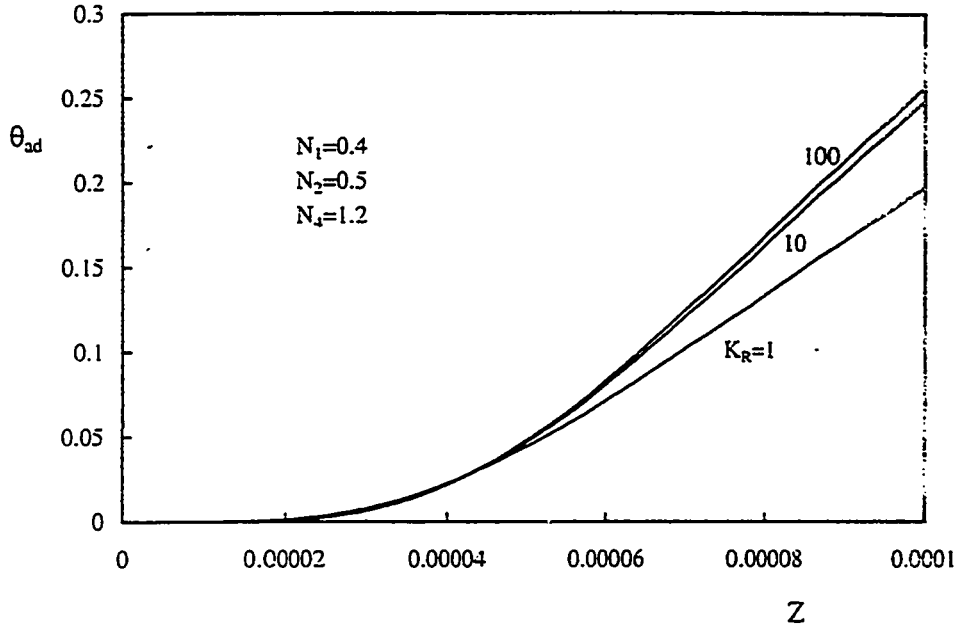

Figure 6.31: Effect of K_R on the adiabatic surface temperature, $Gr^* = 10^4$

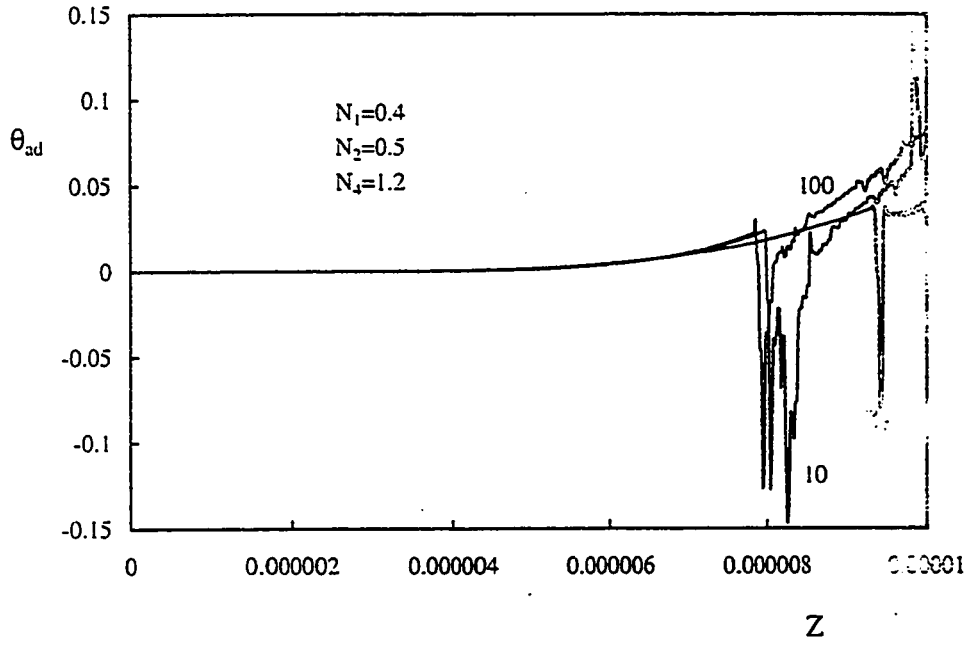

Figure 6.32: Effect of K_R on the adiabatic surface temperature, $Gr^* = 10^5$

6.2.5 Pressure

Figures 6.33 through 6.36 present the effect of K_R on the pressure-defect distribution along the annulus for $Gr^* = 500, 10^3, 10^4$ *and* 10^5, respectively. As can be seen from these figures, the pressure at the annulus entrance has the value $P = -\frac{1}{2}U_o^2$ (U_o is the inlet uniform axial velocity). As the fluid moves upwards, the pressure decreases to a minimum and then increases until it reaches zero at the exit cross-section. This behavior of the pressure can be explained by the fact that the pressure is affected by two variables, the buoyancy force and the wall and fluid friction(viscous force). At the entrance the buoyancy force is small compared with the friction force and as a result the pressure decreases. As the fluid moves upwards and absorbs more heat, the buoyancy force develops until it becomes equal to the friction force at the axial distance where the pressure is minimum. Then the buoyancy force becomes larger than the friction force and hence the pressure increases.

Moreover, it can be seen also that, as Gr^* increases (i.e., shorter annuli), the axial location at which the minimum pressure occurs moves towards the entrance. This is because for large values of Gr^* there is larger temperature difference and hence the buoyancy force develops faster. However, Fig. 6.36 shows that the pressure profiles near the exit cross-section have some distortions. This distortion is attributed to the presence of flow reversal at that axial position.

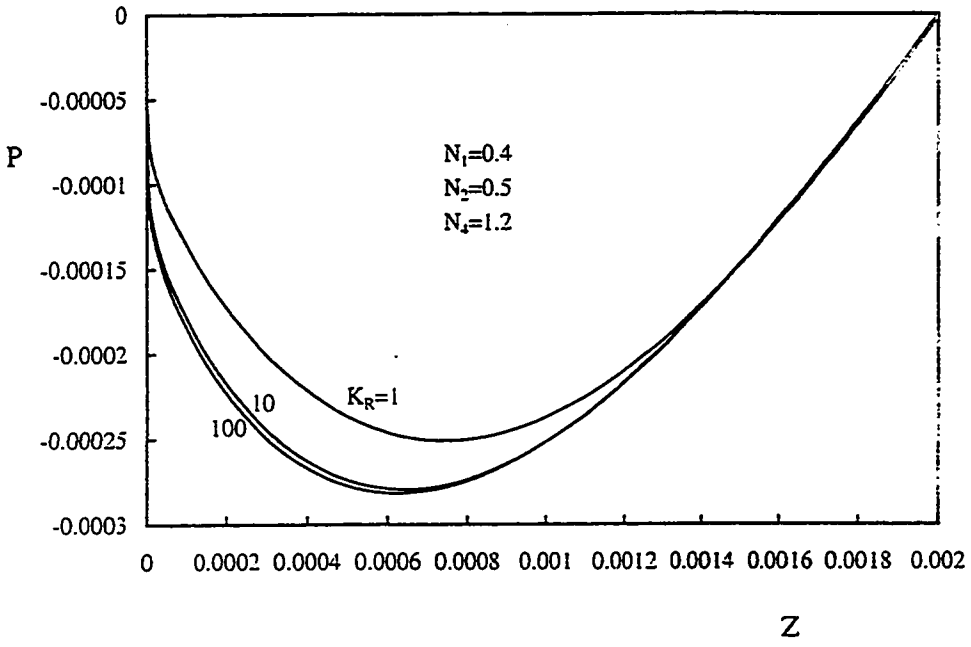

Figure 6.33: Effect of K_R on the pressure distribution along the annulus, $Gr^* = 500$

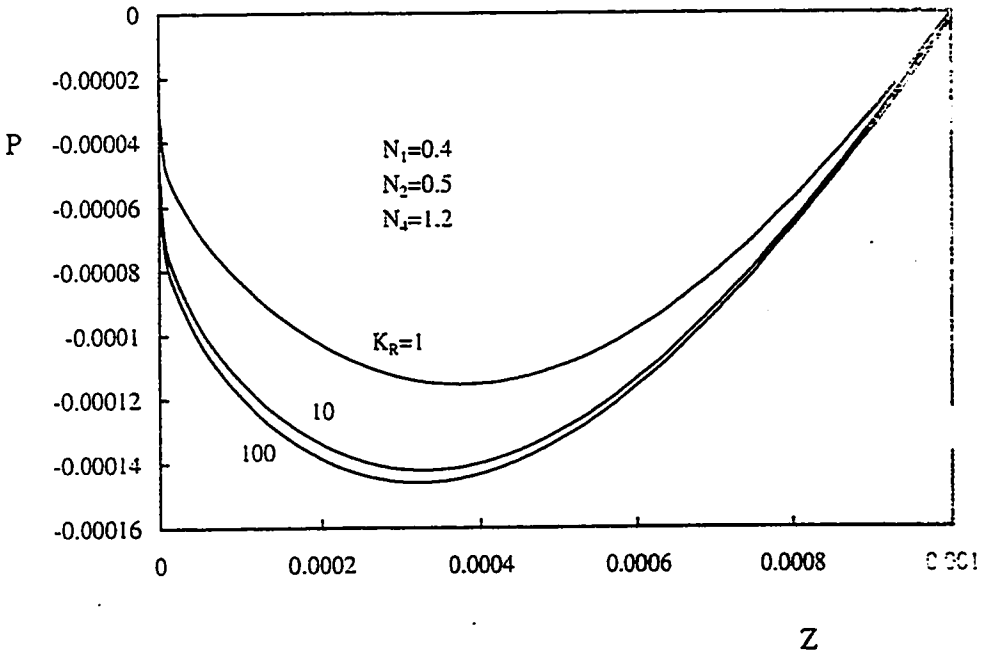

Figure 6.34: Effect of K_R on the pressure distribution along the annulus, $Gr^* = 10^3$

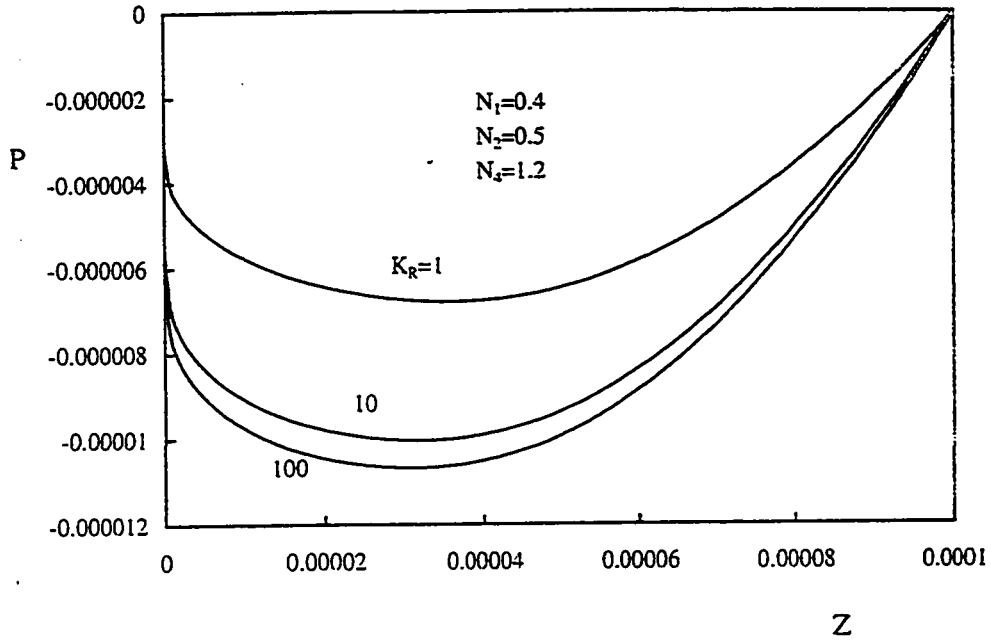

Figure 6.35: Effect of K_R on the pressure distribution along the annulus, $Gr^* = 10^4$

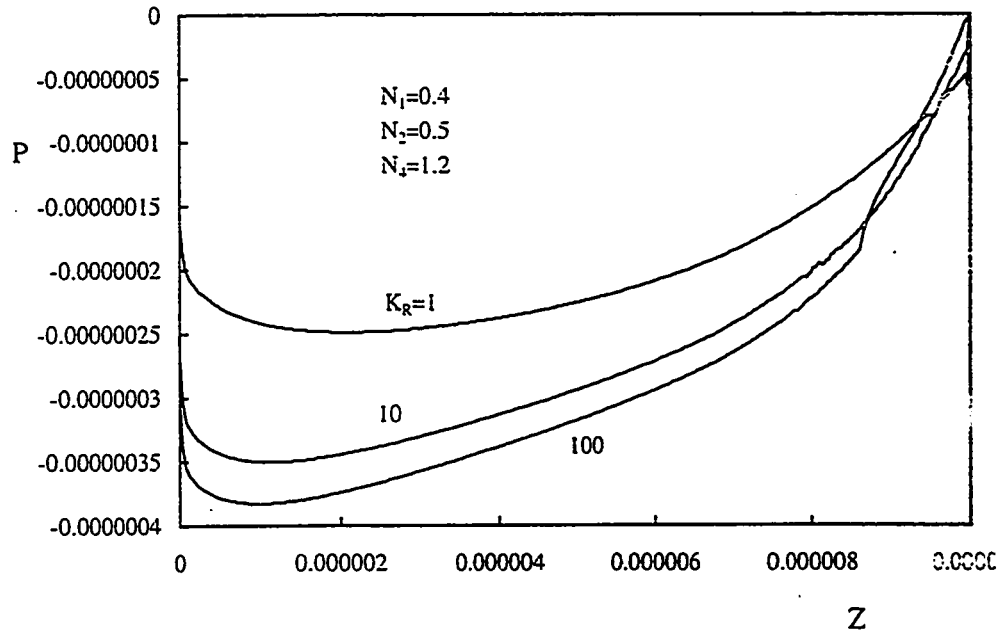

Figure 6.36: Effect of K_R on the pressure distribution along the annulus, $Gr^* = 10^5$

6.2.6 Fluid-Solid Interface Temperatures(θ_2 and θ_3)

In this section, the effect of K_R on the temperatures of both the outer surface of the inner tube and the inner surface of the outer tube will be presented. Figure 6.37 shows the effect of K_R on the temperature of the inner surface of the outer tube for two given values of Gr^*, viz., $Gr^* = 500\ and\ 10^3$ while such effect is shown in Fig. 6.38 for $Gr^* = 10^4\ and\ 10^5$. It is seen from both figures that the increase in K_R leads to an increase in θ_3. Moreover, for $K_R = 100$, θ_3 attains a value $\theta_3 \simeq 1$, which is the maximum value that can be attained (this value is the temperature of the outer surface of the outer tube). This leads to the conclusion that for $K_R = 100$ the wall thermal resistance(according to the specification of the problem under consideration) can be neglected and the results presented by El-Shaarawi and Sarhan [23] can be used. Similar to Figs. 6.37 and 6.38, Figs. 6.39 and 6.40 present the effect of K_R on the temperature of the outer surface of the inner tube(θ_2)for $Gr^* = 500\&10^3\ and\ Gr^* = 10^4\&10^5$, respectively. In Fig. 6.40, the distortions in the temperature profiles for $Gr^* = 10^5$ are due to the flow reversal.

Figures 6.41 and 6.42 present the effect of K_R on the variation of the exit temperature with the induced flow rate for both the inner surface of the outer tube($\theta_{3,e}$) and the outer surface of the inner tube($\theta_{2,e}$), respectively. In both of these figures, the effect of K_R is very pronounced especially at small values of the flow rate(F). However, as the flow rate increases the exit temperature profiles for the given values of K_R approach the value of fully-developed flow($\theta_2 = \theta_3 = \theta = 1$). El-Shaarawi and Sarhan [23] reported that for a given annulus of $N_2 = 0.5$ with a fully-developed flow(i.e., $\theta = 1$ and $\frac{\partial}{\partial Z} = 0$),

the maximum flow rate that can be sucked through that annulus (i.e., the limiting fully-developed value) is $F = 0.015748$. This may explain why at large values of F(values which gives fully-developed state) the temperatures ($\theta_{2,e}$ and $\theta_{3,e}$) approach the fully-developed value.

Figures 6.43 and 6.44 present the effect of K_R on the variation of the exit temperatures of the inner surface of the outer tube and the outer surface of the inner tube with the annulus height, respectively. It is seen from both of these figures that the effect of K_R is easily pronounced at small values of the annulus height, L (which corresponds to small values of F). However, for long annuli(large values of L or F) the temperatures for all given values of K_R approach the full-developed value, i.e., $\theta = 1$. This is because for long annuli the induced fluid(corresponds to any value of K_R) has enough distance to approach the fully-developed state.

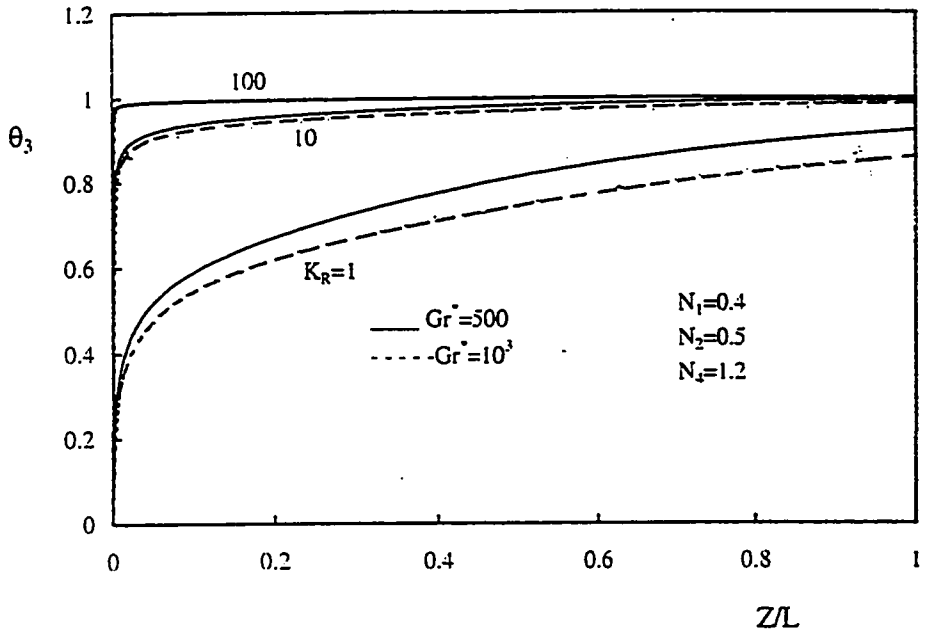

Figure 6.37: Effect of K_R on the outer tube interface temperature, $Gr^* = 500\&10^3$

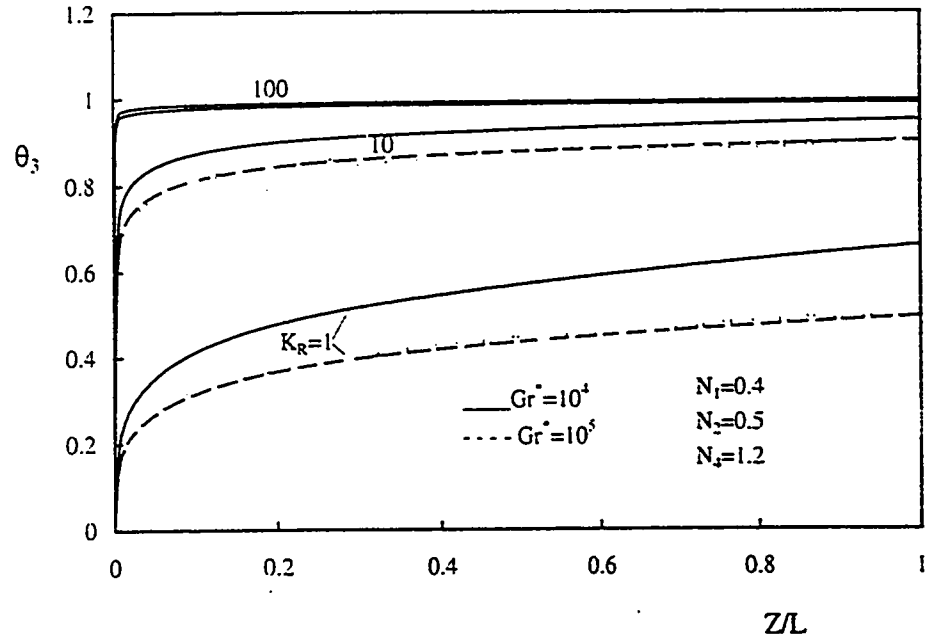

Figure 6.38: Effect of K_R on the outer tube interface temperature, $Gr^* = 10^4\&10^5$

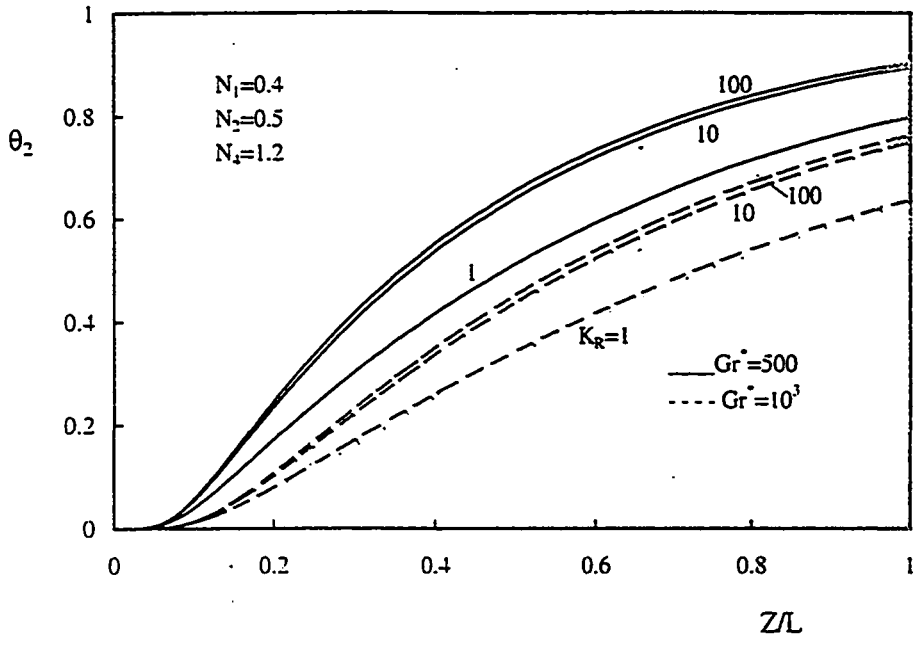

Figure 6.39: Effect of K_R on the inner tube interface temperature. $Gr^* = 500\&10^3$

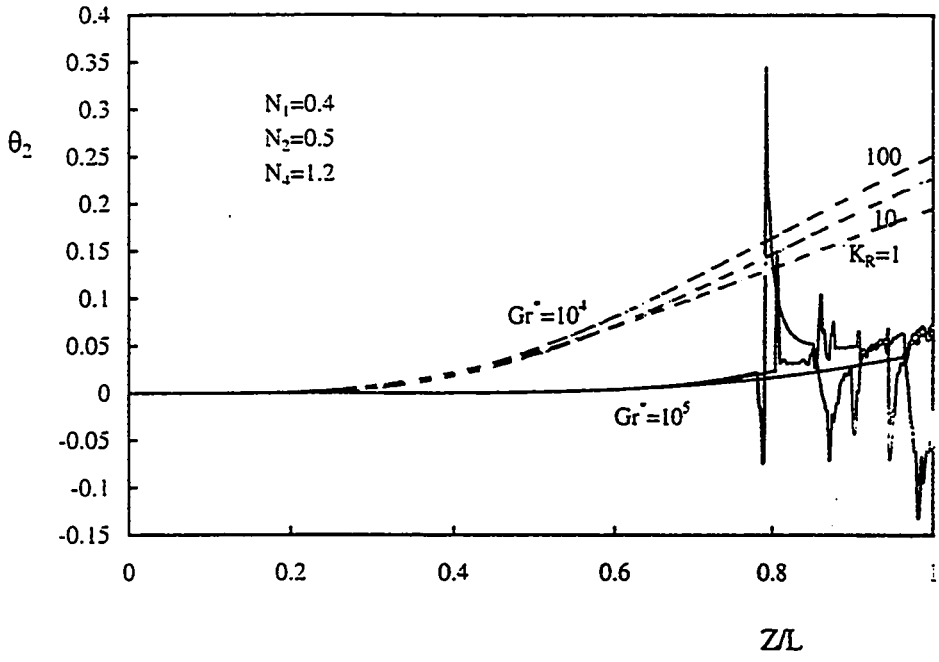

Figure 6.40: Effect of K_R on the inner tube interface temperature, $Gr^* = 10^4\&10^5$

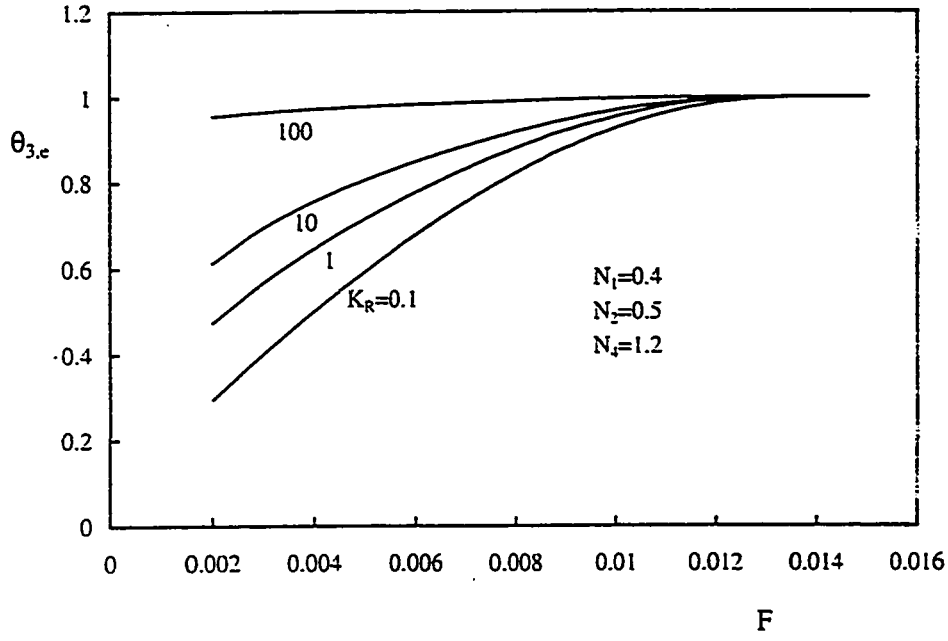

Figure 6.41: Effect of K_R on the exit temperature of the outer tube interface versus F

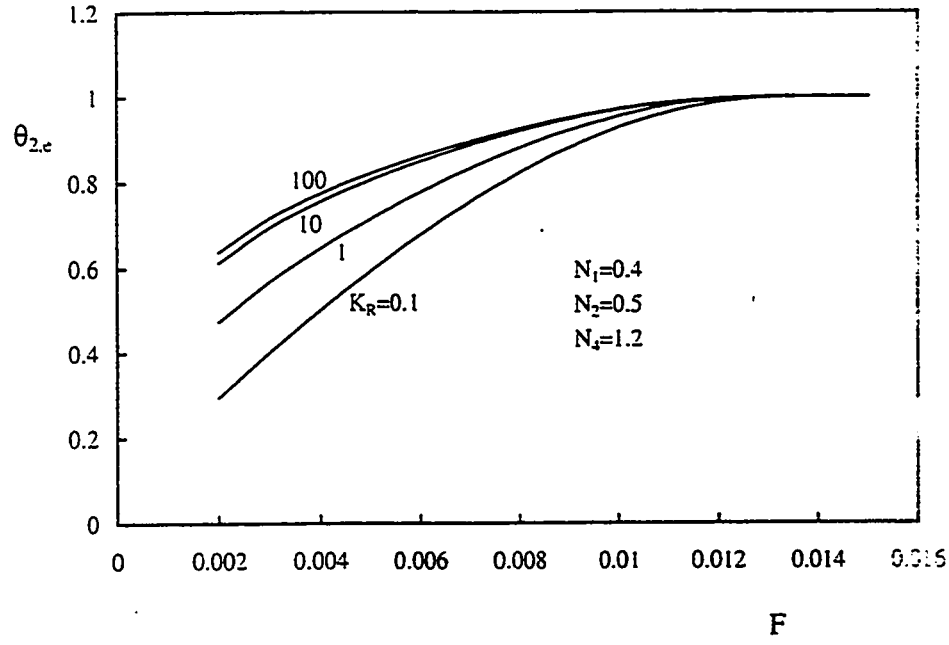

Figure 6.42: Effect of K_R on the exit temperature of the inner tube interface versus F

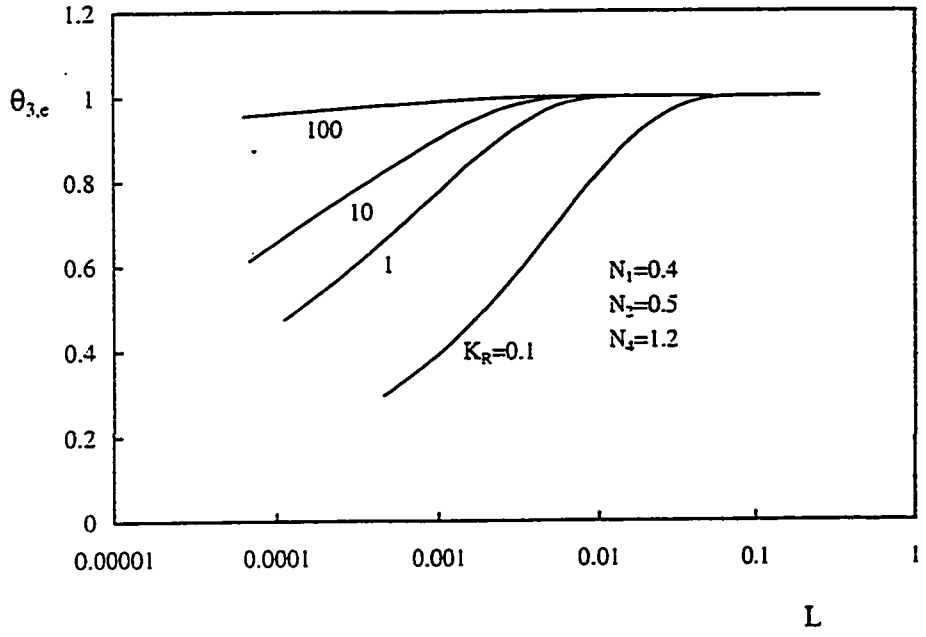

Figure 6.43: Effect of K_R on the exit temperature of the outer tube interface versus L

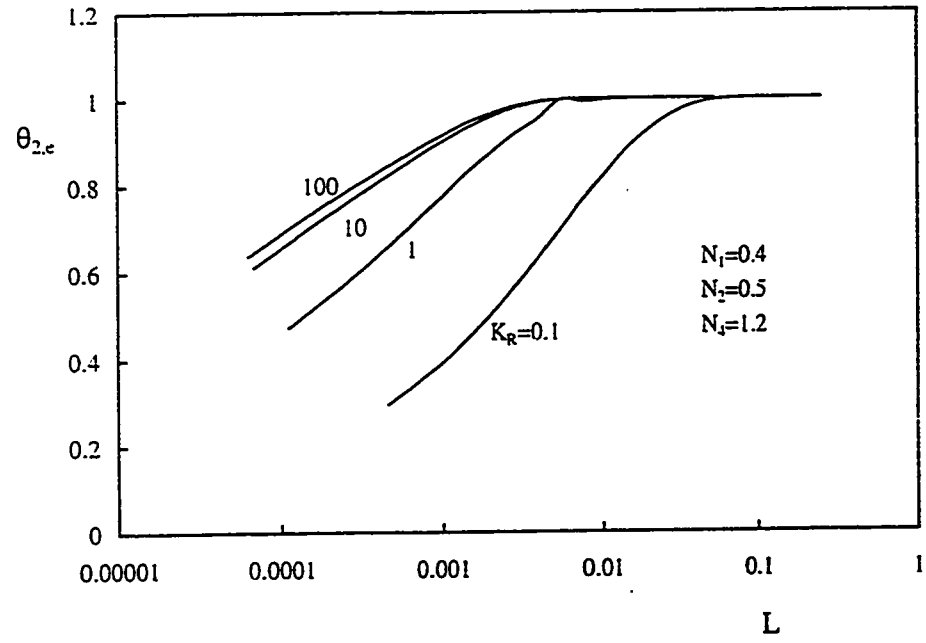

Figure 6.44: Effect of K_R on the exit temperature of the inner tube interface versus L

6.2.7 The Mixing-Cup Temperature

Figure 6.45 presents the effect of K_R on the mixing-cup temperature for $Gr^* = 500$ and 10^3 while such effect is shown in Fig. 6.46 for $Gr^* = 10^4$ and 10^5. It is seen in these two figures that θ_m increases with the increase in the value of K_R. Thermal control engineers are usually interested in the exit mixing-cup temperature rather than the local one. Figure 6.47 presents the effect of K_R on the exit mixing-cup temperature as it varies with the flow rate(F) while such effect is shown in Fig. 6.48 as it varies with the annulus height. As can be seen from both figures, for large values of F or L, $\theta_{m,e}$ approaches the fully-developed value, i.e., $\theta_{m,e} = 1$.

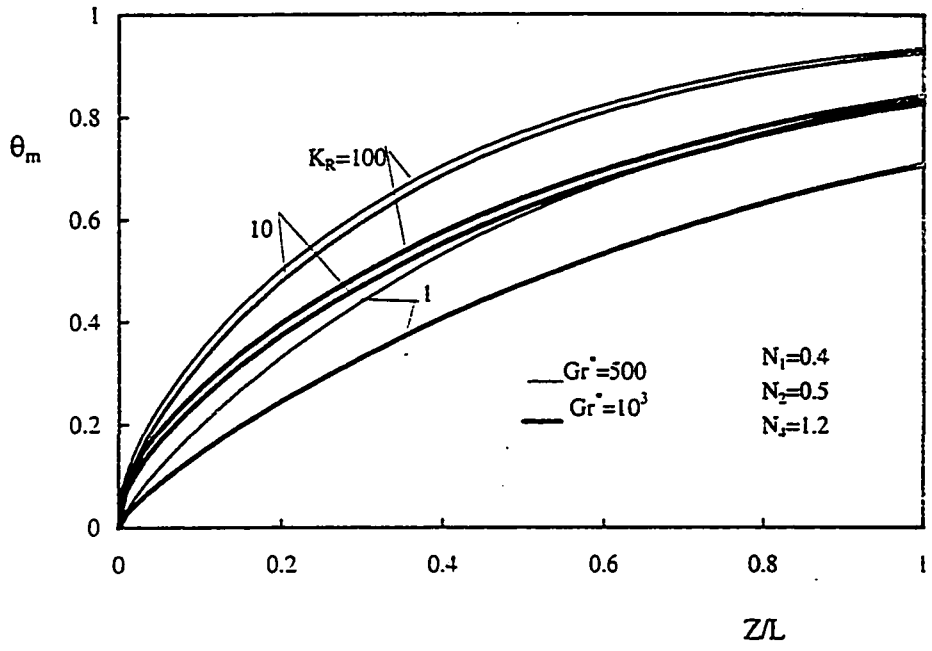

Figure 6.45: Effect of K_R^* on the mixing-cup temperature, $Gr^* = 500\&10^3$

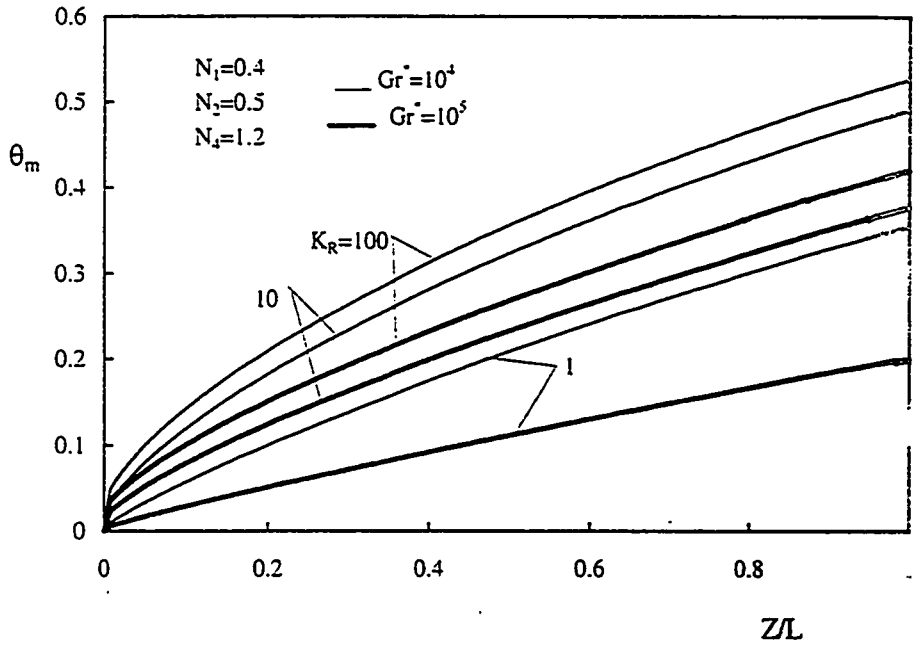

Figure 6.46: Effect of K_R^* on the mixing-cup temperature, $Gr^* = 10^4\&10^5$

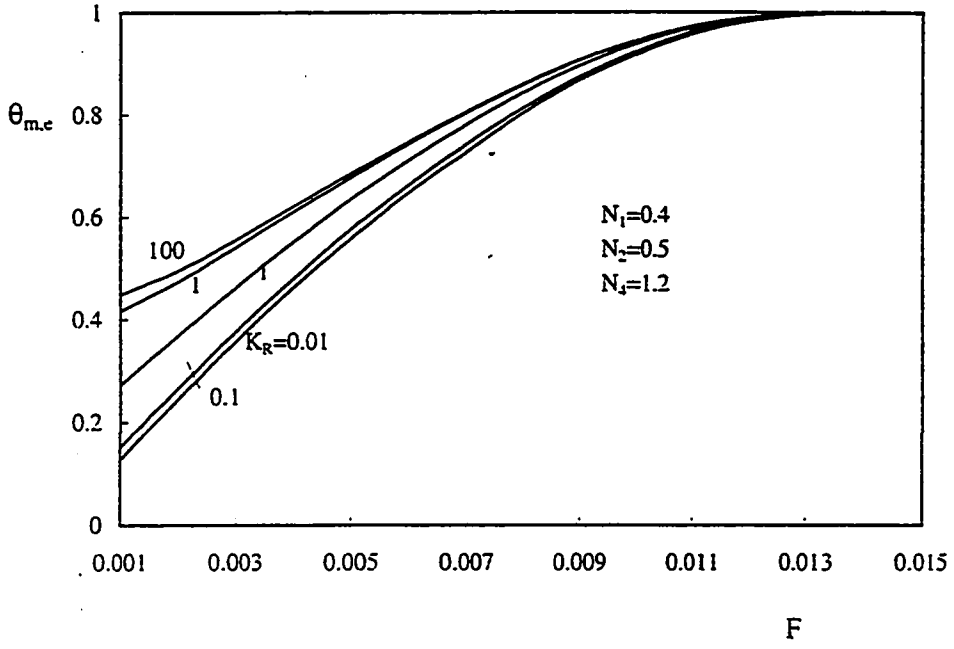

Figure 6.47: Effect of K_R on the exit mixing-cup temperature versus F

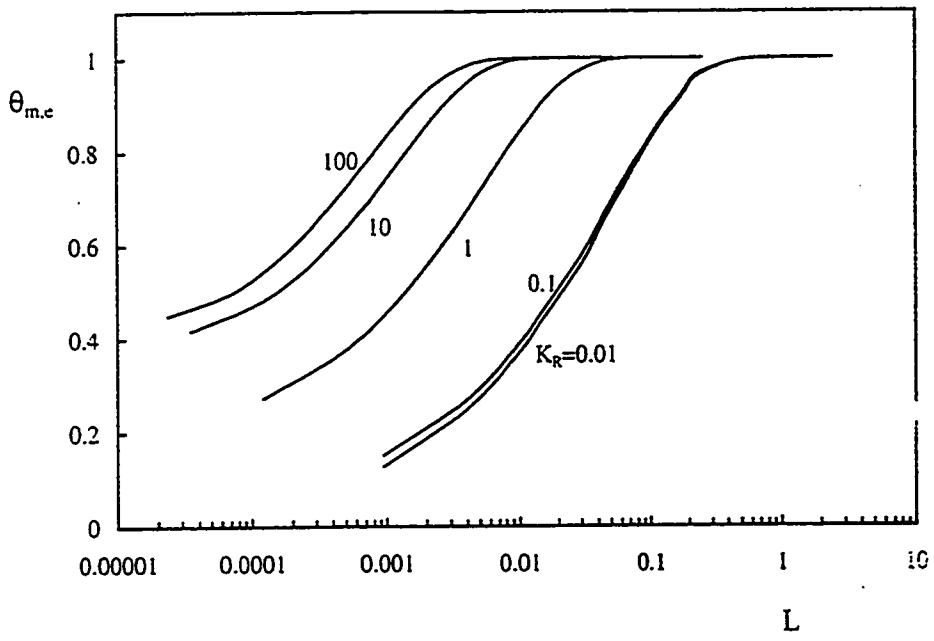

Figure 6.48: Effect of K_R on the exit mixing-cup temperature versus L

6.2.8 The Heat Absorbed

Figs. 6.49 and 6.50 present the effect of K_R on the local heat absorbed for the four given values of $Gr^* = 500, 10^3, 10^4 \; and \; 10^5$, respectively. It is seen that the graph of H have the same behavior as that of θ_m, so there is no need to mention the same comments again here. For the design and thermal control engineers, Figs. 6.51 and 6.52 present very important results. These two figures present the effect of K_R on the variation with the annulus height of both the total heat absorbed and the induced flow rate, respectively. In both of these two figures, as K_R increases the wall thermal resistance decreases. Indeed, for $K_R \geq 100$ the wall thermal resistance can be neglected and the results of the conventional case(i.e., $K_R = \infty$) that has been investigated by El-Shaarawi and Sarhan [23] can be used with a maximum error 2.95% in the induced flow rate. Finally, it is worth mentioning that a special run was made for $K_R = 1000$ and when plotted, it was found to lie completely on top of results for $K_R = 100$.

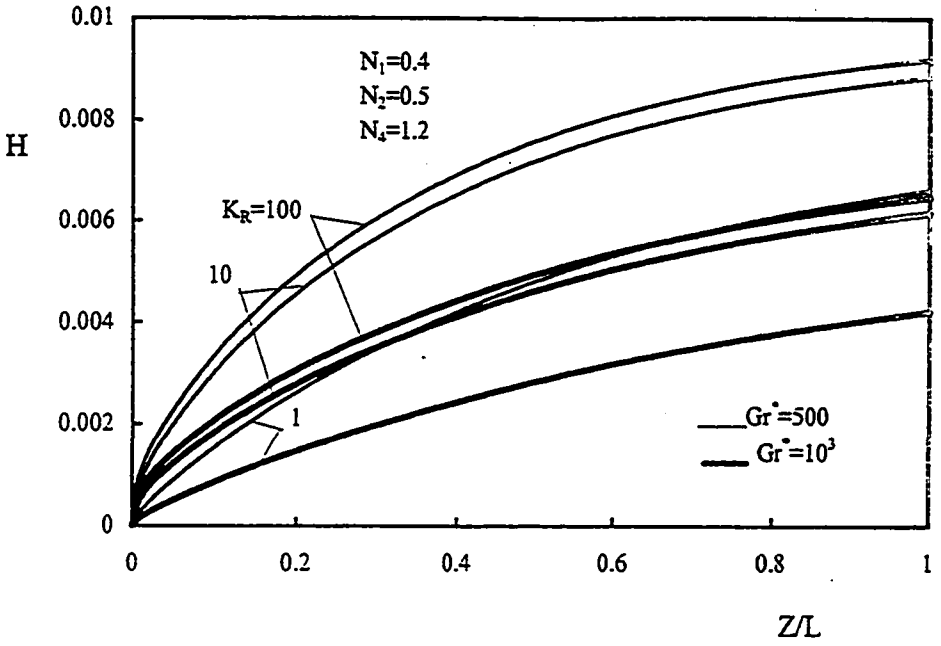

Figure 6.49: Effect of K_R on the local heat absorbed, $Gr^* = 500\&10^3$

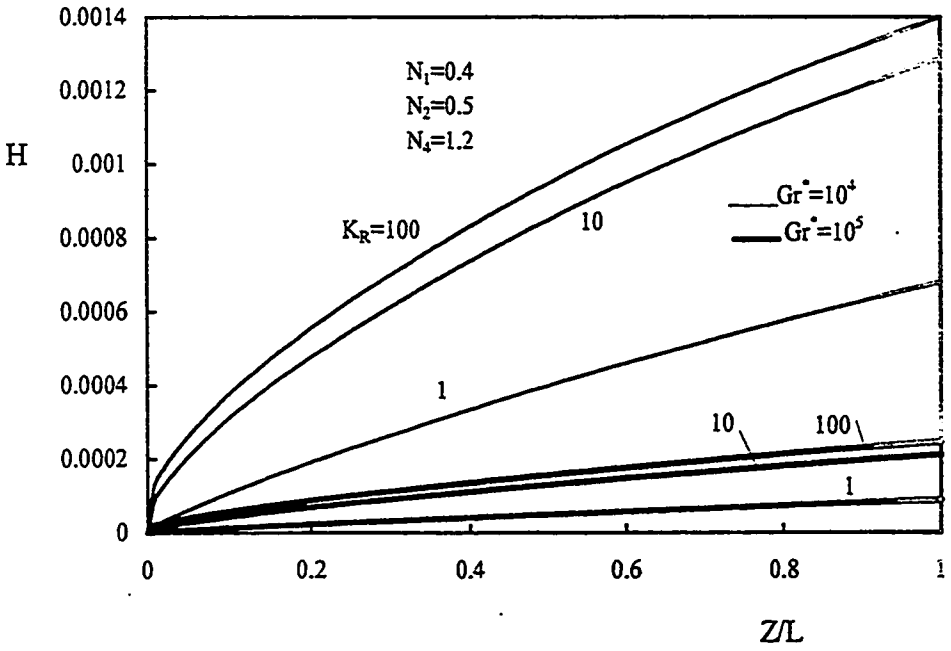

Figure 6.50: Effect of K_R on the outer tube interface temperature, $Gr^* = 10^4\&10^5$

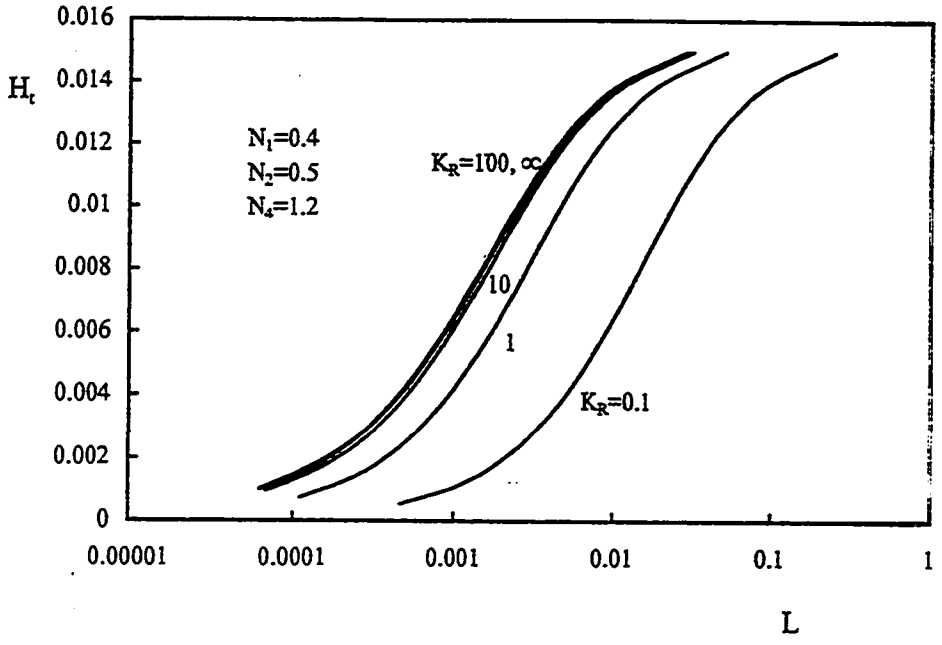

Figure 6.51: Effect of K_R on the total heat absorbed

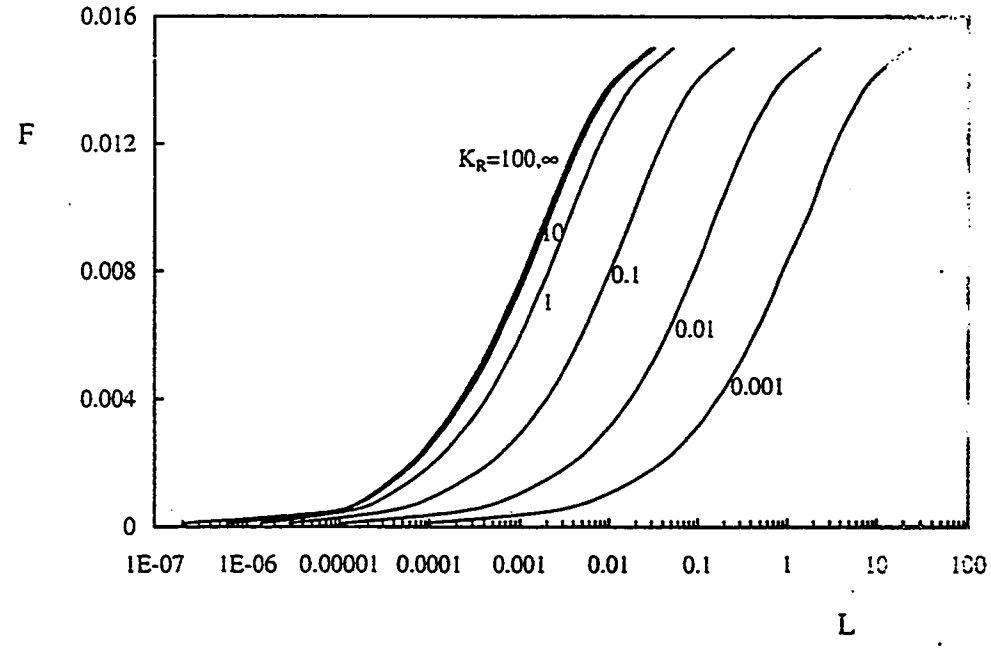

Figure 6.52: Effect of K_R on the induced flow rate

CHAPTER 7

Conclusions

In this investigation, an iterative implicit finite-difference scheme has been developed to solve the transient conjugate free convection in an open-ended vertical concentric annulus. The outer surface of the outer tube is heated isothermally while the inner surface of the inner tube is kept adiabatic. The effect of both the wall thermal conductivity and thermal diffusivity on the flow characteristics and some engineering parameters has been investigated.. From the presented results, the following conclusions can be drawn out:

- The thermal conductivity of the wall material, and hence the thermal conductivity ratio K_R, has a prominent effect on the flow characteristics and on the engineering parameters for both the transient and steady free convection modes.
- For the steady-state free convection, the effect of the wall thermal resistance decreases as K_R increases. Indeed, for $K_R \geq 100$, the wall thermal resistance can be neglected and the results of the conventional case that has be reported by El-Shaarawi and Sarhan [23] can be used with a great accuracy.
- For the transient free convection mode, the wall thermal diffusivity and the thermal

conductivity have strong effects on the flow characteristics and on the engineering parameters. For the selected range of values of Gr^*, it was seen that for an annulus with $K_R = 100$ and $\alpha_R = 1000$, the wall thermal resistance can be neglected and the results of the conventional case that has been reported by Al-Attas [24] can be used with a maximum error ranging from 1.35% for $Gr^* = 500$ to 2.35% for $Gr^* = 10^4$.

- For short annuli, i.e., annuli of large values of Gr^* the phenomenon of flow reversal occurs and its strength may be large compared with the main stream. Hence, the boundary-layer model in invalid in this case and another scheme for the elliptic equations must be used to investigate such cases.

APPENDICES

APPENDIX A: Boundary-Layer Formulation

To Obtain the boundary-layer equations, equations (3.1) through (3.4) are transformed into dimensionless forms using a group of dimensionless parameters, e.g., characterstics length, velocity, ...etc. Then, applying the order of magnitude analysis on each equation; terms of small order of magnitude will be neglected. The following dimensionless parameters are used to replace the dimensional ones in the governing equations:

$$U = \frac{u}{u_*}$$
$$V = \frac{v}{u_*}$$
$$Z = \frac{z}{l}$$
$$t = \frac{u_* \tau}{l}$$
$$V = \frac{v}{u_*}$$
$$R = \frac{r}{l}$$
$$P = \frac{p}{\rho u_*^2}$$
$$\theta = \frac{T - T_o}{T_w - T_o}$$
$$Re = \frac{u_* l}{\gamma}$$

In the above parameters, the references characterstics length l and velocity u_* are selected so that the dependent and independented variables R, Z, t, U and θ and the derivatives $\frac{\partial u}{\partial z}$ and $\frac{\partial T}{\partial z}$ are of order 1. For simplicity, velocity and thermal boundary-layers are assumed to be of the same order of magnitude δ, i.e., the value of Prandtl number is near unity.

As discussed by El-Shaarawi [27] the governing equations should not expanded to their elementary terms. This is to avoid neglecting some improtant ele

mentary-terms when compared with some other terms in the governing equation.

Substituting the above dimensionless parameters in the continuity eqaution (1), it becomes:

$$\frac{\partial}{\partial R}(RV) + \frac{\partial U}{\partial Z} = 0$$
$$(\frac{1\delta}{\delta}) \quad (\frac{1}{1})$$

The order of magnitude of each term is written under it, and they are estimated as follows. Since, $\frac{\partial U}{\partial Z}$ is of order (1), the second term in the above equation should also be of order (1). Hence, both terms add to zero. Furthermore, Since R is of order (1), ∂R is of order δ, and $(\frac{\partial(RV)}{\partial R})$ is of order (1), then V is of order (δ).

Following the same technique, the axial momentum equation in non-dimensional form has the form:

$$\rho(\frac{u_2}{l})\left[\frac{\partial U}{\partial \tau} + V\frac{\partial U}{\partial R} + U\frac{\partial U}{\partial Z}\right] = \rho(\frac{u_2}{l})\left[-\frac{\partial P}{\partial Z} + \frac{Gr\theta}{Re^2} + \frac{1}{Re}\left[\frac{\partial^2 U}{\partial Z^2} + \frac{1}{R}\frac{\partial}{\partial R}(R\frac{\partial U}{\partial R})\right]\right]$$

Discard the common term $\rho(\frac{u_2}{l})$ from both equations, we get;

$$\frac{\partial U}{\partial \tau} + V\frac{\partial U}{\partial R} + U\frac{\partial U}{\partial Z} = -\frac{\partial P}{\partial Z} + \frac{Gr\theta}{Re^2} + \frac{1}{Re}\left[\frac{\partial^2 U}{\partial Z^2} + \frac{1}{R}\frac{\partial}{\partial R}(R\frac{\partial U}{\partial R})\right]$$
$$(\frac{1}{1}) \quad (\delta)(\frac{1}{\delta}) \quad (1)(\frac{1}{1}) \quad -\frac{\partial P}{\partial Z} \quad \frac{Gr}{Re^2}(1) \quad \frac{1}{Re}\left[(\frac{1}{1}) \quad (\frac{1}{1})(\frac{1}{\delta})((1)(\frac{1}{\delta})\right]$$
$$1 \quad 1 \quad 1 \quad \frac{\partial P}{\partial Z} \quad \frac{Gr}{Re^2} \quad \delta^2 \; [1 \quad \frac{1}{\delta^2}]$$

From the above oders of magnitude, it can be deduced that Re must be of order $\frac{1}{\delta^2}$ in order that the viscous terms on the RHS of the equation can balance, with the inertia terms on its LHS. Moreover, the buoyancy term can not be neglected in the present case because it is establishing the flow field. This implies that the coefficiet of (θ), which $\frac{Gr}{Re^2}$, should be of order (1) and consequently Gr is of order $\frac{1}{\delta^4}$. Furhthermore, $\frac{\partial P}{\partial Z}$ can not be dropped because it balances the inertia forces, which means that it is of order (1). Thus, after drooping all the terms of order δ and higher powers, the axial momentum equation reduces to

$$\frac{\partial U}{\partial \tau} + V\frac{\partial U}{\partial R} + U\frac{\partial U}{\partial Z} = -\frac{\partial P}{\partial Z} + \frac{Gr\theta}{\mathrm{Re}^2} + \frac{1}{\mathrm{Re}}\left[\frac{\partial^2 U}{\partial Z^2} + \frac{1}{R}\frac{\partial}{\partial R}(R\frac{\partial U}{\partial R})\right]$$

Applying the same technique on the radial momentum equation:

$$\rho(\frac{u_2}{l})\left[\frac{\partial V}{\partial \tau} + V\frac{\partial V}{\partial R} + U\frac{\partial V}{\partial Z}\right] = \rho(\frac{u_2}{l})\left[-\frac{\partial P}{\partial R} + \frac{1}{\mathrm{Re}}\left[\frac{\partial^2 V}{\partial Z^2} + \frac{\partial}{\partial R}(\frac{1}{R}\frac{\partial RV}{\partial R})\right]\right]$$

Dropping the common term from both sides of the equation, it becomes:

$$\begin{array}{cccccccccc}
\frac{\partial V}{\partial \tau} & + & V\frac{\partial V}{\partial R} & + & U\frac{\partial V}{\partial Z} & = & -\frac{\partial P}{\partial R} & + & \frac{Gr\theta}{Re^2} & + & \frac{1}{Re}\left[\frac{\partial^2 V}{\partial Z^2} + \frac{\partial}{\partial R}(\frac{1}{R}\frac{\partial RV}{\partial R})\right] \\
(\frac{\delta}{1}) & & (\delta)(\frac{\delta}{\delta}) & & (1)(\frac{\delta}{1}) & & -\frac{\partial P}{\partial R} & & \frac{Gr}{Re^2}(1) & & \delta^2\left[(\frac{\delta}{1}) + (\frac{1}{\delta})(\frac{\delta.\delta}{\delta.\delta})\right] \\
\delta & & \delta & & \delta & & \frac{\partial P}{\partial R} & & \frac{Gr}{Re^2} & & \delta^2\left[\delta + \frac{1}{\delta}\right]
\end{array}$$

Dropping the terms of order δ and the higher powers, the radial momentum equation is reduced to

$$\frac{\partial P}{\partial R} = 0$$

Which means that the variation of the pressure in the transverse direction is negligible. Thus, the pressure in the annulus is a function of time and the streamwise direction only.

For the energy equation in the fluid, after substituting the dimensionless parameters, it becomes:

$$\frac{u_*}{(Tw - T_o)l}\left[\frac{\partial\theta}{\partial\tau} + V\frac{\partial\theta}{\partial R} + U\frac{\partial\theta}{\partial Z}\right] = \frac{u_*}{(Tw - T_o)l}\left[\frac{1}{\mathrm{Pr}\,\mathrm{Re}}\left(\frac{1}{R}\frac{\partial}{\partial R}\left(R\frac{\partial\theta}{\partial R}\right)\right) + \frac{\partial^2\theta}{\partial Z^2}\right]$$

After discarding the common term $\frac{u_*}{(Tw - T_o)l}$ from the equation, it becomes:

$$\frac{\partial\theta}{\partial\tau} + V\frac{\partial\theta}{\partial R} + U\frac{\partial\theta}{\partial Z} = \frac{1}{\mathrm{Pr}\,Re}\left[\frac{1}{R}\frac{\partial}{\partial R}\left(R\frac{\partial\theta}{\partial R}\right) + \frac{\partial^2\theta}{\partial Z^2}\right]$$

$$\left(\tfrac{1}{1}\right) \quad (\delta)\left(\tfrac{\delta}{\delta}\right) \quad (1)\left(\tfrac{1}{1}\right) \quad \delta^2 \quad \left[\left(\tfrac{\delta}{1}\right) \quad \left(\tfrac{1}{\delta}\right)\left(\tfrac{\delta.\delta}{\delta.\delta}\right)\right]$$

$$\delta \quad \delta \quad \delta \quad \delta^2 \quad \left[\frac{1}{\delta^2} \quad \frac{1}{1}\right]$$

Thus the equation reduces to the following form:

$$\left[\frac{\partial\theta}{\partial\tau} + V\frac{\partial\theta}{\partial R} + U\frac{\partial\theta}{\partial Z}\right] = \left[\frac{1}{\mathrm{Pr}\,\mathrm{Re}}\left(\frac{1}{R}\frac{\partial}{\partial R}\left(R\frac{\partial\theta}{\partial R}\right)\right)\right]$$

The dropped term, $\frac{1}{\mathrm{Pr}\,Re}\frac{\partial^2\theta}{\partial Z^2}$, represents the axial diffusion of heat which is very small compared with the radial heat diffusion of heat.

APPENDIX B: FORTRAN PROGRAM FOR THE TRANSIENT CASE

```
C This Program is Written to Solve Two-Dimension Transient Conduction-Laminar
C Natural Convection in Vertical Concentric Annulus using Boundary-Layer Assump-
tions.
      REAL U(50,52,202), V(50,52,202), T(80,52,202), P(52,202), A(80), B(80), C(80),
D(80),
     *                                X(50), AP(50), E(50), AS(50,50), ATH(100), DTH(100)
     C COMMON AS, X
      REAL N1, N2, N3, N4, NEPS, EPS, R, LZ, DZ, KR
      INTEGER N, NS1, NS2
     C ——KR=100, ALPHAR=100, GR=1000
      OPEN(3,FILE='UMH100')
      OPEN(4,FILE='UZ100')
      OPEN(5,FILE='VMH100')
      OPEN(6,FILE='VZ100')
      OPEN(7,FILE='P100')
      OPEN(8,FILE='TMH100')
      OPEN(9,FILE='TZ100')
      OPEN(10,FILE='TAD100')
```

```
OPEN(11,FILE='TMC100')
OPEN(12,FILE='H100')
OPEN(14,FILE='F100')
OPEN(16,FILE='UZZ100')
OPEN(17,FILE='VZZ100')
OPEN(18,FILE='TZZ100')
OPEN(19,FILE='UZZZ100')
OPEN(20,FILE='VZZZ100')
OPEN(21,FILE='TZZZ100')
OPEN(22,FILE='UEXIT100')
OPEN(23,FILE='VEXIT100')
OPEN(24,FILE='TEXIT100')
OPEN(25,FILE='TMCZ100')
OPEN(26,FILE='HZ100')
C here constants will be added
C time, radial and radial steps
DT= 0.001
DR= 0.0125
DRS= 0.0125
DZ= 2.E-5
```

N=40

N1=0.4

N2=0.5

N3=1.0

N4=1.2

NS1=8

NS2=16

NTS= NS1+N+NS2+1

NSI= NS1+N+2

NSF= NS1+N+NS2

KC= 200

LZ=1E-5

JC=50

IC=41

U1=0.000005

PR= 0.7

ALPHAR=100

KR=100

FACD= 0.97

FACI= 1.03

EPS= 1E-7

```
NEPS= -EPS
C ———— INITILIZATION
DO 10 K= 1,KC
DO 10 J= 1,JC
DO 101 I= 1,IC
U(I,J,1)= 0.0
101 V(I,J,1)= 0.0
DO 102 I= 1,NTS
102 T(I,J,K)= 0.0
P(J,K)= 0.0
10 CONTINUE
C ———————— TEMPERATURE BOUNDARY CONDITIONS
C ———————— LEFT SIDE BOUNDARY CONDITIONS
DO 2000 K= 1,KC
DO 2000 J= 1,JC+1
2000 T(NTS,J,K+1)= 1.0
DO 1 I= 2,N
1 U(I,1,2)= U1
C ———— MAIN LOOP
1002 DO 1000 K=1,KC
IT= 0.0
```

```
C ———— AXIAL DIRECTION
 1001 P(1,K+1)= -0.5*(U1**2)
 F=(1-N2**2)*U1
 DO 999 J=1,JC
C ———— COEFFICIENTS ESTIMATION FOR TEMPERATURE CALCU-
LATION
C ———— COEFFICIENTS OF CONDUCTION EQUATION FOR THE IN-
NER
C CYLINDER THICKNESS
 DO 100 I= 2,NS1
 R= N1+(I-1)*DRS
 PRDR= 2*PR*DRS

 A(I)= ALPHAR/(PRDR*R) - ALPHAR/(PR*(DRS**2))
 B(I)= (1.0/DT) + (2*ALPHAR)/(PR*(DRS**2))
 C(I)= -ALPHAR/(PRDR*R) - ALPHAR/(PR*(DRS**2))
 D(I)= T(I,J+1,K)/DT
 100 CONTINUE
C ———— COEFFICIENTS OF ENERGY EQUATION FOR THE FLUID
 DO 99 I= NS1+2, NS1+N
 II= I-NS1
```

```
R= N2+(I-1)*DR
PRDR= 2*PR*DR
A(I)= 1.0/(PRDR*R)-1.0/(PR*(DR**2))- V(II,J,K)/(2*DR)
B(I)= 1.0/DT+ U(II,J,K)/DZ+2.0/(PR*(DR**2))
C(I)= V(II,J,K)/(2*DR) - 1.0/(PRDR*R)-1.0/(PR*(DR**2))
D(I)= T(I,J+1,K)/DT+(U(II,J,K)/DZ)*T(I,J,K+1)
99 CONTINUE
C————— COEFFICIENTS OF CONDUCTION EQUATION FOR THE OUTER
C CYLINDER THICKNESS
DO 98 I= NSI, NSF
R= N3+(I-1)*DRS
PRDR= 2.0*PR*DRS
A(I)= ALPHAR/(PRDR*R) - ALPHAR/(PR*(DRS**2))
B(I)= 1.0/DT+(2.0*ALPHAR)/(PR*(DRS**2))
C(I)= -ALPHAR/(PRDR*R) - ALPHAR/(PR*(DRS**2))
D(I)= T(I,J+1,K)/DT
98 CONTINUE
C YOU KNOW THIS OK!
D(NSF)= D(NSF)-C(NSF)*T(NTS,J+1,K+1)
C————— COEFFICIENTS AT THE INTERFACE BETWEEN THE FLUID
C————————AND THE OUTER SURFACES OF THE INNER CYLINDER
```

```
      A(NS1+1)= -KR*DR/DRS
      B(NS1+1)= (KR*DR/DRS+1)
      C(NS1+1)= -1.0
      D(NS1+1)= 0.0
      C ———— COEFFICIENTS AT THE INTERFACE BETWEEN THE FLUID
      C ————AND THE INNER SURFACES OF THE OUTER CYLINDER
      A(NS1+N+1)= -1.0
      B(NS1+N+1)= (1.0+KR*DR/DRS)
      C(NS1+N+1)= -KR*DR/DRS
      D(NS1+N+1)= 0.0
      C ———— INNER CYLINDER SURFACE CONDITION(ADIABATIC)
      A(1)= 0.0
      B(1)= +1.0
      C(1)= -1.0
      D(1)= 0.0
      C ——— APPLYING THOMAS ALGORITHM TO GET THE TEMPERA-
TURES
      C ——— FORWARD ELIMINATION
      ATH(1)= B(1)
      DTH(1)= D(1)
      DO 500 I= 2,NTS-1
```

```
      ATH(I)= B(I)-A(I)*C(I-1)/ATH(I-1)
      DTH(I)= D(I)-A(I)*DTH(I-1)/ATH(I-1)
      500 CONTINUE
     C ———— BACK SUBSTITUTION
      T(NTS-1,J+1,K+1)= DTH(NTS-1)/ATH(NTS-1)
      DO 550 I= NTS-2,1,-1
      T(I,J+1,K+1)=(DTH(I)-C(I)*T(I+1,J+1,K+1))/ATH(I)
      550 CONTINUE
     C —— ESTIMATION OF COEFFICIENTS OF AXIAL VELOCITY EQUA-
TION
      DO 400 I=2,N
      A(I)= (DZ/DR)*(-V(I,J,K)/2.0+1.0/(2.0*(N2+(I-1)*DR))-1.0/DR)
      B(I)= U(I,J,K)+DZ/DT+2.0*DZ/DR**2
      C(I)= (DZ/DR)*(V(I,J,K)/2.0-1.0/(2.0*(N2+(I-1)*DR))-1.0/DR)
      D(I)= U(I,J,K)*U(I,J,K+1)+U(I,J,K)*DZ/DT+P(J,K+1)+
     * DZ*T(NS1+I,J+1,K+1)/(16*((1-N2)**4))
      AP(I)=1.0
      400 CONTINUE
     C ———— VELOCITY AT THE BOUNDARIES
      U(1,J+1,K+1)= 0.0
      V(1,J+1,K+1)= 0.0
```

```
U(N+1,J+1,K+1)= 0.0
V(N+1,J+1,K+1)= 0.0
C ——— VELOCITY COEFFICIENTS OF CONTINUITY(IN INTEGRAL FORM)
DI= (1-N2**2)*U1/(2.0*DR)
DO 200 I=2,N
E(I)= N2+(I-1)*DR
200 CONTINUE
C ———— INITILIZATION AND PREPARING
DO 401 I=1,N+1
DO 401 L=1,N+1
AS(I,L)= 0.0
401 CONTINUE
C PREPARING THE VELOCITY AND PRESSURE COEFFICIENTS OR
C THE SUBROUTINE GAUSS 1ST COEFF. RESULTING FROM
C CONTINUITY INTEGRAL EQUATION
DO 300 I=2,N
AS(1,I-1)= E(I)
300 CONTINUE
AS(1,N)= 0.0
AS(1,N+1)= DI
C 2ND COEFF. RESULTING FROM AXIAL VELOCITY COEFF.
```

```
      DO 301 I=2,N
      AS(I,I-1)= B(I)
      AS(I,N+1)= D(I)
      AS(I,N)= AP(I)
      IF(I.EQ.N) GO TO 301
      AS(I,I)= C(I)
      AS(I+1,I-1)= A(I+1)
  301 CONTINUE
      CALL GAUSS(N,AS,X)
C ————————— VELOCITY AND PRESSURE VALUES
      DO 600 I= 2,N
      U(I,J+1,K+1)= X(I-1)
      P(J+1,K+1)= X(N)
  600 CONTINUE
C ——— VERTICAL VELOCITY ESTIMATION USING THE CONTINUITY
C ———EQUATION
      DO 700 I=1,N-1
      C1= N2+I*DR
      C2= N2+(I-1)*DR
      C3= 2*N2+(2*I-1)*DR
      A(I)= C2/C1
```

```
B(I)= (C3/C1)*DR/(4*DZ)

UT= U(I+1,J+1,K+1)+U(I,J+1,K+1)-U(I+1,J,K+1)-U(I,J,K+1)

V(I+1,J+1,K+1)= A(I)*V(I,J+1,K+1)-B(I)*UT

700 CONTINUE

C ———————— PROCEEDING IN THE AXIAL DIRECTION

999 CONTINUE


C ———PESSURE CONVERGENCE AND INITIAL VELOCITY GUESS

PF= P(JC+1,K+1)

IF(ABS(PF).LE.EPS) GO TO 8000

IF(PF .GT. EPS) THEN

U2= FACI*U1

U1= (U2+U1)/2.0

IT= IT+1

C ———————— INLET VELOCITY

DO 2 I= 2,N

2 U(I,1,K+1)= U1

GO TO 1001


ELSEIF(PF .LT. NEPS) THEN

U2= FACD*U1
```

```
U1= (U2+U1)/2.0
IT= IT+1
C ———————— INLET VELOCITY
DO 3 I= 2,N
3 U(I,1,K+1)= U1
GO TO 1001
ENDIF
8000 WRITE(*,*) IT, K, U1, PF, P(JC/2,K+1)
WRITE(14,901) K*DT, F
C ———————— VARIATION WITH TIME
1000 CONTINUE
C —ESTIMATION OF MIXING CUP AND HEAT ABSORBED AT EXIT
DO 4100 J=10,JC+1,10
SRU=0.0
SRUT=0.0
DO 4200 K= 2,KC+1,1
SRU=0.0
SRUT=0.0
DO 3000 I=2,N
II=NS1+I
R=N2+(I-1)*DR
```

```
RUT=R*U(I,J+1,K)*T(II,J+1,K)
RU= R*U(I,J+1,K)
SRU=SRU+RU
SRUT=SRUT+RUT
3000 CONTINUE
TM= SRUT/SRU
H= 2*DR*SRUT
WRITE(11,901) (K-1)*DT, TM
WRITE(12,901) (K-1)*DT, H
4200 CONTINUE
4100 CONTINUE
SRU=0.0
SRUT=0.0
DO 4500 K= 2,21,1
SRU=0.0
SRUT=0.0
DO 4600 J=1,JC
SRU=0.0
SRUT=0.0
DO 3100 I=2,N
II=NS1+I
```

```
R=N2+(I-1)*DR

RUT=R*U(I,J+1,K)*T(II,J+1,K)

RU= R*U(I,J+1,K)

SRU=SRU+RU

SRUT=SRUT+RUT

3100 CONTINUE


TM= SRUT/SRU

H= 2*DR*SRUT

WRITE(25,*) J, TM

WRITE(26,*) J, H

4600 CONTINUE

4500 CONTINUE


WRITE(3,900) ((U(I,JC/2,K),I=1,N+1),K=2,21,1)

WRITE(5,900) ((V(I,JC/2,K),I=1,N+1),K=2,21,1)

WRITE(8,900) ((T(I,JC/2,K),I=1,NTS),K=2,21,1)

WRITE(10,900) ((T(1,J,K),J=1,JC+1),K=2,21,1)


WRITE(22,333) ((U(I,JC+1,K),I=1,N+1),K=2,21,1)

WRITE(23,333) ((V(I,JC+1,K),I=1,N+1),K=2,21,1)
```

```
WRITE(24,333) ((T(I,JC+1,K),I=1,NTS),K=2,26,1)
WRITE(4,444) (U(I,2,20),I=1,N+1)
WRITE(4,444) (U(I,8,20),I=1,N+1)
WRITE(4,444) (U(I,10,20),I=1,N+1)
WRITE(4,444) (U(I,12,20),I=1,N+1)
WRITE(4,444) (U(I,20,20),I=1,N+1)
WRITE(4,444) (U(I,25,20),I=1,N+1)
WRITE(4,444) (U(I,30,20),I=1,N+1)
WRITE(4,444) (U(I,40,20),I=1,N+1)
WRITE(4,444) (U(I,50,20),I=1,N+1)
WRITE(6,666) (V(I,2,20),I=1,N+1)
WRITE(6,666) (V(I,6,20),I=1,N+1)
WRITE(6,666) (V(I,12,20),I=1,N+1)
WRITE(6,666) (V(I,15,20),I=1,N+1)
WRITE(6,666) (V(I,20,20),I=1,N+1)
WRITE(6,666) (V(I,25,20),I=1,N+1)
WRITE(6,666) (V(I,30,20),I=1,N+1)
WRITE(6,666) (V(I,35,20),I=1,N+1)
WRITE(6,666) (V(I,40,20),I=1,N+1)
WRITE(6,666) (V(I,50,20),I=1,N+1)
WRITE(7,777) (P(J,2),J=1,JC+1)
```

```
WRITE(7,777) (P(J,3),J=1,JC+1)
WRITE(7,777) (P(J,5),J=1,JC+1)
WRITE(7,777) (P(J,7),J=1,JC+1)
WRITE(7,777) (P(J,9),J=1,JC+1)
WRITE(7,777) (P(J,12),J=1,JC+1)
WRITE(7,777) (P(J,15),J=1,JC+1)
WRITE(7,777) (P(J,18),J=1,JC+1)
WRITE(7,777) (P(J,20),J=1,JC+1)
WRITE(7,777) (P(J,30),J=1,JC+1)
WRITE(7,777) (P(J,50),J=1,JC+1)
WRITE(7,777) (P(J,60),J=1,JC+1)
WRITE(7,777) (P(J,70),J=1,JC+1)
WRITE(7,777) (P(J,80),J=1,JC+1)
WRITE(7,777) (P(J,90),J=1,JC+1)
WRITE(7,777) (P(J,100),J=1,JC+1)
WRITE(9,900) (T(I,6,20),I=1,NTS)
WRITE(9,900) (T(I,8,20),I=1,NTS)
WRITE(9,900) (T(I,10,20),I=1,NTS)
WRITE(9,900) (T(I,15,20),I=1,NTS)
WRITE(9,900) (T(I,20,20),I=1,NTS)
WRITE(9,900) (T(I,25,20),I=1,NTS)
```

```
WRITE(9,900) (T(I,30,20),I=1,NTS)
WRITE(9,900) (T(I,35,20),I=1,NTS)
WRITE(9,900) (T(I,40,20),I=1,NTS)
WRITE(9,900) (T(I,45,20),I=1,NTS)
WRITE(9,900) (T(I,50,20),I=1,NTS)
WRITE(16,444) (U(I,2,35),I=1,N+1)
WRITE(16,444) (U(I,8,35),I=1,N+1)
WRITE(16,444) (U(I,10,35),I=1,N+1)
WRITE(16,444) (U(I,12,35),I=1,N+1)
WRITE(16,444) (U(I,20,35),I=1,N+1)
WRITE(16,444) (U(I,25,35),I=1,N+1)
WRITE(16,444) (U(I,30,35),I=1,N+1)
WRITE(16,444) (U(I,40,35),I=1,N+1)
WRITE(16,444) (U(I,50,35),I=1,N+1)
WRITE(17,666) (V(I,2,35),I=1,N+1)
WRITE(17,666) (V(I,6,35),I=1,N+1)
WRITE(17,666) (V(I,12,35),I=1,N+1)
WRITE(17,666) (V(I,15,35),I=1,N+1)
WRITE(17,666) (V(I,20,35),I=1,N+1)
WRITE(17,666) (V(I,25,35),I=1,N+1)
WRITE(17,666) (V(I,30,35),I=1,N+1)
```

```
WRITE(17,666) (V(I,35,35),I=1,N+1)
WRITE(17,666) (V(I,40,35),I=1,N+1)
WRITE(17,666) (V(I,50,35),I=1,N+1)
WRITE(18,900) (T(I,6,35),I=1,NTS)
WRITE(18,900) (T(I,8,35),I=1,NTS)
WRITE(18,900) (T(I,10,35),I=1,NTS)
WRITE(18,900) (T(I,15,35),I=1,NTS)
WRITE(18,900) (T(I,20,35),I=1,NTS)
WRITE(18,900) (T(I,25,35),I=1,NTS)
WRITE(18,900) (T(I,30,35),I=1,NTS)
WRITE(18,900) (T(I,35,35),I=1,NTS)
WRITE(18,900) (T(I,40,35),I=1,NTS)
WRITE(18,900) (T(I,50,35),I=1,NTS)
WRITE(19,444) (U(I,2,45),I=1,N+1)
WRITE(19,444) (U(I,8,45),I=1,N+1)
WRITE(19,444) (U(I,10,45),I=1,N+1)
WRITE(19,444) (U(I,12,45),I=1,N+1)
WRITE(19,444) (U(I,20,45),I=1,N+1)
WRITE(19,444) (U(I,25,45),I=1,N+1)
WRITE(19,444) (U(I,30,45),I=1,N+1)
WRITE(19,444) (U(I,40,45),I=1,N+1)
```

```
WRITE(19,444) (U(I,50,45),I=1,N+1)
WRITE(20,666) (V(I,2,45),I=1,N+1)
WRITE(20,666) (V(I,6,45),I=1,N+1)
WRITE(20,666) (V(I,12,45),I=1,N+1)
WRITE(20,666) (V(I,15,45),I=1,N+1)
WRITE(20,666) (V(I,20,45),I=1,N+1)
WRITE(20,666) (V(I,25,45),I=1,N+1)
WRITE(20,666) (V(I,30,45),I=1,N+1)
WRITE(20,666) (V(I,35,45),I=1,N+1)
WRITE(20,666) (V(I,40,45),I=1,N+1)
WRITE(20,666) (V(I,50,45),I=1,N+1)
WRITE(21,900) (T(I,6,45),I=1,NTS)
WRITE(21,900) (T(I,8,45),I=1,NTS)
WRITE(21,900) (T(I,10,45),I=1,NTS)
WRITE(21,900) (T(I,15,45),I=1,NTS)
WRITE(21,900) (T(I,20,45),I=1,NTS)
WRITE(21,900) (T(I,25,45),I=1,NTS)
WRITE(21,900) (T(I,30,45),I=1,NTS)
WRITE(21,900) (T(I,35,45),I=1,NTS)
WRITE(21,900) (T(I,40,45),I=1,NTS)
WRITE(21,900) (T(I,50,45),I=1,NTS)
```

```
333 FORMAT(F20.10)
444 FORMAT(F20.10)
555 FORMAT(F20.10)
666 FORMAT(F20.10)
777 FORMAT(F20.10)
888 FORMAT(F20.10)
900 FORMAT(F20.10)
901 FORMAT(F10.7, 5X, F20.10)
STOP
END
SUBROUTINE GAUSS(N,AS,X)
REAL AS(50,50), X(50)
INTEGER I,J,K
K=1
5 T=1.0/AS(K,K)
J=K
1 AS(K,J)=AS(K,J)*T
J=J+1
IF(J.LE.N+1) GO TO 1
I=1
4 IF(K.EQ.I) GO TO 2
```

```
T= AS(I,K)
C MODIFICATION OF THE GAUSS-JORDAN METHOD TO GET
C BENEFIT FROM THE MANY ZEROS
IF(T.EQ.0.0) GO TO 2
J=K
3 AS(I,J)= AS(I,J)-T*AS(K,J)
J=J+1
IF(J.LE.N+1) GO TO 3
2 I=I+1
IF(I.LE.N) GO TO 4
K=K+1
IF(K.LE.N) GO TO 5
DO 11 I=1,N
X(I)=AS(I,N+1)
11 CONTINUE
RETURN
END
```

APPENDIX C: FORTRAN PROGRAM FOR THE STEADY-STATE CASE

```
C This Program is Written to Solve the Combined Conduction-Laminar C Natural Convection in Vertical Concentric Annulus Using the
C Boundary-Layer Assumptions (Steady-State Case).
      REAL U(155,4000), V(155,4000), T(155,4000), P(4000), A(155), B(155), C(155), D(155),
     * X(155), AP(155), E(155), AS(155,155), ATH(155), DTH(155)

      REAL N1, N2, N3, N4, KR, NEPS, EPS, R
      INTEGER N, NS1, NS2
      OPEN(3,FILE='OU')
      OPEN(4,FILE='OV')
      OPEN(5,FILE='OP')
      OPEN(6,FILE='OTM')
      OPEN(7,FILE='OHM')
      OPEN(8,FILE='OT')
      OPEN(9,FILE='OTNS10')
C ********** GRID SIZE AND NUMBER
      JZ= 3999
```

```
DZ= 2E-7

DR= 0.0125

DRS= 0.0125

N= 40

NS1= 8

NS2= 16

N1=0.4

N2=0.5

N3=1.0

N4=1.2

NTS=NS1+N+NS2+1

C ********** ENGINEERING PARAMETERS

KR= 0.001

PR= 0.7

FR= 0.0001057

C ********** INITIALIZATION OF:

C ———————— AXIAL & RADIAL & PRESSURE

DO 10 J=1,JZ

DO 11 I=1,N+1

U(I,J)=0.0

11 V(I,J)=0.0
```

```
 10 P(J)= 0.0
C ————————— TEMPERATURE
 DO 12 J=1,JZ
 DO 12 I=1,NTS
 T(I,J)=0.0
 12 CONTINUE
C ********** BOUNDARY CONDITIONS AT THE ENTRANCE
C ———— INLET VELOCITY U0
 U0= FR/(1.0-N2**2)
 DO 79 I= 2,N
 U(I,1)= U0
 V(I,1)= 0.0
 79 CONTINUE
C ********** PRESSURE AT THE INLET
 P(1)= -0.5*(FR/(1.0-N2**2))**2
C ———— TEMPERATURE AT THE INLET
 DO 80 I=1,NTS
 T(I,1)= 0.0
 80 CONTINUE
C ————— BOUNDARY CONDITIONS AT THE INNER AND
C ————————THE OUTER WALLS.
```

```
      DO 81 J=1,JZ+1
      U(1,J)= 0.0
      U(N+1,J)= 0.0
      V(1,J)= 0.0
      V(N+1,J)= 0.0
      T(NTS,J)= 1.0
   81 CONTINUE
      ZL=0.0
      DO 3 KC= 1,1000
C ************************** MAIN LOOP
      DO 1000 J= 1,JZ
C IN STEADY STATE WE GIVE INPUT FR (INLET FLOW RATE)
C AND CONTINUE CALCULATIONS UNTIL THE PRESSURE
C (P) IS ZERO WHICH MEANS THE END OF THE CHANNEL
      IF(KC.GT.1) DZ=2E-6
      IF(KC.GT.2) DZ=2E-5
      IF(KC.GT.3) DZ=2E-3
      IF(KC.GT.4) DZ=2E-2
      Z= J*DZ
C ——— COEFFICIENTS ESTIMATION FOR TEMPERATURE
C CALCULATIONS COEFFICIENTS OF CONDUCTION EQUATION
```

```
C FOR THE INNER CYLINDER THICKNESS
 DO 100 I=2,NS1
 R=N1+(I-1)*DRS
 A(I)=-1.0/DRS**2 + 1.0/(2.0*R*DRS)
 B(I)=+2.0/DRS**2
 C(I)=-1.0/DRS**2 - 1.0/(2.0*R*DRS)
 D(I)= 0.0
 100 CONTINUE
C ------- COEFFICIENTS OF ENERGY EQUATION FOR FLUID
 NFI=NS1+2
 NFF=NS1+N
 DO 99 I= NFI,NFF
 R=N2+(I-1)*DR
 PRDR=2*PR*DR
 II=I-NS1
 A(I)=1.0/(PRDR*R) - 1.0/(PR*(DR**2)) - V(II,J)/(2*DR)
 B(I)=U(II,J)/DZ+2.0/(PR*(DR**2))
 C(I)=V(II,J)/(2.0*DR) - 1.0/(PRDR*R)-1.0/(PR*(DR**2))
 D(I)=T(I,J)*U(II,J)/DZ
 99 CONTINUE
C ------- COEFFICIENTS OF CONDUCTION EQUATION FOR
```

```
C THE OUTER CYLINDER THICKNESS

 NSI=NS1+N+2

 NSF=NS1+N+NS2

 DO 98 I=NSI, NSF

 R=N3+(I-1)*DRS

 A(I)=-1.0/DRS**2 + 1.0/(2*R*DRS)

 B(I)=+2.0/DRS**2

 C(I)=-1.0/DRS**2 - 1.0/(2*R*DRS)

 D(I)= 0.0

 98 CONTINUE

C YOU KNOW THIS OK!

 D(NSF)=D(NSF)-C(NSF)*T(NTS,J+1)

C ——— COEFFICIENTS AT THE INTERFACE BETWEEN

C THE FLUID AND THE OUTER SURFACE OF THE INNER CYLINDER

 A(NS1+1)= -KR*DR/DRS

 B(NS1+1)= (KR*DR/DRS+1)

 C(NS1+1)= -1.0

 D(NS1+1)= 0.0

C ——— COEFFICIENTS AT THE INTERFACE BETWEEN

C THE FLUID AND THE INNER SURFACE OF THE OUTER CYLINDER
```

```
A(NS1+N+1)= -1.0

B(NS1+N+1)= (1.0+KR*DR/DRS)

C(NS1+N+1)= -KR*DR/DRS

D(NS1+N+1)= 0.0

C ——— INNER CYLINDER SURFACE CONDITION (ADIABATIC)

A(1)= 0.0

B(1)= +1.0

C(1)= -1.0

D(1)= 0.0


C APPLYING THOMAS ALGORITHM TO GET THE TEMPERATURES

C ——— FORWARD ELIMINATION

ATH(1)=B(1)

DTH(1)=D(1)

DO 500 I=2,NTS-1

ATH(I)= B(I)- A(I)*C(I-1)/ATH(I-1)

DTH(I)= D(I)- A(I)*DTH(I-1)/ATH(I-1)

500 CONTINUE

C ——— BACKWARD SUBSTITUTION

T(NTS-1,J+1)= DTH(NTS-1)/ATH(NTS-1)

DO 550 I=NTS-2,1,-1
```

```
T(I,J+1)=(DTH(I)-C(I)*T(I+1,J+1))/ATH(I)

550 CONTINUE

C ********** AXIAL VELOCITY

DO 400 I=2,N

R= N2+(I-1)*DR

A(I)= DZ/(2.0*R*DR) - V(I,J)*DZ/(2.0*DR) - DZ/(DR**2)

B(I)= U(I,J) + 2.0*DZ/(DR**2)

C(I)= V(I,J)*DZ/(2.0*DR) - DZ/(DR**2) - DZ/(2.0*R*DR)

D(I)= DZ*T(NS1+I,J+1)/(16*((1.0-N2)**4)) + U(I,J)*U(I,J) + P(J)

AP(I)= 1.0

400 CONTINUE

C ——— VELOCITY AT THE BOUNDARIES

U(1,J+1) = 0.0

V(1,J+1) = 0.0

U(N+1,J+1) =0.0

V(N+1,J+1) =0.0

C ——— VELOCITY COEFFICIENTS OF CONTINUITY (INTEGRAL FORM)

DI=FR/(2.0*DR)

DO 200 I=2,N

E(I)= N2+(I-1)*DR

200 CONTINUE
```

```
C ********** INITIALIZATION AND PREPARING FOR GAUSS SUBROU-
TINE
      DO 401 I=1,N+1
      DO 401 L=1,N+1
      AS(I,L)= 0.0
      401 CONTINUE
      C PREPARING THE VELOCITY AND PRESSURE COEFFICIENTS FOR
      C THE SUBROUTINE GAUSS 1ST COEFF. RESULTING FROM
      C CONTINUITY INTEGRAL EQUATION
      DO 300 I=2,N
      AS(1,I-1)= E(I)
      300 CONTINUE
      AS(1,N)= 0.0
      AS(1,N+1)= DI
      C 2ND COEFF. RESULTING FROM AXIAL VELOCITY COEFF.
      DO 301 I=2,N
      AS(I,I-1)=B(I)
      AS(I,N+1)=D(I)
      AS(I,N)=AP(I)
      IF(I.EQ.N) GO TO 301
      AS(I,I)=C(I)
```

```
      AS(I+1,I-1)=A(I+1)
  301 CONTINUE
C ——— CALLING THE SUB. GAUSS TO SOLVE THE AXIAL
C VELOCITY U AND THE PRESSURE P
      CALL GAUSS(N,AS,X)
      DO 600 I=2,N
      U(I,J+1)= X(I-1)
  600 CONTINUE
      P(J+1)= X(N)
C —— VERTICAL VELOCITY (V) ESTIMATION USING
C THE CONTINUITY EQUATION
      DO 700 I=1,N-1
      C1=N2+I*DR
      C2=N2+(I-1)*DR
      C3=2*N2+(2*I-1)*DR
      A(I)= C2/C1
      B(I)= (C3/C1)*DR/(4*DZ)
      UT= U(I+1,J+1)+U(I,J+1)-U(I+1,J)-U(I,J)
      V(I+1,J+1)= A(I)*V(I,J+1)-B(I)*UT
  700 CONTINUE
C ESTIMATION OF MIXING CUP AND HEAT ABSORBED AT EXIT
```

```
SRU=0.0

SRUT=0.0


DO 3000 I=2,N

II=NS1+I

R=N2+(I-1)*DR

RUT=R*U(I,J+1)*T(II,J+1)

RU= R*U(I,J+1)

SRU=SRU+RU

SRUT=SRUT+RUT

3000 CONTINUE


TM= SRUT/SRU

HM= 2*DR*SRU*TM

WRITE(6,*) ZI+Z, TM

WRITE(7,*) ZI+Z, HM

C——— EXAMINING IF THE FLOW REACHE THE

C ———EXIT CONDITIONS, i.e.

C P IS ~ZERO

JC= J+1

PF=P(JC)
```

```
IF(PF.GT.0.0) GO TO 1001
C ******** PROCEEDING IN THE AXIAL DIRECTION
1000 CONTINUE
WRITE(*,*) PF, KC, T(N,JC), T(NS1+N,JC), T(NS1+N+NS2,JC)
ZL= ZL+Z
C ————————— REPACKAGE
DO 1 I=1,NTS
1 T(I,1)= T(I,JC)
DO 2 I=2,N
V(I,1)= V(I,JC)
2 U(I,1)= U(I,JC)
P(1)=P(JC)
3 CONTINUE
1001 CONTINUE
ZL=ZL+Z
WRITE(*,*) ZL, PF, KC
C ********* WRITING SECTION ************
R=N2+(I-1)*DR

WRITE(3,*) R,U(I,4),U(I,20),U(I,150),U(I,250),U(I,400),U(I,500)
WRITE(4,*) R,V(I,4),V(I,8),V(I,16),V(I,32), V(I,64), V(I,128)
```

```
6000 CONTINUE
DO 7000 J=1,JC
WRITE(5,2003) (J-1)*DZ, P(J)
7000 CONTINUE
DO 8000 I=1,NTS
R=N1+(I-1)*DR
WRITE(8,*) R,T(I,4),T(I,20),T(I,150),T(I,250),T(I,500)
8000 CONTINUE
DO 8000 I=1,NTS
R=N1+(I-1)*DR
WRITE(8,*) R,T(I,J)
8000 CONTINUE
2001 FORMAT(F15.10,3X,F15.9)
2002 FORMAT(F15.10,3X,F15.9)
2003 FORMAT(F15.10,3X,5PF15.9)
2004 FORMAT(F15.10,3X,F15.9)
2005 FORMAT(F15.10,3X,F15.9)
STOP
END
C THIS SUBROUTINE IS TO SOLVE THE MATRIX OF THE
C AXIAL VELOCITY USING A MODIFIED METHOD
```

```
C OF GUASS-GORDAN
 SUBROUTINE GAUSS(N,AS,X)
 REAL AS(155,155), X(155)
 INTEGER I,J,K
 K=1
 5 T=1.0/AS(K,K)
 J=K
 1 AS(K,J)= AS(K,J)*T
 J=J+1
 IF(J.LE.N+1) GO TO 1
 I=1
 4 IF(K.EQ.I) GO TO 2
 T=AS(I,K)
 IF(T.EQ.0.0) GO TO 2
 J=K
 3 AS(I,J)=AS(I,J)-T*AS(K,J)
 J=J+1
 IF(J.LE.N+1) GO TO 3
 2 I=I+1
 IF(I.LE.N) GO TO 4
 K=K+1
```

```
IF(K.LE.N) GO TO 5
DO 11 I=1,N
X(I)=AS(I,N+1)
11 CONTINUE
RETURN
END
```

REFERENCES

1. A. E. Zinnes. The coupling of conduction with laminar natural convection from a vertical flat plate with arbitrary surface heating. *J. Heat Transfer*, 92:528–535, 1970.

2. M. Miyamoto, J. Sumikawa, T. Akiyoshi, and T. Nakamura. Effects of axial heat conduction in a vertical flat plate on free convection heat transfer. *Int. J. Heat and Mass Transfer*, 23:1545–1553, 1980.

3. A. Pozzi and M. Lupo. The coupling of conduction with laminar natural convection along a flat plate. *Int. J. Heat Mass Transfer*, 31(9):1807–1814, 1988.

4. S. Lee and M. N. Yovanovich. Conjugate heat transfer from a vertical plate with discrete heat sources under natural convection. *J. Electronics Packaging*, 111(4):261–267, 1989.

5. H. Chen and L. Fang. Simple computational method for conjugate conduction-natural convection along a vertical plate fin. *Engineering Analysis with Boundary Elements*, 10:93–98, 1992.

6. W. S. Yu and H. T. Lin. Conjugate problems of conduction and free convection on vertical and horizontal flat plates. *Int. J. Heat and Mass Transfer*, 36:1303–1313, 1993.

7. M. Vynnycky and S. Kimura. Conjugate free convection due to a heated vertical plate. *Int. J. Heat Mass Transfer*, 39:1067–1080, 1996.

8. J. H. Merkin and I. Pop. Conjugate free convection on a vertical surface. *Int. J. Heat Mass Transfer*, 39(7):1527–1534, 1996.

9. M. D. Kelleher and K. Yang. A steady conjugate heat transfer problem with conduction and free convection. *Appl. Sci. Res.*, pages 249–269, 1967.

10. G. S. H. Lock and R. S. Ko. Coupling through a wall between two free convection systems. *Int. J. Heat Mass Transfer*, 16:2087–2096, 1973.

11. R. Anderson and A. Bejan. Natural convection on both sides of a vertical wall separating fluids at different temperatures. *Int. J. Heat Mass Transfer*, 102:630–635, 1980.

12. R. Viskanta and D. W. Lankford. Coupling of heat transfer between two natural convection systems separated by a vertical wall. *Int. J. Heat Mass Transfer*, 24:1171–1177, 1981.

13. M. Sikakibara, H. Amaya, S. Mori, and A. Tanimoto. Conjugate heat transfer between two

natural convection separated by a vertical plate. *Int. J. Heat Mass Transfer*, 35:2289–2297, 1992.

14. T. Burch, T. Rhodes, and S. Acharya. Laminar natural convection between finitely conducting vertical plates. *Int. J. Heat and Mass Transfer*, 28(6):1173–1186, 1985.

15. J. P. Yeh, H. Shaw, and M. J. Huang. Analysis of conjugate laminar natural convection beetween finitely top heating vertical channel flow. *WaermeOund Stoffuebertraging/Thermo- and Fluid Dynamics*, 25(6):321–329, 1990.

16. M. Lacroix and A. Joyeux. Coupling of wall conduction with natural convection from heated cylinders in rectangular enclosure. *Int. Comm. Heat Mass Transfer*, 23:143–151, 1996.

17. M. Molki and M. Faghri. Conjugate natural convection heat transfer in a vertical annulus with internal circunferential fins. *Numerical Heat Transfer, Part A*, 25:457–476, 1994.

18. Y. Huang and S. Aggarwal. Effect of wall conduction on natural convection in an enclosure with a centered heat source. *J. Elecrotnic Packaging*, 117:301–306, 1995.

19. S. Kimura and I. Pop. Conjugate natural convection from a horizontal circular cylinder. *Numerical Heat Transfer, Part A*, 25:347–361, 1994.

20. Y. S. Sun and A. F. Emery. Effects of wall conduction, internal heat sources and an internal baffle on natural convection heat transfer in rectangular enclosure. *Int. J. Heat Mass Transfer*, 40:915–929, 1997.

21. H. Schlichting. Boundary-layer theory. *McGrawHill*, 1979.

22. J. R. Bodoia and J. F. Osterle. The development of free convection between heated vertical plates. *J. Heat Transfer*, 84:44–50, 1962.

23. M. A. I. El-Shaarawi and A. Sarhan. Developing laminar free convection in an open ended vertical concentric annulus with a rotating inner cylinder. *J. Heat Transfer*, 103:552–558, 1981.

24. M. Attas. Unsteady natural convection in open ended vertical concentric annuli. 1992.

25. C. Cheng and S. Huang. Enhancement of flare method for predicting buoyancy-induced flow reversal in vertical ducts via parabolic model. *Numerical Heat Traansfer, Part B*, 31:327–345, 1997.

26. H. M. Joshi. Transient effects in natural convection cooling of vertical parallel plates. *Int. Comm. Heat Mass Transfer*, 15:227–238, 1988.

27. M. A. I. El-Shaarwi. Derivation of boundary-layer equations for cases with curved boundaries. *Int. J. Engineering Fluid Mechanics*, 3:113–128, 1990.

IMAGE EVALUATION TEST TARGET (QA-3)

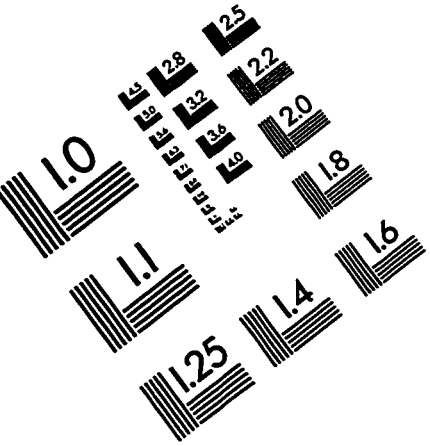

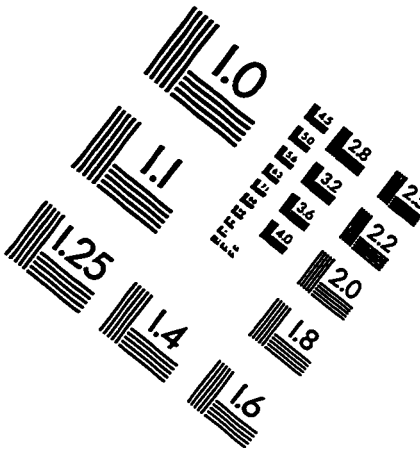

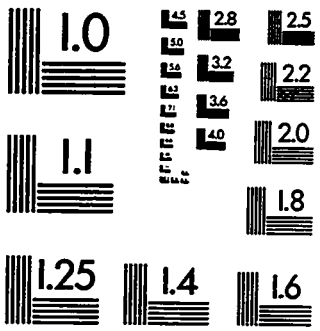

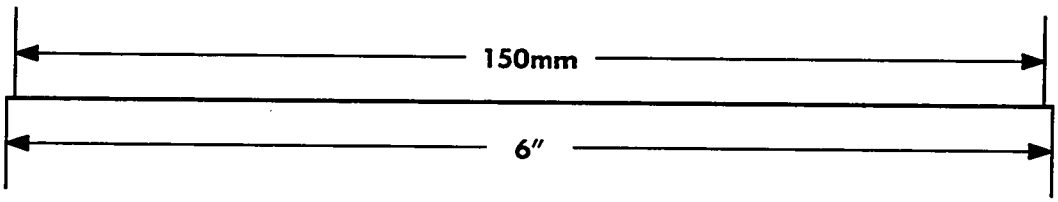

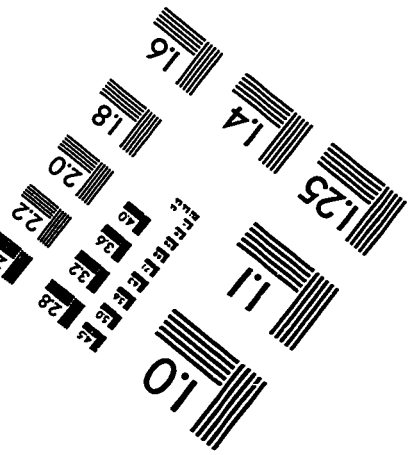

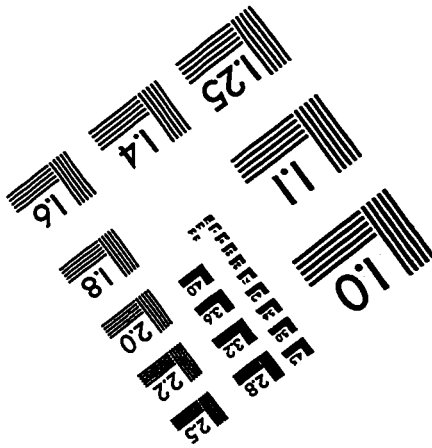

APPLIED IMAGE, Inc
1653 East Main Street
Rochester, NY 14609 USA
Phone: 716/482-0300
Fax: 716/288-5989